DISSERTATION

HYDROLOGICAL ASSESSMENT OF FIELD-SCALE GEOWASTE AND WASTE ROCK TEST PILES

Submitted by

Mohammad Reza Hassanzadeh Gorakhki

Department of Civil and Environmental Engineering

In partial fulfillment of the requirements

For the Degree of Doctor of Philosophy

Colorado State University

Fort Collins, Colorado

Spring 2020

Doctoral Committee:

Advisor: Christopher Bareither

Charles Shackelford
Joseph Scalia
Paul Heyliger
Greg Butters

ABSTRACT

HYDROLOGICAL ASSESSMENT OF FIELD-SCALE GEOWASTE AND WASTE ROCK TEST PILES

Mine waste rock and mine tailings are generated in substantial quantities an d must be managed to protect human health and the environment. Challenges in mine waste management facilities include geotechnical stability, environmental contamination, water management, and post operation (long term) closure. Waste rock and tailings co-disposal is a management technique that can address many of the aforementioned challenges. GeoWaste is a mixture of fast-filtered tailings and waste rock blended to isolate waste rock particles within a tailings-dominated matrix. A field-scale experiment that included a waste rock pile and GeoWaste pile was conducted at a mine in Central America to evaluate if GeoWaste suppresses sulfide oxidation and production of metal-rich acid rock drainage relative to waste rock. The objectives of this study were to (i) evaluate hydrologic performance of the piles, (ii) conduct in situ infiltration tests on the piles, (iii) determine field-scale hydraulic parameters for GeoWaste and waste rock, and (iv) develop numerical models to predict water content and oxygen concentrations within the piles. Water content, temperature, electrical conductivity, and oxygen concentration within the piles were monitored for 26 months. Sealed double ring infiltrometer tests were conducted at the end of the pile experiment and test pile subsequently were excavated to assess the spatial distribution in geotechnical characteristics. Inverse modeling was completed in HYDRUS-2D based on infiltration data to determine hydraulic conductivity and moisture retention parameters for the test piles. Field- and laboratory-scale hydraulic parameters were used in HYDRUS-1D and HYDRUS-2D to develop seepage models to predict moisture movement during the 26-month

pile experiment. Oxygen concentration was predicted for the GeoWaste pile in HYDRUS-1D via the solute transport module, Fick's 2^{nd} law, the oxygen consumption rate, oxygen diffusion in gas and water phases, and Henry's constant.

ACKNOWLEDGEMENTS

I would never have been able to finish my thesis without the guidance of my committee members, help from colleagues, and support from my family.

First and foremost, I would like to thank Dr. Christopher Bareither for guiding me through seven years of graduate school. The knowledge I gained from working with him is priceless. I would also like to extend my thanks to Dr. Scalia for providing support and guidance throughout my Ph.D. I would like to thank Professor Shackelford, Professor Butters, and Professor Heyliger for serving as committee members.

I would like to thank the entire geo-group at the Colorado State University. I would like to thank Matteus Hamade and Raquel Borja for their assistance with all my laboratory testing.

Financial support for this study was provided by the National Science Foundation (CMMI #1538344), Newmont (originally as Goldcorp and then Newmont Goldcorp), and Colorado State University. The opinions, findings, and conclusions expressed herein are those of the author and do not represent the views of the National Science Foundation, Newmont, or Colorado State University.

TABLE OF CONTENTS

LIST OF TABLES

LIST OF FIGURES

LIST OF SYMBOLS

A_{ir}	area of inner ring	G_s	specific gravity
C	gas concentration	h	pressure head
C_{py}	pyrite content	H	Henry's constant
C_u	coefficient of uniformity	I	infiltration rate
D_{10}	particle size at 10% passing on a particle size distribution curve	i	hydraulic cgradient
D_a	effective diffusion coefficient in the gas phase	k	hydraulic conductivity
D_a^0	free diffusion coefficient in air	k_{ext}	extinction coefficient
D_e	effective diffusion coefficient	K_r	reaction rate coefficient
D_f	depth of the wetting front	k_s	saturated hydraulic conductivity
D_H	equivalent particle-size diameter	L	lateral drainage
D_p	depth of water pond	LAI	leaf area index
D_w	effective diffusion coefficient in the liquid phase	LL	Liquid Limit
D_w^0	free diffusion coefficient in water	n	Porosity
e	void ratio	n	van Genuchten fitting parameter
EC	electrical conductivity	P	Precipitation
EC_b	bulk soil electrical conductivity	PE	potential evaporation
EC_{pf}	pore fluid electrical conductivity	PET	potential evapotranspiration
ET	evapotranspiration	PL	Plastic limit
$Evap_{pan}$	pan evaporation	PI	plasticity index
F	diffusion flux	P_r	Percolation

PT	potential transpiration	w_{opt}	optimum water content
$q_k^*(x,t_j)$	specific measurement at time t_j for the k^{th} measurement at location x	y_k	weights associated with a particular measurement
R	mixture ratio	z	Depth
r	radial coordinate	α	van Genuchten fitting parameter
RH	relative humidity	Δt	elapsed time
RO	surface runoff	ΔS	change in soil water storage
R_{opt}	optimum mixture ratio	ΔW_{bag}	change in the weight of bag
R_t	total mixture ratio	ε'_b	soil permittivity at EC=0
$R_{t,opt}$	optimum total mixture ratio	ε'_p	pore fluid permittivity
S	Saturation Degree	θ	volumetric water content
S_e	effective saturation	θ_a	volumetric air content
T	Temperature	θ_{eq}	equivalent porosity
t	Time	θ_r	residual volumetric water content
T_a	air phase tortuosity	θ_s	saturated volumetric water content
TDS	total dissolved solids	θ_w	volumetric water content
T_n	normalized tensiometer reading	ρ_d	dry density
T_w	water phase tortuosity	$\rho_{d\text{-}max}$	maximum dry unit density
V	volume of infiltrated water	ρ_w	water density
VWC	volumetric water content	Ψ_a	air entry suction
$w_{j,k}$	weights associated with a particular measurement	Ψ_f	suction head at the wetting front

1 EXECUTIVE SUMMARY

1.1 Introduction

Mining operations produce substantial volumes of waste materials during ore extraction processes. The two predominant waste materials that require short- and long-term management are tailings and waste rock (WR) (Bussière 2007; Blight 2009). Mine tailings are composed of sand-, silt-, and clay-size particles and commonly are managed as slurry (high water content, low solids content). In contrast, WR primarily consists of coarse-grained particles (sand, gravel, cobbles) and is generated during excavation of non-economical rock to access ore. Due to differences in generation, handling, and composition of these two materials, mine tailings are managed in tailings storage facilities (TSF) and WR is managed in piles.

Mine waste present numerous challenged including mechanical stability, potential environmental contamination, water management, and closure and reclamation (Williams et al. 2003; Leduc et al. 2004; Wickland et al. 2006; Bussière 2007; Blight 2010). Mixing and co-managing WR and tailings (WR&T) has been evaluated as an alternative mine waste management option based on potential to achieve: (i) reduced environmental disturbance by decreasing the footprint for waste disposal; (ii) improved water management by rapid extraction of water in tailings; (iii) increased stability of waste deposits to reduce risk of failure; (iv) immediate reclamation of mine waste facilities; and (v) reduced acid production potential of WR (e.g., Williams et al. 2003; Leduc et al. 2004; Wickland et al. 2006; Bussière 2007; Hamade and Bareither 2019).

Mixed WR&T enhances shear strength and reduces compressibility of tailings, while also decreasing the permeability of WR to improve overall impoundment stability and limit infiltration and migration of water and oxygen (Bussière 2007; Wickland et al. 2010). Alternatively, WR&T can be reused in climate engineering applications, and in particular, in water balance covers (WBCs) for waste containment facilities (e.g., Williams et al. 2003; Gorakhki and Bareither 2017).

In a WBC, mixed WR&T can serve as a water storage layer that limits infiltration of water and oxygen into underlying waste materials to reduce acid and leachate generation. Beneficial reuse of mine waste also reduces the final mine waste volume for disposal and long-term management (Wilson et al. 2003).

The design of a mixed WR&T impoundment, pile, or WBC requires appropriate hydraulic parameters, such as hydraulic conductivity and water retention, for design, seepage analysis, and estimations of acid generation from mine waste. Schematics of different particle structures for WR&T mixtures are shown in Fig. 1.1. The total mixture ratio (R_t) is defined as the ratio of bulk mass of WR to bulk mass of tailings. The optimum mixture ratio ($R_{t,opt}$) represents a mixture where tailings “just fill” all WR void space (Fig. 1.1-c). The mechanical parameters (i.e., shear strength and compressibility) and hydraulic parameters (i.e., hydraulic conductivity and water retention) of WR&T mixtures are controlled by WR for $R_t > R_{t,opt}$ (Fig. 1.1-b), whereas mechanical and hydraulic parameters of WR&T mixtures are controlled by the tailings portion for $R_t < R_{t,opt}$ (Fig. 1.1-d).

GeoWaste (GW) is a WR&T mixture whereby fast-filtered tailings and WR are blended to isolate WR particles within a tailings-dominated matrix. The premise of GW is that potentially acid-generating WR can be co-disposed within non-acid-generating tailings, whereby the tailings fraction increases moisture retention relative to WR alone to decrease oxygen ingress and mitigate acid generation. Moreover, the tailing-dominated fraction caused the mixture to have lower permeability and higher water retention relative to WR alone, which can support the use of GW in a water balance cover (Gorakhki and Bareither 2017).

Laboratory hydraulic conductivity and soil water retention tests were conducted to compare the hydraulic parameters of mine tailings and GW (Gorakhki et al. 2019). Hydraulic parameters of GW were controlled by the tailings portion of the mixture, which resulted in similar hydraulic conductivity and soil water retention as pure tailings. Preliminary modeling results focused on assessing the potential of mixed WR&Ts in theoretical tailings-dominated mixture to function as WBCs for a semiarid region. Modeling results suggested that low percolation rates were possible for covers the employed tailings or tailings-dominated WR&T as the water storage layer, which suggests that a material such as GW has potential for use in a WBC.

The following research hypotheses initially were proposed: (1) water retention of GW at varying density can be predicted based on knowing water retention of tailings at different void ratios and compression behavior of the mixtures; (2) GW mixtures have hydrologic parameters comparable to conventional earthen materials used in WBCs; and (3) the water balance of GW can be predicted accurately with variably-saturated models. In the 3rd hypothesis, water balance includes water content and soil suction profiles, soil water storage, and percolation from the bottom of a simulated layer.

To test the first hypothesis, additional water retention and compression tests were proposed to add to preliminary large- and small-scale laboratory reported in Bareither et al. (2018). However, proposed additional water retention and compression tests were not completely performed due to extenuating circumstances, and thus 1st hypothesis was not evaluated herein. The 2nd and 3rd hypotheses were evaluated via field-scale test piles at a mine in Central America. A set of column experiments also was constructed in Fort Collins, Colorado, with the intent to provide a secondary data set to evaluate the 2nd and 3rd hypothesis. Although the columns have been successfully operating for 16 months, sufficient data necessary to test the hypotheses was not available at the time of preparing this document. Thus, the columns will continue to be operated in the future to provide additional data sets to build on the analyses presented herein.

1.2 Major Findings

The overarching focus of this study was to evaluate hydrologic behavior and determine hydraulic parameters for GW and WR. Data used in this study were collected from GW and WR test piles operated for a period of 26 months. These test piles were constructed by a mining company which sponsored this project in collaboration with a consulting company. Infiltration tests and destructive sampling were completed on both test piles at the end of the 26-month experiment. There were four main objectives completed for this study: (i) evaluate and compare hydrologic behavior of the GW and WR test piles under natural climatic conditions; (ii) determine field-scale hydraulic conductivity and in situ dry densities in the GW and WR test piles; (iii) determine saturated hydraulic conductivity and water retention parameters for the GW and WR test piles via inverse modeling; and (iv) develop seepage models to predict water content and oxygen concentration within the GW and WR test piles during the 26-month experiment. Each of the aforementioned objectives is discussed in detail in Chapter 2 to Chapter 5. Each chapter has been prepared as a stand-alone document and will be submitted for potential publication in peer-reviewed journals.

Chapter 2 is titled *Hydrologic and Environmental Comparison of Field-Scale GeoWaste and Waste Rock Test Piles.* The focus of this chapter is on the evaluation and comparison of hydrologic and environmental behavior observed in the GW and WR test piles that were operated for 26 months under natural climatic conditions. The test piles were constructed in the shape of truncated 5-m tall pyramids with 25-m base sides and flat 5-m × 5-m surfaces. Water content, temperature, electrical conductivity, and oxygen concentration were monitored in situ in four layers and at five locations within each layer for both test piles. In addition, 5-m × 5-m lysimeters were installed at the base of each pile to collect leachate. A total of 2662 mm of water was added to the piles via precipitation and irrigation. Based on the measured saturation, oxygen concentration, EC, and temperature in GW and WR piles during the 26 months of experiment, a larger acid mine reaction happened in WR pile in comparison with the GW pile. This behavior suggests disposing mine waste as GW reduces acid generation compared to separated WR and tailings deposition method.

Volumetric water content in the GW pile exhibited a downward progressing wetting from in the top two layers (< 2.0 m deep) of the pile due to irrigation and the first wet season. However, the average volumetric water content monitored in Layers 3 and 4 (> 3.5 m deep) expressed negligible change during the experiment. The increase in saturation in Layer 1 (0.5 m deep) of the GW pile during the first wet season corresponded with a decrease in oxygen in Layer 1 as well as in Layers 2, 3, and 4. However, oxygen within the GW pile increased during the first dry season as saturation of Layer 1 decreased.

An increase in volumetric water content in all four layers of the WR pile was observed during the pile experiment. The water content increase corresponded with an increase in saturation to 100% in Layers 1 and 2, and an increase in Layers 3 and 4 above 70%. The higher water contents and degree of saturation within the WR pile was attributed to higher infiltration and absence of vegetation on the pile surface. Thus, there was a greater propensity for water to infiltrate into the WR and lower potential for water to be removed at depth within the pile. The higher levels of saturation corresponded with considerably reduced levels of oxygen relative to the GW pile. The presence of sulphide minerals in the WR combined with water and oxygen in Layer 1 is believed to have resulted in a minor amount of sulphide oxidation.

Chapter 3 is titled *Hydraulic Conductivity Testing and Destructive Sampling of Field-Scale GeoWaste and Waste Rock Test Piles*. The focus of this chapter is on infiltration tests conducted to determine in situ hydraulic conductivity and destructive sampling completed to assess in situ density in both test piles. In addition, destructive samples for GW were processed to assess the mixture ratio. At the end of the 26-month experiment duration, sealed double ring infiltrometer (SDRI) tests were conducted on the GW and WR test piles to measure in situ hydraulic conductivity. The SDRI tests included a 2.4-m square outer ring and 1-m square inner ring. Tensiometers and in situ water content sensors were used to measure progression of the wetting front, and final extent of the wetting front in the GW pile was directly measured during decommissioning.

The average hydraulic conductivity in the WR pile was 2.8×10^{-6} m/s, and approximately constant during the duration of the experiment. The average hydraulic conductivity of the GW pile was 1.4×10^{-6} m/s for the first two days of experiment and 9.0×10^{-7} m/s for the last three days of experiment. The reduction in hydraulic conductivity of the GW was attributed to the possibility of a macroporous structure near the surface that produced a higher hydraulic conductivity at the start of the experiment and/or settlement that increased the density at depth in the pile and decrease the hydraulic conductivity as infiltration progressed. Generally, in situ hydraulic conductivity of GW pile was 53 to 82 times larger than laboratory measured hydraulic conductivity. This behavior can be due to spatial variation in particle-size distribution, pedeogenesis, and the difference between WR particle size between laboratory and field experiments. Moreover, in situ hydraulic conductivity of GW pile was approximately three times smaller than WR pile. This behavior suggests that a GW pile generates lower volume of leachate in comparison with a WR pile.

The average dry density measured in Layers 1 and 4 in the GW pile were similar (1.53 and 1.54 Mg/m^3), whereas the average dry density was higher in Layer 2 (1.85 Mg/m^3) and Layer 3 (1.63 Mg/m^3). The highest dry density measured in Layer 2 was attributed to settlement in the GW. The average dry densities measured in the WR pile were larger than the GW pile. The largest average dry density in the WR pile was measured in Layer 2 (1.94 Mg/m^3) and the smallest average dry density in the WR pile was measured in Layer 4 (1.71 Mg/m^3). The average porosity of the GW pile was 0.38 and the average porosity of the WR pile was 0.31. The lower porosity of the WR pile in comparison to the GW pile was consistent with the post-construction report, which indicated an average porosity of 0.42 for the GW pile and 0.37 for the WR pile.

Chapter 4 is titled *Inverse Numerical Solutions to Determine Hydraulic Parameters for GeoWaste and Waste Rock Test Piles*. The focus of this chapter is on inverse numerical solutions conducted in HYDRUS-2D to determine saturated hydraulic conductivity and soil water retention parameters representative of the GW and WR test piles. Infiltration data from the SDRI tests conducted on the test piles were used as input data for the inverse solutions. Infiltration during the SDRI test in the GW pile lasted 6.45 d, and infiltration data were separated into an initial part (0 to 2.7 d) and final part (2.7 to 6.45 d) based on a change in inflow. Infiltration during the SDRI test in the WR pile lasted 3.67 d and was consistent during the entire duration of the experiment.

Cumulative inflow during infiltration and in situ volumetric water contents at different depths were used as input data for inverse solutions of the GW pile, whereas only cumulative inflow data were available for the WR pile.

Inverse solutions were solved considering two scenarios: (i) hydraulic conductivity was known based on analytical solution of the SDRI data and van Genuchten water retention parameters α and *n* were solved; and (ii) hydraulic conductivity and van Genuchten water retention parameters α and *n* were solved. Hydraulic conductivity for the WR pile determined via inverse modeling (2.6×10^{-6} m/s) and analytically from SDRI data (2.8×10^{-6} m/s) were similar. Hydraulic conductivity in the GW pile determined via inverse modeling was 2.9×10^{-6} to 7.2×10^{-7} m/s, which was 0.8 to 2 times the hydraulic conductivity computed analytically from SDRI test data. In addition, in situ hydraulic conductivity was 50X to 300X larger than laboratory-measured hydraulic conductivity on GW. The in situ air entry pressure obtained via inverse solution was approximately 10X smaller near the surface and approximately equal at depths > 2.0 m relative to laboratory-measured values. Differences in hydraulic parameters determined in situ relative to in the laboratory were attributed to pedogenesis that created a more macroporous structure near the surface of the GW pile.

Chapter 5 is titled *Hydrologic Predictions of Water Content and Oxygen Concentration in GeoWaste and Waste Rock Test Piles*. The focus of this chapter is on predictions of water content and oxygen concentration within the GW and WR test piles. Predictions were compared to in situ monitoring data collected during the 26-month experiment. Hydrologic predictions in HYDRUS-1D and HYDRUS-2D were conducted using the initial water content distribution, field- and laboratory scale hydraulic parameters, site-specific metrological data and site vegetation information. Oxygen flow was predicted in HYDRUS-1D using the solute transport module and Fick's 2nd Law along with the oxygen consumption rate, oxygen diffusion in gas and water phases, and Henry's constant. The 1D and 2D volumetric water content predictions for the GW pile were accurate; however, volumetric water content within the WR pile was consistently underpredicted.

HYDRUS-1D yielded an accurate prediction of oxygen concentration in the GW pile for the entire 26-month duration. Historic precipitation data from the past 48 yr was used to predict saturation and oxygen concentrations within a hypothetical GW pile. The simulations suggested that saturation in the top 0.5 m ranged between 5% and 70%, whereas saturation at depths > 0.5 m ranged between 10% and 60%. Generally, HYDRUS can effectively be used to predict the water content and O_2 concentration profile of a GW pile. Validating HYDRUS can help to understand the volume of leachate and/or acid rock generation potential in the long-term or in extreme conditions in any field.

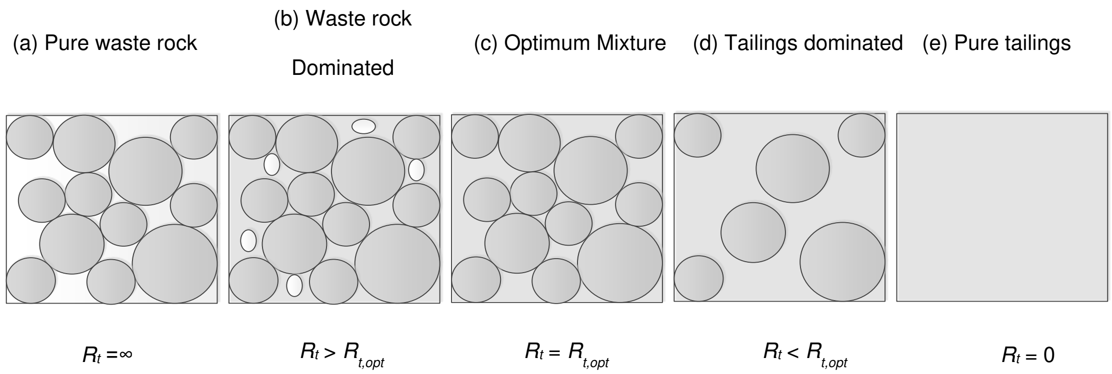

Fig. 1.1. Particle structure of waste rock and tailings mixture at different mixture ratios (R_t) (adapted from Wickland et al. 2006).

2 HYDROLOGIC AND ACID GENERATION COMPARISON OF FIELD-SCALE GEOWASTE AND WASTE ROCK TEST PILES

2.1 Introduction

Increased global consumption of raw materials combined with exhaustion of higher-grade ore bodies and an increased the ability to extract metals from lower-grade ore bodies has led the mining industry to generate even larger volumes of waste that require innovative and sustainable approaches to waste management (Blight 2009; Yilmaz 2011). The two predominant solid wastes at mine sites are waste rock (WR) and tailings. Waste rock includes material ranging from boulders to fine particles and commonly is managed by placement in piles. The main challenges facing WR management are acid rock drainage and mechanical stability (Johnson and Hallberg 2005; Akcil and Koldas 2006; Tutu et al. 2008). Tailings are the residuum from ore extraction, contain sand- to clay-sized particles, and typically exist as slurry after metallurgical processing (Qiu and Sego 2001; Bussière 2007). Mine tailings generated at ore processing plants typically contain low solids content (SC) due to ore extraction process. Dewatering of mine tailings often conducted to reclaim water and Bussière (2007) reported the following levels of dewatered tailings: (i) thickened tailings; SC = 50–70 %; (ii) paste tailings; SC = 70-85 %; and filtered tailings; SC > 85 %. Management of slurry, thickened, or paste tailings commonly is within a tailings impoundment that requires retention via tailings dams, whereas filtered tailings can be deposited without the need for tailings dams (Bussière 2007; Davies 2011; simms et al. 2011). Management of tailings impoundments and dams has presented challenges throughout the history of mining, and recent failures (Morgenstern et al. 2015; Morgenstern et al. 2016; Robertson et al. 2019) have highlighted the need to re-evaluate the existing methods of mine waste management and to create alternative approaches that improve stability and decrease potential risks to human health and the environment.

Mixing WR and tailings (WR&T) has been evaluated as an alternative mine waste management technique to: (i) increase waste stability to reduce risk of failure; (ii) improve water management to reduce contamination potential; (iii) mitigate acid production from WR; (iv) facilitate reclamation of mine waste facilities; and (v) eliminate tailings dams (e.g., Williams et al. 2003; Leduc et al. 2004; Wickland et al. 2006; Bussière 2007; Bareither et al. 2018). A mixture of WR&T can be described by the mixture ratio (R), defined as the dry mass of WR divided by dry mass of tailings. Mixtures can exist as WR dominated (high R), tailings dominated (low R), or as an optimum mixture (R_{opt}), which represents a mixture where tailings fill all available void space within a WR skeleton that maintains WR particle-to-particle contacts. Mechanical (i.e., shear strength and compressibility) and hydraulic properties of WR&T mixtures are more influenced by WR for $R > R_{opt}$, whereas mechanical and hydraulic properties of WR&T mixtures are more influenced by the tailings portion for $R < R_{opt}$ (e.g., Williams et al. 2003; Wickland et al. 2006; Bareither et al. 2018; Hamade and Bareither 2019).

GeoWaste (GW) is a mixture of fast-filtered tailings and WR prepared in a tailings-dominated mixture ($R < R_{opt}$). The concept of GW is that potentially acid-generating WR can be co-disposed within non-acid-generating tailings, with greater water retention within the tailings to retain water & reduce oxygen diffusion to mitigate acid generation. GeoWaste is a mine-waste management alternative that has potential to be deposited in geotechnically and geochemically stable piles that do not require dams of embankments (Bareither et al. 2018). Recent research on GW has focused on shear strength (Burden et al. 2017; Borja 2019), compressibility (Bareither et al. 2018), and hydraulic behavior (Gorakhki et al. 2018; Gorakhki et al. 2019). Laboratory- and field-scale experiments have supported that the hydraulic conductivity is lower and water retention capacity is higher for GW in comparison to WR. These differences in hydraulic parameters suggest that GW can maintain higher saturation and generate less seepage compared to WR alone.

The purpose of this study was to evaluate the ability of GW to mitigate acid generation in field-scale test piles under natural climatic conditions and irrigation. Test piles were constructed with WR and GW, whereby the WR pile contained potentially acid-generated (PAG) WR and the GW pile contained the same PAG WR, but mixed with non-PAG tailings. The test piles were constructed at a mine in Central America and operated for 26 months. Instrumentation was included to monitor water content, oxygen concentration, electrical conductivity, and temperature at 20 locations within each pile. Leachate generation was monitored via lysimeters at the base of each pile. Results are compared to hydrological and acid generation in a GW and WR pile.

2.2 Acid Rock Drainage

An environmental challenge for mine waste management is surface and groundwater contamination, especially when sulphide minerals such as pyrite, pyrrhotite, and arsenopyrite are present (Blowes et al. 2003; Akcil and Koldas 2006; Bussiere 2007). Although there are other potential contaminants in mine waste (e.g., cyanides, heavy metals, radioactive elements), sulphate-rich mineral oxidation is often the predominant environmental concern (Bussiere 2007). Acid rock drainage (ARD) develops from the oxidation of sulphide minerals in the presence of water and oxygen (O_2) (Akcil and Koldas 2006). Mine WR and tailings can both produce ARD if they contain sulfide minerals, and water and oxygen are present. Mitigating contamination from mine waste (e.g., WR piles, tailings impoundments, filtered tailings stacks) requires controlling production and release of ARD to the environment. Acid rock drainage develops through a series of reactions and release of ARD depends on the water balance within the tailings and WR.

2.2.1 Leachate Volume

The volume of generated leachate from a mine waste impoundment depends on the climatic condition, vegetation, and mine waste properties. The water balance of a mine waste impoundment can be computed as

$$P_r = P - R - ET - L - \Delta S \tag{2.1}$$

where P_r is leachate percolation at the base of the impoundment, P is precipitation, R is surface runoff, ET is evapotranspiration, L is lateral drainage, and ΔS is the change in water storage. A low permeability mine waste deposit increases surface runoff and maintains the wetting front of precipitation infiltrating shallow enough for water to be removed by evapotranspiration. High water retention increases the storage capacity (ΔS) of a deposit, which reduces percolation. Presence of vegetation helps remove water by root water uptake and transpiration.

2.2.2 Leachate Chemistry

The most common ARD reaction is the oxidation of pyrite (FeS_2) as shown in Eq. 2.2.

$$FeS_2 + \frac{7}{2}O_2 + H_2O \rightarrow Fe^{2+} + 2SO_4^{\ 2+} + 2H^+ \tag{2.2}$$

The generation of H^+ decreases the pH and the generation of Fe^{2+} and SO_4^{2+} increases total dissolved solids and electrical conductivity (Akcil and Koldas 2006). If the concentration of O_2, pH, and bacterial community are suitable, ferrous iron (Fe^{2+}) oxidizes to ferric iron (Fe^{3+}) as shown in Eq. 2.3.

$$Fe^{2+} + \frac{1}{4}O_2 + H^+ \rightarrow Fe^{3+} + \frac{1}{2}H_2O \tag{2.3}$$

At a pH of 2.3 to 3.5, ferric iron precipitates as shown in Eq. 2.4, which further lowers pH.

$$Fe^{3+} + 3H_2O \rightarrow Fe(OH)_{3solid} + 3H^+ \tag{2.4}$$

Any ferric iron that does not precipitate as $Fe(OH)_3$ can be used to oxidize additional pyrite based on the reaction outlined in Eq. 2.5.

$$FeS_2 + 14Fe^{3+} + 8H_2O \rightarrow 15Fe^{2+} + 2SO_4^{\ 2+} + 16H^+ \tag{2.5}$$

Pyrite oxidation is an exothermic reaction, and thus, a WR pile can have reach temperatures in excess of 60 °C during oxidation (Harries and Ritchie 1985; Blowes et al. 2003).

Important factors that determine the rate of acid generation are pH, temperature, O_2 concentration in the gas phase, O_2 concentration in the water phase, chemical activity of Fe^{3+}, surface area of exposed metal sulphides, and bacterial community (Blowes et al. 2003). Changes in any of these factors can increase or decrease the acid generation process.

Consumption of O_2 in the pore spaces via Eqs. 2.2 and 2.3 lowers the O_2 concentration, which promotes additional oxygen diffusion into the pore space by an O_2 gradient with the atmosphere. The diffusive flux (F) of O_2 can be calculated as

$$F(z,t) = -D_e \frac{\partial C(z,t)}{\partial_z} \tag{2.6}$$

where D_e is the effective diffusion coefficient, C is the gas concentration, z is depth, and t is time. A relatively lower D_e will decrease the ingress of O_2 and limit the sequence of ARD reactions (e.g., Eqs. 2.2-2.5).

The D_e is composed of two components (Collin 1987):

$$D_e = D_a + 0.03 D_w \tag{2.7}$$

where D_a is the effective diffusion coefficient in the gas phase and D_w is the effective diffusion coefficient in the liquid phase. Oxygen diffusion through water contributes much less than diffusion through the air phase. Equation 2.7 can be expanded as

$$D_e = \theta_a \cdot T_a \cdot D_a^{\,0} + 0.03(\theta_w \cdot T_w \cdot D_w^{\,0}) \tag{2.8}$$

where θ_a and θ_w are the volumetric air and water content ($\theta_a + \theta_w$ = porosity), T_a and T_w are the air and water phase tortuosity, and D_a^0 and D_w^0 are the free diffusion coefficient in air and water, respectively ($D_a^0 = 1.8\times10^{-5}$ and $D_w^0 = 2.2\times10^{-9}$ m^2/s). The parameters T_a and T_w can be estimated as a function of saturation (Penman 1940, Millington-Quirk 1960, Millington-Quirk 1961, Elberling et al. 1994). In general, D_e reduces approximately two to three orders of magnitude by increasing saturation from 50% to 90% (Millington and Quirk 1960; Elberling et al. 1994). A reduction in D_e produces a corresponding reduction in the diffusive flux of O_2 (Eq. 2.6).

2.2.3 Generation and Mitigation of ARD in Mine Waste

Schematics of mine waste where ARD develops, where "saturated" mine waste can impede oxygen ingress, and where mine waste acts as a water balance cover are shown in Fig. 2.1 In the scenario where ARD develops, mine waste includes large pore spaces that allow water and oxygen ingress to enable sulphide oxidation. If the mine waste has low moisture holding capacity and high water and air conductivity, ARD and develop and seep out of the mine waste deposit. An in situ signature of ARD would be an increase in pore fluid EC from an increasing concentration of soluble metals and increase in temperature from exothermic reactions.

The "saturated" oxygen barrier and water balance cover are two different approaches that can be used to mitigate sulphide oxidation and ARD. In the "saturated" mine waste scenario, the material contains small pores that have high moisture holding capacity and low hydraulic conductivity. In this scenario, the mine waste maintains a high saturation, ideally near saturation, to prevent oxygen ingress and mitigate ARD. In situ signatures of a "saturated" mine waste barrier would be high moisture content, reduced to near zero O_2, and no noticeable increase in pore fluid EC or temperature. An assessment of mine waste to impede oxygen diffusion was evaluated by Bussière and Aubertin (1999), whereby they created a layer of mine tailings above mine waste with the goal of maintaining elevated saturation within the tailings. They reported that the layer of mine tailings increased effluent pH from pyrite-rich mine waste, which suggested that the mine tailings cover prevented O_2 ingress into the mine waste.

The water balance cover concept relies on a balance between available water storage capacity to retain infiltration and evapotranspirative energy to remove water and restore the storage capacity (Albright et al. 2010; Benson and Bareither 2012). Effective water balance covers have a broad distribution of pore sizes to soil water storage and moderate to low hydraulic conductivity to reduce seepage. In situ signatures in a water balance cover show fluctuating, or seasonal, changes in water content, but no deep percolation. Although oxygen can be present in the pore spaces, vegetative uptake of O2 would be preferable relative to sulphide oxidation.

Regardless of potentially minor acid development, the unsaturated state of a water balance cover ideally limits drainage.

The scenarios of ARD development and mitigation in mine waste shown in Fig. 3.1 were hypothesized to represent potential realizations of the GW and WR pile at Marlin. Enhanced water retention of GW in comparison with WR was envisioned to increase the level of saturation to mitigate oxygen ingress and development of ARD. In contrast, lower saturation in WR due to larger pore spaces and less water holding potential would lead to the presence of oxygen and water within the sulphide-rich WR to promote ARD. The potential scenarios in Fig. 3.1 were used to compare and contrast in situ measurement of the WR and GW test piles during the 26-month experiment.

2.3 Materials and Methods

2.3.1 Materials

Geotechnical characterization of mine tailings and WR samples representative of mine waste used to construct the GW and WR piles, was completed via mechanical sieve and hydrometer (ASTM D422, ASTM 2007), Atterberg limits (ASTM D4318, ASTM 2014a), and standard-effort compaction (ASTM D698, ASTM 2014c). Material characteristics of the tailings and WR are summarized in Table 2.1.

The liquid limit (*LL*) of tailings agreed with the reported range in literature for hard rock mine tailings (i.e., $18\% < LL < 40\%$) (Matyas et al. 1984; Aubertin et al. 1996; Qiu and Sego 2001; Wickland and Wilson 2005; Khalili et al. 2010; Wickland et al. 2010; Dailiri et al. 2014). Jehring and Bareither (2016) presented an average, upper-bound, and lower-bound particle-size distribution for tailings and WR based on a compilation of data from literature. Characteristics compiled in Table 2.1 for the tailings and WR evaluated in this study were compared to the PSD ranges in Jehring and Bareither (2016). Tailings were comparable with average tailings properties; however, WR in this study was more well-graded and had a higher fines content (fine content > 23%) compared to the average WR PSD in literature (fines content < 2%).

2.3.2 Test Piles

Aerial photographs of the GW and WR (WR) piles at the end-of-construction and during operation are shown in Fig. 2.2. The piles were constructed at the end of January 2017 at a mine in Central America. The piles were designed as truncated 5 m tall pyramids with 25 m base sides and flat 5 m × 5 m top surfaces. The WR pile was constructed with potentially acid generating (PAG) WR within the central core of the pile (5 m x 5 m x 5 m) and non-PAG WR was used on the side slopes. Non-PAG WR on the side slopes supported vegetative growth during the experiment, whereas vegetation never established on the PAG WR placed in the central core of the WR pile (Fig. 2.2). The GW pile was constructed with GW prepared to a mixture ratio of 0.43 (R = dry mass of WR / dry mass of tailings). Potentially acid generating WR was used in GW placed in the central core of the pile and non-PAG WR was used in GW placed on the side slopes. Vegetation established on the side slopes and within the central core of the GW pile during operation (Fig. 2.2).

GeoWaste was prepared with filtered mine tailings and either PAG or non-PAG WR. All materials were mixed on site using an excavator prior to placement. GeoWaste for the side slopes of the test pile, which included non-PAG WR, was placed using an excavator to create a 5 m × 5 m ring to form the central core. GeoWaste prepared with PAG WR was dropped from a height of 2 to 3 m using an excavator to form the central core of the pile. This deposition process for the central core simulated the anticipated full-scale GW final placement process via disposal at the end of a conveyor system. The WR test pile was constructed with compacted non-PAG WR on the side slopes placed by a dozer and PAG WR dropped and pushed in-place in the central core by a dozer. Thus, a higher level of compaction effort was used to prepare the central core of the WR test pile as compared to the GW test pile, both of which simulated conditions anticipated in full-scale mine waste management operations.

Plan view and cross-section schematics of the test piles are shown in Fig. 2.3. Each pile was instrumented with four layers of sensors, and each layer contained five sets of sensors: one set in the center and four sets positioned approximately 2-m radially from the center on each side of the piles (Fig. 2.3). Each sensor set contained (i) a TDR-315L Acclima sensor (Acclima, Merdian, Idaho) to measure volumetric water content, temperature, and electrical conductivity, and (ii) a SO-110 Apogee (Apogee, Logan, Utah) sensor to measure oxygen concentration and temperature. All sensors from a given pile were connected to a CR-1000 Campbell Scientific (Campbell Scientific, Inc., Logan, Utah) datalogger interfaced with an AM 16/32B Campbell Scientific multiplexer. The instrumentation stations had a solar panel that provided excitation voltage for the sensors and power to the datalogger. Each sensor in this study collected a measurement every 2 hr; however, every 12 data points were averaged to calculate daily averages to assess temporal trends for the 26-month study.

Monitoring began on 31 January 2017 (t = 0 D) and continued until 18 March 2019 (t = 776 D). Precipitation and atmospheric temperature data were collected by a weather station located approximately 12 km northwest of the piles in a similar climatic condition. Irrigation was performed on both piles from Day 23 to Day 92. Irrigated water was obtained from a well at the mine and had total dissolved solids ranging from 2400 to 2500 mg/L and electrical conductivity ranging from 3100 to 3400 µS/cm.

A cistern was connected to the lysimeters installed at the base of both piles to collect and measure the leachate volume. Leachate did generate from the WR Pile, but leachate never generated from the GW pile. However, all cistern data was deemed unreliable due to cracks discovered in cisterns and associated pipes connected to the lysimeter, which likely allowed entrance of surface water not associated with the experiments.

2.3.3 Data Processing

A summary of the location of all sensors used in GW and WR piles as well as the period that sensors were functional is listed in Table I-1 in Appendix I. In general, no measurements were available for 92 days between Day 122 to Day 212 in the WR pile. The last data recorded in the TDR-315L Acclima was Day 303 for one sensor and Day 484 for 18 sensors in WR pile. One O_2 sensor stopped working at Day 121; however, other 19 O_2 sensors were functional in the WR pile until the last day of experiment.

Twelve TDR-315L Acclima sensors were functional during the whole experiment in the GW pile; however, four sensors worked until Day 506 in the GW pile. Four TDR-315L Acclima sensors were not functional from Day 122 to Day 209 and one of these sensors stopped working at Day 698 while the other three sensors worked until the last day of experiment (i.e., Day 776). Nineteen O_2 sensors were functional during the whole period of experiment while one sensor stopped working at Day 415 in the GW pile.

A summary of the daily average of VWC, EC, temperature, and O_2 concentration for each sensor is shown in Appendix II in Figs. II1-II8. In general, temperature measured by any group of five sensors in a given layer in the GW or WR piles were very close. However, some variabilities were observed between VWC, EC, and O_2 concentration in different sensors of the same level at each layer. The large variability in O_2 concentration sensors were observed mainly in the GW pile in Layers 3 and 4. A larger O_2 concentration was measured in O_2 (B3) and O_2 (B8) sensors which both were located in the northeast side of the GW pile. No reason was identified for the higher O_2 concentration in the northeast of the GW pile; however, a leak was detected in the cistern that was connected to the bottom of the GW pile. The larger O_2 concentration may be due to presence of larger pores between the bottom of pile and northeast side of the GW pile. A relatively large variability was observed in the VWC and EC measurements in GW and WR piles. The large variability of VWC in different locations is hypothesized to have been caused by preferential flow paths in the GW and WR piles.

The analysis in this study was performed by averaging the daily data in five sensors at each layer to make a single daily value that represents the layer. There were periods that data from one or multiple sensors in one layer were not available (i.e., Table I-1, Appendix I). Absence of one or multiple sensor measurements occasionally resulted in a sharp change in the average value of the interested parameter of the layer at the time that sensor(s) stopped working. This sharp change is only due to the analysis method and is not present a change in the behavior of the investigated parameter in piles. Temporal trends tend to be smoother when all five sensors at each layer were available, whereas a noisier signal was observed when fewer sensors were available.

Saturation degree of each layer was computed using the VWC data and in-situ porosity data obtained during pile decommissioning (destructive in-situ density tests were performed after period of the experiment). Five in-situ density tests were performed at each layer of GW and WR pile. The average porosity in the GW and WR piles were 0.4 and 0.34, respectively. The saturation degree of each layer was obtained by dividing the daily VWC by porosity of the pile.

The TDR-315L Acclima sensors provided a measurement of bulk soil EC (EC_b). Equation 2.9 was used to convert the EC_b to pore fluid EC (EC_{pf}) (Hilhorst 2000)

$$EC_{pf} = \frac{\varepsilon'_p \bullet EC_b}{\varepsilon'_b - \varepsilon'_{b=0}} \tag{2.9}$$

where ε'_p is pore fluid permittivity, ε'_b is the soil permittivity, ε'_b is soil permittivity at EC=0. ε'_b considered to be 4.1 as suggested in Hilhorst (2000), since direct measurement of this value was not available. The ε'_p parameter can be calculated based on temperature (T) as shown in Eq. 2.10 (Hilhorst 2000).

$$\varepsilon'_p = 80.3 - 0.37(T - 20) \tag{2.10}$$

2.4 Results

2.4.1 Volumetric Water Content and Saturation

Temporal relationships of average VWC in each of the four layers in the GW pile and cumulative precipitation and irrigation are shown in Fig. 2.4a. Irrigation began on Day 23 and continued until Day 92. The VWC at the start of the experiment was similar in all layers and ranged between 8.4% and 10.1%. The average VWC of the GW pile ranged between approximately 8% and 25% for the duration of the experiment. The most pronounced responses in VWC to precipitation and irrigation were observed in Layers 1 and 2, whereas negligible change in VWC were observed in Layers 3 and 4. The increase in VWC to irrigation only was observed in Layer 1; however, precipitation during the first wet season pushed the wetting front deeper after irrigation ceased such that an increase in VWC occurred in Layer 2 between approximately 160 and 200 d (Fig. 2.4a). The cessation of precipitation and onset of high evapotranspiration during the first dry season reduced the VWC in Layers 1 and 2, with a more pronounced and rapid reduction in Layer 1 starting approximately on Day 240. The VWC in Layers 1 and 2 from Day 240 until termination of the experiment were approximately constant, with only a small increase observed in Layer 1 the developed in response to precipitation between Day 480 and 520.

In the GW pile, the average VWC increased in Layer 1 between Day 34 and Day 131, and subsequently reduced from Day 250 until approximately Day 440. This period of reduction in VWC coincided with the first dry season (≈ Day 270 to Day 430), during which evapotranspiration was considerably greater than precipitation. Transpiration contributed to removal of water from the GW based on natural establishment of vegetation (i.e., the pile was not seeded) on top of the pile (Fig. 2.2). The VWC stabilized near 10% to 12% at the end of the first dry season, which was similar to the VWC at the beginning of experiment. Subsequently, only minor variations in the VWC in Layer 1 were observed during the second wet and dry seasons.

In the GW pile, the increase in VWC in Layer 2 due to irrigation and precipitation initiated around Day 180, which was approximately 120 d after the increase in VWC was observed in Layer 1. The peak average VWC in Layer 2 was 4% lower than peak average VWC measured in Layer 1. This progression in the wetting front is logical considering propagation downward from the more saturated zone in Layer 1 towards Layer 2. The VWC in Layer 2 reduced similar to Layer

1 during the first dry season; however, the average VWC stabilized at approximately 3% wetter than the initial condition of the GW pile. Subsequent precipitation and evapotranspiration after Day 480 did not influence the VWC in Layer 2 (Fig. 2.4a).

The average VWC in Layers 3 and 4 of the GW pile were nearly constant for the duration of the experiment (Fig. 2.4a). The change in VWC in Layer 3 was less than 2%, which suggests that the wetting front did not appreciably reach Layer 3 (i.e., depth of 3.5 m). The limited change in VWC in Layers 3 and 4 concurs with zero leachate generated from the GW pile (i.e., based on visual observation in the cistern).

Temporal relationships of average VWC in each of the four layers of the WR pile and cumulative precipitation and irrigation are shown in Fig. 2.4b. Irrigation was conducted on the surface of the WR pile from Day 23 until Day 92. The VWC at the beginning of experiment was similar in all layers and ranged between 8% and 10%. Subsequently, an increase in VWC was observed in each of the four layers that was indicative of a downward progressing wetting front. The average VWC in the WR pile ranged between 8% and 37% throughout the WR pile during the experiment based on available data.

The temporal relationship of the average VWC in Layer 1 showed an increase in VWC after 60-75 d. Although the elapsed time between onset of irrigation and change in VWC in Layer 1 of the WR was similar to the GW pile, the peak VWC in the WR pile was higher. The average porosities of the WR and GW piles were close (n = 0.40 in GW pile and n = 0.34 in WR pile); thus, the higher peak VWC in Layer 1 of the WR pile suggests more pronounced infiltration on the surface of the WR pile. A 3X-larger infiltration rate of the WR pile compared to the GW pile was measured via field-scale infiltration testing (Gorakhki et al. 2019), which supports increased infiltration in the WR pile during the 26-months pile experiment.

The VWC in Layer 1 of the WR pile peaked on Day 238 and subsequently decreased to an average of approximately 26% in response to the first dry season. The rate of reduction in the VWC as a function of time was slower in the WR pile compared to the GW pile, and the stabilized

VWC at the end of the dry season was higher in the WR pile (≈ 26%) compared to the GW pile (≈ 11%). These observations were attributed to (i) the absence of vegetation on the surface of the WR pile (Fig. 2.2), which negated root water uptake and transpiration, and (ii) a higher infiltration rate in the WR pile. Thus, more water could infiltrate into the WR and there was less potential to remove water once retained within the WR pore space. Unfortunately, the water content sensors in Layer 1 of the WR pile were non-functional after Day 484 (Fig. 2.4b).

The temporal relationship of the average VWC in Layer 2 of the WR pile suggests that the wetting front reached Layer 2 between Day 120 and Day 200, a period when data collection was non-functional. The peak VWC in Layer 2 ranged between 30% and 36%, which was near or at saturation. After the peak in VWC, the VWC reduced slowly to an average of 27% on Day 484, which was the last day the sensors functioned in Layer 2.

The temporal relationships of the average VWC in Layers 3 and 4 of the WR pile show an increase in VWC that coincides with arrival of the wetting front. The wetting front passed through Layer 3 between 250 and 270 d, and subsequently passed through Layer 4 between 344 and 400 d. The average VWC in Layer 3 peaked at 29% and only a single sensor measured active until the end of the experiment (southeast sensor in Layer 3). This single sensor reported a VWC of approximately 28% from Day 484 (i.e., last day majority of VWC sensors were active) until the end of the experiment. A VWC of 28% measured in Layer 3 can be attributed to the 3.5 m of WR above this location, which shielded the effects of evaporation occurring at the surface of the WR pile.

Temporal relationships of average saturation degree in each of the four layers of the GW pile and cumulative precipitation and irrigation are shown in Fig. 2.5a. In general, increase in the saturation degree was observed in two periods. A total of 1608 mm precipitation and irrigation was applied in 150 D (average precipitation + irrigation = 10.7 mm/d). This case is representative of an extremely wet period since the wettest month on the record (during the last 48 years) had an average precipitation = 13.9 mm/d. The highest daily saturation degree of the GW pile was

63% (averaging all sensors in the first layer in this extreme condition) (base saturation degree at the beginning of experiment = 27%). The first wet season plus aggressive irrigation increased saturation degree of the second layer to 53% relative to the initial saturation degree of 29% at the beginning of experiment. Layers 3 and 4 did not show a notable increase in the saturation degree.

In the second wet season, the average saturation degree increased to the maximum of 35% relative to the initial saturation degree of 27% in responds to the two-month wet season (average precipitation = 5.4 mm/d). Layers 2, 3, and 4 did not show an increase in saturation degree in respond to the regular wet season in GW pile (Fig. 2.5a).

Temporal relationships of average saturation degree in each of the four layers of the WR pile and cumulative precipitation and irrigation are shown in Fig. 2.5b. During the first wet season plus aggressive irrigation, the average saturation degree of Layers 1 and 2 reached 100% at the peak; however, the peak saturation degree was followed by a reduction to approximately 80% at the end of experiment. The saturation degree in Layer 3 reached to 80% and stayed at this level until the end of the experiment. The saturation degree in the Layer 4 was largely varied between sensors (Appendix II, Fig. II1-II2) and ranged between 50 to 97%. The high degree of saturation in the WR pile is due to large volume of infiltrated water due to high hydraulic conductivity of WR and relatively high fine content of WR (fine content > 23 %). The data in the second wet season was not available because only one sensor was functional (southeast sensor in the third layer) in the WR pile.

2.4.2 Oxygen Concentration

Temporal relationships of the average O_2 concentration in each of the four layers of GW pile is shown in Fig. 2.6. Temporal relationships of water saturation in the top layer (i.e., Layer 1) as well as the layer that corresponds to the average O_2 concentration are also shown in Fig. 2.6. In general, oxygen sensors recorded O_2 concentrations ranging between 0% and 19% (atmospheric O_2 concentration is 21%).

Temporal relationships of the average O_2 concentration and saturation in Layer 1 of the GW pile are shown in Fig. 2.6a. The O_2 concentration started near 15% and decreased to approximately 0% by Day 140, which corresponded with an increase in saturation to 63%. The O_2 concentration then fluctuated with saturation until Day 240, whereupon O_2 concentration increased as saturation reduced in response to the first dry season. Subsequently, the O_2 concentration remained approximately constant at 16-17% with minor reductions occurring concurrently with small spikes in saturation. In general, lower saturation corresponded with higher O_2 concentration due to more open pore spaces within the GW that allowed for atmospheric air to enter the pile.

The temporal relationship of average O_2 concentration in Layer 2 of the GW pile as well as saturation in Layers 1 and 2 are shown in Fig. 2.6b. The O_2 concentration decreased at the beginning of the experiment and reached 0% on Day 128. This decrease in O_2 concentration in Layer 2 corresponded with the spike in saturation in Layer 1, whereas during this same time the average saturation in Layer 2 had not changed since the onset of the experiment. The O_2 in Layer 2 remained at 0% until Day 262 and then increased concurrently with a reduction in saturation of Layer 1. Interestingly, the increase in O_2 concentration in Layer 2 between Days 240 and 300 occurred while saturation in Layer 2 was increased above 50%. Although minor reductions in the O_2 concentration of Layer 2 were observed after Day 400 that coincided with small increases in saturation in Layer 1, the O_2 concentration in Layer 2 steadily increased and stabilized at approximately 15-16% for the last 100 d of the experiment. The main factor controlling the O_2 concentration in Layer 2 was the saturation of Layer 1, whereas no dependency was observed between the saturation and O_2 concentration of Layer 2.

Temporal relationships of the average O_2 concentration in Layers 3 and 4 in the GW pile are shown in Figs. 2.6c and 2.6d, respectively. The saturation trend in Layer 1 is reproduced in both figures along with the respective saturation in Layers 3 and 4. The trends in O_2 concentration in Layers 3 and 4 corresponded to the saturation of Layer 1 in a similar manner to the behavior described for Layer 2. Thus, maintaining an elevated saturation in the surface layer (Layer 1) aids in restricting the O_2 flux into the GW pile. Furthermore, once the O_2 concentration in a given layer at depth (e.g., Layers 2, 3, or 4) reduced to near zero, the subsequent rate of increase in O_2 concentration depended proximity to the surface layer. As observed in the O_2 concentration trends for Layers 2, 3, and 4, the rate of increase in O_2 concentration decreased with depth because a longer distance to the atmospheric boundary (i.e., surface of pile) reduced the oxygen gradient while the difference in concentration was the same (ΔO_2 concentration ≈ 20%).

The measured O_2 concentration in Layer 4 was consistently above 0%, whereas the O_2 concentration in Layers 2 and 3 decreased to 0%. During the experiment, a small leak was detected in the cistern connected to the lysimeter at the base of the GW pile, which increased the O_2 concentration in the Layer 4. The amount of increase in the O_2 concentration due to the small leak and the influence on O_2 concentrations measured within the GW pile was not quantified.

Temporal relationships of the average O_2 concentration in each layer of the WR pile as well as saturation in Layer 1 and saturation of the layer of interest are shown in Fig. 2.7. In general, O_2 concentration ranged between 0 and 18%.

The temporal relationship of the average O_2 concentration and saturation degree of Layer 1 in WR pile is shown in Fig. 2.7a. The O_2 concentration in Layer 1 approximately reached 0% on Day 113 as saturation in Layer 1 reached 54%. Although data were not available between Day 121 and Day 213, the O_2 concentration appears to have stabilized at 0% concurrent with an increase in saturation to 100%. Subsequent reduction in saturation of Layer 1 resulting from the first dry season allowed the O_2 concentration at Layer 1 to increase and ultimately stabilize near 8% at the end of the experiment.

The temporal relationships of average O_2 concentration and saturation in Layers 2 and 3 of the WR pile were similar to Layer 1 (Fig. 2.7) over the period of available data — sharp reduction in O_2 concentration at the beginning of experiment concurrent with increase in saturation in Layer 1. Following the period in which data were not collected (Day 121 to Day 213) all oxygen sensors in Layers 2, 3, and 4 reported 0%, and the O_2 concentration remained near 0% until the end of the experiment. The negligible oxygen present in the WR pile was attributed to a high saturation (≥ 80%) in Layer 1 (when data were available) combined with increasing and/or elevated and stable oxygen concentrations in Layers 2, 3, and 4. Thus, the higher saturation in Layer 1 reduced the oxygen flux into the WR pile and the higher saturations in Layers 2, 3, and 4 further minimized transport of oxygen from Layer 1 deeper into the WR pile.

In general, throughout the duration of the experiment the O_2 concentrations were lower in the WR pile compared to the GW pile. Waste rock used in this study was well graded and had a fines content of 23%, which contributed to achieving a dense particle packing with small pore spaces. This porous structure promoted retention of pore water once surface water infiltrated into the pile, which is apparent from a degree of saturation greater than 70% in all four layers on Day 480. Secondly, in this study only the WR fraction was PAG and tailings was categorized as non-PAG. As a result, 100% of material in the WR pile had potential to consume oxygen while only 33% of material in the GW pile (by mass) had potential to consume oxygen. Consequently, the oxygen consumption rate in WR pile was larger than GW pile. Results might be different if both tailings and WR in this study were PAG materials. Lastly, the leak in the cistern in GW pile resulted in exposing GW pile to O_2 from both sides.

2.4.3 Electrical Conductivity

Sulphide oxidation and ARD release dissolved metals and sulphate that increase the ionic strength and EC of pore fluid and leachate (Akcil and Koldas 2006). The temporal relationship of the layer-average EC in the GW pile as well as temporal relationship of saturation degree and O_2 concentration in GW pile is shown in Fig. 2.8. Saturation degree of each layer, O_2 concentration, and EC are plotted in the same graph to evaluate if EC increases during the time that O_2 and water were present in piles. In general, the EC in the GW pile at the beginning of experiment was ranged between 6300 to 8200 µS/cm. The high EC of the pore fluid at the beginning of experiment is due to the high salt concentration of the tailings fraction.

The temporal relationships of EC, O_2, and saturation degree of Layer 1 in the GW pile are shown in Fig. 2.8a. In general, the EC fluctuated in a close range to Day 370. After Day 370, EC increased from 6600 µS/cm to 7400 µS/cm at Day 483. This period coincides with a reduction in saturation degree and increase of O_2 in the same layer. Electrical conductivity decreased in the second wet season to 6350 µS/cm. This reduction in the EC may be due to one or both of the following mechanisms: (i) downward migration of the wetting front from low EC precipitation water to sensors in the first layer, and (ii) slight decrease in the O_2 concentration in response to the increase in saturation degree. After the saturation degree decreased at the end of second wet season, the EC increased to 6800 µS/cm and stayed at the same level until the end of experiment.

The temporal relationships of EC, O_2, and saturation degree of the Layer 2 in the GW pile is shown in Fig. 2.8b. The EC decreased from 7750 µS/cm at the beginning of experiment to 6400 µS/cm at Day 280. This reduction coincides with an increase in the degree of saturation in the Layer 1 and reduction of O_2 concentration in the Layer 2. However, after Day 280, the saturation degree in Layer 1 decreased resulting in an increase in O_2 concentration in Layer 2 and EC increased to 7200 µS/cm by Day 480. The EC in Layer 2 decreased in respond to the second wet season to 6650 µS/cm by Day 515. The saturation degree of Layer 2 did not change during the second wet season, as a result the reduction in EC is hypothesized to have resulted from the increasing the saturation degree in Layer 1 resulting in a slight reduction in the O_2 concentration of Layer 2.

The temporal relationships of EC, O_2 concentration, and saturation degree of Layers 3 and 4 in GW pile are shown in Figs. 2.8c and 2.8d, respectively. In general, EC ranged between 6850 µS/cm to 7350 µS/cm during the experiment in Layer 3. The EC in Layer 4 decreased initially from 8000 µS/cm at the beginning of experiment to 6800 µS/cm at Day 40. Then the rate of reduction in the EC decreased and EC reached 6250 µS/cm at Day 280. The EC fluctuated between 6150 to 6300 µS/cm from Day 280 to the end of experiment.

In general, EC increased in the Layers 1 and 2 in response to the first dry season consistent with the increase in O_2 concentration (and decrease in saturation degree of Layer 1). The difference between the initial EC (beginning of experiment) and the maximum EC of Layers 1 and 2 were 1450 µS/cm and 250 µS/cm, respectively, and 150 µS/cm and 0 µS/cm (i.e., the maximum EC was at the beginning of experiment for Layer 4) for Layers 3 and 4, respectively. This behavior may be due to increased pyrite oxidation in Layer 1 or evaporative concentration for salt during dry season.

The temporal relationship of the average EC in different layers of WR pile as well as temporal relationship of saturation degree and O_2 concentration are shown in Fig. 2.9. The initial EC of the WR pile ranged between 3900 µS/cm to 4750 µS/cm in different layers which is approximately half of the values measured in the GW pile. The lower initial EC in the WR pile compare to the GW pile is due to the high salt content of the tailings pore fluid in the GW mixture.

The temporal relationships between EC, O_2 concentration, and saturation degree in Layer 1 are shown in Fig. 2.9a. The EC decreased from 3800 µS/cm at the beginning of experiment to 3300 µS/cm at Day 58 of experiment. This behavior was followed by an increase in EC to 4450 µS/cm at the time of the data gap (Day 121 to Day 212). After Day 212, EC was higher and recorded as 5650 µS/cm and exhibited a decreasing trend which continued until Day 270 at an EC= 5150 µS/cm. After Day 270, EC increased to 6500 µS/cm at Day 483 which is the last day that data was available.

The temporal relationships between EC, O_2 concentration, and saturation degree in Layer 2 are shown in Fig. 2.9b. The EC was 4550 µS/cm at the beginning of experiment. Similar behavior to Layer 1 was observed in Layer 2 with smaller magnitude EC values (between 3950 µS/cm to 4900 µS/cm). The EC initially dropped in the first 44 days, followed by an increase in EC to up to Day 212 (a data gap exists unto Day 270). Comparison of EC values before and after data gap suggests a gradual increase in EC, followed by a gradual decrease in EC due to pore fluid dilution. Increase in EC was reported after Layer 1 saturation degree was reduced and O_2

concentration increased after Day 330.

The temporal relationships between EC, O_2 concentration, and saturation degree in Layers 3 and 4 are shown in Figs. 2.8c and 2.8d, respectively. In general, similar behavior to Layers 1 and 2 was observed before data gap (0 D < t < 121 D): — an initially decrease in EC, followed by an increase in EC. The EC reached a maximum after the data gap in both Layers 3 and 4. After Day 212, EC decreased as O_2 concentration was at approximately 0% for the rest of experiment in both layers. Making a conclusion about acid generation is hard for these two layers due to unavailability of data between Day 121 and Day 212 and after Day 484.

In general, the difference between the EC at the beginning of experiment and the maximum EC reported in Layers 1 and 2 of the WR pile were 6750 µS/cm and 350 µS/cm, respectively. The EC increase in Layer 1 of WR pile was 4.7 times larger than the EC increase Layer 1 of GW pile. The increase in EC in Layer 2 of WR pile may was 1.4 times larger than the increase in EC in Layer 2 of GW pile. Greater increase in EC in the WR pile may indicate greater pyrite oxidation in the WR pile in compare with the GW pile because the lower relative evapotranspiration of the WR pile should yield a lesser degree of evaporative concentration.

2.4.4 Temperature

Temperature within the piles was monitored to assess potential heat generation due to exothermic ARD reactions (Eq. 2.2-2.5). Temperature trends in the four layers of the GW and WR piles are shown in Fig. 2.10 along with the atmospheric temperature. The temperature trend in Layer 1 of the GW pile closely followed the atmospheric temperature, which was anticipated considering the sensors were only 0.5 m below the surface. Temperature trends in Layers 2, 3, and 4 of the GW pile exhibited considerably less fluctuations compared to Layer 1, which indicates that atmospheric changes in temperature did not substantially penetrate past Layer 1. The average temperature in Layers 2, 3, and 4 increased during the first 120 d of the experiment and then were generally more stable with greater depth in the pile for the duration of the experiment.

Temporal relationships of temperature in Layer 1 of the WR pile also exhibited fluctuations influenced by the atmosphere (Fig. 2.10b). Furthermore, similar trends of increasing temperature during the first 120 d followed by more consistent temperatures with depth in the WR pile were observed in Layers 2, 3, and 4. A notable difference in the temperature trends between the WR pile and GW pile was observed for Layers 1 and 2 starting approximately on Day 360. An increase in temperature was observed in Layer 1 of the WR pile that was elevated relative to Layer 1 in the GW pile. In addition, temperature in Layer 2 of the WR also increased, whereas temperature in Layer 2 of the GW pile decreased. The more pronounced increase in temperature in Layer 1 of the WR pile combined with the increase in temperature of Layer 2 may suggest sulphate oxidation occurred in the WR pile. Both piles were initially irrigated and had a high degree of saturation until the Day 240; however, the degree of saturation began to decrease at the beginning of dry season (Fig. 2.4b). Reduction in saturation degree of the first layer resulted in entering O_2 from atmosphere which is believed to have caused exothermic acid mine generation reactions. Moreover, this time coincides with a sharp increase in EC in Layer 1 (Fig. 2.9a) and slight increase in EC in Layer 2 (Fig. 2.9b).

2.4.5 Leachate Chemistry

The result of leachate chemistry from the bottom of WR pile are shown in Table 2.2 for three samples collected between in day 219 and 284. Leachate chemistry data suggests pyrite oxidation and acid generation was occurring in the WR pile: (i) pH had circum-neutral range but the trend was decreasing (more acidic) with time; (ii) EC was increasing with time suggesting increasing TDS due to acid generating process, (iii) sulphate concentration increased with time and reached to higher than 1 g/L at Day 284 of experiment. The GW pile did not generate any leachate; as a result, no leachate chemistry analysis is available for GW pile.

2.5 Practical Implication

The environmental properties of mine waste deposits can be evaluated by (i) leachate volume, and (ii) leachate chemistry. A mine waste management technique that generates a lower leachate volume decreases the transfer of contaminant in the environment. A mine waste management technique that generates leachate with neutral pH, lower TDS, and lower sulphate concentration also a lower risk to the environment. The main hypothesis of this study was that disposing of mine waste as GW generates a lower leachate volume and a leachate with a better quality (i.e., neutral pH, lower sulphate content, and lower TDS).

A GW pile and a WR pile were designed as truncated 5 m tall pyramids with 25 m base sides and flat 5 m × 5 m top surfaces. The WR pile was constructed with PAG WR and the GW pile was constructed with a mixture of PAG WR and tailings at a mixture ratio of 0.43 (R = dry mass of WR / dry mass of tailings). Piles were monitored for more than two years such that the first year was simulated as an extremely wet year with irrigation added to the natural precipitation, and second year was simulated with only natural precipitation.

During the 26 months of running the experiment no leachate was observed at the bottom of GW pile. The VWC results suggest that water only reached a depth between 2.0 m – 3.5 m in the extremely wet year and 0.5 m to 2.0 m for the natural precipitation. This behavior suggests that a cover with 3.5 m of GW provides sufficient storage capacity to balance the evapotranspiration and precipitation in a wet year.

Leachate was collected from the bottom of WR pile after approximately one year. Although the volume of leachate from the bottom of WR pile was not measured, however, no leachate was collected from the bottom of GW pile while leachate was generated from the WR pile suggests that the GW pile improve soil water storage compare with tradition mine waste management technique (WR piles) from a leachate generation perspective.

Saturation, oxygen concentration, EC, and temperature measured within the GW and WR piles during the 26-month experiment suggests that some level of pyrite oxidation was occurring in Layers 1 and 2 of GW and WR piles. However, the EC and temperature results suggest that a stronger ARD reaction happened in the WR pile in comparison with the GW pile. The surface of the WR pile showed visual signs of weathering, potentially due to sulfide oxidation. Also, vegetation never established on the WR pile core while vegetation established on the GW pile. In addition, effluent leachate chemistry evaluated on a limited number of samples from the WR pile indicated a decreasing pH as well as increasing TDS and EC, and increasing iron and sulphate concentration during a period of 65 d during the first year of the experiment. These observations support disposing of mine waste as GW improves the leachate chemistry and reduces the leachate volume compare to traditional WR pile under the conditions of the pile experiment reported herein.

2.6 Conclusions

The focus of this study was to evaluate hydrologic and environmental behavior of a GeoWaste (GW) and a waste rock (WR) test pile operated under natural climatic conditions for 26 months. Each pile was equipped with sensor sets in four layers at depths of 0.5 m (Layer 1), 2.0 m (Layer 2), 3.5 m (Layer 3), and 4.8 m (Layer 4) from the pile surfaces. Each sensor set provided measurements for volumetric water content, temperature, oxygen concentration, and electrical conductivity. Additional leachate chemistry samples from the WR pile were collected for a limited period of time were also evaluated. The following conclusions are drawn from this study.

- No leachate was collected from the bottom of GW pile during the 26-month experiment, whereas leachate was collected after approximately one year at the bottom of the WR pile. Using GW method as mine waste management technique results in lowering the quantity of leachate generation which decreases the environmental risk associated with environmental contamination associated with the acid mine generation.
- An increase in saturation in Layer 1 of the GW pile corresponded to a decrease in oxygen concentrations within all four layers of the pile. Conversely, saturation of Layer 1 reduced

during the first dry season and the oxygen concentration subsequently increased in all four layers. Small sulphide oxidation may have occurred in the GW pile based on an increase in pore fluid electrical conductivity in Layers 1 and 2 when water and oxygen were present. However, the GW pile supported vegetation throughout the experiment, which indicates that sulphide oxidation was sufficiently suppressed to allow biological activity.

- The water content and saturation of the WR pile were considerably greater than the GW pile, which was attributed to a higher infiltration rate and absence of vegetation at the surface of the WR pile. Saturation in Layers 1 and 2 of the WR pile reached 100% towards the end of the 1st wet season, which effectively eliminated oxygen ingress into the pile. A modest increase in pore fluid electrical conductivity and temperature in Layer 1 of the WR pile corresponded with water and oxygen present in the surface layer, which suggests that some sulphide oxidation occurred within the WR pile. This development of acid is consistent with the absence of vegetation on the surface of the WR pile.
- Based on the measured saturation, oxygen concentration, EC, and temperature in GW and WR piles during the 26 months of experiment, a larger acid mine reaction happened in WR pile in comparison with the GW pile. This behavior suggests disposing mine waste as GW reduces acid generation compared to separated WR and tailings deposition method.

Table 2.1. Summary of physical characteristics and classification for tailings and waste rock.

Material	*LL* (%)	*PI* (%)	USCS	Gravel Content (%)	Sand Content (%)	Fines Content (%)	Clay-Size Content (%)	As-Received Water Content (%)	G_s	w_{opt} (%)	$\rho_{d\text{-}max}$ (g/cm^3)
Tailings	30.1	9.2	CL	0	14.3	85.7	23.6	21.5	2.68	15.8	1.69
Waste Rock	NA	NA	GM	45.0	31.7	23.3	NA	5.8	2.64	NM	NM

Notes: *LL* = liquid limit; *PI* = plasticity index; USCS = Unified Soil Classification System; clay-size content taken as percent particles by mass < 0.002 mm; G_s = specific gravity; w_{opt} = optimum water content and $\rho_{d\text{-}max}$ = maximum dry unit density determine from Standard effort compaction tests; NA = not applicable; NM = not measured.

Table 2.2. Leachate chemistry from waste rock pile effluent collected from the lysimeter.

Parameter	Units	Elapsed Time (d)		
		219	248	284
pH	NA	NM	6.5	5.5
Electrical Conductivity	µS/cm	645	1853	2249
Sulphate	mg/L	185	680	1070
Iron	mg/L	<0.2	0.7	3.4

Note: NA = not applicable, NM = not measured.

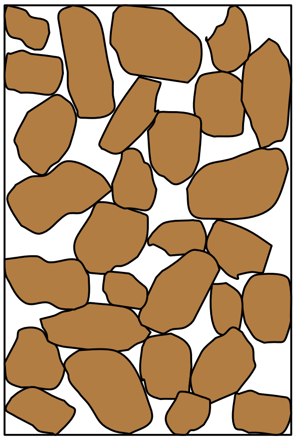

Mine Waste with Active Acid Rock Drainage

Characteristics:
- Large pores enabling water and oxygen ingress
- Low moisture holding capacity
- High water and air conductivity

Monitoring signatures:
- Moisture pulses with atmospheric oxygen typically present
- Gradual increase in EC due to sulphide oxidation
- Gradual increase in temperature due to exothermic (sulphide oxidation) reactions

→ Acid drainage

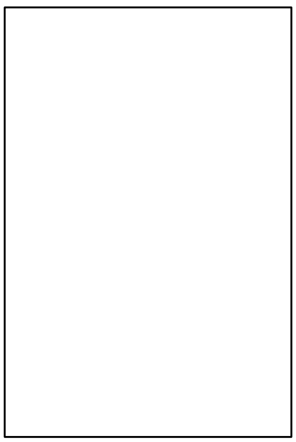

'Saturated' Mine Waste as Oxygen Barrier (No Vegetation)

Characteristics:
- Small pores that retain water and when saturated prevent oxygen ingress (moderate to high relative compaction)
- High moisture holding capacity
- Low hydraulic conductivity

Monitoring signatures:
- Increase to constant high moisture content
- Reduction in oxygen to near zero due to minimal pore gas and reactions
- No increase in temperature or pore fluid EC

→ Possible drainage, but not acidic

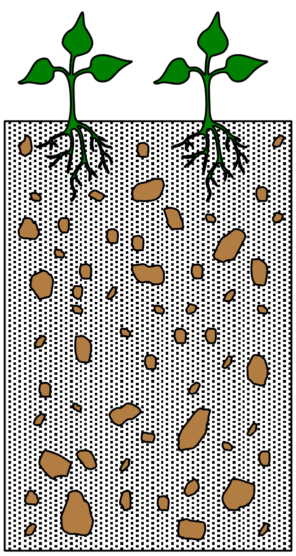

Mine Waste as Water Balance Cover (Vegetation)

Characteristics:
- Broad distribution of pore sizes for soil water storage (low relative compaction)
- Developed vegetation to promote transpiration
- Moderate to low hydraulic conductivity

Monitoring signatures:
- Fluctuating, seasonal water content near surface but no deep percolation
- Stable moisture content below environmental (near surface) boundary layer
- Potentially high oxygen content across profile
- Increasing EC in pore fluid below environmental boundary layer

→ Negligible drainage (no deep percolation)

Fig. 2. 1. Schematics of mine waste and typical characteristics and monitoring signatures associated with (i) active acid rock drainage, (ii) a "saturated" system created as an oxygen barrier, and (iii) a water balance cover.

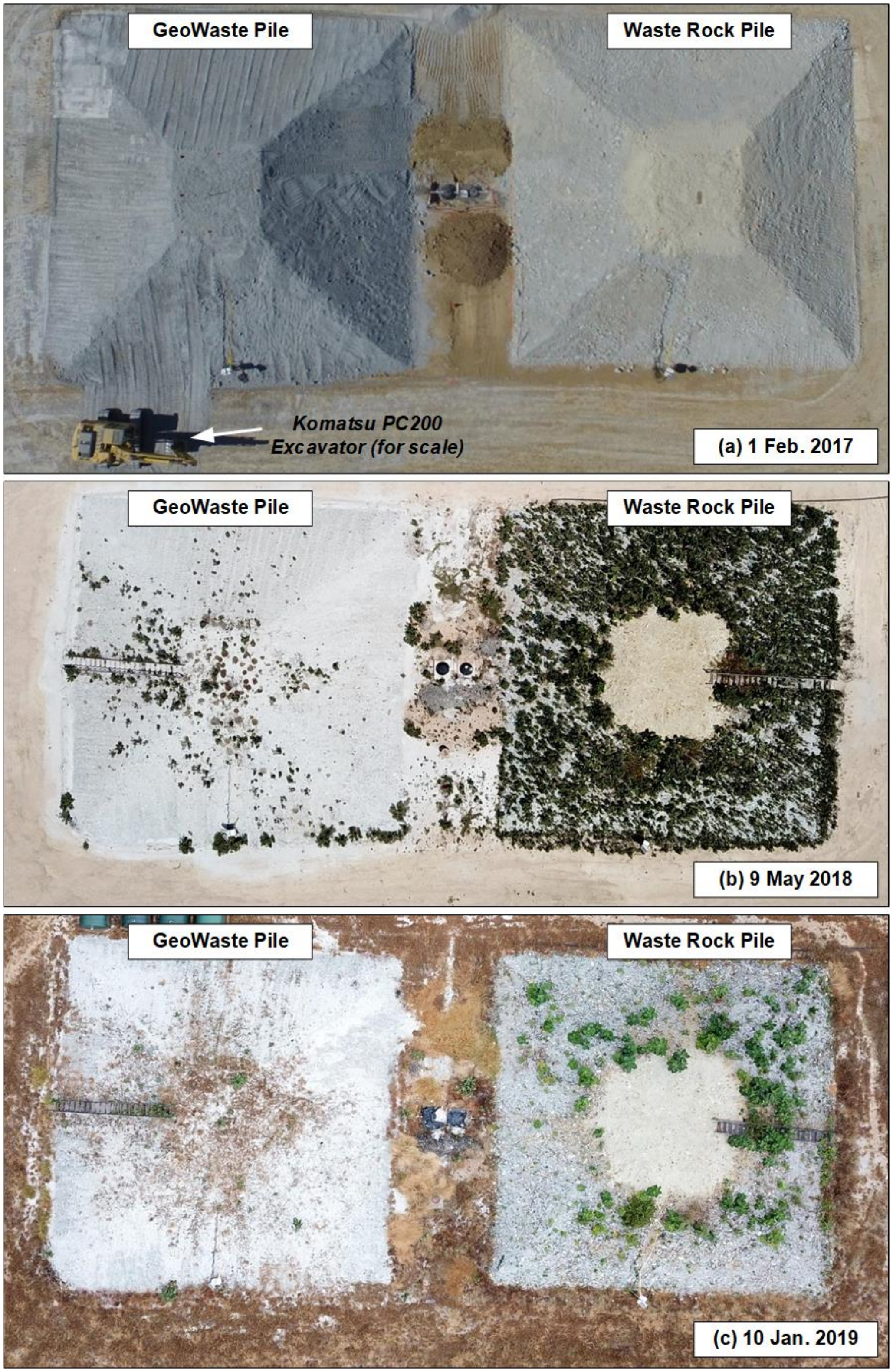

Fig. 2. 2. Aerial photographs of the GeoWaste and waste rock piles taken on (a) 1 Feb. 2017 (i.e., end of construction), (b) 9 May 2018, and (c) 10 Jan. 2019. Vegetation was trimmed approximately after 9 May 2018 and then allowed to re-establish.

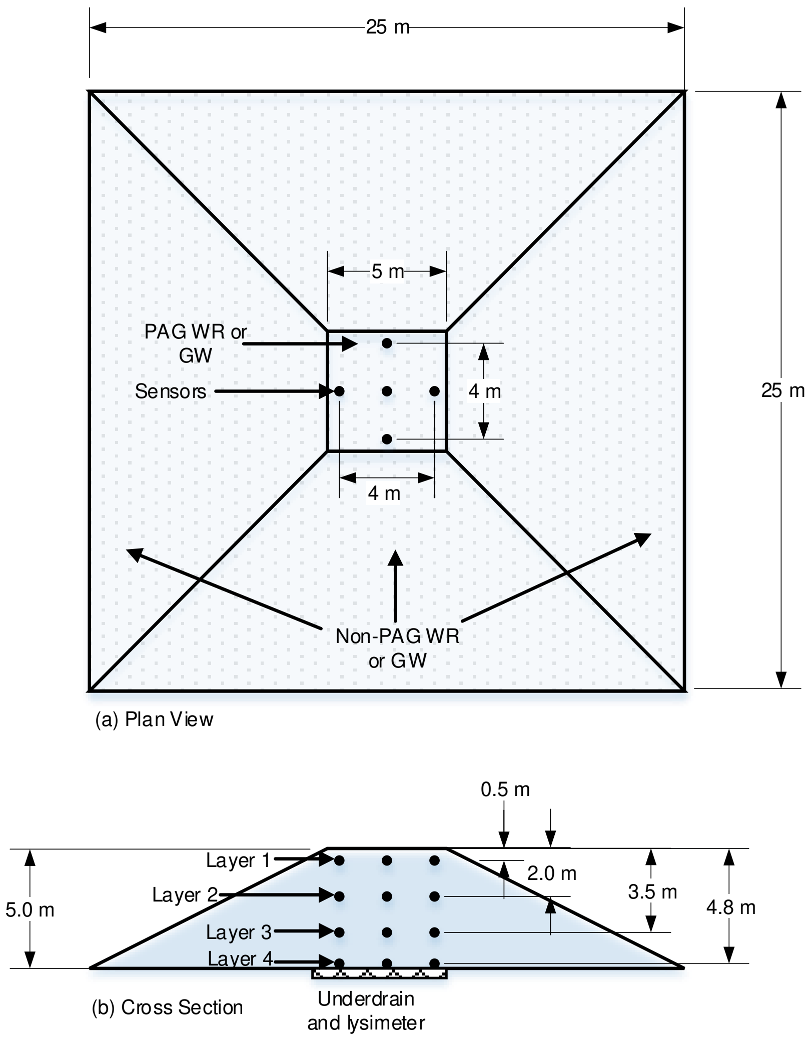

Fig. 2. 3. Schematic of dimensions and sensor location for GeoWaste and waste rock piles: (a) plan view, and (b) cross sectional view. PAG = potential acid generating.

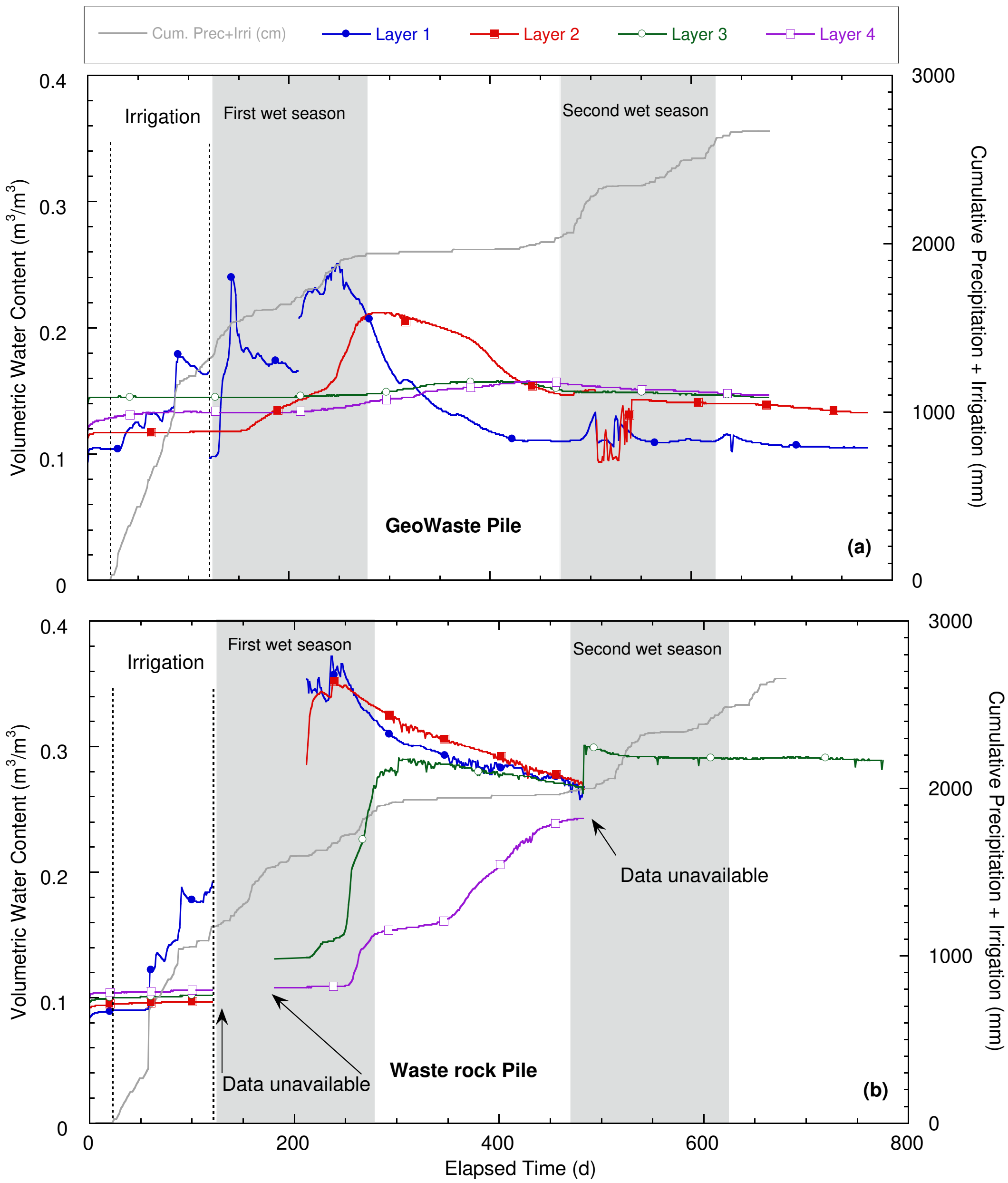

Fig. 2. 4. Temporal trends of average volumetric water content measurements from five sensors in four different layers in the (a) GeoWaste pile; and (b) waste rock pile. Layer 1 = 0.5 m deep, Layer 2 = 2.0 m deep, Layer 3 = 3.5 m deep, and Layer 4 = 4.8 m deep. All depths relative to original surface elevation. Cumulative precipitation and irrigation (Prec+Irri) on the surface of the pile is included for comparison in each plot.

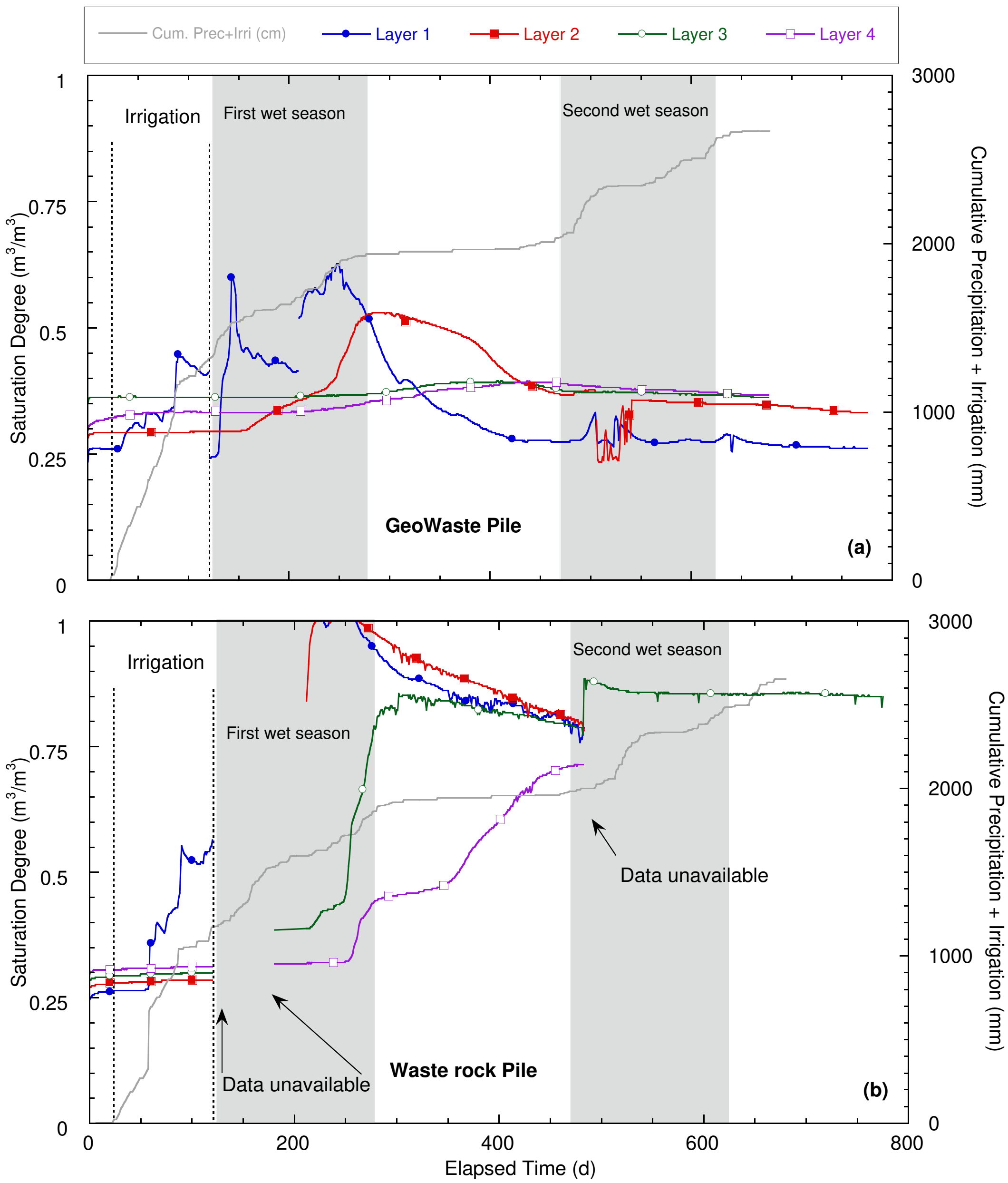

Fig. 2. 5. Temporal trends of average volumetric water saturation degree measurements from five sensors in four different layers in the (a) GeoWaste pile; and (b) waste rock pile. Layer 1 = 0.5 m deep, Layer 2 = 2.0 m deep, Layer 3 = 3.5 m deep, and Layer 4 = 4.8 m deep. All depths relative to original surface elevation. Cumulative precipitation and

irrigation (Prec+Irri) on the surface of the pile is included for comparison in each plot.

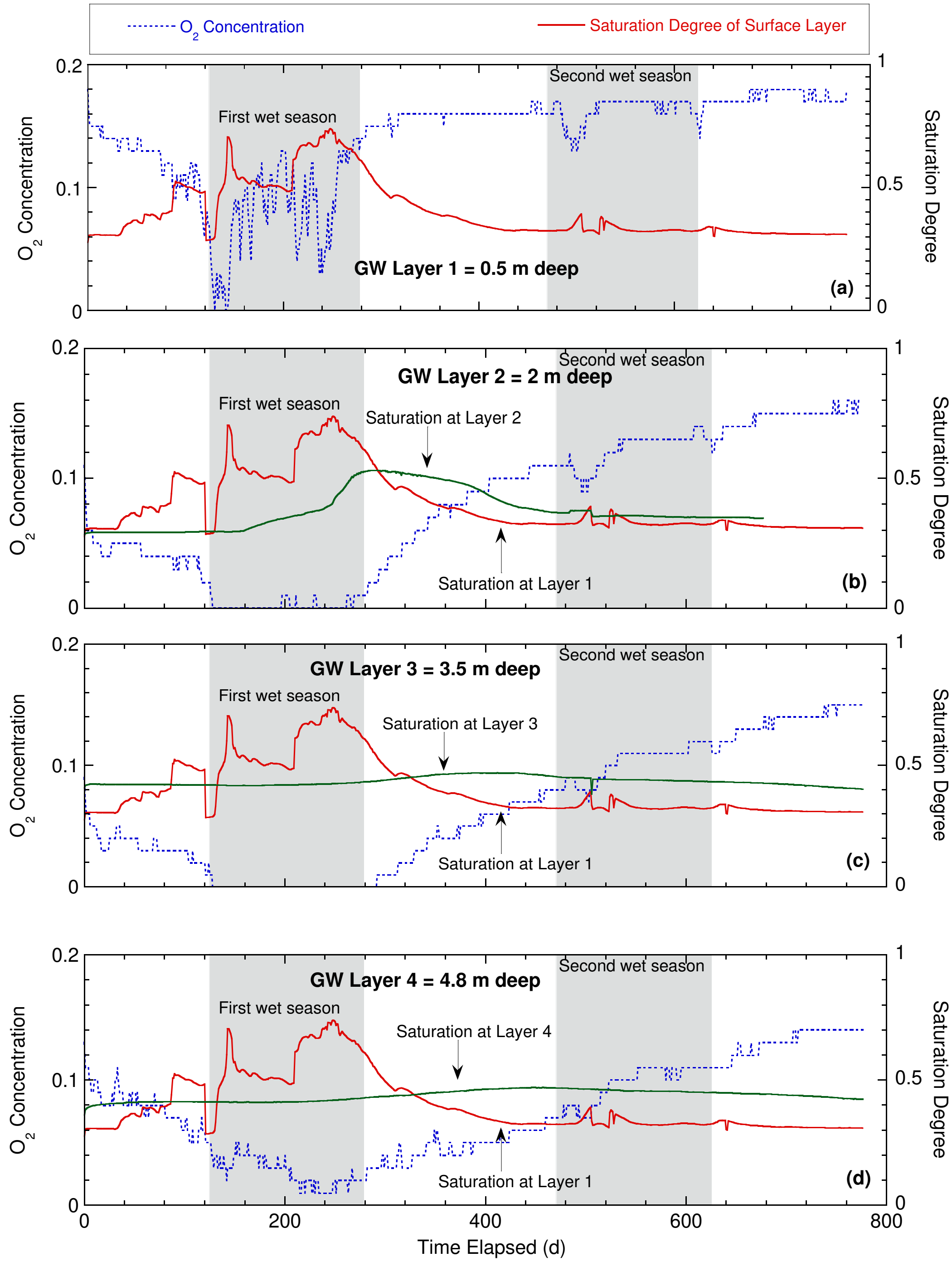

Fig. 2. 6. Temporal trends of oxygen concentration measurements from five sensors in four different layers in the waste rock pile (a) Layer 1 = 0.5 m deep, (b) Layer 2 = 2 m deep, (c) Layer 3 = 3.5 m deep, and (d) Layer 4 = 4.8 m deep. All depths relative to original surface elevation. Water saturation degree of different layers is included for comparison in each plot. S1, S2, S3, and S4 = saturation degree in the first, second, third, and fourth

layers respectively.

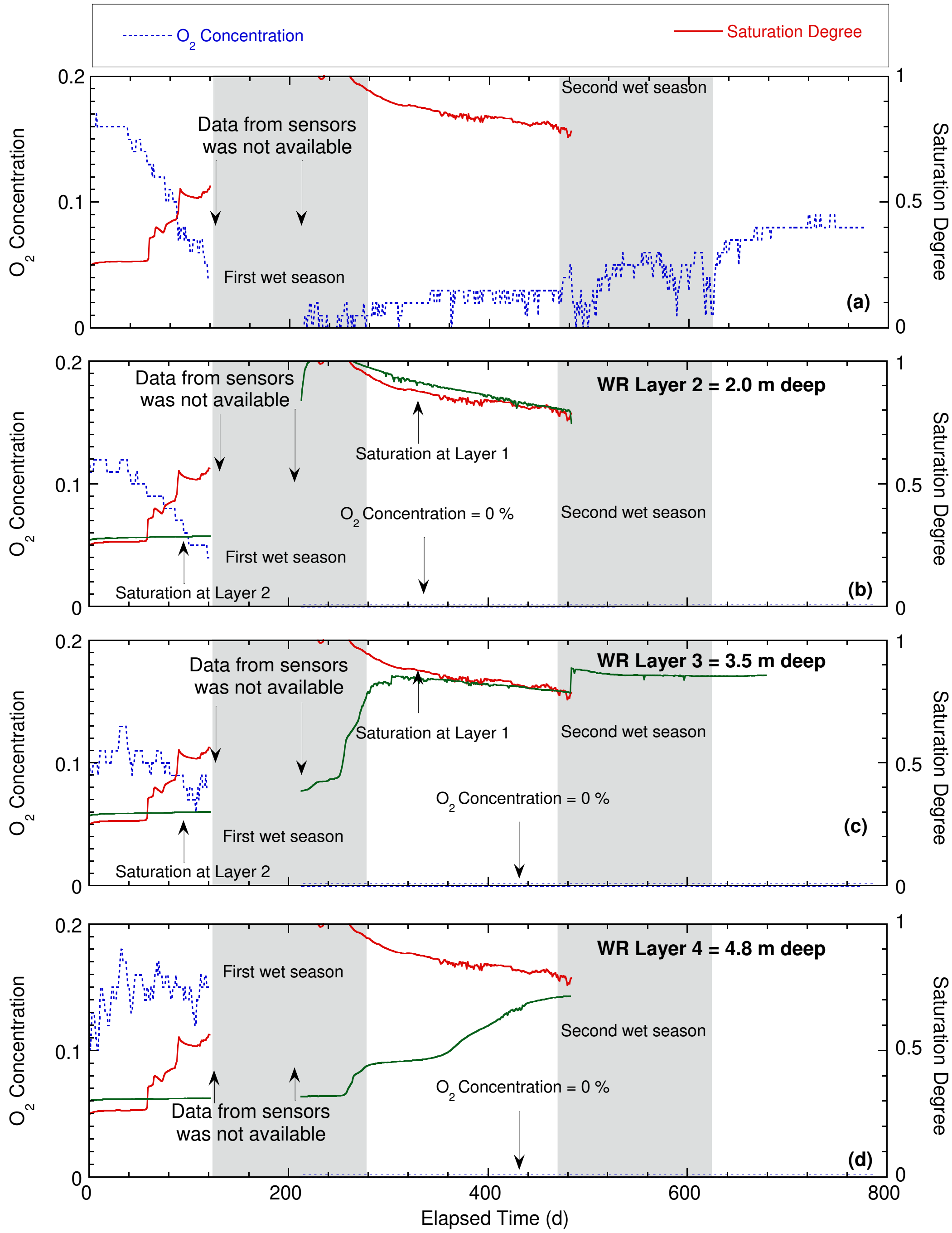

Fig. 2. 7. Temporal trends of average oxygen (O_2) concentration measurements from five sensors in four different layers in the waste rock pile (a) Layer 1 = 0.5 m deep, (b) Layer 2 = 2 m deep, (c) Layer 3 = 3.5 m deep, and (d) Layer 4 = 4.8 m deep. All depths relative to original surface elevation. Saturation degree of different layers is included for comparison in each plot.

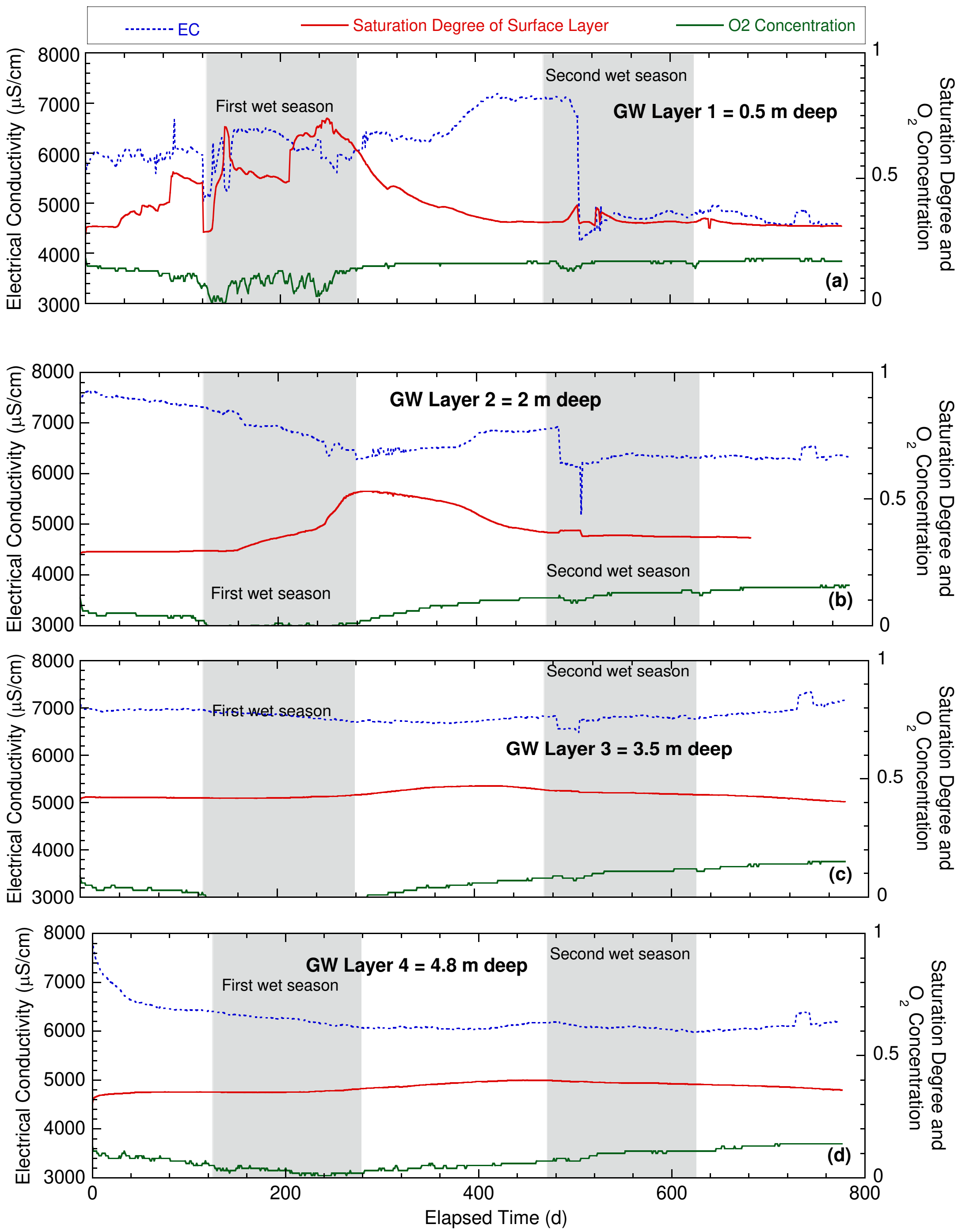

Fig. 2. 8. Temporal trends of layer-average electrical conductivity (EC) measurements from five sensors in four different layers in the GeoWaste pile. Saturation degree and O_2 concentration of different layers is included for comparison in each plot.

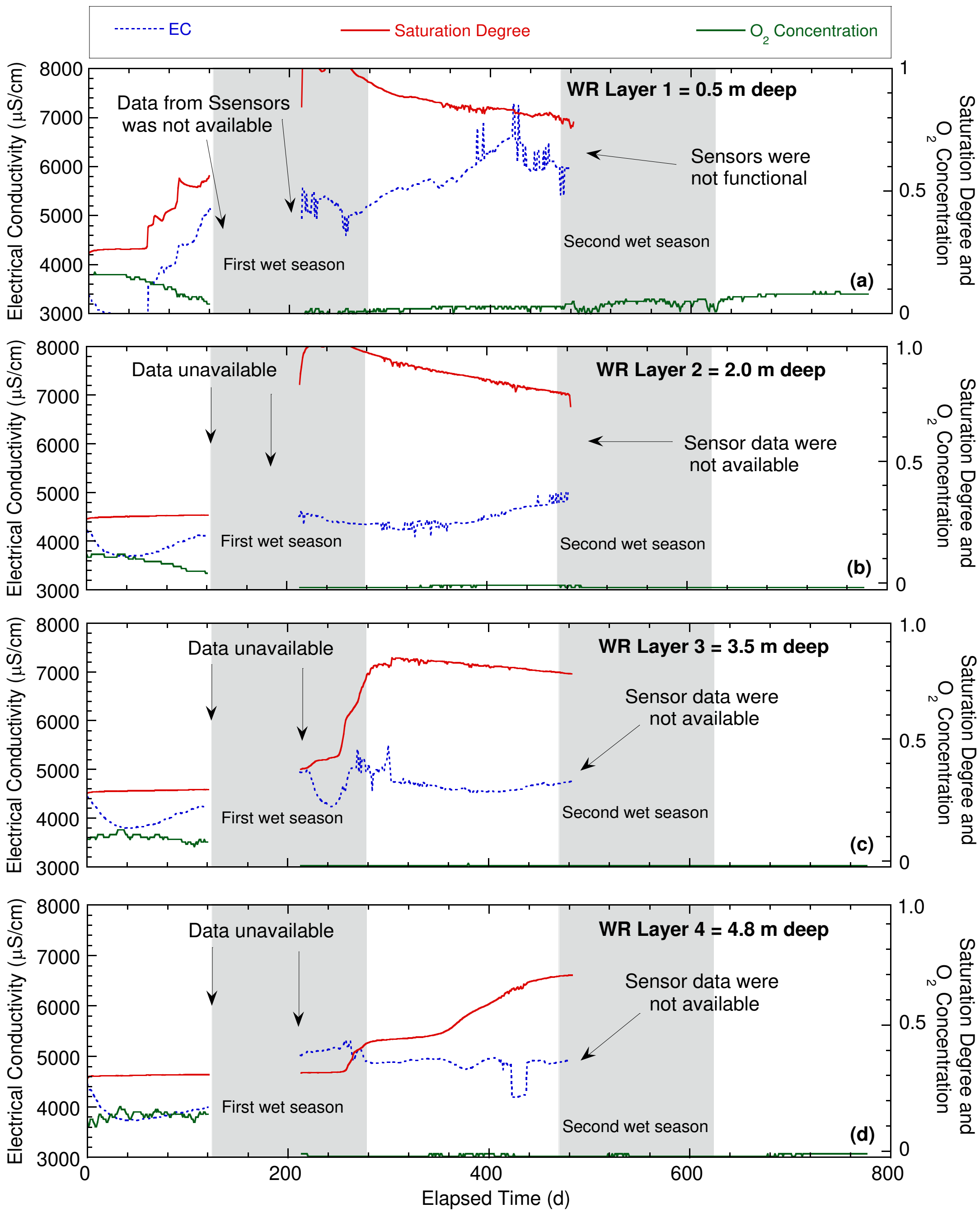

Fig. 2. 9. Temporal trends of layer-average electrical conductivity (EC) measurements from five sensors in four different layers in the waste rock pile. Saturation degree and O_2 concentration of different layers is included for comparison in each plot.

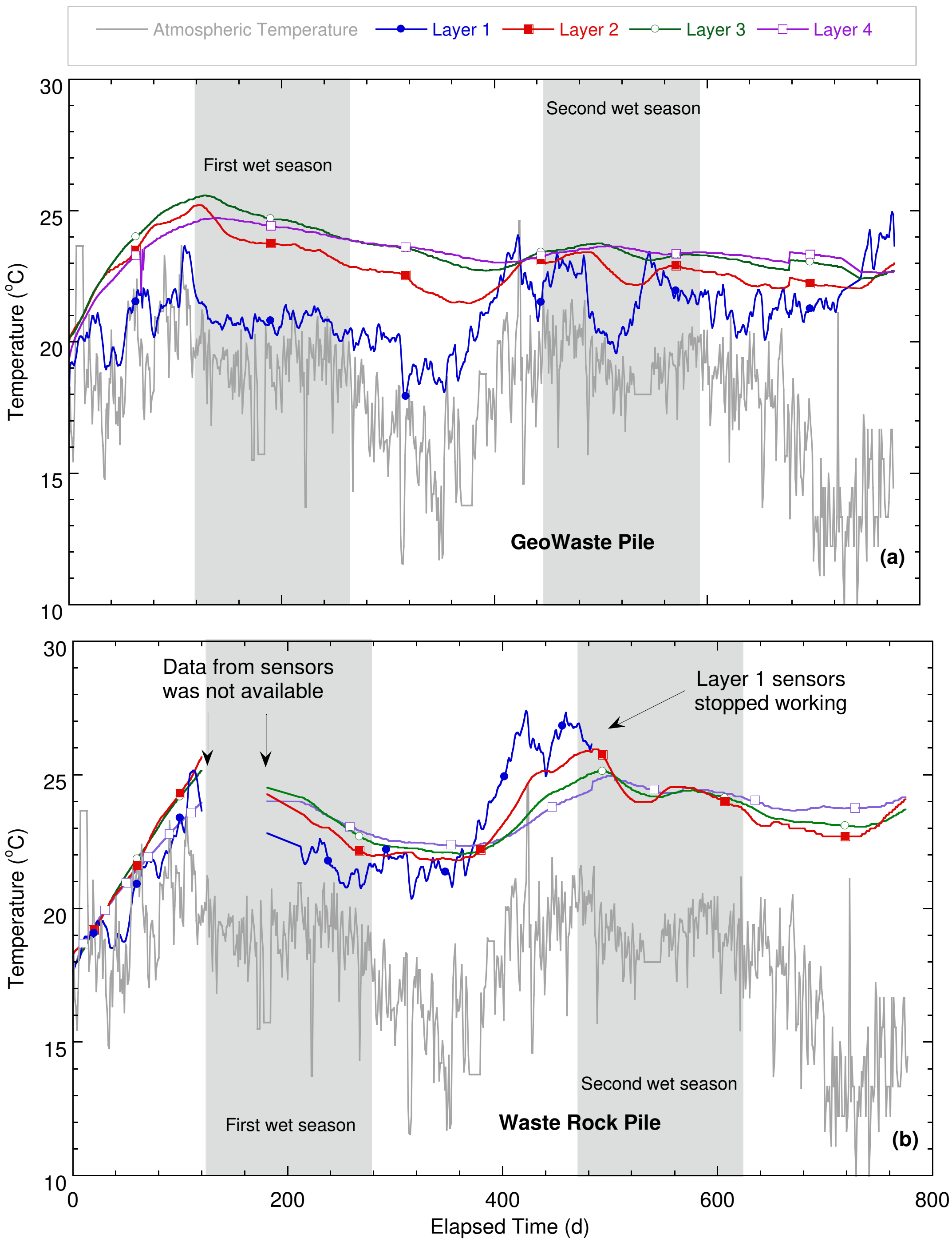

Fig. 2.10. Temporal trends of temperature measurements in four different layers in the (a) GeoWaste pile, and (b) waste rock pile. Layer 1 = 0.5 m deep, Layer 2 = 2 m deep, Layer 3 = 3.5 m deep, and Layer 4 = 4.8 m deep. All depths relative to original surface elevation. T = atmospheric temperature.

3 HYDRAULIC CONDUCTIVITY TESTING AND DESTRUCTIVE SAMPLING OF FIELD-SCALE GEOWASTE AND WASTE ROCK TEST PILES

3.1 Introduction

Mine waste (i.e., waste rock and tailings) are generated in large quantities in the mining industry. Mine waste present numerous challenges including mechanical stability, potential environmental contamination, water management, and closure and reclamation (Willimas et al. 2003; Leduc et al. 2004). Mixing and co-managing waste rock (WR) and tailings (WR&T) has been evaluated as an alternative mine waste management option based on potential to achieve environmental sustainability and mechanical stability. (Williams et al. 2003; Wick;and et al. 2006; Hamade and Bareither 2019). GeoWaste (GW) is a WR&T mixture whereby fast-filtered tailings and WR are blended to isolate WR particles within a tailings-dominated matrix.

The focus of this study is the reduced acid production potential of WR disposed of as GW mixture. Hydraulic properties (i.e., hydraulic conductivity and soil water characteristics) of GW mixture controls the leachate volume and leachate quality (pH, total dissolved solids) of mine waste. GeoWaste mixture with low hydraulic conductivity (*k*) reduces the infiltration of water from precipitation and thus reduces the volume of water to be potentially contaminated. Moreover, mine waste with high water retention is more likely to maintain a high degree of water saturation which prevent oxygen diffusion into the mine waste and limits the sulphate oxidation and resulting acid generation.

The laboratory hydraulic conductivity of GW is investigated in the literature and results in literature suggests lower hydraulic conductivity in GW mixture in comparison with WR; however, no field comparison was provided for the hydraulic properties of GW and WR. Some studies in the literature have reported significant variations in laboratory and field measured soil hydraulic properties. Benson et al. (1999) showed that on average field measured k is 11.2-times larger than 75 mm-diameter laboratory measured k for material that has $k > 10^{-9}$ m/s suggesting pore-size distribution in the laboratory samples are not representative of pore structures in the field. Moreover, Benson et al. (2007) compared the hydraulic properties of test sections constructed across the United States after a few years in service. They reported as-built k increased on average two to three orders of magnitude after two to three years in service. Benson et al. (2007) also reported an increase in saturated volumetric water content (θ_s) and van Genuchten's α parameter (i.e., decrease in air entry pressure, Ψ_a), and a decrease in van Genuchten's n parameter. These changes are due to pedeogenesis which is a natural soil formation process that can create a macroporous structure near the surface of the soil due to bio-intrusion, freeze-thaw, and wet-dry cycles under natural climatic conditions.

The purpose of this study is to investigate the in-situ k, density, and spatial variability of mixture ratio in the GW and WR piles. Comparison between the in-situ k of GW and WR piles can provide information about the quantity of generated leachate in each pile. Spatial variability of in-situ density and mixture ratio provide information regarding capability of creating a homogenize GW deposit. Two piles were constructed, one from WR and a second from GW at a mine in Central America. Piles were monitored for 26 months under enhanced (irrigated initially) natural climatic conditions.

3.2 Test Piles

Aerial photographs of the GW and WR piles at the end-of-construction and during operation are shown in Fig. 3.1. The piles were constructed in January 2017 as truncated 5-m tall pyramids with 25-m base sides and flat 5 m × 5 m top surfaces. The WR pile was constructed with potentially acid generating (PAG) WR within the central core of the pile (5 m x 5 m x 5 m) with non-PAG WR was used on the side slopes. Non-PAG WR on the side slopes supported vegetative growth during the experiment, whereas vegetation never established on the PAG WR placed in the central core of the WR pile (Fig. 3.1). The GW pile was constructed with GW prepared to a total mass mixture ratio of 0.4 (R_t = total mass of WR / total mass of tailings), which corresponded to a dry mass mixture ratio of approximately 0.43 (R = dry mass of WR / dry mass of tailings). At this R_t, WR exists as floating inclusion within a tailings dominated matrix. Potentially acid generating WR was used in GW placed in the central core of the pile and non-PAG WR was used in GW placed on the side slopes. Vegetation established on the side slopes and within the central core of the GW pile during operation (Fig. 3.1). The focus of this study was to evaluate hydraulic properties of the central cores of the GW and WR piles.

GeoWaste placed in the central core of the GW pile was prepared with filtered mine tailings and PAG WR. These materials were mixed on site using an excavator prior to placement. After thorough mixing, the GW was dropped from a height of approximately 2 to 3 m into the central core of the pile using an excavator. This process simulated the anticipated full-scale GW final placement process via disposal at the end of a conveyor system. GeoWaste for the side slopes of the GW test pile was prepared in a similar manner with non-PAG WR and placed with an excavator to form a ring to support the central core. The WR pile was constructed following a similar process as the GW pile; non-PAG WR was placed via an excavator to form a ring that ultimately supported disposal of PAG WR that was dropped from a height of 2 to 3 m to form the central core. Thus, similar construction processes were used for both piles in which the central cores represented anticipated mine waste deposition processes in full-scale mine waste management operations.

Plan view and cross-section schematics of the inner core of the test piles are shown in Fig. 3.2. Each pile was instrumented with four layers of sensors, and each layer contained five sets of sensors: one set in the center and four sets positioned approximately 2-m radially from the center on each side of the piles (Fig. 3.2a). Each sensor set contained a TDR-315L Acclima sensor to measure volumetric water content, electrical conductivity, permittivity, and temperature (TDR sensor), and a SO-110 Apogee sensor to measure oxygen concentration (O_2 sensor). All sensors from a given pile were connected to a CR-1000 Campbell Scientific datalogger that interfaced with an AM 16/32B Campbell Scientific multiplexer. The instrumentation stations for each pile had a solar panel power supply. Details on instrumentation is provided in Chapter 2.

The test piles were operated for approximately 26 months. At the end of the experiment, SDRI tests were conducted on each pile followed by destructive sampling. The destructive samples approximately aligned with the sensor sets in plan view (Fig. 3.2) and were exhumed at depths just above the sensors. Spatial location of all samples was obtained using GPS. Each destructive sample was excavated as part of an in situ density test and additional testing was completed on exhumed material in the laboratory (described subsequently). Approximately 0.4 m of the surface of the GW pile was removed prior to installation of the SDRI to clean the surface of vegetation and conduct the first layer of destructive samples. The WR pile had no vegetation on the surface such that destructive samples were collected at the surface, and the surface was then smoothed to approximately 0.2-m down for SDRI installation.

3.3 Materials and Methods

3.3.1 Materials

Geotechnical material characterization of mine tailings and WR included mechanical sieve and hydrometer (ASTM D422, ASTM 2007), Atterberg limits (ASTM D4318, ASTM 2014a), specific gravity (ASTM D854, ASTM 2014b), and standard-effort compaction testing (ASTM D698, ASTM 2014c). Material characteristics of the tailings and WR are summarized in Table 3.1. These characteristics were measured on representative samples shipped to the laboratory at the time that piles were constructed. The particle-size distributions (PSD) for tailings and WR were used to analyze the R distribution in the GW pile. Moreover, the PSD of WR in Table 3.1 was compared with the measured PSD of WR pile at 20 locations to evaluate weathering of WR.

Characteristics of tailings and WR in this study were compared to the literature. The liquid limit (LL) of tailings agreed with the reported range in literature (i.e., 18% < LL < 40%). Jehring and Bareither (2016) presented an average, upper-bound, and lower-bound particle-size distribution (PSD) for tailings and WR based on a compilation of data from literature (Morris and Williams 1997, Qiu and Sego 2001, Khalili et al. 2005, Wickland and Wilson 2005, Wickland et al. 2006, Bussière 2007, Khalili et al. 2010, and Wickland et al. 2010). The characteristics compiled in Table 3.1 and PSD ranges shown in Jehring and Bareither (2016) suggest that the tailings was generally comparable with average hard rock mine tailings properties. Waste rock in this study was more well-graded and had a higher fines content (fine content > 23%) when compared to the average WR in literature (fine content < 2%).

3.3.2 In Situ Density Testing and Sample Processing

In situ density tests were conducted following ASTM D 5030 (ASTM 2013) because both test piles had WR particles ≥ 37.5-mm in diameter. Testing was conducted in the GW pile at depths of 0.2, 1.5, 3.0, and 4.0 m from the surface and in the WR pile at depths of 0.0, 1.5, 2.3, 3.9 m from the surface. Five in situ density tests were conducted in each layer in a given test pile (Fig. 3.2). The in situ density tests were performed as follows: (i) the surface of a given layer was manually smoothened and excavation locations marked; (ii) a hemisphere-shaped volume of approximately 20-L was excavated and exhumed material was transferred to a clean bucket and sealed; (iii) a thin plastic sheet was placed in the excavation and filled with a measured mass of water that was converted to a volume assuming density of water = 1 Mg/m^3; (iv) the mass of excavated material in sealed buckets was determined; and (v) sealed buckets were shipped to the laboratory for subsequent testing.

Water content was measured by oven-drying the entirety of each in situ density sample. Oven-drying was conducted at 115 °C for at least 24 h and until no change in mass was recorded over 2-h intervals. Subsequently, the entirety of each in situ density sample was subjected to particle-size analysis. Sieve analyses on the in situ density samples were conducted by wet sieving through a stack of sieves to separate materials ranging in size from 25.4 mm to 0.075 mm. Material retained on each sieve was then oven dried at 115 °C for at least 24 h and until no change in mass was recorded over 2-h intervals.

3.3.3 Sealed-Double Ring Infiltrometer

Sealed-double ring infiltrometer tests were conducted and data were evaluated in accordance with ASTM 5093 and recommendations in Daniel (1989). The outer ring had dimensions of 2.4 m x 2.4 m and was constructed from 13-mm-thick plywood, whereas the inner-ring had dimensions of 1 m x 1 m and was constructed of 3.2-mm-thick sheet metal. The outer- and inner-rings were centered on the surface of the test piles to focus infiltration in the central cores of the piles. Plywood for the outer-rings was treated with polyurethane paint and sealed along the edges with wood glue and waterproof caulk to create a watertight ring. Inflow into the inner ring was monitored via a 5-L flexible plastic bag and the level of water ponded within the outer ring was monitored via a meter stick attached to the outer ring.

Depth of the wetting front during infiltration from the SDRIs was monitored by tensiometers, embedded water content sensors (Fig. 3.2), and observations post-testing during destructive sampling. Three tensiometers were installed between the outer- and inner-rings of the SDRIs in each of the test piles at different depths from the surface. One of the tensiometers in the WR pile failed and was not included in the analysis. During the SDRI tests, there were 10 water content sensors from the 20 originally installed in the GW pile that were functioning and capable of monitoring progression of the wetting front; however, unfortunately none of the original 20 water content sensors installed in the WR pile remained functional at the time of testing.

The SDRI test in the GW pile was operated for 7 d and the ponded water depth was maintained between 0.11 m and 0.43 m. The SDRI test in the WR pile was operated for 4 d and ponded water height was maintained between 0.0 to 0.49 m. During SDRI testing inflow measurements from the flexible plastic bag connected to the inner ring and the ponded water height within the outer ring were recorded at a frequency of approximately once or twice per hour. Hydraulic conductivity of the test piles was computed (Daniel 1989) as

$$k = \frac{I}{i} \tag{3.1}$$

where I is infiltration rate and i is hydraulic gradient. The infiltration rate was computed as

$$I = \frac{V}{A_{ir} \bullet \Delta t} = \frac{\Delta W_{bag}}{\rho_w \bullet A_{ir} \bullet \Delta t} \tag{3.2}$$

where V is the volume of infiltrated water in the inner ring, A_{ir} is the area of inner ring, Δt is the elapsed time of inner ring infiltration, ΔW_{bag} is the change in the weight of bag connected to inner ring, and ρ_w is the water density. The hydraulic gradient was computed as

$$i = \frac{D_p + D_f + \Psi_f}{D_f} \tag{3.3}$$

where D_p is depth of water ponded in the outer ring, D_f is depth of the wetting front, and ψ_f is suction head at the wetting front. Several suggestions are provided in literature to estimate ψ_f. Daniel (1989) suggested to consider $\psi_f = 0$ to obtain the most conservative case with the largest k. Wang and Benson (1995) the following to estimate ψ_f

$$\Psi_f = \frac{\Psi_a}{3}\left[1 - \frac{D_f}{L}\right] \tag{3.4}$$

where L is the total thickness of test pad.

The ψ_a in Eq. 3.4 in this study was obtained based on laboratory testing for GW and soil water characteristic estimation based on PSD from Rosetta (USDA 2008) for WR. Two ψ_a for each material were considered for each material representative of highest and lowest ψ_a to bound calculated k.

3.4 Results

3.4.1 *In Situ Density*

A summary of total and dry density, water content, porosity, and void ratio of samples from the in situ density tests in the GW and WR piles is in Table 3.2. Destructive sampling was conducted in Layer 1 prior to installation of the SDRI tests; thus, Layer 1 reflects natural moisture conditions present in the GW and WR at the time of sampling. In contrast, destructive sampling in Layers 2, 3, and 4 was conducted after infiltration from the SDRIs. In general, the total density and water content increased in both piles in Layers 2, 3, and 4 relative to Layer 1, which was due to infiltration from the SDRI as well as compression from an increase in surface loading from the SDRI and infiltrated water atop an unsaturated layer. In particular, surface settlement of the GW pile was observed throughout the duration of the SDRI test.

Dot plots of dry density in the GW and WR piles are shown in Fig. 3.3. The average dry densities of Layers 1 and 4 in the GW pile were similar (1.53 and 1.54 Mg/m^3) and the average dry densities were higher for Layer 2 (1.85 Mg/m^3) and Layer 3 (1.63 Mg/m^3). The highest dry density (measured in Layer 2) was attributed to settlement in the GW that occurred due to loading from the ponded water in the SDRI combined with a potential increase in effective stress as total density increased in the absence of positive pore pressure. Settlement in the range of 20 to 70 mm was observed in the vicinity of the SDRI test relative to the edges of the central core, which were not subjected to loading from the ponded water or the wetted zone of the GW. This settlement most likely was concentrated within Layer 2, which resulted in the highest average dry density measured, and diminished with depth. The diminishing influence of loading and settlement below the SDRI is observed as a decrease in average dry density from Layer 2 to Layer 3 and ultimately to Layer 4 at the bottom of the GW pile. The wetting front was not observed to reach Layer 4, which is supported by the lower average water content (0.13) relative to the average water contents of Layers 2 and 3 (0.22 and 0.23). Water content in Layer 4 is consistent with results of VWC sensors prior to beginning of the SDRI experiment.

The trend in dry density as a function of layer depth in the WR pile was similar to that observed in the GW pile (Fig. 3.3b), however, there were notable differences. Although surface settlement was not observed in the WR pile, minor settlement may have occurred that resulted in an increase in average dry density in Layer 2 (1.94 Mg/m^3) relative to Layer 1 (1.87 Mg/m^3). The average dry density of Layer 3 (1.83 Mg/m^3) was similar to Layer 1, which suggests that perhaps minor settlement occurred beneath the SDRI in the WR pile and was concentrated within Layer 2. The lowest average dry density was measured for Layer 4 (1.71 Mg/m^3). The reason for the lower dry density at the base of the WR pile was not identified but could be a result of different compaction effort during pile construction.

In general, the GW pile had lower total and dry density, and higher porosity and void ratio than the WR pile. The average porosity of the GW pile was 0.38 and the average porosity of the WR pile was 0.31. Waste rock in this study was well-graded and contained approximately 45% gravel, 32% sand, and 23% fines (Table 3.1). This broad distribution of particles sizes can be attributed to factors such as mineralogy, mining process, and weathering. The lower porosity of the WR pile in comparison to the GW pile was consistent with the post-construction report, which indicated an average porosity of 0.42 for the GW pile and 0.37 for the WR pile. These values from the post-construction report agree with measurements from Layer 1 in both piles, which were not influenced by the SDRI test.

3.4.2 Particle-Size Analysis and Mixture Ratio

Particle-size distributions of WR and tailings used for construction of the test piles are shown in Fig. 3.4a. The WR was run-of-mine and included particles up to 300-mm diameter. Particle-size distributions determined for two run-of-mine WR samples show similar shape but had fines contents of approximately 11% and 27%. The tailings consisted of 85.7% fine-grained particles and all particles passed a 0.42-mm sieve. Computed PSDs for GW are also in Fig. 3.4a. These PSDs were computed assuming the tailings and WR PSDs were representative of materials used to create GW at a mixture ratio of $R = 0.43$. The range of GW PSDs was developed for comparison with PSDs measured on in situ density samples collected during destructive sampling of the GW pile.

Particle-size distributions determined for ten in situ density samples collected from the GW pile using wet sieve are shown in Fig. 3.4b along with the computed GW PSD range (dry sieved) from Fig. 3.4a. The PSDs determined for the in situ density samples appeared to contain coarser fraction, in general, compared to the computed PSDs for GW at $R = 0.43$. The fine-grained fraction of the in situ samples was finer, in general, and ranged between 36% and 62%, whereas the computed fine-grained fraction of GW was 63% to 68%.

The in situ mixture ratio for GW was computed with the following assumptions: (i) all particles retained on a No. 4 sieve (> 4.75 mm) originated from WR; (ii) the percent mass of the WR fraction retained on the No. 4 sieve ranged between 60% and 72% (average ≈ 66%); and (iii) the mass of tailings equaled the difference between the total dry mass of the sample and mass of WR. The particle-size threshold of 4.75 mm between WR and tailings was adopted based on the certainty that all material larger than 4.75 mm originated from the WR. Thus, after completing a PSD analysis on a given in situ density sample, the mass of material retained on a No. 4 sieve was assumed to be 60%, 66%, or 72% to compute the total mass of WR within the GW.

Dot plots of dry-mass and total-mass mixture ratios for in situ GW samples are shown in Fig. 3.5. The R_t was estimated assuming WR and tailings were placed in the GW pile at water contents of 9.8% and 17%, respectively, as reported by mine personnel involved in test pile construction. Three calculations for each mixture ratio were made pertaining to the range of WR retained on a No. 4 sieve. The target R_t for the GW pile was 0.4, which corresponded to $R = 0.43$ based on as-constructed water contents of the WR and tailings. The average mixture ratios (i.e., horizontal solid lines in Fig. 3.5) were all larger than the target mixture ratios for the three considerations of the percent WR retained on a No. 4 sieve. A single high mixture ratio computed for sample GW-L4-S (Fig. 3.4b) modestly skewed the average mixture ratios to higher values. The modestly higher mixture ratios computed from the in situ samples suggest that a higher fraction of WR was present in the GW than what was originally targeted. The effect of R variability in the hydraulic conductivity of GW needs further investigation.

3.4.3 Sealed-Double Ring Infiltrometer Tests

3.4.3.1 Wetting Front Assessment

Temporal trends of normalized tensiometer (T_n) readings in the GW pile during the first day of the SDRI test are shown in Fig. 3.6a. The T_n was calculated as suction measured by a tensiometer during infiltration divided by the equilibrated suction of the same tensiometer measured prior to infiltration (i.e., at t = 0 d). Normalized tensiometer readings were used to identify the time at which the wetting front reached a given tensiometer depth. A modest increase in T_n above 1.0 at the onset of infiltration from the SDRI was observed in all tensiometers in the GW pile, which was subsequently followed by a sharp reduction in T_n that identified arrival of the wetting front. The sharp reduction in T_n was used to determine arrival of the wetting front that corresponded to the installed depth of the tensiometer.

Temporal trends of normalized tensiometer readings in the WR pile for the first day of the SDRI test are shown in Fig. 3.6b. Only two tensiometers were available in that WR pile because the deepest tensiometer failed at the beginning of experiment. The wetting front was observed to penetrate more rapidly in the near surface material of the WR pile relative to the GW pile. Similar to the tensiometer results and wetting from evaluation from the GW pile, the pronounced reductions in T_n identified the time at which the wetting front passed tensiometers installed at two depths in the WR pile.

Volumetric water content was monitored in the GW pile during the SDRI test via sensors installed at four levels (Fig. 3.2). During the SDRI test there were two sensors active in Layer 2 (depth = 1.6 m), three sensors active in Layer 3 (depth = 3.1 m), and five sensors active in Layer 4 (depth = 4.4 m). Average volumetric water contents for each of the three layers (Layer 2, 3, and 4) in the GW pile during the SDRI test are shown in Fig. 3.7a. The average volumetric water content was similar in all three layers at the onset of the SDRI and ranged between 0.12 and 0.14.

The average water content in Layer 2 (depth = 1.6 m) exhibited a pronounced increased at t = 1.3 d, which correspond to arrival of the wetting front. The average volumetric water content in Layer 3 exhibited a slight increase at t = 6.0 d, which corresponded to the time the datalogger station was powered down.

A photograph of the GW pile during excavation is shown in Fig. 3.7b in which the wetting front is marked by a yellow line. The wetting front was tracked during pile excavation and destructive sampling. The photograph in Fig. 3.7b was taken as excavation progressed past the sensor set in Layer 3. The wetting front was visually identified via color and textural contrast, and within the excavation the wetting front was observed to just intersect sensors in Layer 3. Observations made during excavation were used to confirm that the small increase in volumetric water content observed in Layer 3 as the datalogger station was powered down approximately corresponded to arrival of the wetting front. The average volumetric water content in Layer 4 (depth = 4.4 m) did not exhibit a marked change (Fig. 3.7a), which agreed with observations made during excavation that the wetting front did not reach the deepest set of sensors.

The depth of the wetting front as a function of time during an SDRI test can be estimated via a wetting front-time relationship. The wetting front-time relationship for the GW pile is shown in Fig. 3.8a, which was constructed using tensiometers at depths of 0.17, 0.27, and 0.41 m (Fig. 3.5a) and water content sensors at depths of 1.60 and 3.10 m (Fig. 3.7a). Least squares linear regression of the wetting depth versus square-root of time data set yielded the wetting front-time relationship to estimate D_f in Eq. 3.3 at any time during operation of the SDRI in the GW pile.

The wetting front-time relationship for the WR pile is shown in Fig. 3.8b. The data set for the WR pile was limited to two tensiometers at depths of 0.13 m and 0.33 m (Fig. 3.6b) as well as one observation near the base of the pile. The WR test pile was excavated to maximum depth of 3.8 m from the surface of the SDRI during destructive sampling. The wetting front was observed across the entire surface of the inner core of the WR test pile at the excavated depth of 3.8 m. However, water was not collected in the lysimeter at the bottom of the test pile, which suggests the wetting front likely did not reach the bottom of the pile. Thus, three depth of wetting front scenarios were considered for the WR test pile corresponding to a maximum (4.8 m), average (4.3 m), and minimum (3.8 m) depth of wetting front. The three considerations for the final depth of the wetting front in the WR pile yielded three unique wetting front-relationships. However, preliminary calculations of hydraulic conductivity considering these three relationships varied by no more than 2%. Thus, the average, final wetting front depth in the WR pile of 4.3 m (Fig. 3.8b) was used in the calculation of D_f for Eq. 3.3 in this analysis.

3.4.3.2 Infiltration Rate and Hydraulic Conductivity

Temporal trends of infiltration rate in the GW pile computed from fluctuations of ponded water depth in the outer ring and measurements of inner-ring inflow via the flexible plastic bag are shown in Fig. 3.9a. Readings of the water depth in the outer ring are also shown in Fig. 3.9a. The target water depth in the outer ring was approximately 0.4 m. In general, the infiltration rate for the outer ring was larger than the infiltration rate for the inner ring during the first three days of the SDRI test. Subsequently, infiltration rates from both rings converged on Day 4 and remained similar until the end of the experiment. The initial larger infiltration rate for the outer ring was attributed to a more pronounced 2-dimensionsal (2D) flow path relative to the constrained 1-dimensional (1D) flow path of the inner ring. As infiltration from the SDRI continued and the wetting front progressed deeper in the GW pile, infiltration rates from the outer and inner ring converged due to a reduced contribution of the horizontal component of flow to total infiltration in the outer ring.

The infiltration rates for the outer and inner rings decreased during the first three days and approached a constant value of approximately 10^{-6} m/s for the last four days of the SDRI test. The decrease in infiltration rate as a function of time may be a result of two mechanisms: (i) decrease in hydraulic gradient or (ii) decrease in hydraulic conductivity. The hydraulic gradient decreased from 2.6 (at t = 0.2 d) to 1.15 (at t = 6.0 d) as depth of the wetting front increased.

Hydraulic conductivity is equal to the infiltration rate divided by the hydraulic gradient (Eq. 3.1), which implies that for a constant hydraulic conductivity the infiltration would decrease by a factor of approximately two as the hydraulic gradient decreased. However, the infiltration rate decreased by a factor of four during the SDRI test (Fig. 3.9a), which suggests that hydraulic conductivity also decreased with depth and/or time.

Temporal trends of hydraulic conductivity for the GW pile are shown in Fig. 3.9b. Hydraulic conductivity was calculated based on three assumptions to calculate suction at the wetting front: (i) ψ_f = 0 m; (ii) ψ_a = 2.5 m; and (iii) ψ_a = 1 m. Air-entry pressures of 2.5 m and 1.0 m were the maximum and minimum measured values for GW based on laboratory specimens prepared to represent field conditions (Gorakhki et al. 2019). The three assumptions for ψ_a yielded hydraulic conductivities that varied no more than a factor of 1.6 (Fig. 3.9b). Furthermore, differences in hydraulic conductivity between the three assumptions were a maximum at the beginning of the SDRI test and reduced as the wetting front progressed (i.e., increase in D_f in Eq. 3.3). The average hydraulic conductivity of the GW pile was 1.4×10^{-6} m/s for the first two days of experiment and 9.0×10^{-7} m/s for the last three days of experiment using ψ_a = 1.0 m.

Hydraulic conductivity of the GW pile reduced by a factor of approximately two from the start of the SDRI test until reaching a nearly constant value at the start of Day 4. This reduction in hydraulic conductivity could be attributed to two mechanisms: (i) decreased effects of pedeogenesis with depths and/or (ii) settlement. Pedeogenesis is a natural soil formation process could have created a macroporous structure near the surface of the GW pile due wet/dry cycling and biological instruction (e.g., plant roots and animals). During excavation of the GW pile, a dense concentration of roots was observed up to 0.75 m below surface, which correlated with surface vegetation conditions observed for the GW pile (Fig. 3.1c). A macroporous structure in the surficial GW may have resulted in a higher hydraulic conductivity during the first few days of the SDRI test when infiltration was controlled by the hydraulic conductivity of the more surficial GW (Fig. 3.9b). Settlement of the GW pile surface occurred during the SDRI test, which is believed to have contributed to the increased dry density computed for Layers 2 and 3 (Fig. 3.3a) that constituted the main wetting zone of the GW during the SDRI test. A decrease in dry density would result in a reduction in hydraulic conductivity with time as the wetting front progressed. The two mechanisms of pedogenesis and surface settlement both support the measurements of a higher initial hydraulic conductivity in the GW pile followed by a reduction in hydraulic conductivity with time as the wetting progressed.

A few minor issues were observed during the SDRI test in the GW pile that contributed to abnormally low infiltration rates and hydraulic conductivities (Fig. 3.9). The flexible plastic bag completely emptied during the first few measurements due to a higher than anticipated infiltration rate. Towards the end of the third day, a small piping zone below the SDRI outer ring reduced the water level (i.e., ≈ 0.1 m at t = 2.8 d) and allowed air bubbles to enter the inner ring. The piping was mitigated, air-bubbles were removed from the inner ring, and the water depth in the outer ring was increased. Abnormally low hydraulic conductivities computed during these two events are identified in Fig. 3.9b and were considered non-representative of the actual hydraulic conductivity of the GW pile.

Temporal relationships of infiltration rate in the inner and outer ring as well as water depth in the outer ring for WR pile are shown in Fig. 3.10a. Similar to observations made for the GW pile, infiltration rate from the outer ring was larger than infiltration from the inner ring due to 2D flow versus 1D flow. The difference between the infiltration rates of the inner and outer rings reduced with time as the wetting front progressed in the WR pile. The decrease in infiltration rate during the first two days of the SDRI test was calculated to be the result of a reduction in hydraulic gradient from 2.19 (t = 0.06 d) to 1.14 (t = 2 d), as length of the wetting front increased.

Temporal relationships of hydraulic conductivity and wetting front in the WR pile are shown in Fig. 3.10b. Hydraulic conductivity for the WR pile was also computed considering three different assumptions for suction at the wetting front (i.e., ψ_f = 0 m, ψ_a = 0.1 m, and ψ_a = 0.2 m); however, air-entry pressures for WR were estimated using PSD and density in the USDA Rosetta tool

(USDA 2008). Negligible differences were observed in hydraulic conductivity computed based on the three assumptions to compute suction at the wetting front. The average hydraulic conductivity during Days 2 and 3 of the SDRI test in the WR pile was 2.8×10^{-6} m/s. The approximately consistent hydraulic conductivity with time in the WR pile suggested that potential influence from pedeogenesis and settlement during SDRI were negligible. This inference is consistent with the observations of no biological activity in the central core of the WR pile (Fig. 3.1) and no observable surface settlement.

The first few measurements of infiltration from the inner ring in the WR pile were considered erroneous and attributed to clogging of the fittings connecting the flexible plastic bag. These measurements were not considered representative of the hydraulic conductivity of the WR pile. Ponded water in the SDRI for the WR pile completely infiltrated over night during the first day of the experiment. There were no issues observed the morning of the second day. The SDRI was refilled completely and operated successfully until the experiment was terminated on Day 4.

3.5 Practical Implications

In situ density and hydraulic conductivity of GW and WR piles were measured in this study. The measured in situ dry density of the WR pile was approximately 12% higher than the GW pile, on average. The dry density of the WR pile following construction was reported to be 7.4% higher than the dry density of the GW pile. Thus, the end-state dry densities of the two test piles exhibited similarity to the as-constructed condition. The higher dry density for the WR pile was attributed to the well-graded nature of the WR and fines content ≈ 23% (Table 3.1) that led to a densely-packed granular fabric.

Hydraulic conductivity of WR pile was approximately 3 times higher than hydraulic conductivity of the GW pile. The higher hydraulic conductivity of the WR pile was measured despite the dense-packing of the material and higher dry density than the GW pile. The higher fines content and presence of clay-sized particles (Table 3.1) in the tailings used to create GW contributed to a lower hydraulic conductivity. A lower hydraulic conductivity of GW relative to WR will result in less infiltration into the material and reduced percolation of leachate from the bottom of a GW deposit all else being equal.

Laboratory-scale experiments conducted on GW prepared to the same mixture ratio decreased from an average of 1.7×10^{-8} m/s at an effective stress of 10 kPa to approximately 2.0×10^{-9} m/s at an effective stress of 100 kPa (Gorakhki et al. 2019). The hydraulic conductivities measured for the GW pile were 1.4×10^{-6} m/s (first two days) and 9.0×10^{-7} m/s (last three days). Thus, hydraulic conductivity measured via the SDRI in the GW pile was approximately 50 to 100 times larger than hydraulic conductivity measured on laboratory-prepared specimens under a low effective stress of 10 kPa. This low effective stress was more representative of conditions in the GW pile because (i) GW was placed in a loose state, with compaction only developing from pluviation via dropping the material from a height of approximately 2 m, and (ii) infiltration from the SDRI only penetrated top two meters of the GW pile. An increase in compaction of the GW pile and/or increase in effective stress likely would lead to a decrease in hydraulic conductivity, as was observed in the laboratory-scale specimens with an increase in effective stress from 10 to 100 kPa.

The one to two order or magnitude higher hydraulic conductivity measured in the laboratory relative to field agrees with observations made by Benson et al. (1999) and Benson et al. (2007) pertaining to the hydraulic conductivity measured in the laboratory and at field-scale tests. Benson et al. (1999) reported that heterogeneity and macropores existed in field-scale test sections, whereas hand-compacted laboratory-scale specimens were more uniform. On average, field-scale hydraulic conductivity was 11.2 times higher than the 75.2-mm diameter laboratory samples for material with $k > 10^{-9}$ m/s. Data compiled from Benson et al. (2007) that compares in situ hydraulic conductivity from thin field-scale test sections to hydraulic conductivity representing the as-built conditions (e.g., laboratory specimens) is shown in Fig. 3.11. The data compiled in Fig. 3.11 suggest that similar differences between as-built (or lab measured) and in-service hydraulic conductivity were similar to those differences observed between hydraulic conductivity measured in the GW and WR pile SDRIs and on laboratory-prepared specimens. The hydraulic conductivity of the laboratory specimens were 82 and 53 times smaller than GW pile when the wetting fronmt was in the top 2.0 m and lower than 2.0 m heights, respectively.

An additional factor that could have contributed to the difference in hydraulic conductivity measured in the test piles and on laboratory-scale specimens was the size of the WR particles. Waste rock used to prepare the GW specimens in the laboratory was screened on a 25.4-mm sieve to adhere to particle size requirements for hydraulic conductivity testing. However, WR used in the test piles contained particles up to 300-mm diameter. Although the ratio of WR to tailings was maintained constant between the GW pile and laboratory-prepared GW specimens, the influence of the larger-sized particles in the pile on hydraulic conductivity is uncertain. Additional laboratory-scale test specimens are required on GW prepared with larger particles to assess if the presence of larger particles contributes to increasing or decreasing the measured hydraulic conductivity. The sensitivity of the hydraulic conductivity to *R* also warrants further study.

3.6 Conclusion

In-situ properties of two piles constructed with GeoWaste and waste rock were investigated in this study. Saturated hydraulic conductivities of GeoWaste and waste rock were measured using sealed double ring infiltrometers (2.4-m square outer-ring and 1-m square inner-ring). The in situ density was measured for 20 locations at each pile. The following conclusions were drawn from this study:

- In situ density of waste rock was larger than GeoWaste. The GW pile had dry densities ranging from 1.40 to 1.69 Mg/m^3 in Layers 1 and 4, which were not affected by infiltration, whereas dry density of Layers 2 and 3 were higher (1.50 Mg/m^3 < dry density < 1.87 Mg/m^3). The higher dry densities were attributed to settlement of the GeoWaste due to an increase in stress developed during infiltration testing. Waste rock dry density was ranged between 1.65 to 2.05 Mg/m^3. Layer 2 yielded the highest dry density; however, differences between layer densities in the WR pile were smaller than the GW pile due to limited settlement.

- Particle-size distribution test conducted on ten in situ GeoWaste samples yielded in situ mixture ratios ranging from approximately 0.28 to 3.0. A single high mixture ratio of 3.0 was considered an outlier, and removing this outlier resulted in a median mixture ratio of 0.48 for 15 in situ GeoWaste samples. The modestly higher in situ mixture ratio relative to the target suggests that more waste rock was included in the GeoWaste that targeted.
- The average hydraulic conductivity measured in the GW pile was 1.4×10^{-6} m/s in during the first three days and 9.0×10^{-7} m/s during the last three days of experiment. The decrease in hydraulic conductivity was attributed to (i) settlement of pile during experiment and (ii) pedeogenesis in the surface of pile. The average hydraulic conductivity measured in the WR pile was 2.81×10^{-6} m/s, which was larger than the GeoWaste hydraulic conductivity.
- In situ hydraulic conductivity of GeoWaste pile was 53 to 82 times larger than laboratory measured hydraulic conductivity. This behavior can be due to spatial variation in particle-size distribution, pedeogenesis, and the difference between waste rock particle size between laboratory and field experiments.
- In situ hydraulic conductivity of GeoWaste pile was approximately three times smaller than waste rock pile. This behavior suggests that a GeoWaste pile generates lower volume of leachate in comparison with a waste rock pile.

Table 3.1. Summary of physical characteristics and classification for tailings and waste rock.

Material	*LL* (%)	*PI* (%)	USCS	Gravel Content (%)	Sand Content (%)	Fines Content (%)	Clay-Size Content (%)	As-Received Water Content (%)	G_s	w_{opt} (%)	$\rho_{d\text{-}max}$ (g/cm^3)
Tailings	30.1	9.2	CL	0	14.3	85.7	23.6	21.5	2.68	15.8	1.69
Waste Rock	NA	NA	GM	45.0	31.7	23.3	NA	5.8	2.64	NM	NM

Notes: *LL* = liquid limit; *PI* = plasticity index; USCS = Unified Soil Classification System; clay-size content taken as percent particles by mass < 0.002 mm; G_s = specific gravity; w_{opt} = optimum water content and $\rho_{d\text{-}max}$ = maximum dry unit density determine from Standard effort compaction tests; NA = not applicable; NM = not measured.

Table 3.2. Total density, water content, dry density, porosity, and void ratio for in situ density samples collected from the GeoWaste (GW) and waste rock (WR) piles.

Layer	Depth from Surface (m)	Sample	Total Density (Mg/m^3)	Water Content	Dry Density (Mg/m^3)	Porosity	Void Ratio
GW-L1	0.2	GW-L1-M	1.70	0.08	1.57	0.41	0.68
		GW-L1-N	1.71	0.08	1.59	0.40	0.67
		GW-L1-S	1.59	0.07	1.48	0.44	0.79
		GW-L1-E	1.61	0.07	1.50	0.43	0.76
		GW-L1-W	1.64	0.07	1.54	0.42	0.73
GW-L2	1.5	GW-L2-M [a]	2.51	0.13	2.22	0.16	0.19
		GW-L2-N	2.33	0.25	1.87	0.30	0.42
		GW-L2-S	1.97	0.22	1.61	0.39	0.65
		GW-L2-E	2.15	0.27	1.70	0.36	0.56
		GW-L2-W	2.30	0.24	1.85	0.30	0.43
GW-L3	3.0	GW-L3-M	2.05	0.23	1.66	0.37	0.60
		GW-L3-N	1.88	0.25	1.50	0.43	0.76
		GW-L3-S	2.03	0.24	1.63	0.39	0.63
		GW-L3-E	2.04	0.25	1.63	0.38	0.62
		GW-L3-W	2.05	0.19	1.73	0.35	0.54
GW-L4	4.0	GW-L4-M	1.61	0.15	1.40	0.47	0.89
		GW-L4-N	1.62	0.12	1.45	0.45	0.83
		GW-L4-S	1.88	0.11	1.69	0.36	0.57
		GW-L4-E	1.83	0.13	1.62	0.39	0.64
		GW-L4-W	1.70	0.14	1.49	0.44	0.78
WR-L1	0.0	WR-L1-N	1.94	0.07	1.81	0.32	0.46
		WR-L1-S	2.13	0.12	1.90	0.28	0.40
		WR-L1-M	1.98	0.08	1.84	0.31	0.44
		WR-L1-E	2.03	0.09	1.87	0.30	0.42
		WE-L1-W	2.11	0.11	1.91	0.28	0.39
WR-L2	1.5	WR-L2-N	2.35	0.20	1.96	0.26	0.35
		WE-L2-M	2.12	0.15	1.85	0.30	0.44
		WR-L2-E	2.11	0.14	1.85	0.30	0.43
		WR-L2-W	2.39	0.21	1.97	0.26	0.34
		WR-L2-S	2.48	0.21	2.05	0.23	0.29
WR-L3	2.3	WR-L3-N	1.98	0.18	1.68	0.37	0.58
		WR-L3-M	2.26	0.23	1.84	0.31	0.44
		WR-L3-E	2.14	0.21	1.78	0.33	0.49
		WR-L3-W	2.53	0.26	2.01	0.24	0.32
		WR-L3-S	2.19	0.20	1.82	0.31	0.45
WR-L4	3.9	WR-L4-N	2.00	0.16	1.71	0.35	0.55
		WR-L4-S	1.99	0.20	1.65	0.38	0.61
		WR-L4-W	2.01	0.17	1.71	0.35	0.55
		WR-L4-E	1.99	0.17	1.71	0.36	0.55
		WR-L4-M	2.08	0.17	1.77	0.33	0.49

Notes: L1 = Layer 1; L2 = Layer 2; L3 = Layer 3; L4 = Layer 4
[a] Outlier attributed to measurement error

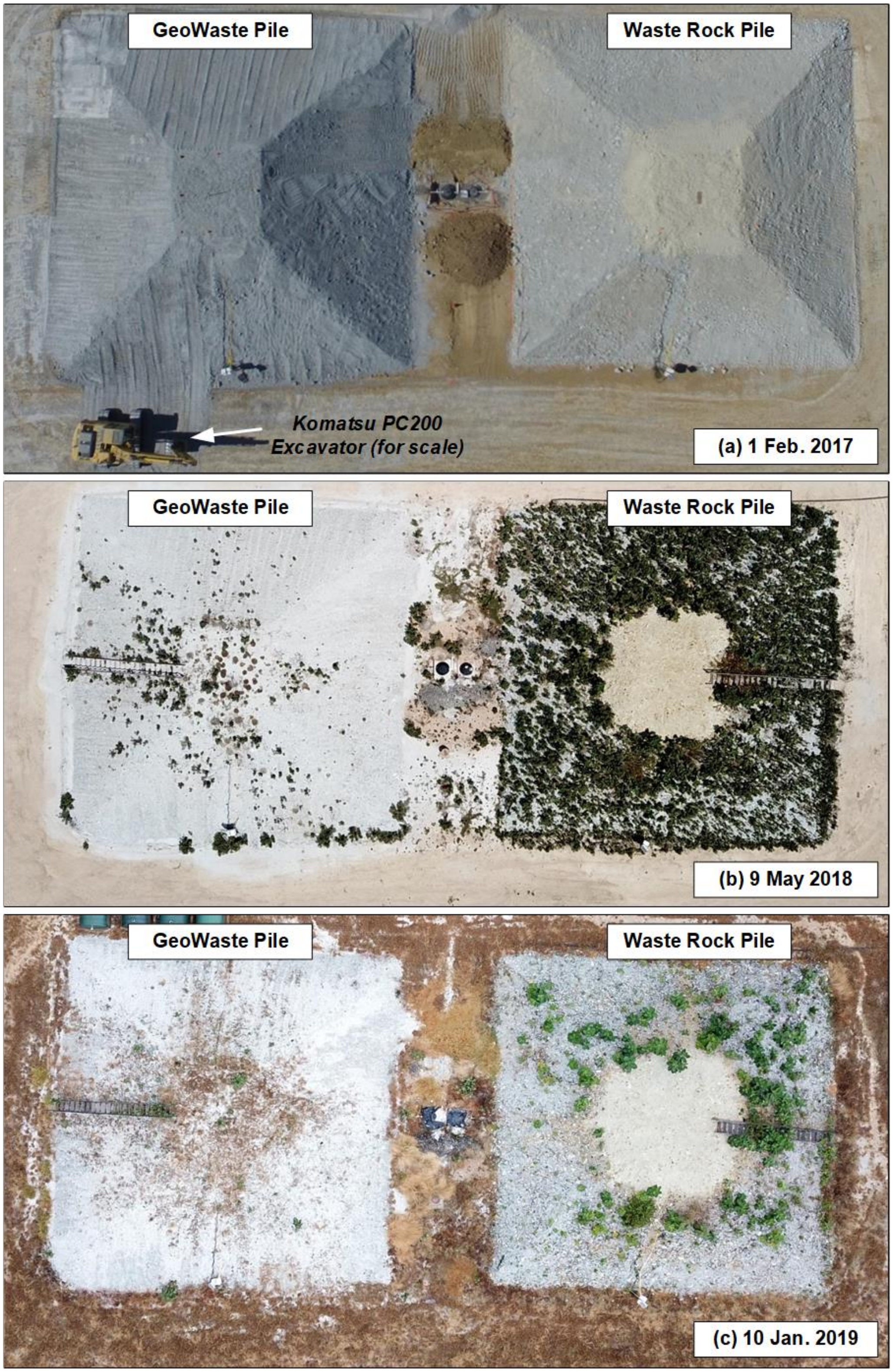

Fig. 3.1. Aerial photographs of the GeoWaste and waste rock piles taken on (a) 1 Feb. 2017 (i.e., end of construction), (b) 9 May 2018, and (c) 10 Jan. 2019. Vegetation was trimmed after 9 May 2018 and then allowed to re-establish.

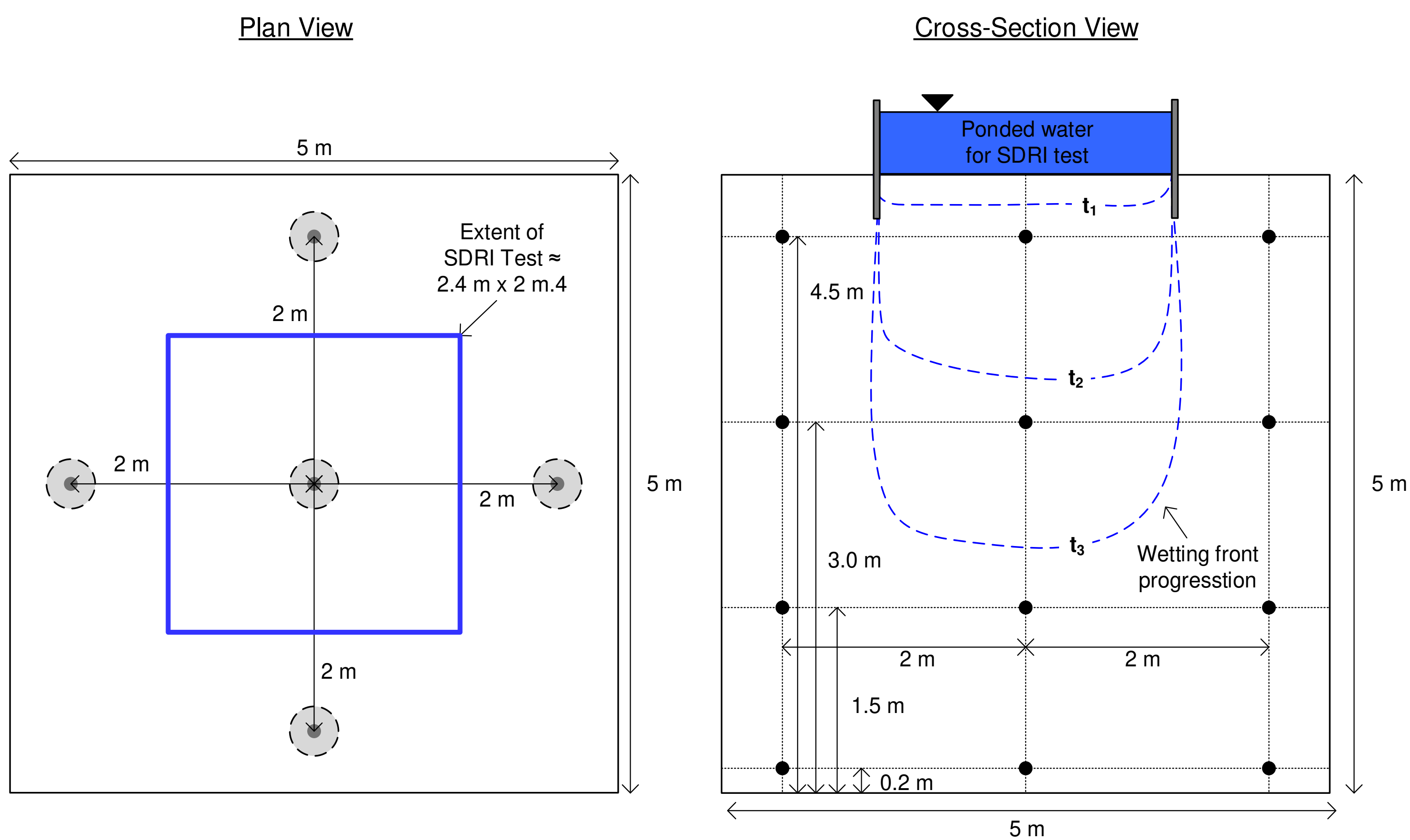

● Instrument location (water content and oxygen sensor)

Destructive sample location (in situ density, moisture, PSD, mixture ratio, void ratio)

Wetting front due to infiltration from SDRI test shown at different elapsed times ($t_1 < t_2 < t_3$).

Fig. 3.2. Plan view and cross-section schematics of the GeoWaste and waste rock test pile central cores that identify approximate locations of instruments (water content and oxygen sensors) and destructive samples as well as the size, location, and anticipated wetting front at different elapsed times from the sealed double-ring infiltrometer (SDRI) tests.

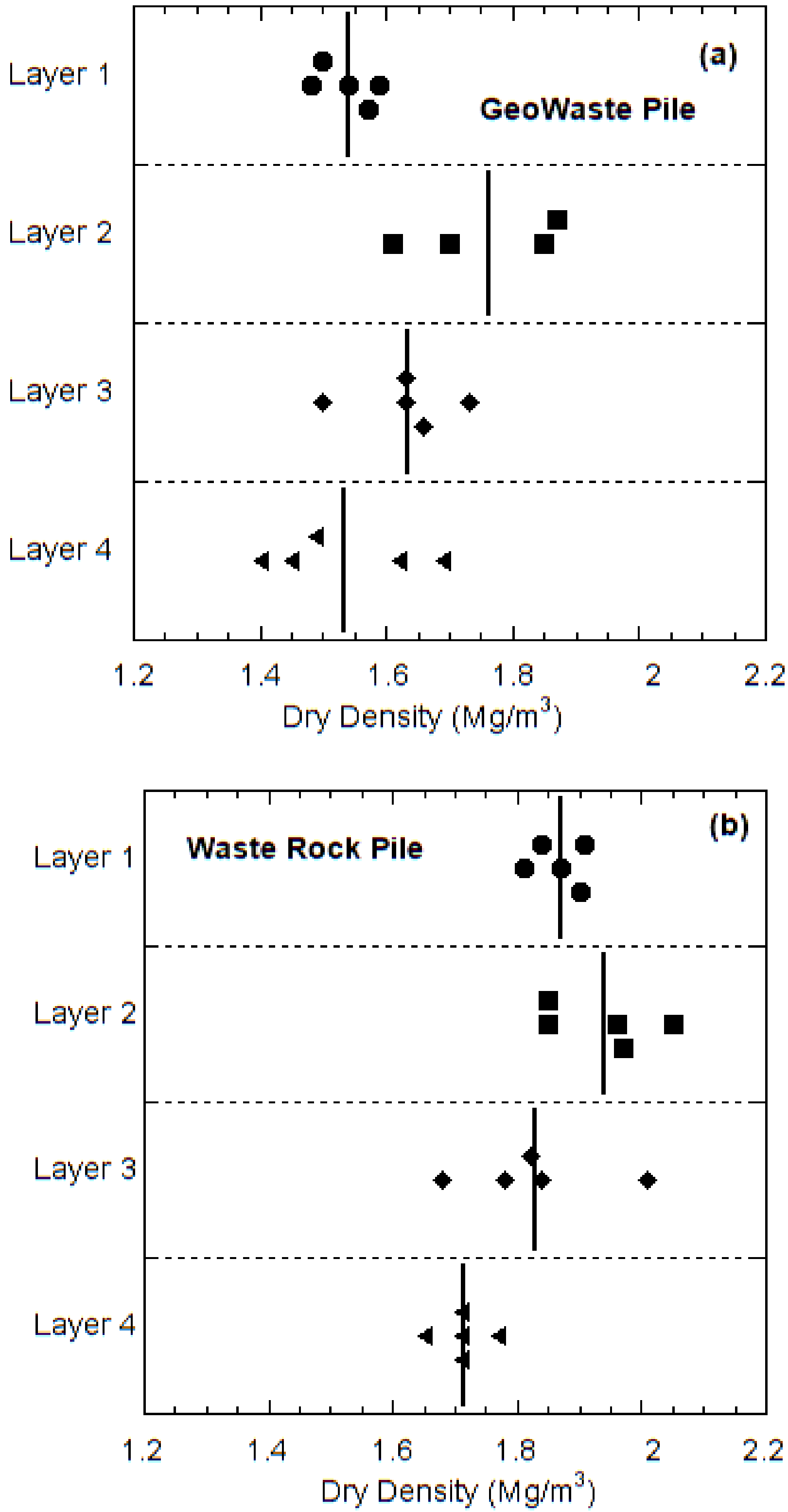

Fig. 3.3. Dry density range for different layers in the (a) GeoWaste and (b) waste rock piles.

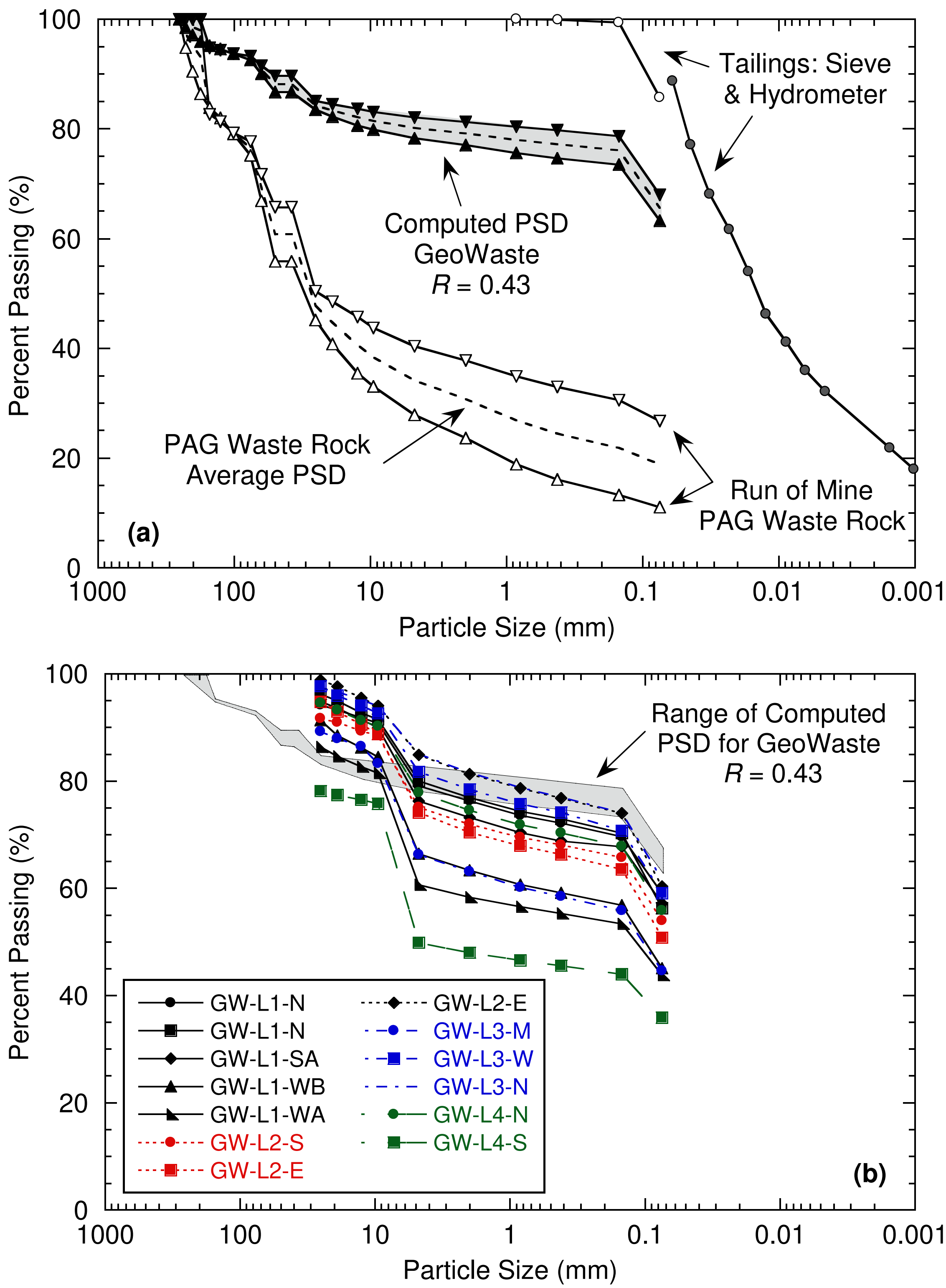

Fig. 3.4. Particle-size distributions for (a) tailings and waste rock samples collected during test pile construction and (b) in situ density samples collected during destructive sampling. The computed GeoWaste particle-size distribution was based on the tailings and waste rock distributions during pile construction and assuming a mixture ratio of 0.43.

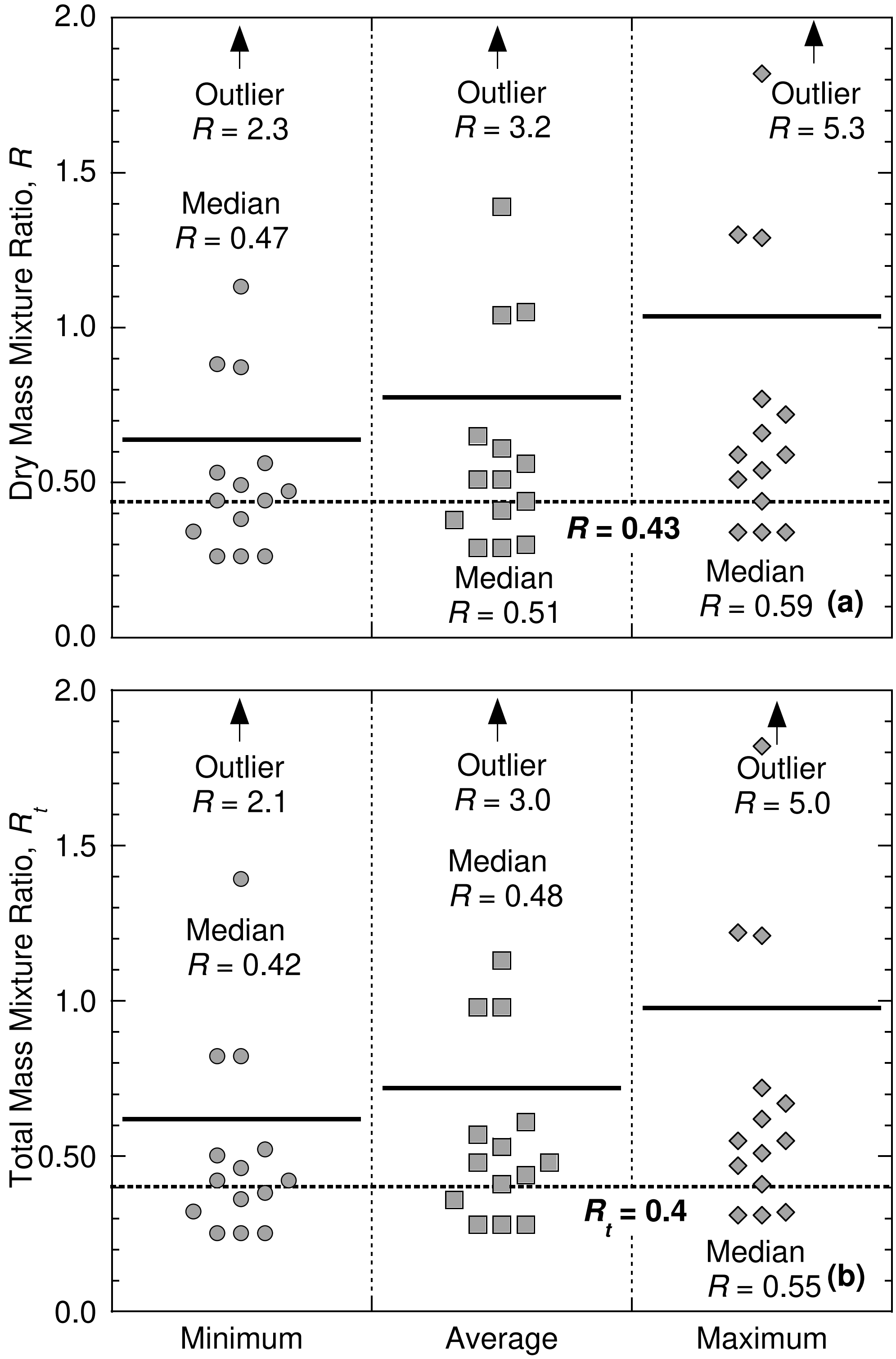

Fig. 3.5. Dot plots of (a) dry mass mixture ratio and (b) total mass mixture ratio from particle size analyses conducted on in situ density samples collected from the GeoWaste pile.

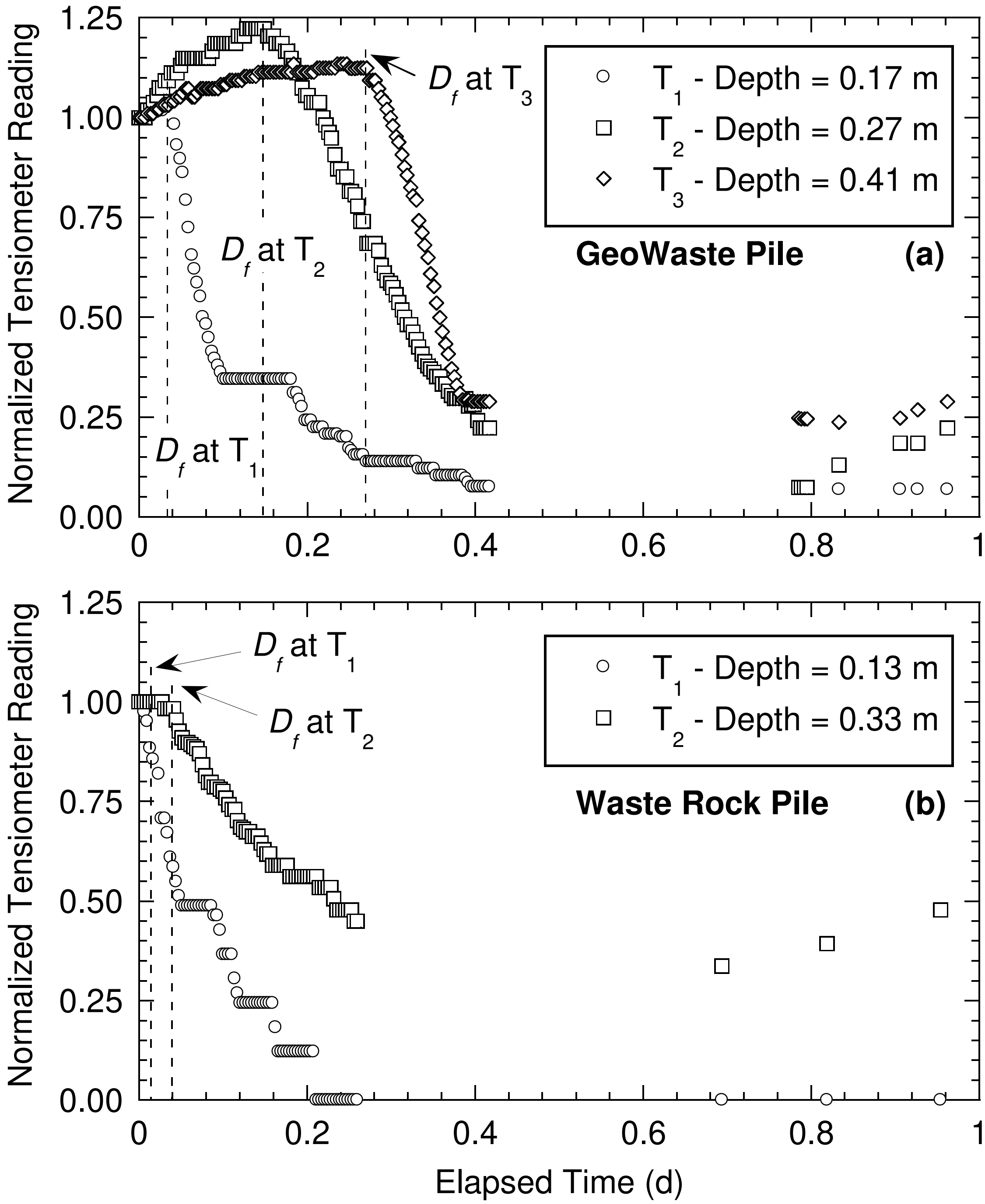

Fig. 3.6. Temporal change of normalized tensiometers (T_n) in: (a) GeoWaste pile; and (b) Waste rock pile. The T_n was computed as tensiometer measurement at any time divided by measurement of tensiometer at $t = 0$ d.

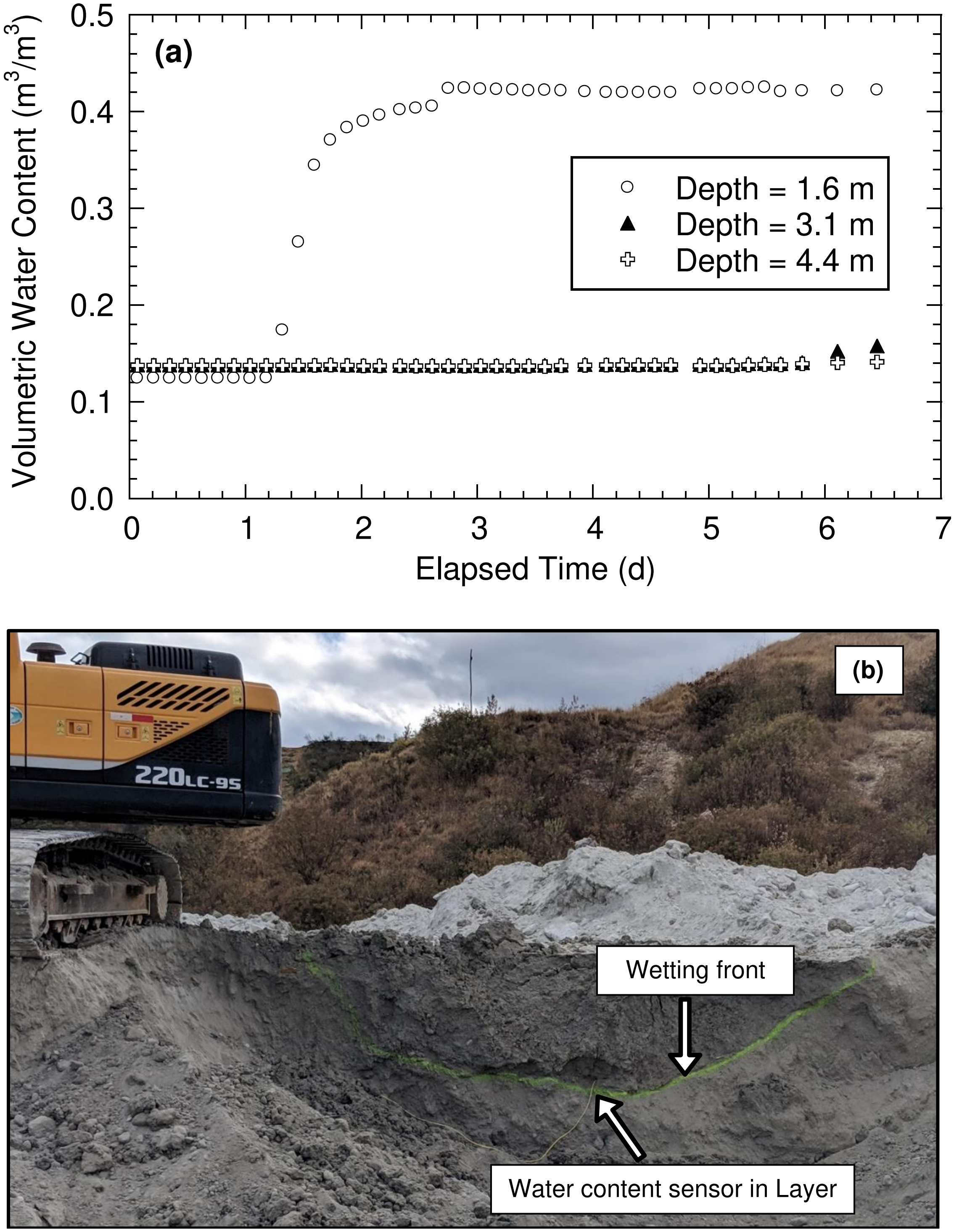

Fig. 3.7. (a) Temporal change of volumetric water content at depths of 1.6, 3.1, 4.4 m in GeoWaste pile; and (b) the wetting front in GeoWaste pile after decommissioning at the depth of approximately 3.2 m.

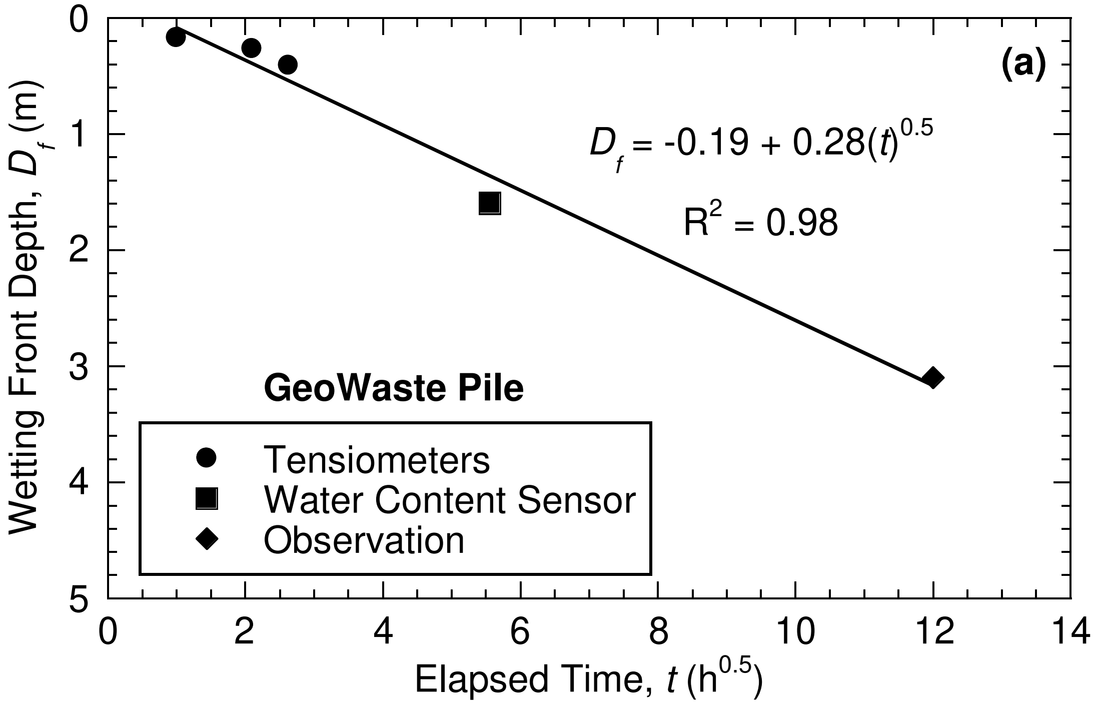

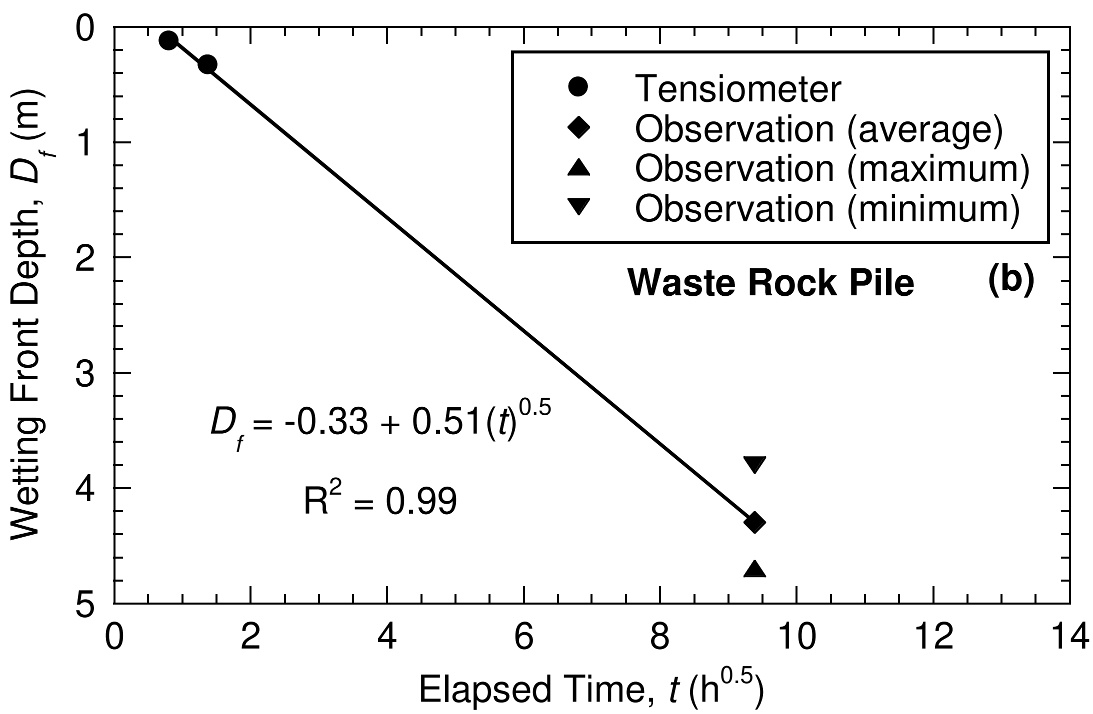

Fig. 3.8. The depth-time relationship of wetting front: (a) GeoWaste pile, and (b) waste rock pile.

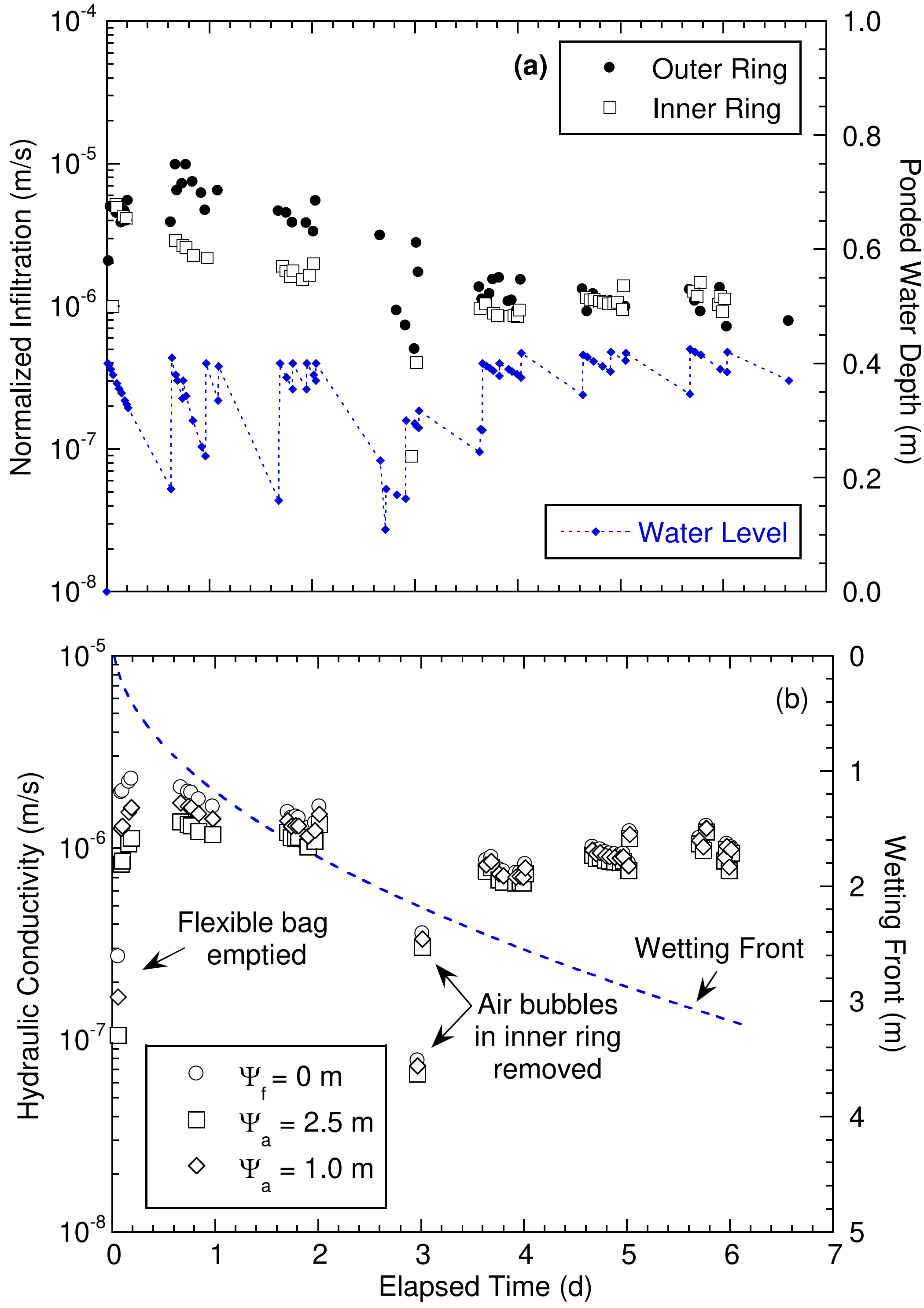

Fig. 3.9. (a) Infiltration rate of the inner and outer ring and depth of ponding on the outer ring of SDRI, and (b) hydraulic conductivity measurements and depth of wetting front relationship with time for GeoWaste pile.

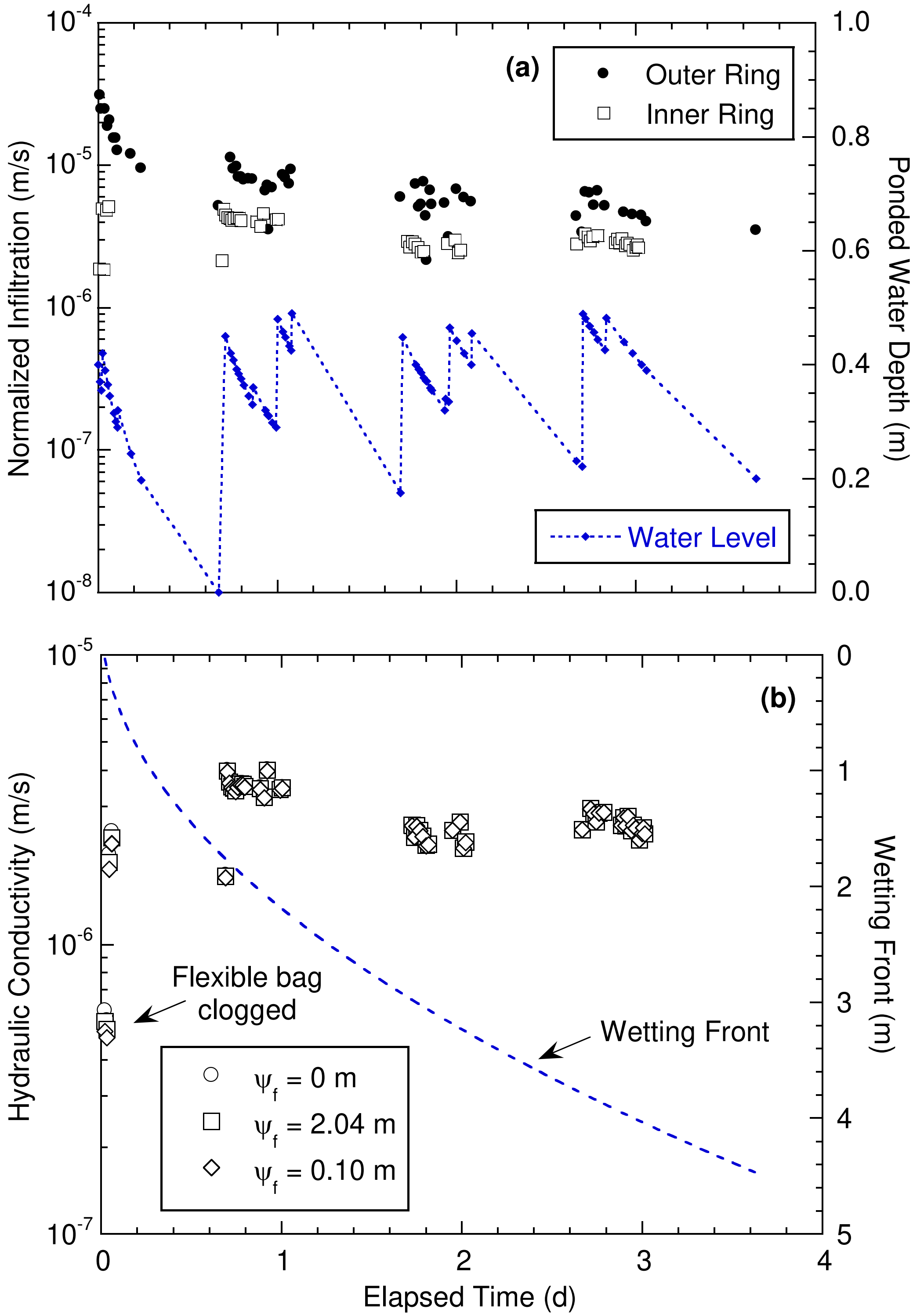

Fig. 3.10. (a) Infiltration rate of the inner and outer ring and depth of ponding on the outer ring of SDRI, and (b) hydraulic conductivity measurements and depth of wetting front relationship with time for waste rock pile.

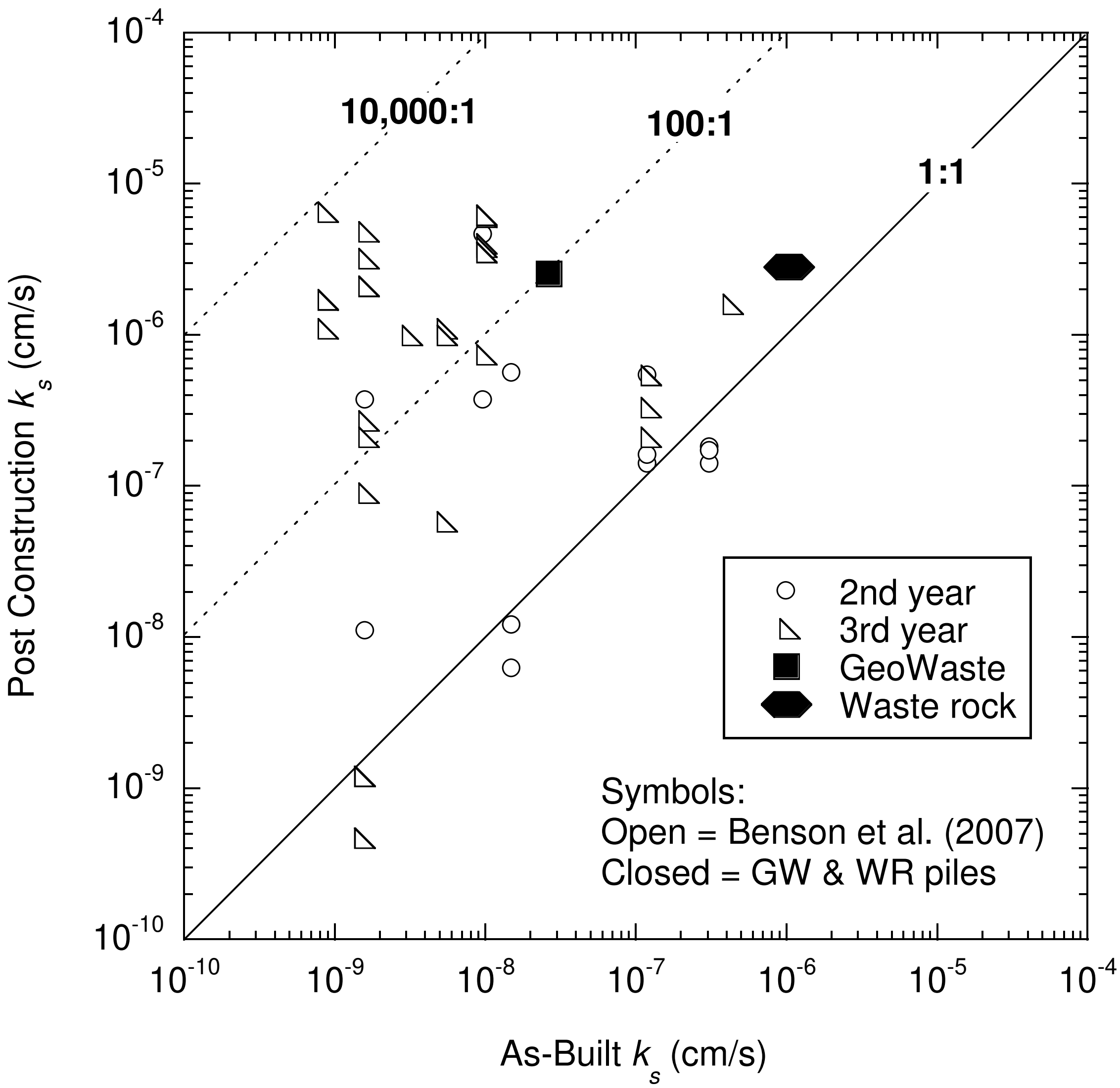

Fig. 3.11. Comparison of as-built or laboratory measured hydraulic conductivities and post construction or in-service hydraulic conductivity. Adapted from Benson et al. (2007).

4 INVERSE NUMERICAL SOLUTIONS TO DETERMINE HYDRAULIC PARAMETERS FOR GEOWASTE AND WASTE ROCK TEST PILES

4.1 Introduction

Mine waste is typically managed by storing mine tailings and waste rock (WR) separately. Although straight-forward to construct, WR placed in piles can lead to acid mine generation (AMG) due to high permeability that permits air and water flow through the WR that can react with sulphide-rich minerals (Nicholson et al. 1989; Blowes et al. 2003). Furthermore, although slurry tailings deposition in impoundments is standard practice, recent failures (Morgenstern et al. 2015; Morgenstern et al. 2016; Robertson et al. 2019) have put pressure on the mining industry to evaluate alternative tailings management strategies. Waste rock and tailings (WR&T) co-disposal is an alternative mine waste management technique to address AMG in WR piles and potential tailings instability in impoundments (Williams et al. 2003; Leduc et al. 2004; Wickland et al. 2006; Bussière 2007; Bareither et al. 2018). Various WR&T co-disposal techniques have been evaluated that include different mixing and placement methods (Wickland et al. 2006). Co-mixing of WR&T is a co-disposal technique where WR and tailings are blended to form a homogeneous mixture. GeoWaste (GW) is a co-mixed WR&T created from fast-filtered tailings and WR blended to isolate WR particles within a tailings matrix (Gorakhki et al. 2019).

A key premise of GW is that a decrease in hydraulic conductivity and increase water retention relative to WR reduces the rates of infiltration and seepage, which can minimize the quantity of leachate generation. In addition, greater water retention capacity maintains a higher degree of water saturation under natural climatic conditions, which reduces oxygen diffusion into a mine waste deposit limiting AMG reactions and reduction in leachate quality. The hydraulic parameters of a mine waste deposit, which include hydraulic conductivity and water retention, describe infiltration into, seepage within, and the quantity of leachate out of a deposit.

The objective of this study was to use inverse modeling during pile decommissioning to determine in situ hydraulic conductivity and water retention parameters of WR and GW test piles operated for 26 months. Infiltration tests were performed on field-scale WR and GW piles. Cumulative inflow (both piles) and volumetric water content (GW pile) were used as an input data for the inverse models to determine hydraulic parameters. A secondary focus of this study was to compare the hydraulic parameters of GW measured in the laboratory, measured in situ, and back-calculated via inverse modeling.

4.2 Background

Flow through porous medium can be approximated using Richards equation (Richards 1931):

$$\frac{\partial\theta}{\partial t} = \frac{\partial}{\partial z}[D\frac{\partial\theta}{\partial z} + k] \tag{4.1}$$

where θ is volumetric water content, z is a vertical coordinate, t is time, and k is hydraulic conductivity. Hydraulic conductivity, soil water retention parameters, and specific boundary conditions are required to solve Richards equation. Mathematical expressions for soil water retention and hydraulic conductivity are defined in Eq. 4.2 (van Genuchten 1980) and Eq. 4.3 (Mualem 1976), respectively:

$$S_e = \frac{\theta(h) - \theta_r}{\theta_s - \theta_r} = \frac{1}{(r + (\alpha h)^n)^{(1-1/n)}} \tag{4.2}$$

$$k(\theta) = kS_e^{0.5}[1 - (1 - S_e^{1/(1-1/n)})^{(1-1/n)}]^2 \tag{4.3}$$

where S_e is effective saturation, k is saturated hydraulic conductivity, θ_r is residual volumetric water content, θ_s is saturated volumetric water content, and α and n are fitting parameters. The air entry pressure (Ψ_a), which is the suction at which the largest pores of a given saturated porous medium start to drain, is approximated as 1/α.

Hydraulic parameters identified in Eqs. 4.1-4.3 are needed to compute water distribution (e.g., volumetric water content) and movement (e.g., seepage) within a mine waste deposit.

However, hydraulic parameters that represent field conditions are not always available and while laboratory-measured parameters may be more readily available they may not necessarily represent field conditions. Numerical solutions have been developed to inversely solve Richards equation to determine hydraulic parameters when, for example, inflow volume and/or volumetric water content at different locations and times are available (Rashid et al. 2015; Nascimento et al. 2018). The objective of an inverse solution is to systematically change hydraulic parameters to minimize the error between observed and modeled responses. Physical experiments with controlled boundary conditions and periodic measurements are ideal to determine soil hydraulic parameters via inversely solving Richards equation.

HYDRUS is a commonly-used model that is free in 1D and commercially available for 2D and 3D conditions. An inverse solution module based on equations developed in Šimůnek et al. (1999) is available within HYDRUS, which uses the Marquardt-Levenberg parameter optimization algorithm (Šimůnek et al. 2012). The objective of this method is to minimize the Φ function identified in Eq. 4.4 by changing the soil hydraulic properties:

$$\phi(b,q) = \sum_{k=1}^{m} y_k \sum_{j=1}^{n_k} w_{j,k} [q_k^{*}(x,t_i) - q_k(x,t_j,b)]^2 \tag{4.4}$$

where m is the number of different sets of measurements, n_k is the number of measurements in a particular measurement set, $q_k^{*}(x,t_j)$ is a specific measurement at time t_j for the k^{th} measurement at location x, $q_k(x,t_j b)$ is the corresponding model prediction for the vector of optimized parameter b, and y_k and $w_{j,k}$ are weights associated with a particular measurement. The right side of Eq. 4.4 represents deviations between measured and calculated space-time variables.

Numerous studies have used the HYDRUS inverse solution to determine soil parameters (Šimůnek et al. 1999; Nakhaei and Simunek 2014; Rashid et al. 2015; Šimůnek et al. 2016; Nascimento et al. 2018). Nakhaei and Simunek (2014) reported that an inverse solution that only uses cumulative inflow does not yield unique estimates of k, α, and n simultaneously. They suggested that cumulative inflow be paired with temporal measurements of head or water content to uniquely solve for *k*, α, and *n* simultaneously.

4.3 Methods and Materials

4.3.1 Material Characteristics

Geotechnical characterization of mine tailings and WR included mechanical sieve and hydrometer (ASTM D422, ASTM 2007), Atterberg limits (ASTM D4318, ASTM 2014a), and standard-effort compaction (ASTM D698, ASTM 2014c). Material characteristics of tailings and WR are summarized in Table 4.1. Characteristics were measured on samples representative of mine waste used to construct the GW and WR piles.

Laboratory hydraulic conductivity tests were conducted using flexible-wall permeameters in accordance with ASTM D5084 (ASTM 2016a). The falling headwater-constant tailwater and falling headwater-rising tailwater methods were used. Hydraulic conductivity of tailings was measured on 102-mm-diameter specimens, whereas hydraulic conductivity of GW was measured on 152-mm-diameter specimens. WR was screened on a 25.4-mm sieve prior to preparation of GW specimens to limit the maximum WR particle size. Details of laboratory hydraulic conductivity testing and analysis are in Gorakhki et al. (2019).

The in situ hydraulic conductivity of GW and WR piles were measured using sealed double ring infiltrometers (SDRIs) that included a 2.4-m-square outer ring and 1-m-square inner ring. Tensiometers and in situ water content sensors measured progression of the wetting front, and final location of the wetting front in the GW pile was confirmed during destructive sampling of the test pile. Details of the SDRI experiment are reported in Chapter 3.

A summary of laboratory and in situ measured *k* in at 10 kPa effective stress is in Table 4.2. Laboratory *k* ranged between 6.9×10^{-9} m/s and 9.0×10^{-8} m/s for tailings, and between 2.6×10^{-8} and 8.6×10^{-9} m/s for GW. The SDRI experiment conducted on the GW pile yielded two unique *k*: (i) 1.4×10^{-6} m/s when the wetting front was 0.0 to 2.0 m deep, and (ii) 9.0×10^{-7} m/s when the wetting front was 2.0 to 3.5 m deep. The *k* measured in the WR pile was 2.8×10^{-6} m/s.

A summary of laboratory-measured water retention characteristics and van Genuchten parameters of tailings and GW is in Table 4.3. Soil water retention tests were conducted in accordance with the drying curve method described in ASTM D6836 (ASTM 2016b). Air pressure ranging from 5 kPa to 1500 kPa was applied in pressure plates and converted to matric soil suction (Ψ) by axis translation. Tailings specimens were prepared in odometer rings with an inside diameter of 63.5 mm and height of 25.4 mm, whereas GW specimens were prepared in PVC rings with inside diameter of 152 mm and height of 76.2 mm. Chilled mirror hygrometers (WP4C, Metergroups, Pullman, WA) were used to measure soil suction between 1500 kPa and 120,000 kPa in tailings specimens. Details of soil water retention measurements on tailings and GW specimens are in Gorakhki et al. (2019).

4.3.2 Test Piles

The piles were designed as truncated 5-m tall pyramids with 25-m base sides and flat 5 m × 5 m top surfaces. The GW pile was constructed with GW prepared to a target mixture ratio of 0.43 (R = dry mass of WR / dry mass of tailings). GeoWaste placed in the central core of the GW pile was prepared with fast-filtered mine tailings mixed with potentially acid generating WR. Filtered tailings and WR were mixed on site using an excavator prior to placement. Subsequently, the GW was dropped from a height of approximately 2-3 m into the central core of the pile using an excavator. This process simulated the anticipated full-scale GW mixing process with final material disposal at the end of a conveyor system.

The WR pile was constructed with potentially acid generating WR within the central core of the pile (5 m x 5 m x 5 m). The WR test pile was constructed with compacted WR on the side slopes and potentially acid generating WR dropped and pushed in-place in the central core via a dozer. Thus, a higher level of compaction effort was used to prepare the central core of the WR test pile as compared to the GW test pile.

Each pile was instrumented with four layers of sensors, of which the uppermost layer was deactivated (i.e., wires were cut) during construction of the SDRI tests. Each layer contained five sets of sensors: one set in the center and four sets positioned 2-m radially from the center on each side of the piles. Depths from the pile surfaces to of each layer of non-deactivate sensors were 1.5 m, 3.0 m, and 4.3 m. None of sensors in the WR pile were functional during the SDRI experiment; however, 11 out of 15 sensors in the GW pile were working. Each sensor set contained a TDR-315L Acclima sensor to measure volumetric water content (VWC), which were used for monitoring in situ water content during infiltration. Additional details on pile instrumentation are in Chapter 2. The test piles were operated for approximately 26 months after which SDRI tests were performed.

4.3.3 Sealed Double Ring Infiltrometer Test

The SDRI test had outer-ring dimensions of 2.4 m x 2.4 m and inner ring dimensions of 1.0 m x 1.0 m. The rings were centered on the surface of the test piles to focus infiltration in the central cores of the piles. Complete details of the SDRI tests are in Chapter 3.

Cumulative inflow from the SDRI tests in the GW and WR piles are shown in Fig. 4.1. The SDRI test in the GW pile was operated for 6.45 d and the ponded water depth was maintained between 0.11 m and 0.43 m. The SDRI test in the WR pile was operated for 3.67 d and ponded water was maintained between 0.0 to 0.49 m. The infiltration rate was computed based on the change in ponded water depth and surface area contained within the outer ring; infiltration was corrected for evaporation based on pan evaporation recorded on site during the SDRI tests. The inflow rate of the WR pile was 2.1 times larger than the GW pile; the average inflow rate in the GW pile was 1.38 m^3/d and average inflow rate in the WR pile was 2.92 m^3/d.

Settlement was observed during the start of infiltration in the GW pile, in particular at 2.70 d. Settlement resulted in a small leak in the outer ring during infiltration at 2.70 d, which was subsequently fixed and infiltration continued. Infiltration in the GW pile was considered as three periods for analysis: (i) entire infiltration data set = 6.45 d of infiltration from the beginning to the end of the SDRI test; (ii) initial part of infiltration experiment = infiltration between 0 and 2.70 d; and (iii) final part of infiltration experiment = infiltration between 2.70 and 6.45 d.

4.3.4 Numerical Solution

Numerical modeling of infiltration during the SDRI tests in the WR and GW test piles was completed in HYDRUS 2D (version 2.05) to determine hydraulic parameters of WR and GW. Water retention parameters were defined using the van Genuchten (1980) formulation (Eq. 4.2) and unsaturated hydraulic conductivity was defined using the Mualem-van Genuchten (Mualem 1976) formulation (Eq. 4.3). The model domain was 26-m wide and 6-m deep. The domain was discretized into 628 nodes and 1166 2-dimensional elements as shown in Fig. 4.2. A larger number of nodes and elements did not change inverse model results, but did slow down run time of models.

Initial conditions of the piles simulated in the models were based on in situ volume water contents (VWCs) measured within the piles and on exhumed samples from the surface of piles. All water content measurements for the GW pile suggest a VWC ranging between 0.12 and 0.15 at the time infiltration from the SDRI began. Thus, the initial VWC of the GW pile was set at 0.13, which was the average of in situ and surface measurements. Initial conditions were adjusted for models that simulated the final part of infiltration (Fig. 4.1). The final water content profile of the GW pile for the first 2.70 d was used as the initial condition for models that simulated the final part of infiltration (2.7 d < t < 6.45 d). The model that provided the closest fit between measured and modeled values was used for obtaining initial VWCs for the final part of infiltration (Model GW-I6).

The average VWC measured on exhumed samples from the surface of the WR pile was 0.16; however, no in situ VWC sensors in the WR pile were functional at the start of the SDRI test. The last data collected from the VWC sensors were on Day 395 (294 d prior to start of the SDRI test) and indicated an average VWC of 0.27 in all four layers. Thus, the initial VWC in the WR pile was set to 0.16 at the surface and the VWC was assumed to increase linearly to 0.27 at

3.20-m deep in Layer 2. A VWC of 0.27 was assumed representative at all depths below Layer 2.

The porosity (i.e., θ_s) of the GW pile and WR piles were 0.40 and 0.34, respectively, which were based on the average of five in situ density measurements in the top 0.5 m prior to SDRI testing. The θ_r for the GW and WR piles were assigned to be 0.02. The θ_r for GW was based on chilled mirror hygrometer tests on tailings. The θ_r for WR was estimated in the Rosetta module in HYDRUS-1D (USDA 2008). The gravel fraction of WR was considered to be sand in the Rosetta module because the module does not include gravel size particles.

Three scenarios for input data were considered for the GW test pile: (i) *k* provided as input and set equal to the minimum value determined from the SDRI test (Chapter 3); (ii) *k* provided as input and set equal to the maximum value determined from the SDRI test (Chapter 3); and (iii) *k* as a fit parameter optimized as part of the inverse solution along with water retention parameters α and *n*.

Two inverse solutions were conducted on the WR pile: (i) *k* provided as input based on the value measured during the SDRI test; and (ii) *k* as a fit parameter. The *k* determined from the SDRI test in the WR pile exhibited minor variability with different calculation methods, which supported the use of a single *k* in the inverse solution (Chapter 3).

Input data for inverse the solution of the GW pile included VWC sensor measurements for eight sensors in three layers (3744 data points) and cumulative inflow from the SDRI test (53 data points). The weight of each VWC sensor was set at 0.014 to provide the same total weight between VWC and cumulative inflow data. Only cumulative inflow data (54 data points) were used in the WR pile because the in situ VWC sensors were not functional during infiltration.

The surface of the test piles was modeled as a no-flow boundary, except for beneath the ponded water where cumulative inflow data were specified as a variable head boundary condition. The no-flow boundary was justified by the short duration of the inverse models (i.e., 6.45 d for the GW pile and 3.67 d for the WR pile), such that vegetation and atmosphere interactions were considered negligible (no rainfall occurred during testing and evaporation of outer ring was included in the inflow volume analysis). Cumulative inflow data from the SDRI test was used to define the variable head boundary condition, which corresponded to measurements of water depth in the SDRIs (75 measurements for the GW pile and 67 measurements for the WR pile). The lower boundary condition was modeled as a seepage face because a gravel layer existed underneath the central cores of both piles to collect leachate; however, the wetting front did not reach the bottom of piles during the SDRI tests.

Some inverse models did not provide unique solutions when initial guesses for parameters were provided. The issue of uniqueness typically occurs when there are a large number of variables relative to the number of input parameters. To address this issue, multiple models were conducted with the same model setup and different initial guesses for the soil hydraulic parameters, such that the model with the highest coefficient of determination (R^2) was selected as the most appropriate solution. Initial guesses typically ranged between values obtained from the SDRI tests, laboratory tests, and relevant literature.

4.4 Results

4.4.1 GeoWaste Pile

Results of the inverse solutions for the GW test pile to determine k and water retention parameters (i.e., α and n) are in Table 4.4. Saturated hydraulic conductivity was used as an input parameter for models GW-I1, GW-I2, GW-I4, GW-I5, and GW-I7. The different k identified in Table 4.4 correspond to minimum (GW-I1, GW-I4), maximum (GW-I2, GW-I5), and average (GW-I7) values computed during the initial 2.7 d, final 3.75 d, or entire 6.45 d of infiltration. A minimum and maximum k were computed in the SDRI analysis for the initial part of infiltration and entire data set due to different assumptions that can be made for suction head at the wetting front (Chapter 3); however, these different assumptions had no influence on k for the final part of infiltration. All models were solved to obtain van Genuchten water retention parameters α and n. Saturated hydraulic conductivity was determined in models GW-I3, GW-I6, and GW-I7 to compare to k

measured in the SDRI experiment.

4.4.1.1 Inverse Solutions for the Entire Infiltration Data Set (0 d < *t* < 6.45 d)

Comparison of predicted and measured VWC and cumulative inflow in the GW pile for Models GW-I1 and GW-I2 are shown in Figs. 4.3 and 4.4, respectively. In Model GW-I1, the wetting front was predicted to reach Layer 2 after 1.5 d, whereas measurements indicated the wetting front reached Layer 2 earlier, after 1.3 d. In addition, the predicted rate of increase in VWC in Layer 2 was slower than measured. In Model GW-I2, the wetting front was predicted to reach Layer 2 at approximately the same time as observed in the VWC measurements; however, the predicted rate of increase in VWC was slower than measured (Fig. 4.3b). Following the infiltration test, the GW pile was excavated and the wetting front was observed to have reached sensors in Layer 3 immediately after SDRI test. the wetting front was predicted by Model GW-I2 to reach Layer 3 after 5.2 d, whereas the VWC sensors did not identify arrival of the wetting front during infiltration. This observation suggests that GW-I2 predicted arrival of the wetting front to Layer 3 approximately 1.25 d earlier than observed in the GW pile.

Predicted cumulative inflows for GW-I1 and GW-I2 were consistently less than the measured cumulative inflow for the GW pile after 0.6 d (Fig. 4.4). The rate of inflow predicted by both models appeared to be more representative of the rate observed in the GW pile during the final part of the infiltration test (i.e., after 2.7 d). The R^2 of GW-1 model was 0.03 and R^2 of model GW-I2 was 0.02, which implies that neither model was effective at describing unsaturated flow in the GW pile during infiltration from the SDRI test.

A third model, GW-I3, was performed to solve for *k*, α, and *n* based on the entire infiltration test data set (Table 4.4). This model did not converge .

4.4.1.2 Inverse Solutions for the Initial Part of Infiltration (0 d < *t* < 2.70 d)

Predicted and measured VWC and cumulative inflow in the GW pile for Models GW-I4, GW-I5, and GW-I6 that included infiltration data from 0 to 2.7 d are shown in Figs. 4.5 and 4.6, respectively. The predicted progression of the wetting front and cumulative inflow for models GW-I4 and GW-I5 were similar, which was attributed to similarity of the input parameters, in particular the saturated hydraulic conductivity (Table 4.4). Model GW-I4 predicted arrival of the wetting front to Layer 2 approximately 0.9 d earlier than measured during infiltration (Fig. 4.5a), whereas Model GW-I5 predicted arrival of the wetting front approximately 0.8 d earlier than measured (Fig. 4.5b). The earlier arrival of the wetting front for Model GW-I5 compared to Model GW-I4 was attributed to a higher *k* used in the inverse solution (Table 4.4). In contrast to these predictions, the in situ VWC sensors indicated arrival of the wetting front at 1.3 d and a more rapid increase in water content as the wetting front passed through this depth.

Predicted cumulative inflow for models GW-I4 and GW-I5 were similar, both overpredicted inflow for t < 1.0 d and subsequently underpredicted inflow (Figs. 4.6a and 4.6b). The R^2 for Model GW-I4 based on cumulative inflow was 0.96 and R^2 for Model GW-I5 was 0.97. The inverse solutions for the initial part of the infiltration data set yielded much improved fits to the data relative to inverse solutions for the entire data set. The main differences between Models GW-I4 and GW-I5 were the estimated Ψ_a, which corresponded to Ψ_a = 5.06 m for GW-I4 and Ψ_a = 2.46 m for GW-I5 (Table 4.4). Laboratory measurements of Ψ_a ranged between 1.05 and 2.55 m (Gorakhki et al. 2019). After the wetting front reached Layer 2, the rate of increase in the VWC in models GW-I4 and GW-I5 did not fit with the measured VWC.

Model GW-I6 solved for *k* in addition to water retention parameters (α and *n*). Predictions of arrival of the wetting front to Layer 2 (Fig. 4.5c) and cumulative inflow (Fig. 4.6c) were both improved by allowing *k* to vary. Model GW-I6 predicted arrival of the wetting front to Layer 2 at 1.0 d, which was close to the measured arrival at 1.3 d (Fig. 4.5c). In addition, the rate of increase in VWC in Layer 2 closely matched laboratory measurements, suggesting that the Ψ_a obtained in Model GW-I6 was more representative of the actual value in the pile. The *k* solved for in Model GW-I6 was 2.9×10^{-6} m/s, which was approximately two-times larger than the average *k* measured in the SDRI test. The computed Ψ_a in Model GW-I6 was 0.29 m, which was smaller than the laboratory-measured values. Benson et al. (2007) reported reduction in Ψ_a up to 100-times for in situ surficial soils in water balance covers after 1-4 yr in service relative to laboratory measurements. Thus, the lower Ψ_a obtained from Model GW-I6 relative to laboratory-measured values agrees with changes observed in full-scale field experiments.

4.4.1.3 Inverse Solutions for the Final Part of the Infiltration Test (2.70 d < *t* < 6.45 d)

Predicted and measured VWC and cumulative inflow in the GW pile for Models GW-I7 and GW-I8 that included infiltration data from 2.7 to 6.45 d are shown in Figs. 4.7 and 4.8, respectively. Initial VWCs throughout the model domain for Models GW-I7 and GW-I8 were based on end-state conditions from Model GW-I6 because this model yielded the most accurate predictions for the initial part of infiltration (highest R^2). The main difference between Models GW-I7 and GW-I8 was that k was assumed known in GW-I7 and k was set as a variable to solve for in GW-I8 (Table 4.4).

Model GW-I7 predicted that the wetting front reached Layer 3 at 4.6 d, whereas the in situ VWC sensors in Layer 3 did not show an increase until the end of experiment (t = 6.45 d). Model GW-I8 predicted that the wetting front reached Layer 3 at approximately 5.0 d, and also predicted a slower rate of increase in VWC relative to Model GW-I7. The slight delay in the wetting front reaching Layer 3 and slower rate of increase in VWC for Model GW-I8 was attributed to k computed as 7.2×10^{-7} m/s, which was lower than $k = 9.2\times10^{-7}$ m/s in Model GW-I7.

Cumulative inflow results indicate close comparison between measured values and predictions in Model GW-I7 and GW-I8, which both yielded $R^2 = 1.0$ (Fig. 4.8). The computed Ψ_a was 6.94 m for Model GW-I7 and 2.61 m for Model GW-I8. The Ψ_a obtained in GW-I7 (Ψ_a = 6.94 m) was larger than laboratory-measured parameters on similar materials (Gorakhki et al. 2019); however, the Ψ_a obtained in GW-I8 (Ψ_a = 2.61 m) is close to laboratory measured Ψ_a for the GW with the same mixture ratio and density (1.04 m ≤ Ψ_a ≤ 2.55 m). As a result, hydraulic parameters obtained in GW-I7 are considered more reasonable for GW pile.

4.4.1.4 GeoWaste Inverse Solution Comparison

The weak predictions of Models GW-I1 and GW-I2 suggest that the hydraulic response of the GW pile during infiltration from the SDRI test cannot be defined by a single set of hydraulic parameters. In Chapter 3, the hydraulic parameters of the GW pile were argued to change during infiltration due to (i) pedeogenesis that influenced GW closer to the pile surface and (ii) settlement that occurred during infiltration. Thus, a single set of hydraulic parameters used in Models GW-I1 and GW-I2 were not anticipated to effectively capture infiltration and changes in VWC during the entire duration of the SDRI test. This observation from the inverse models further supports the conclusion from the SDRI analysis that saturated hydraulic conductivity was higher in the surficial GW and lower in the GW at greater depth (Chapter 3).

Model GW-I6 was conducted for the initial part of infiltration that solved for k, α, and n, and Model GW-I8 was conducted for the final part of infiltration that solved for k, α, and n (Table 4.4). Model GW-I6 yielded an improvement on simulated VWC data relative to the other models conducted for the initial part of infiltration (Models GW-I4 and GW-I5), which suggests hydraulic parameters for GW-I6 are more effective at representing seepage in the GW pile for the initial part of infiltration (Fig. 4.5). Model GW-I8 yielded a modest improvement relative to Model GW-17 when simulating VWC and cumulative inflow data for the final part of infiltration (Figs. 4.7 and 4.8). Thus, Models GW-I6 and GW-I8 were selected as the inverse models for the GW pile that most effective simulated the initial and final parts of infiltration, respectively, to provide consistency in the inverse modeling approach to determine hydraulic parameters.

The optimized Ψ_a in Model GW-I8 was 2.61 m, which was larger than Ψ_a = 0.29 m obtained for Model GW-I6. The optimized k in Model GW-I8 was 7.2×10^{-7} m/s, which was four-times smaller than the k of 2.9×10^{-6} m/s obtained for Model GW-I6. In the first 2.70 d of the SDRI test, the wetting front progressed from the surface to a depth of 2.06 m. These top 2 m of the GW pile had greater opportunity to be subjected to wet-dry cycling and biotic interaction (e.g., root growth) that contribute to pedogenesis. Thus, Model GW-I6 simulated seepage in the GW pile where a more macroporous structure likely formed from pedoegenesis that contributed to a lower Ψ_a and higher k. In contrast, the wetting front progressed from 2.06 m to 3.20 m during the final part of infiltration from the SDRI test (i.e., 2.70 d < t < 6.45 d). In addition to a lower contribution of pedogenesis developing at depth in the pile, settlement developed due to additional stress from water ponded on the surface and water contained within the GW. This settlement likely increased the density of GW, which can increase Ψ_a and lower k. Thus, the larger Ψ_a and smaller k in Model GW-I8 compared to Model GW-I6 were hydraulic parameters that represented the final part of infiltration when seepage was controlled by GW deeper within the GW test pile.

4.4.2 Waste Rock Pile

Inverse model results for the WR test pile to determine k and water retention parameters (α and n) are summarized in Table 4.4. Two inverse models were conducted to simulate the entire duration of infiltration from the SDRI test in the WR pile: (i) Model WR-I1 solved α and n using k = 2.6×10^{-6} m/s obtained from the SDRI test (Chapter 3); and (ii) Model WR-I2 solved α, n, and k. The number of inverse solutions was limited for the WR pile because a single k was determined for the entire 3.75 d of infiltration during the SDRI test since the minimum and maximum k computed during SDRI test were close.

Predicted and measured cumulative inflow in the WR pile for Models WR-I1 and WR-I2 are shown in Fig. 4.9. Simulated cumulative inflow from both models were similar to measured values and both models yielded an R^2 = 1.0. Saturated hydraulic conductivity determined in WR-I2 was equal to 2.6×10^{-6} m/s, which was approximately equal to k = 2.8×10^{-6} m/s obtained directly from the SDRI experiment and used in WR-I1. The Ψ_a and n determined in both models were also similar (Table 4.4). The values of Ψ_a = 1.95 m for WR-I1 and Ψ_a = 1.86 m for WR-I2 are larger than expected for a typical WR. Newman et al. (1997) measured water retention parameters for WR with 0% to 5% fines content (particles < 0.075 mm) and reported Ψ_a ranging between 0.01 to

0.5 m. O'Kane et al. (1998) reported Ψ_a ranging between 0.5 to 1.0 m for WR with 22% fines. The particle-size distribution for WR used in the WR pile (Chapter 3) indicates an average fines content of 22%. The Ψ_a determined for the WR pile based on the two inverse solutions were larger relative to literature, but generally agree with values reported by O'Kane et al. (1998) for WR with higher fines content.

The two inverse solutions conducted for the WR pile yielded similar hydraulic parameters. The only available input monitoring data for the WR pile were cumulative inflow because no in situ water content sensors were functional during the SDRI test. Nakhaei and Simunek (2014) suggested that an inverse solution is less accurate if the temporal behavior of profile (e.g., water content or head) is not provided. Thus, the degree of certainty in the inverse solutions for the WR pile is less than that of the GW pile due to the absence of in situ water content measurements during infiltration.

4.4.3 Field-Scale Hydraulic Conductivity in the Test Piles

Hydraulic conductivity of a geomaterial that is subjected to an in situ infiltration experiment, such as the SDRI test, can be determined by analytical and numerical solutions. A common analytical approach for an SDRI test is described in Daniel (1989), which was used in Chapter 3 along with different assumptions for suction head at the wetting front as descried in Wang and Benson (1995). A numerical approach implemented herein, whereby an inverse model was used to find best-fit hydraulic parameters based on minimizing the error between measured and predicted data (e.g., cumulative inflow, volumetric water content). In addition to conducting inverse models in HYDRUS-2D for the GW and WR test piles, an additional objective of this study was to compare field-scale hydraulic conductivity from analytical and numerical solutions.

Justifiable values of hydraulic conductivity were determined via inverse solutions and analytical solutions for: (i) the initial part of infiltration in the GW pile from 0 to 2.70 d; (ii) the final part of infiltration in the GW pile from 2.70 to 6.45 d; and (iii) the entire infiltration duration in the

WR pile. The analytical solution for the initial part of infiltration in the GW pile yielded *k* ranging between 1.1×10^{-6} m/s and 1.7×10^{-6} m/s based on varying assumptions for suction head at the wetting front (suction at the wetting front, Ψ_f = 0.0 to 0.80 m). In comparison, *k* determined via the inverse solution in Model GW-I6 was 2.9×10^{-6} m/s. Hydraulic conductivity obtained via the inverse solution was twice the *k* obtained analytically for the initial part of infiltration in the SDRI test when the wetting front within the top 2 m. However, the *k* obtained for the final part of infiltration in the SDRI test when wetting front was deeper than 2.0 m were approximately the same via analytical (7.2×10^{-7} m/s) and numerical solutions (7.2×10^{-7} m/s).

Hydraulic conductivity computed via the analytical solution for the SDRI test used infiltration rate of the inner ring, whereas cumulative inflow for the numerical inverse model was based on inflow from the inner and outer rings of the SDRI. A key factor that can influence *k* determined analytically and numerically is anisotropy between vertical and horizontal *k*. Water flow under the inner ring in the SDRI test is essentially 1-dimensional in the vertical direction. However, horizontal flow can result in error when flow is 2-dimensional. Based on periodic observation of the water content profile in the HYDRUS-2D model, flow was developing both horizontally and vertically in the first 2.0 d of infiltration. In contrast, observations of the water content profile for infiltration occurring after 2.0 d suggests predominantly 1-dimensional flow. This observation suggests *k* may be overestimated via numerical solutions in HYDRUS 2D when horizontal flow is larger than vertical flow, which was more prominent during the initial part of infiltration relative to the final part of infiltration.

4.4.4 Comparison of Field and Laboratory Hydraulic Properties in GW Pile

Laboratory hydraulic parameters of GW measured by Gorakhki et al. (2019) are tabulated in Table 4.2. Three mechanisms suggested for difference between laboratory and field hydraulic properties of GW pile:

- (i) spatial variability in *R*: Results of spatial variability of *R* discussed in Chapter 3 and while the target R was 0.43, the result of sieve analysis suggested that R ranged between 0.2 to 3.2. While R varied in the GW pile, the hand-mixed laboratory specimen was prepared with low spatial R variability;

- (ii) variation in construction methods: GW pile was constructed by dropping the mixed material from a height of 2-3 m while laboratory specimens were created to a target porosity by tamping the GW. This difference can result in change in pore structure between laboratory specimens and field piles; and
- (iii) pedogenesis: pedogenesis is a natural, soil-structure formation process due to processes such as freeze-thaw, wet-dry cycling, root growth and decay, and burrowing animals (Othman and Benson 1992; Buol et al. 1997; Albercht and Benson 2001; Melchior et al. 2010).

The laboratory k for GW ranged between 2.6×10^{-8} and 8.6×10^{-9} m/s for comparably porosity as measured in the field-scale test pile. Relationships between post-construction k for earthen cover systems 2, 3, and 4 yr after construction and as-built k from Benson et al. (2007) is shown in Fig. 4.10. Also included in Fig. 4.10 are laboratory measured k, SDRI measured k, and inverse solution k for GW. Post-construction k of earthen cover soils increased relative to the as-built k by a factor ranging from 1 to 10,000. The k of the SDRI test was 50-times to 150-times larger than the laboratory-measured k, whereas k determined via the inverse solutions were 110-times to 340-times larger than laboratory-measured k.

The difference between k determined analytically or numerically via the SDRI and k measured in the laboratory during the final part of the infiltration portion (2.70 to 6.45 d) was smaller relative to the difference during the initial part of the infiltration (0.0 to 2.70 d). The larger difference between k measured in the laboratory and determined for the GW pile in the initial part of infiltration was attributed to a greater prevalence of pedeogenesis influencing the top 2 m of the GW pile where flow was concentrated.

Benson et al. (2007) also evaluated changes in Ψ_a with time following earthen cover construction. The comparison between post-construction Ψ_a and laboratory-measured Ψ_a based on Benson et al. (2007) and GW in this study are shown in Fig. 4.11. Benson et al. (2007) reported that Ψ_a decreased up to 200-times for in-service conditions due to pedogenesis. Laboratory measured GW specimens yielded Ψ_a ranging between 1.05 and 2.55 m (Gorakhki et al. 2019). Comparison between laboratory-measured Ψ_a and Ψ_a determined for Model GW-I6 plot near the 10:1 line, indicating approximately an order-of-magnitude decrease in Ψ_a for the initial part of infiltration when seepage was concentrated in the upper 2.0 m of the GW test pile. In contrast, laboratory-measured Ψ_a and Ψ_a determined for Model GW-I8 plot close to 1:1 line, indicating negligible change in Ψ_a. Model GW-I6 simulated infiltration in the top 2.0 m, which was influenced by pedogenesis, whereas Model GW-I8 simulated infiltration wetting front was below 2.0 m and less influenced by pedogenesis.

4.5 Conclusions

Inverse models in HYDRUS 2D were completed to determine saturated hydraulic conductivity and van Genuchten water retention parameters of a GeoWaste (GW) and waste rock (WR) test pile. Infiltration data were obtained from sealed-double ring infiltrometer tests conducted on the test piles after 26-months of operation under natural climatic conditions. Temporal cumulative inflow volume and volumetric water content at different locations were provided as input in the GeoWaste pile and temporal cumulative inflow volume data was provided for waste rock pile. The following conclusions were drawn from this study:

- A single set of hydraulic parameters could not predict the hydrologic behavior of the GW pile during the 6.45 d of infiltration, which was attributed to unique phases of infiltration during the first 2.7 d (initial part) and from 2.7 to 6.45 d (final part) of the infiltration test.
- Inverse simulations for the GW pile based on the initial and final parts of infiltration yielded a larger *k* and lower Ψ_a representative of the upper 2.0 m of pile (initial part) compared to the lower 2.7 m part of pile (final part). This behavior was attributed to (i) more pronounced

pedeogenesis closer to surface that created a more macroporous structure and (ii) settlement observed during infiltration that may have densified the GeoWaste at depth.

- The *k* obtained via the inverse solution of the GW pile was two times larger than *k* obtained analytically from the SDRI experiment for the first 2.70 d while the wetting front was in the top 2.0 m of pile. The larger *k* determine numerically was attributed to horizontal flow as the wetting front established, whereby two-dimensional flow was more pronounced during the first 2.0 d of infiltration. Subsequently, flow was primarily 1-dimensional as the wetting front penetrated below 2.0 m, which resulted in comparable *k* obtained analytically from the SDRI test and numerically via inverse solution.
- The *k* for the GW pile via the inverse solution was 110 to 340 times larger than laboratory-measured *k* for the first 2.70 d (initial part) and 28 to 83 times larger than laboratory-measured *k* in the last 3.75 d (final part).
- The air entry pressure obtained for the GW pile via the inverse solution was approximately 10-times smaller than laboratory-measured values for the upper 2.0 m and approximately equal for the lower part of pile.
- Comparisons between hydraulic parameters for the GW pile determined numerical via inverse modeling and from laboratory experiments indicate that the top 2.0 m of the pile experienced more pronounced pedogenesis that resulted in a macroporous structure relative to the GeoWaste below 2.0 m.
- The *k* for the WR pile determined analytically from the SDRI test and numerically via inverse modeling were (2.6×10^{-6} to 2.8×10^{-6} m/s). However, the air entry pressure obtained numerically for the WR pile were larger compared with data reported in literature. An inaccurate estimation of air entry pressure in the WR pile may be due to the lack of temporal volumetric water content profile input data.

Table 4.1. Summary of physical characteristics and classification for tailings and waste rock.

Material	*LL* (%)	*PI* (%)	USCS	Gravel Content (%)	Sand Content (%)	Fines Content (%)	Clay-Size Content (%)	w_{opt} (%)	$\rho_{d\text{-}max}$ (g/cm^3)
Tailings	30.1	9.2	CL	0	14.3	85.7	23.6	15.8	1.69
Waste Rock	NA	NA	GM	51.0	27.0	22.0	NA	NM	NM

NA = not applicable; NM = not measured

Table 4.2. Summary of laboratory and field test on the hydraulic conductivity of tailings, GeoWaste, and waste rock.

Sample	Type of Test	Dry Density (Mg/m^3)	Porosity	Hydraulic conductivity, *k* (m/s)
Tailings 1	Laboratory	1.44	0.46	6.9×10^{-9}
Tailings 2	Laboratory	1.43	0.47	9.0×10^{-8}
GeoWaste 1	Laboratory	1.42	0.37	2.6×10^{-8}
GeoWaste 2	Laboratory	1.41	0.38	8.6×10^{-9}
GeoWaste (top 2m)	SDRI	1.54	0.42	1.4×10^{-6}
GeoWaste (deeper than 2 m)	SDRI	1.54	0.42	9.0×10^{-7}
Waste Rock	SDRI	1.89	0.30	2.8×10^{-6}

Table 4.3. Summary of laboratory test on the soil water characteristic curve of tailings and GeoWaste.

Sample	Dry Density (Mg/m^3)	θ_s	θ_r	*n*	α (1/m)	Ψ_a (m)
Tailings (1)	1.43	0.45	0.02	1.61	0.500	2.00
Tailings (2)	1.42	0.47	0.02	1.63	0.324	3.09
Tailings (3)	1.53	0.42	0.00	1.24	0.314	3.18
Tailings (4)	1.63	0.36	0.00	1.37	0.078	12.82
GeoWaste (1)	1.65	0.38	0.02	1.25	0.392	2.55
GeoWaste (2)	1.64	0.38	0.02	1.24	0.960	1.04

Table 4.4. Summary of inverse solution models on piles to obtain the hydraulic properties of GeoWaste and waste rock in the field condition.

Model	**Period of experiment (days)**	**Inputs**			**Outputs**					
		No of input parameters	**Input soil properties**	**k (m/s)**	**Output**	**α (1/m)**	***n***	***k* (m/s)**	**Ψ_a (m)**	**R^2**
GW-I1	6.45	3797	*k*, θ_s, θ_r	9.6×10^{-7}	α, n	0.66	1.75	NA	1.51	0.03
GW-I2	6.45	3797	*k*, θ_s, θ_r	1.3×10^{-6}	α, n	0.97	1.75	NA	1.03	0.02
GW-I3	6.45	3797	θ_s, θ_r	NA	k, α, n	Did not converge				NA
GW-I4	2.70	1577	*k*, θ_s, θ_r	1.1×10^{-6}	α, n	0.20	1.75	NA	5.06	0.96
GW-I5	2.70	1577	*k*, θ_s, θ_r	1.8×10^{-6}	α, n	0.41	1.75	NA	2.46	0.97
GW-I6	2.70	1577	θ_s, θ_r	NA	k, α, n	3.47	1.75	2.9×10^{-6}	0.29	0.99
GW-I7	3.75	2212	*k*, θ_s, θ_r	9.2×10^{-7}	α, n	0.14	1.72	NA	6.94	1.00
GW-I8	3.75	2212	θ_s, θ_r	NA	k, α, n	0.38	1.74	7.2×10^{-7}	2.61	1.00
WR-I1	3.67	54	*k*, θ_s, θ_r	2.8×10^{-6}	α, n	0.51	2.22	NA	1.95	1.00
WR-I2	3.67	54	θ_s, θ_r	NA	k, α, n	0.54	2.09	2.6×10^{-6}	1.86	1.00

GW = GeoWaste; WR = waste roc; I = inverse; *k* = saturated hydraulic conductivity; θ_s = saturated volumetric water content;
θ_r = residual water content; α and *n* = van Genuchten parameters; Ψ_a = air entry pressure, and NA=not applicable

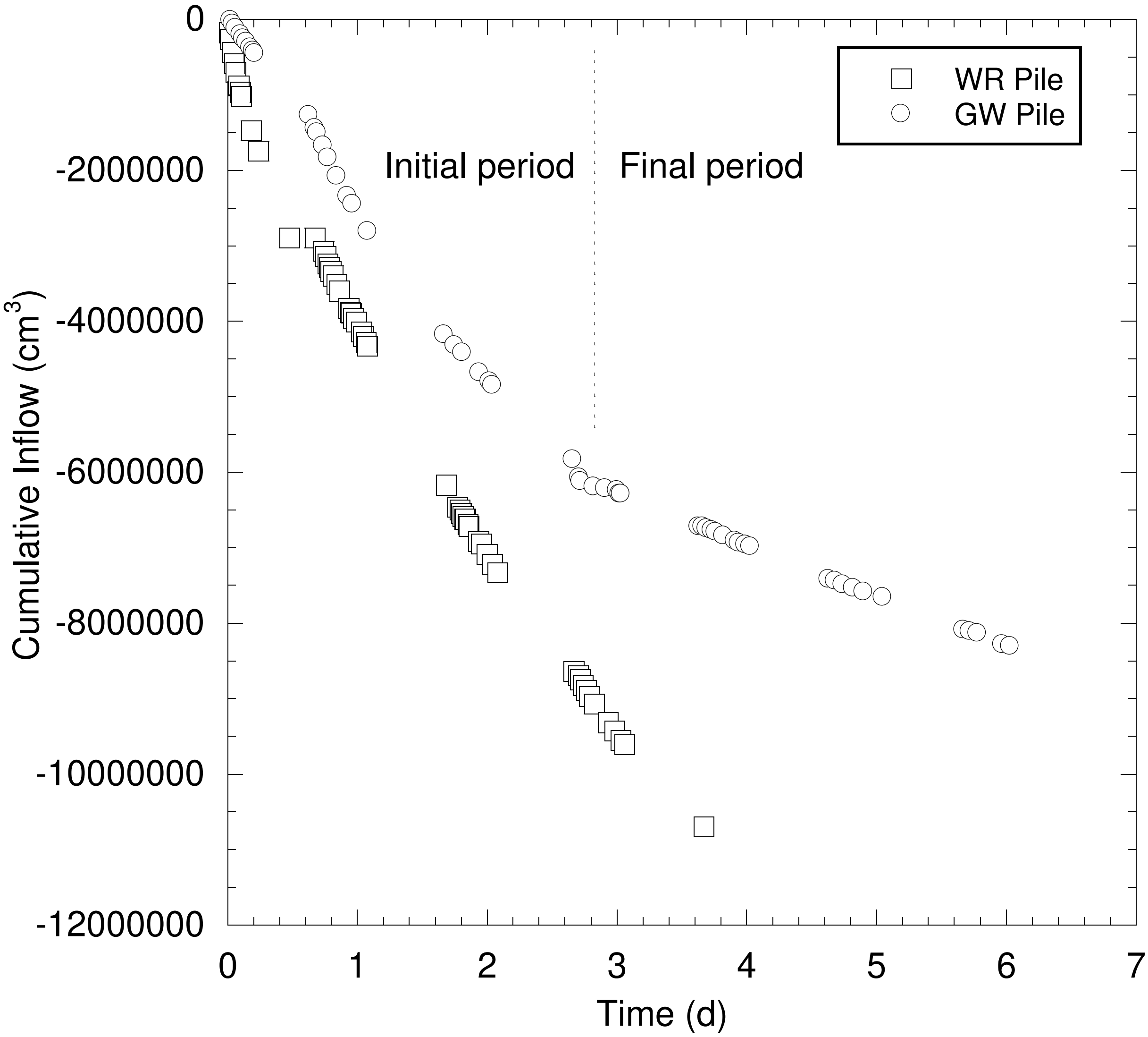

Fig. 4.1. Temporal relationship of cumulative inflow during infiltration experiment in the GeoWaste and waste rock piles. Width of the infiltration ring was 240 cm × 240 cm.

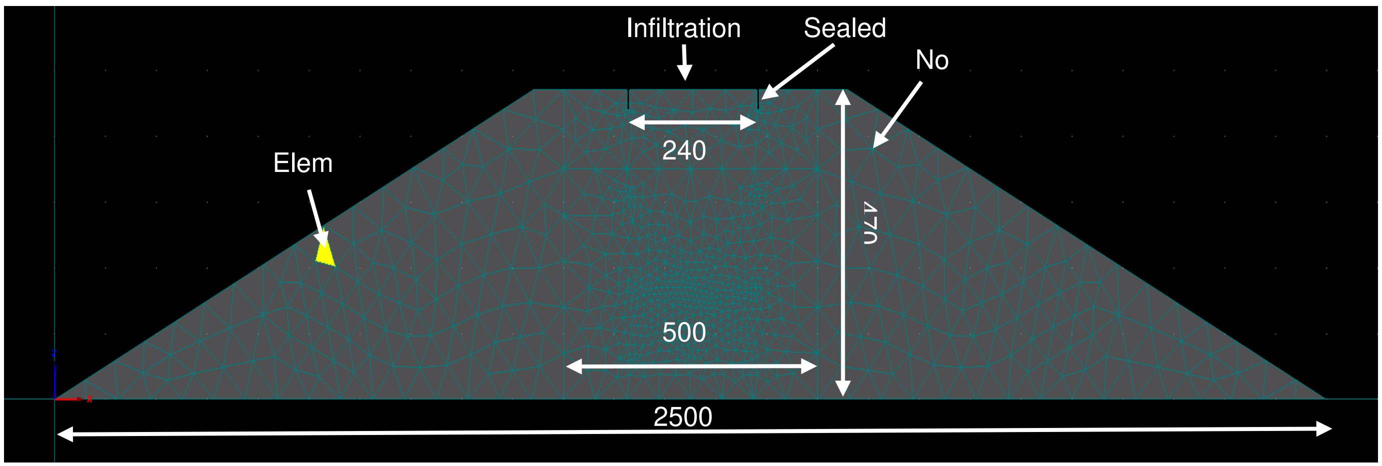

Fig. 4.2. Screenshot of setup model in HYDRUS 2D.

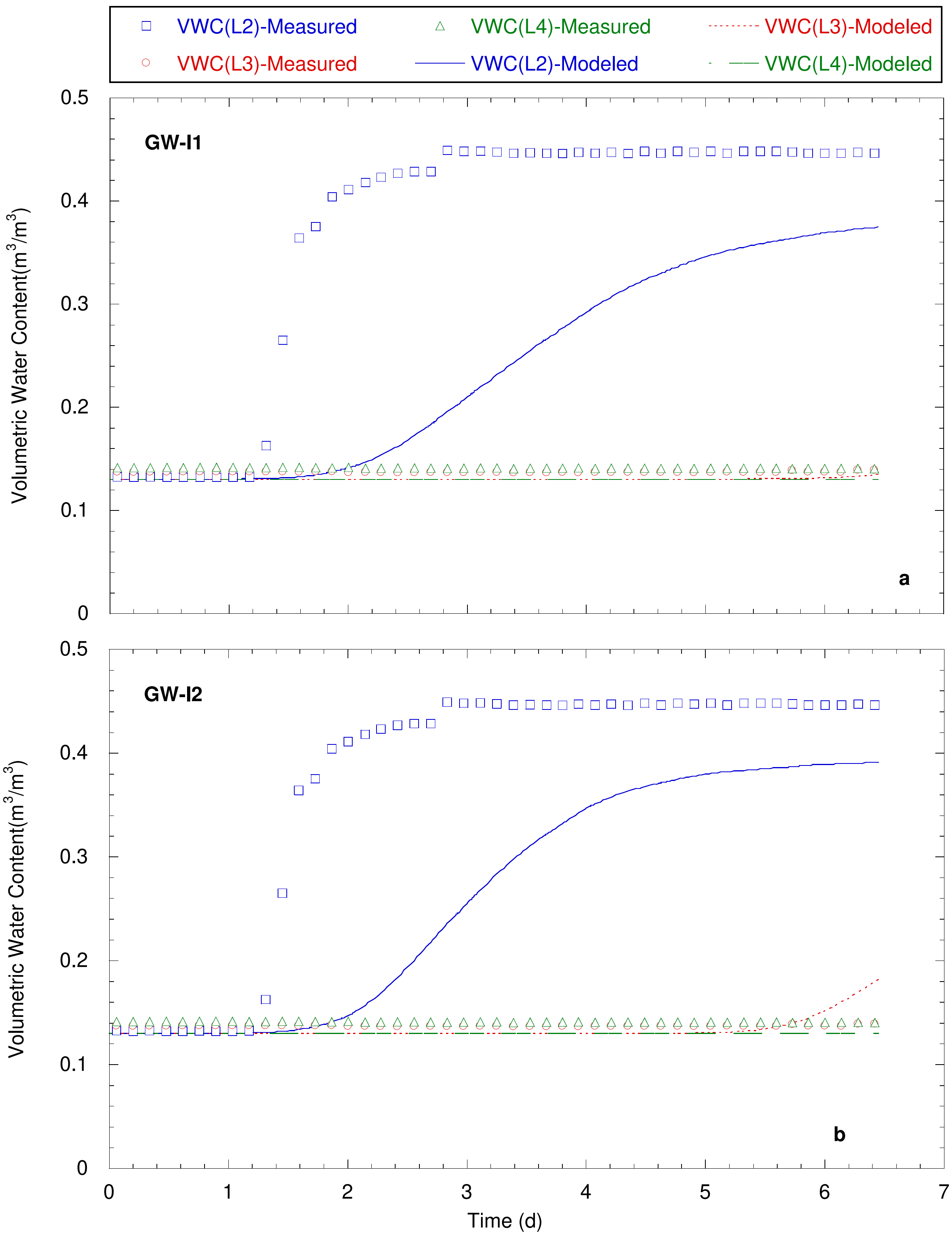

Fig. 4.3. Temporal comparison of measured and modeled volumetric water content in the GeoWaste pile for inverse models simulating the whole period of experiment. L2 = layer 2 (1.7 m from the surface); L3 = layer 3 (3.2 m from the surface); and L4 = layer 4 (4.5 m from the surface).

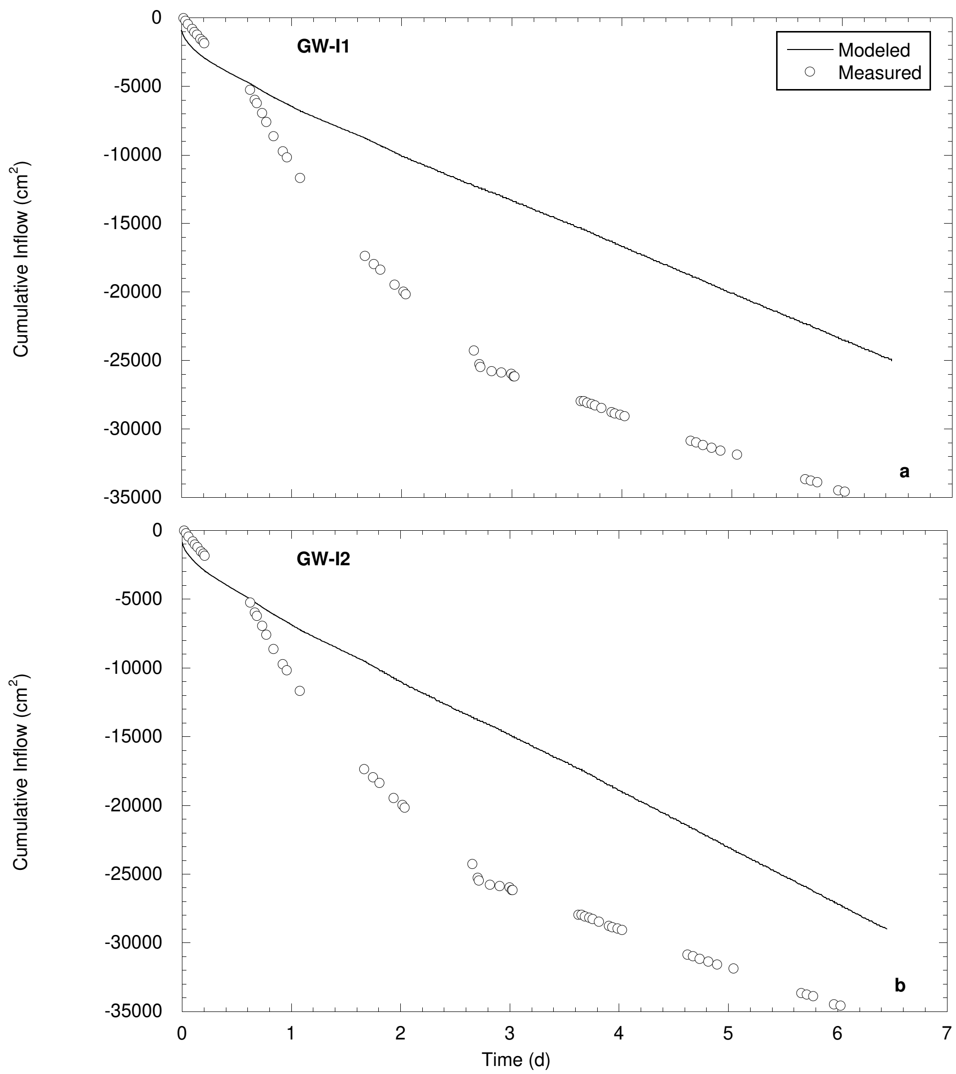

Fig. 4.4. Temporal comparison of measured and modeled cumulative inflow in the GeoWaste pile for inverse models simulating the whole period of experiment

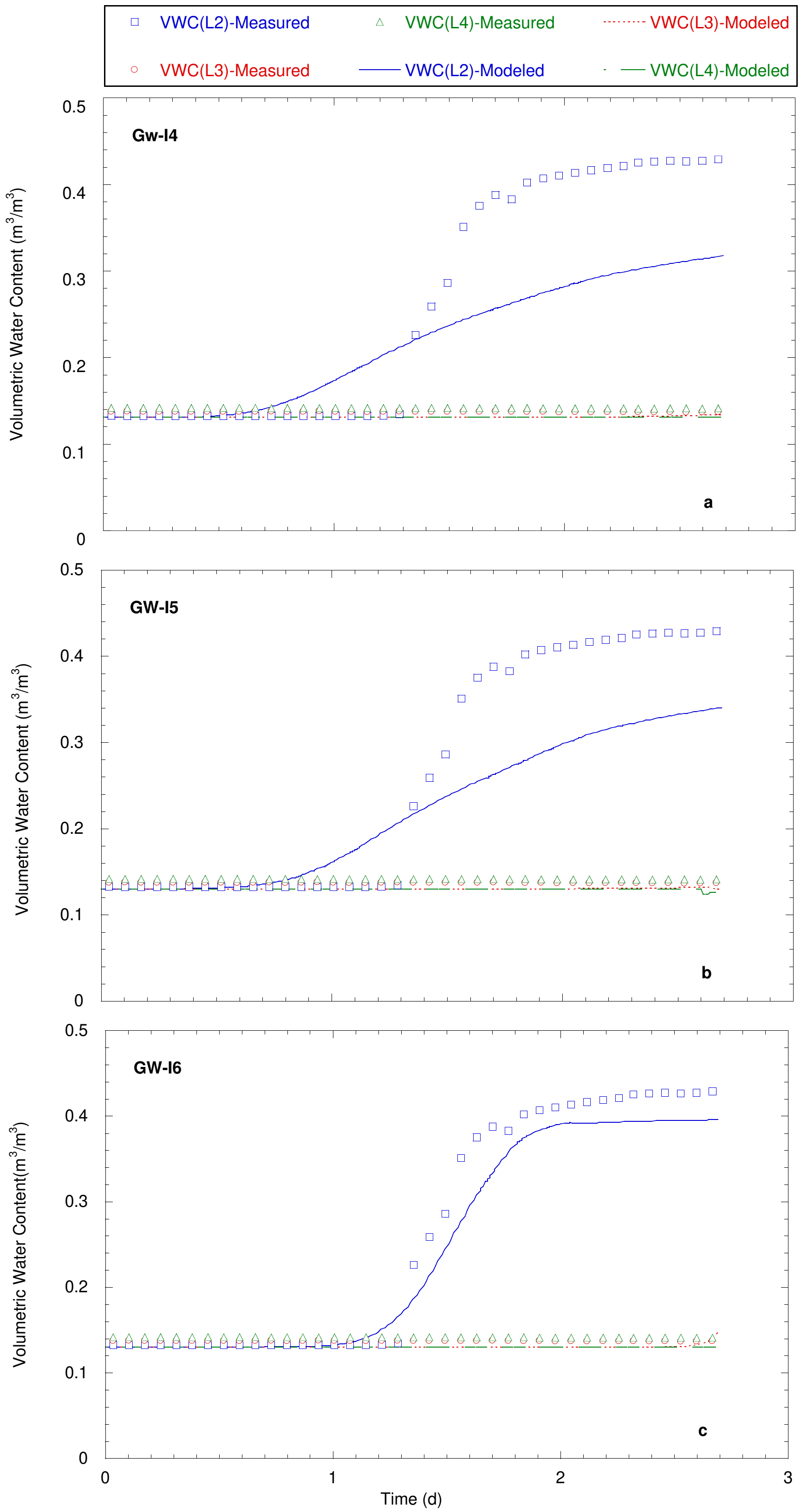

Fig. 4.5. Temporal comparison of measured and modeled volumetric water content in the GeoWaste pile for inverse models simulating the initial 2.70 days of infiltration

experiment.

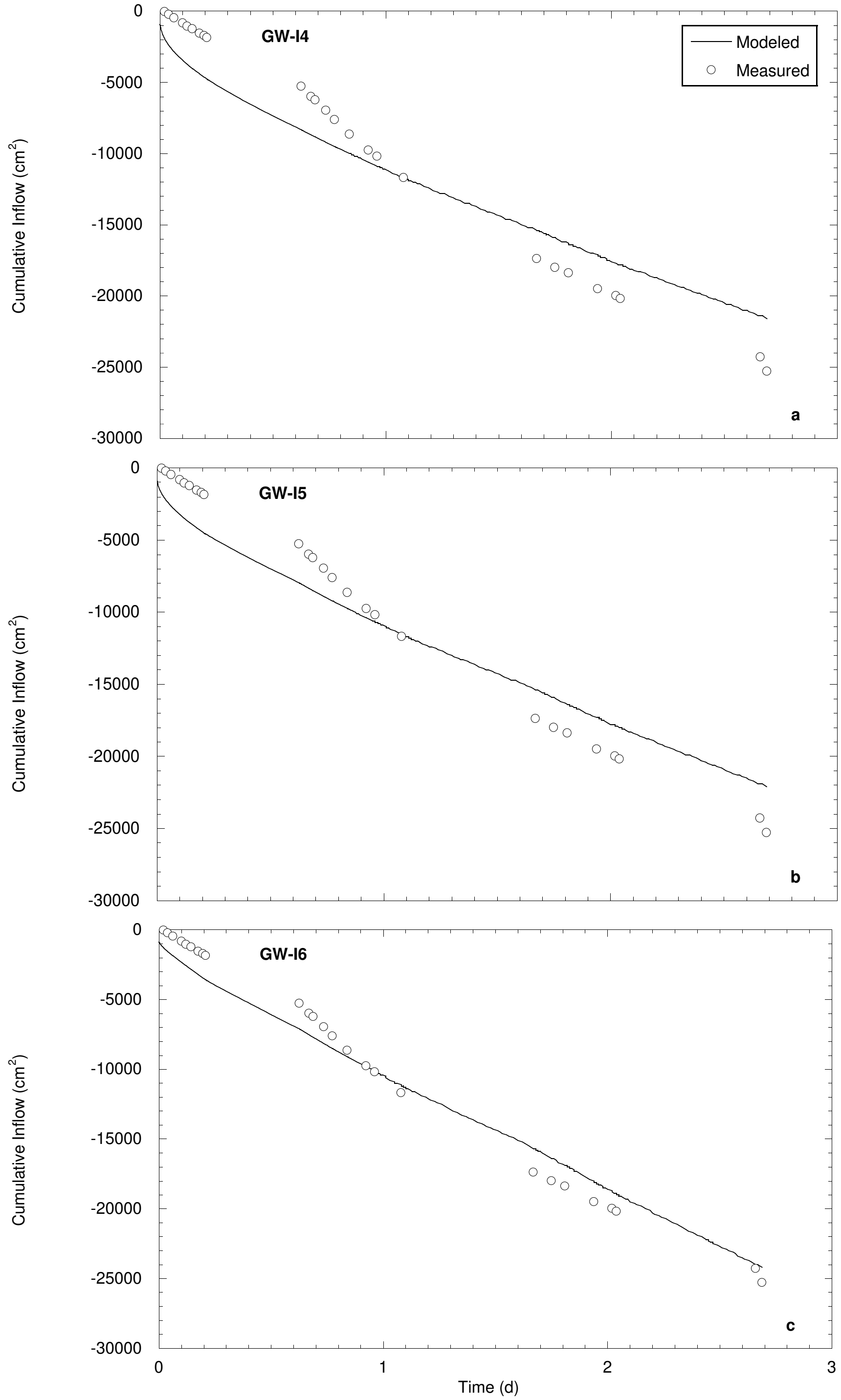

Fig. 4.6. Temporal comparison of measured and modeled cumulative inflow in the GeoWaste pile for inverse models simulating the initial 2.70 days of infiltration experiment.

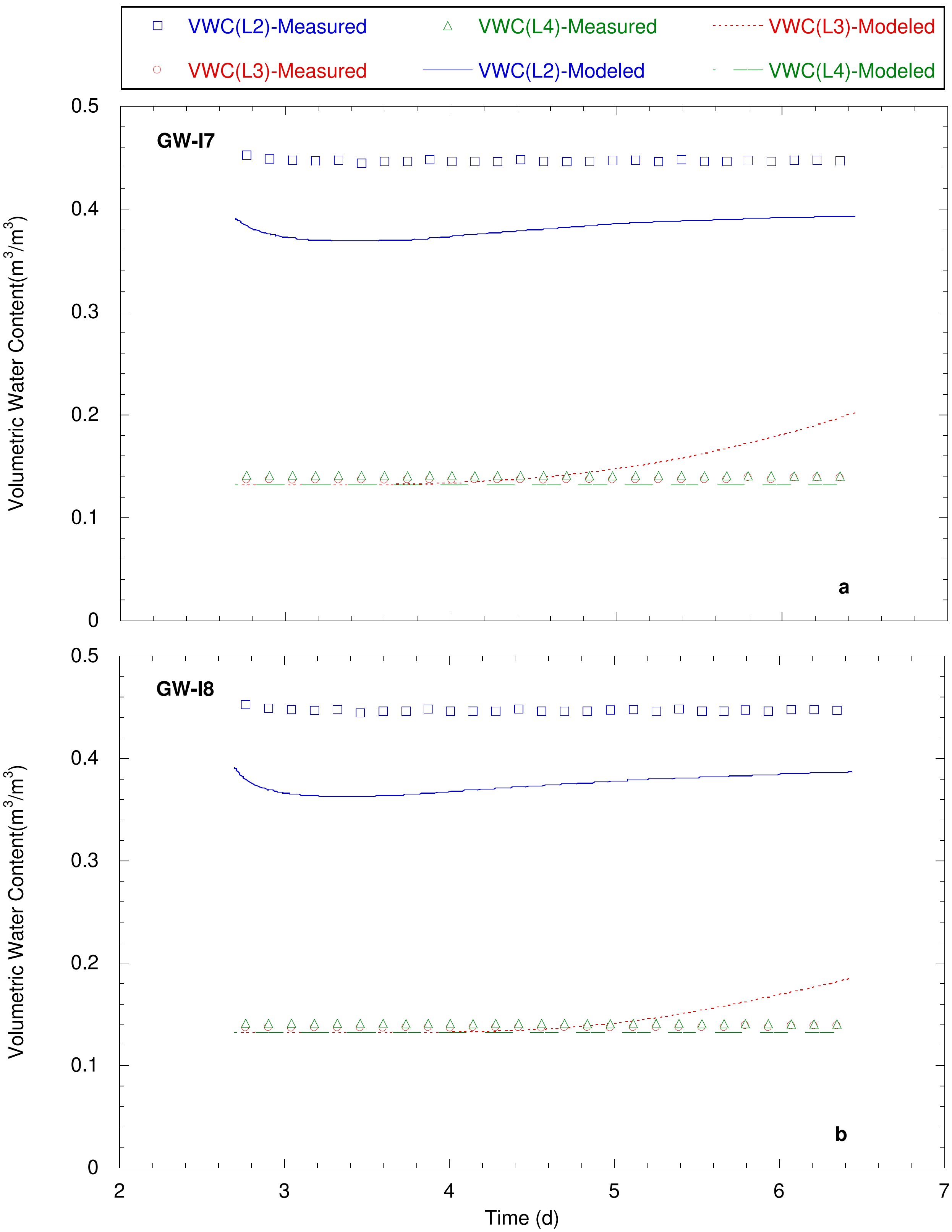

Fig. 4.7. Temporal comparison of measured and modeled volumetric water content in the GeoWaste pile for inverse models simulating the final 3.75 days of infiltration

experiment.

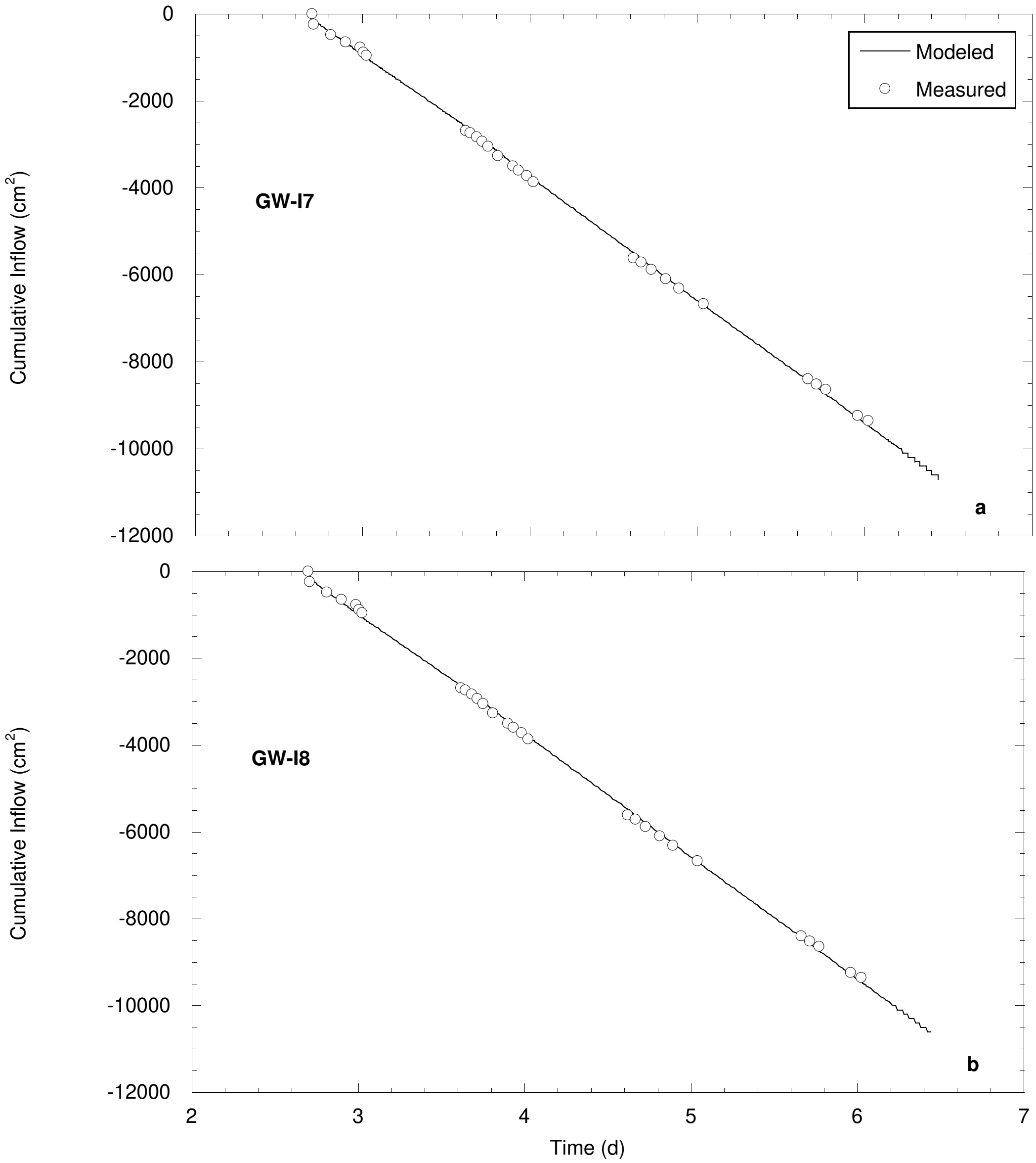

Fig. 4.8. Temporal comparison of measured and modeled cumulative inflow in the GeoWaste

pile for inverse models simulating the final 3.75 days of infiltration experiment.

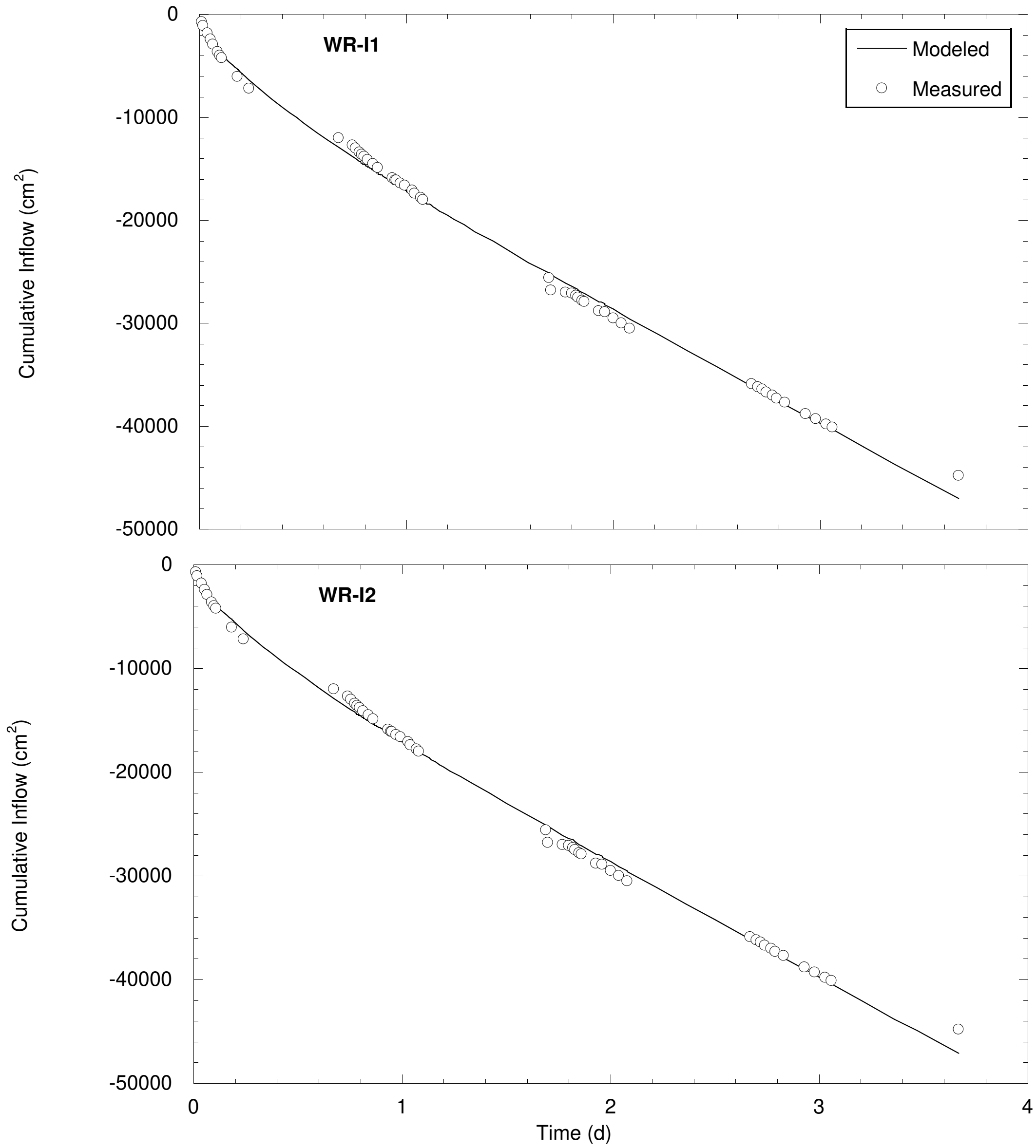

Fig. 4.9. Temporal comparison of measured and modeled cumulative inflow for the inverse models ran based on properties obtained in WR-I1 and WR-I2.

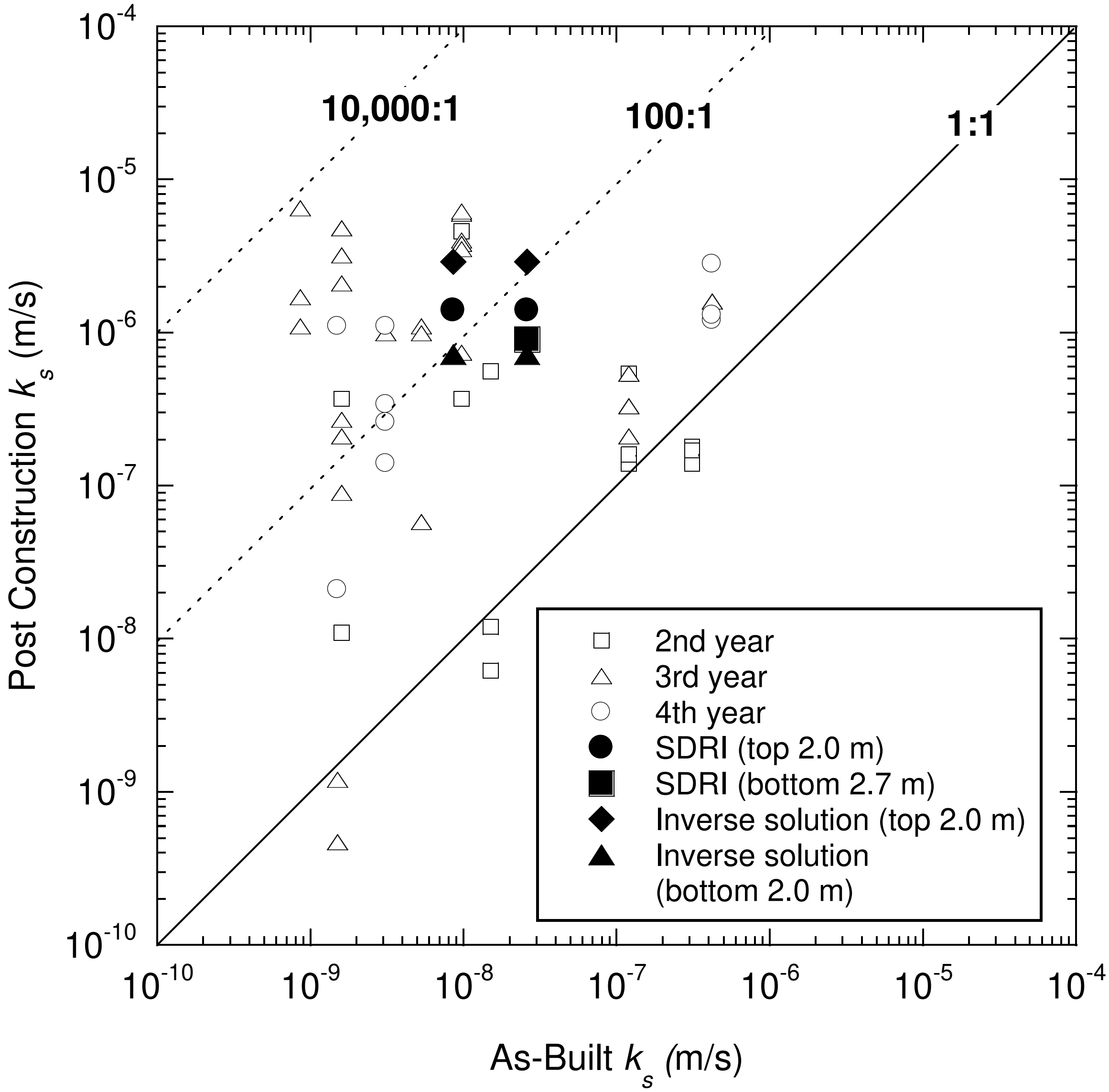

Fig. 4.10. Relationship between post construction and as-built saturated hydraulic conductivity (k) of cover soils adapted from Benson et al. (2007) along with data from the laboratory tests, sealed double ring infiltrometer tests, and inverse solution modeling on GeoWaste.

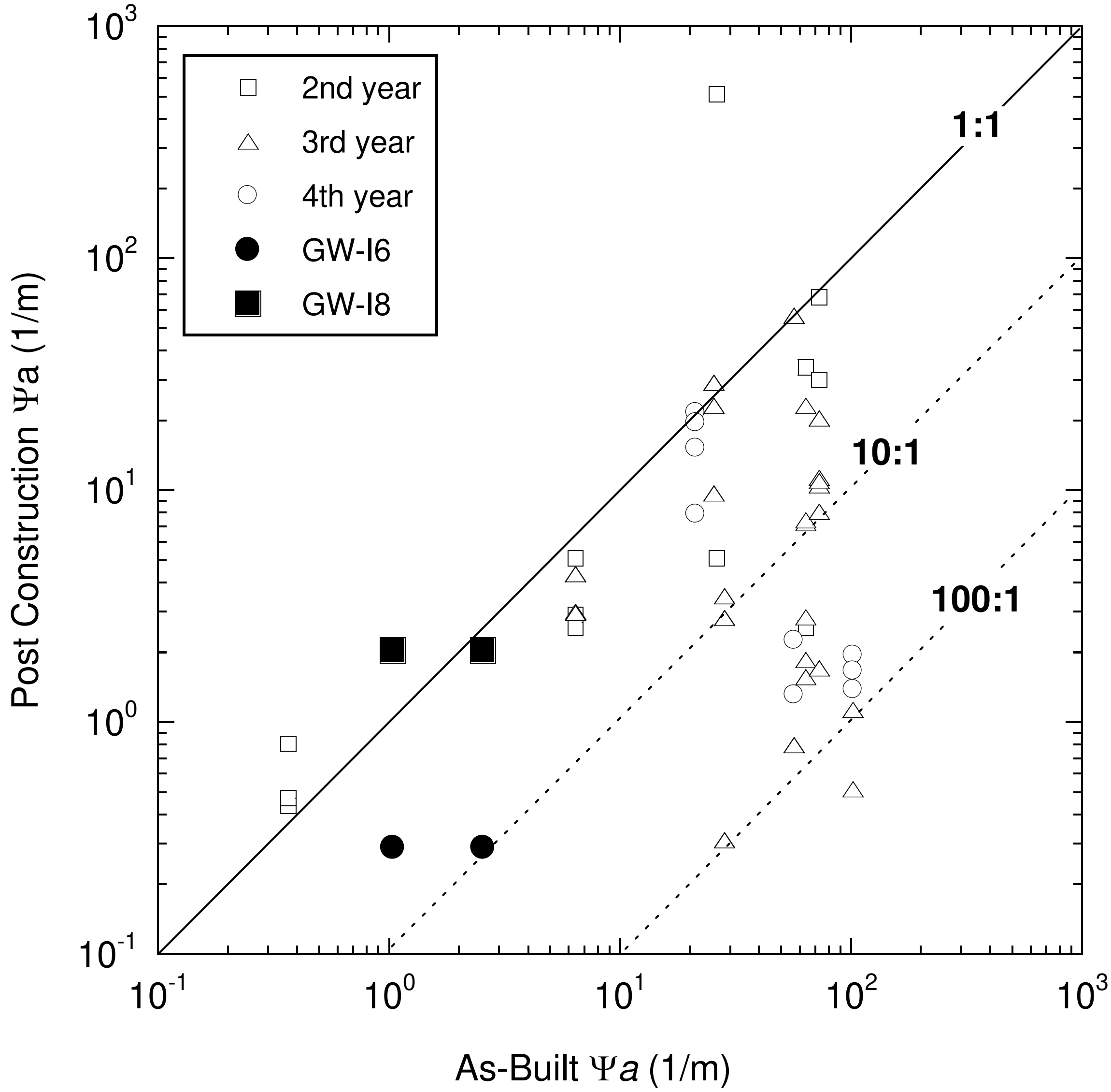

Fig. 4.11. Relationship between post construction and as-built air entry pressure (Ψ_a) of cover soils adapted from Benson et al. (2007) along with data from the laboratory tests and inverse solution modeling on GeoWaste.

5 HYDROLOGIC PREDICTIONS OF WATER CONTENT AND OXYGEN CONCENTRATION IN GEOWASTE AND WASTE ROCK TEST PILES

5.1 Introduction

Standard mine waste management is to store tailings and waste rock (WR) separately. However, WR piles can be susceptible to acid rock drainage (ARD) and tailings storage facilities (TSFs) are susceptible to failure (Blight 2009). The typically high permeability of WR allows ingress of atmospheric oxygen and precipitation, which may lead to ARD when sulfide-rich minerals are present. The loose, contractive nature of slurry-deposited TSFs can lead to low shear strength and potentially liquefiable materials under rapid vertical loading (static liquefaction) and/or seismic loading (dynamic liquefaction), which has resulted in numerous TSF failures over the last century (Azam and Li 2010; Morgenstern et al. 2015; Morgenstern et al. 2016; Robertson et al. 2019). Co-disposal of WR and tailings (WR&T) has been evaluated as an alternative mine waste management technique to address ARD concerns in WR piles and low shear strength / liquefaction concerns in TSFs (Williams et al. 2003; Wickland et al. 2006; Bussière 2007).

The blending of filtered tailings and WR in a tailings-dominated mixture, referred to as GeoWaste (GW), is a co-disposal approach to create a material that facilities placement in deposits that do not require dams or embankments. The addition of WR to filtered tailings improves shear strength of the tailings (e.g., Burden et al. 2017; Borja 2019) to enhance geotechnical stability. The tailings-dominated mixture of GW is envisioned to encapsulate potentially acid-generating WR in tailings to inhibit the ingress of oxygen and mitigate ARD potential, which enhances geochemical stability. Moreover, GW has a lower permeability and higher water retention relative to WR alone, which may enable the use of mixed mine WR and tailings such as GW in a water balance cover (Gorakhki and Bareither 2017). A water balance cover decreases leachate generation by storing precipitated water during the wet part of a year and releasing the stored water back to atmosphere via evapotranspiration during the dry part of a year. Evaluating the water-phase balance (e.g., water content distribution, water percolation) and gas-phase balance (e.g., oxygen concentration distribution) are important factors to consider when comparing the hydrologic and environmental behavior of WR and GW deposits.

Waste rock and GW test piles were constructed and monitored for 26 months at a mine in Central America. Monitoring data and analysis of field performance for the test piles are provided in Chapter 2. The focus of this study was to validate commercially-available hydrological models to compare with measured data. Validation of a hydrologic model via comparison to field data can support use of the model to make long-term predictions or assess different designs. Although commercially-available models have been used for water balance covers (e.g., Albright et al. 2010), a comparison between measured and modeled hydrologic response of a GW deposit is novel. Also, gas phase modeling in the pore volume of a GW deposit is novel.

The purpose of this study was to evaluate the ability of a commercially-available hydrologic model (via HYDRUS) to predict water and gas flow in GeoWase and WR test piles. The test piles were monitored for water content and oxygen concentration for a period of 26 months. HYDRUS 2D and 1D models were conducted for the entire 26 month period using local meteorological data and soil hydraulic properties obtained via field- and laboratory-scale testing. Modeled and measured volumetric water content and oxygen concentration within the piles were compared to assess validity of the numerical models to describe the behavior of GW.

5.2 Unsaturated Modeling of Mine Waste

5.2.1 Water Balance

The volume of generated leachate from a mine waste impoundment depends on the climatic condition, vegetation, and hydrologic parameters. A schematic of a mine waste deposit that documents internal and atmospheric interactions is shown in Fig. 5.1. The water balance of a mine waste deposit was computed as

$$P_r = P - R - ET - L - \Delta S \tag{5.1}$$

where P_r is leachate percolation at the base of the deposit, P is precipitation, R is surface runoff, ET is evapotranspiration, L is lateral drainage, and ΔS is the change in soil water storage. The ET in Eq. 5.1 is a fraction of potential evapotranspiration (PET), which is computed from meteorological data, site latitude and altitude, and surface albedo (Monteith 1981). Albedo (α) is the fraction of the solar radiation reflected relative to the total solar radiation received on a given surface. Albedo depends on different factors such as vegetation and volumetric water content of a surface soil. Surface albedo was calculated using Eq. 5.2 (Zeng et al. 1999):

$$\alpha = 0.38 - 0.3(1 - \exp(-k_{ext} \bullet LAI)) \tag{5.2}$$

where k_{ext} is the extinction coefficient and LAI is the leaf area index. Extinction coefficient describes how easily a beam of energy can penetrate into a material and was assumed to be 0.463 (Allen 1998). Leaf area index is defined as total area of leaves per unit area of ground surface and obtained based on observed vegetation.

5.2.2 Pore-Space Interactions in Mine Waste

5.2.2.1 Acid Rock Drainage Reactions

Acid rock drainage to surface water and groundwater cause lowered pH and increased specific conductivity, which further increases the concentration of iron, aluminum, and manganese, and other metallic ions (Akcil and Koldas 2006). The most common ARD reaction is the oxidation of pyrite (FeS_2), as described in Eq. 5.3.

$$FeS_2 + 3.5O_2 + H_2O \rightarrow Fe^{2+} + 2SO_4{}^{2+} + 2H^+$$

(5.3)

The generation of H^+ decreases the pH and the generation of Fe^{2+} and SO_4^{2-} increase total dissolved solids and electrical conductivity. If the concentration of O_2, pH, and bacterial activity are suitable, ferrous iron (Fe^{2+}) oxidizes to ferric iron (Fe^{3+}) as shown in Eq. 5.4.

$$Fe^{2+} + \frac{1}{4}O_2 + H^+ \rightarrow Fe^{3+} + \frac{1}{2}H_2O$$

(5.4)

At a pH of 2.3 to 3.5, ferric iron precipitates as shown in Eq. 5.5, which further lowers pH.

$$Fe^{3+} + 3H_2O \rightarrow Fe(OH)_{3solid} + 3H^+$$

(5.5)

Any ferric iron that does not precipitate as $Fe(OH)_3$ may then oxidize additional pyrite (Eq. 5.6)

$$FeS_2 + 14Fe^{3+} + 8H_2O \rightarrow 15Fe^{2+} + 2SO_4{}^{2+} + 16H^+$$

(5.6)

Important factors that determine the rate of acid generation include pH, temperature, O_2 concentration in the gas phase, O_2 concentration in the water phase, chemical activity of Fe^{3+}, surface area of exposed metal sulphide, and bacterial activity (Blowes et al. 2003). Changes in any of these factors can increase or decrease the acid generation.

5.2.2.2 Oxygen Diffusion

Consumption of O_2 in the pore spaces via Eqs. 5.3 and 5.4 lowers the O_2 concentration, which promotes oxygen diffusion into the pore space due to an O_2 gradient with the atmosphere (Fig. 5.1). The diffusion flux (F) of O_2 can be calculated in 1-dimensional using Fick's first law

$$F = -D_e \frac{\partial C}{\partial_z} \tag{5.7}$$

where D_e is the effective diffusion coefficient, C is oxygen concentration, and z is vertical distance. A lower O_2 diffusive flux will decrease the rate of replenishment in O_2 resulting in a lower O_2 concentration in the profile and reduce the magnitude of ARD reactions (e.g., Eqs. 5.3-5.6). The main parameters controlling O_2 diffusion into a geomaterial are D_e and concentration gradient.

The effective diffusion coefficient is composed of two components (Collin 1987):

$$D_e = D_a + H \cdot D_w \tag{5.8}$$

where D_a is the effective diffusion coefficient in the gas phase, D_w is the effective diffusion coefficient in the liquid phase, and H is Henry's constant (i.e., approximately 0.03 at 25 °C). Oxygen diffusion through water contributes much less than diffusion through the air phase. The expression in Eq. 5.8 can be expanded as

$$D_e = \theta_a \cdot T_a \cdot D_a^{\ 0} + 0.03(\theta_w \cdot T_w \cdot D_w^{\ 0}) \tag{5.9}$$

where θ_a and θ_w are the volumetric air and water content ($\theta_a + \theta_w$ = porosity), T_a and T_w are the air and water phase tortuosity, and D_{a0} and D_{w0} are the free diffusion coefficient in air and water ($D_{a0} = 1.8\times10^{-5}$ and $D_{w0} = 2.2\times10^{-9}$ m^2/s). The parameters T_a and T_w can be estimated as a function of saturation (Penman 1940; Millington-Quirk 1960; Millington-Quirk 1961; Elberling et al. 1994). In general, D_e reduces approximately two to three orders of magnitude by increasing saturation from 50% to 90% (Millington and Quirk 1960; Elberling et al. 1994). A reduction in D_e produces a corresponding reduction in the diffusive flux of O_2 (Eq. 5.8), and consequently, reduces O_2 within the pore space of mine waste reducing ARD potential as outlined in Eqs. 5.3 to 5.6.

5.2.2.3 Oxygen Consumption Rate

The rate change of O_2 concentration ($\partial C/\partial t$) with O_2 consumption can be computed using a modified version of Fick's second law:

$$\frac{\partial C}{\partial_t} = \frac{D_e}{\theta_{eq}} \bullet \frac{\partial^2 C}{\partial_z{}^2} - \frac{K_r}{\theta_{eq}} \bullet C$$

(5.10)

where K_r is a reaction (consumption) rate coefficient, and θ_{eq} is the equivalent porosity. The equivalent porosity can be calculated as,

$$\theta_{eq} = \theta_a + H \cdot \theta_w$$

(5.11)

where Henry's constant is typically assumed as $H \approx 0.03$. The K_r parameter in Eq. 5.10 depends on soil mineralogy, bacterial activity, mine waste pyrite content (i.e., mineralogy), and particle-size distribution (i.e., surface area) (Demers et al. 2009). The K_r parameter can be measured by monitoring the O_2 concentration in a closed chamber over time.

Empirical relationships can also be used to estimate K_r when O_2 consumption rate experiments are not available. The most commonly used empirical relationship for O_2 consumption rate in mine waste is presented by Collin (1987):

$$K_r = k \frac{6}{D_H}(1-n)C_{py} \tag{5.12}$$

where k is reactivity of pyrite with oxygen [1.58×10^{-2} $m^3(O_2)/m^2$(pyrite)yr], C_{py} is pyrite content (by mass), n is porosity, and D_H is equivalent particle-size diameter. The D_H can be calculated as

$$D_H = [1 + 1.17\log(C_u)]D_{10}$$

(5.13)

where C_u is coefficient of uniformity and D_{10} is the particle size at 10% passing on a PSD. Larger particle sizes typically have lower surface area and lower reactivity, which leads to larger D_H (Eq. 5.13) and lower K_r (Eq. 5.12).

5.3 Materials and Methods

5.3.1 Test Piles

The piles were constructed at the end of January 2017 at a mine in Central America. Plan view and cross-section schematics of the test piles are shown in Fig. 5.2. The piles were designed as truncated 5 m tall pyramids with 25 m base sides and flat 5 m × 5 m top surfaces (Fig. 5.2). The WR pile was constructed with potentially acid generating (PAG) WR within the central core of the pile (5 m x 5 m x 5 m) and non-PAG WR was used on the side slopes. Non-PAG WR on the side slopes supported vegetative growth during the experiment, whereas vegetation never established on the PAG WR placed in the central core of the WR pile. The GW pile was constructed with GW prepared to a target mixture ratio of 0.43 (R = dry mass of WR / dry mass of tailings), which was approximately 2/3 tailings and 1/3 WR.

GeoWaste was prepared with filtered tailings. All materials were mixed on site using an excavator prior to placement. GeoWaste for the side slopes of the test pile (i.e., non-PAG) was placed using an excavator to create a 5 m × 5 m ring to support the central core. GeoWaste prepared with PAG WR for the central core was placed via dropping the mixture from a height of 2 to 3 m using an excavator. This deposition process for the central core simulated the anticipated full-scale GW placement process via disposal at the end of a conveyor system. The WR test pile was constructed with compacted non-PAG WR on the side slopes and PAG WR dropped and pushed in-place in the central core via a dozer. Thus, a higher level of compaction was used to prepare the central core of the WR pile as compared to the GW pile.

Each pile was instrumented with four layers of sensors, and each layer contained five sets of sensors, one set in the center and four sets positioned approximately 2-m radially from the center on each side of the piles (Fig. 5.2). Each sensor set contained (i) a TDR-315L Acclima sensor to measure volumetric water content, and (ii) a SO-110 Apogee sensor to measure oxygen concentration. All sensors from a given pile were connected to a CR-1000

Campbell Scientific datalogger interfaced with an AM 16/32B Campbell Scientific multiplexer. A detail description of sensors and data loggers were provided in Chapter 2. The instrumentation stations had a solar panel that provided excitation voltage for the sensors and power to run the datalogger. Each sensor was measured every 2 hr; however, daily averages were computed for each sensor to assess temporal trends for the 26-month study.

5.3.2 Vegetation Data

Vegetation data was needed to compute the transpiration fraction of evapotranspiration for hydrologic modeling. Parameters required for modeling vegetation are leaf area index (LAI) and root density. Root density is the root mass relative to soil mass as a function of depth. Piles were not seeded and no vegetation was reported on the central core of the WR pile for the entire duration of the pile experiment; however, vegetation did establish on the GW pile. Leaf area index was not measured, but was estimated using a sequence of photos of the surface of the GW pile. Vegetation on the GW pile ranged between short grasses to approximately 600-mm-tall bushes. A maximum LAI = 0.9 was estimated via an assume vegetated surface cover fraction (SCF) of 35% and the expressed SCF = [1 - exp(-k_{ext}×LAI)] (Allen 1998).

Root density samples were collected from three locations on the GW pile that had dense, average, and scattered vegetation as shown in Fig. 5.3. Samples were collected every 0.1 m from the surface to 1.0 m deep at each sampling location. Each sample was soaked for at least 48 h in the laboratory such that the majority of the roots floated to the surface and were collected (Albright et al. 2010). Profiles of root density (i.e., dry mass of root / dry mass of soil) and normalized root density are shown in Figs. 5.3d and 5.3e. Root density profiles indicate that vegetation sample 2 (V2) contained considerably more roots relative to samples at locations 1 and 3 (V1 and V3 in Fig. 5.3). Normalized root density was obtained by dividing root density at each depth by the maximum root density of the sample, which occurred in the first 0.1-m-deep interval of samples (Benson and Bareither 2012). HYDRUS require a triangular distribution where the maximum root density is at the surface and the root density decreases linearly up to a certain depth. Based on the normalized root density profile (Fig. 5.1e), the maximum root density was considered as 0.5-m deep and root distribution approximated by dashed line in Fig. 5.1e. Although numerical modeling was conducted with root distribution up to 0.5 m, minor roots were observed up to 3.0 m deep in the GW pile during decommissioning after 26 months.

5.3.3 Meteorological Data

The pile experiment began on 31 January 2017 (t = 0 d) and continued until 18 March 2019 (t = 778 d). Precipitation, temperature, relative humidity, solar radiation, and wind speed were monitored at a weather station located approximately 12 km northwest of the piles in similar meteorological conditions. A summary of monthly average meteorological (MET) data for the duration of the pile experiment is in Table 5.1. Also included in Table 5.1 are monthly irrigation applied to the surfaces of the GW and WR piles during the first months of the experiments. Daily average wind speed, relative humidity, temperature, and solar radiation for the duration of the pile experiment are shown in Fig. 5.4. In general, average relative humidity exceeded 50% and the average daily temperature ranged between 10 °C and 25 °C.

Daily PET and daily precipitation are needed as input in HYDRUS to compute water added and removed from the simulated system. The PET was calculated via the Penman-Monteith equation (Penman 1984) using site-specific solar radiation, wind speed, minimum and maximum temperature, relative humidity, latitude and altitude of the site, and albedo. Albedo was calculated using Eq. 5.2 independently for the GW and WR piles. Albedo was set at 0.38 for that WR pile since there was no vegetation (LAI = 0).

Pan evaporation measured at the weather station was compared to PET calculated based on the Penman-Monteith equation to validate PET estimates. Past studies have documented that pan evaporation typically is larger than PET. Kohler et al. (1959) proposed the following equation to correct PET based on pan evaporation and relative humidity:

$$PET = [0.56 + (0.00275 \times RH)] \times Evap_{pan}$$

(5.15)

where RH is relative humidity and $Evap_{pan}$ is pan evaporation.

A comparison of cumulative pan evaporation, corrected pan evaporation, and computed PET based on the Penman-Monteith equation is shown in Fig. 5.5. Potential evapotranspiration based on Penman-Monteith equation was 6.5% larger than corrected pan evapotranspiration.

Potential evapotranspiration computed via Penman-Monteith was used as input in HYDRUS. HYDRUS 2D requires potential evaporation (PE) and potential transpiration (PT) input separately. Considering that vegetation did not establish on the WR pile, calculated PET was set as PE and PT was set to zero. The PET for the GW pile was modified Allen (1998) to divide PET into PE and PT components

$$PT = PET \times [1 - \exp(-k_{ext} \times LAI)]$$

(5.16)

$$PE = PET \times [\exp(-k_{ext} \times LAI)]$$

(5.17)

where the expression [1 - exp($-k_{ext}$×LAI)] is surface cover fraction and relates to the percentage of the ground surface covered by vegetation. Based on the observations on the surface of GW pile, SCF was 35%.

Monthly precipitation and irrigation as well as cumulative precipitation plus irrigation for the GW and WR piles are shown in Fig. 5.6. Total precipitation during the pile experiment was 1620 mm and the ratio of precipitation to PET (P/PET) was approximately 0.6. Total precipitation and irrigation were 2671 mm for the GW pile and 2655 mm for the WR piles. The total precipitation plus irrigation over PET was approximately 1.0.

5.3.4 Mine Waste Parameters

Hydraulic parameters required for numerical modeling include parameters describing the soil water characteristic curve (SWCC) and saturated hydraulic conductivity (*k*). The SWCC was approximated the van Genuchten equation (van Genucthen 1980), which includes the following parameters: saturated volumetric water content (θ_s), residual volumetric water content (θ_r), and fitting parameters α and *n*. The θ_s of the GW and WR piles were obtained from in situ density samples. The θ_r for GW was obtained from laboratory tests on tailings, and θ_r for WR was obtained from Rossetta based on pedotransfer function (USDA 2008).

A summary of the numerical models completed for this study is in Table 5.2. Multiple scenarios were considered for SWCC parameters α and *n*, and *k*, which led to two unique models for the WR pile and six unique models for the GW pile. Models developed for the WR pile were Model WR1, which incorporated hydraulic parameters obtained via an inverse solution of infiltration during a sealed double ring infiltrometer (SDRI) test at the end of experiment (see Chapter 4). Model WR2 incorporated *k* obtained analytically from the SDRI test and SWCC parameters were obtained via inverse solution of infiltration during the SDRI test (Chapter 4).

Models GW1, GW2, and GW3 were developed for the GW pile and included hydraulic parameters obtained via an SDRI test conducted at the end of the 26-month pile experiment (Chapter 2). Parameters α, *n*, and *k* in Model GW1 were obtained via inverse solution of the SDRI test when infiltration was constrained to the upper 2.0 m of the pile. Hydraulic parameters in Model GW2 included *k* determined analytically from the SDRI test, and α and *n* from an inverse solution; all parameters were relevant for infiltration constrained to the upper 2.0 m the pile. Parameters α, *n*, and *k* in Model GW3 were obtained from an inverse solution of the SDRI test that included infiltration for the entire pile. The SDRI experiment and inverse solutions are described in Chapters 3 and 4.

Model GW4 included estimates of α, *n*, and *k* from laboratory experiments (Gorakhki et al. 2018). The laboratory experiments were conducted on the same mine waste materials, but did not include soil structure within the GW that would develop during the duration of pile experiment. Also, GW piles constructed by dropping the mixed materials from height of 2-3 m, however, laboratory specimens were prepared using a compaction level. This difference can result in difference between pre structure of GW in laboratory specimens and field pile. Models GW5 and GW6 were developed to incorporate a transient change in soil hydraulic parameters from the laboratory-measured condition to in situ conditions. The transient change was assumed to occur during the first year of the pile experiment as a linear, monthly change from laboratory to in situ hydraulic parameters at the start of Year 2. In situ parameters for Model GW5 were determined for the upper 2.0 m of the pile (i.e., Model GW1), whereas in situ parameters for Model GW6 were determined for the entire pile (i.e., Model GW3). The transient change in hydraulic parameters in Models GW5 and GW6 is supported by findings in Benson et al. (2007), who report that α, *n*, and *k* of surficial soils used in earthen cover systems for waste containment changed during operation due to pedeogenesis.

5.3.5 Model Setup

HYDRUS 1D and 2D models included minimum and maximum time steps of 1×10^{-5} d and 5 d, respectively. The water content and pressure head tolerances were 0.001 and 0.01 m, respectively. The boundary conditions and observation nodes in the 1D and 2D analyses are shown in Fig. 5.7. In the 2D analysis, an atmospheric boundary condition was set for the 5-m-wide pile surface. Although side slopes of the pile were subjected to atmospheric interaction, they were simulated as no flux boundaries because they did not receive irrigation and separation of irrigation and precipitation was not possible. The base boundary condition was set as a seepage face because a gravel layer within a lysimeter underlined bothpiles. In

HYDRUS 1D, the top surface was set as atmospheric boundary the bottom as a seepage face. The initial condition in the 1D and 2D models was based on initial water content readings at the start of the pile experiments, which was an average of 12% in the GW pile and 9% in the WR pile.

A preliminary comparison between 1D and 2D simulations for the GW6 model was performed to assess any differences between water content profiles. Temporal changes in water content for the 26-month simulation were evaluated at four locations representative of each layer of sensor measurements corresponding to depths of 0.5 m, 2.0 m, 3.5 m, and 4.8 m from the pile surface. Furthermore, two observation points were identified in each layer in the 2D simulation: at the center of each layer and 2 m radially outward from the center (i.e., representative of where sensors were located in each layer, Fig. 5.1). A single (average) observation node was identified for each layer in 1D simulation. Water contents in the 1D simulation were within the range of water contents predicted for the two observation nodes in the 2D simulation, which implied similarity of hydrologic predictions between 1D and 2D simulations (discussed subsequently in more detail).

Similarity of 1D and 2D hydrologic predictions for the GW pile supported the use of gas-phase modeling in HYDRUS 1D. Although HYDRUS does not have direct capabilities to predict gas flow, the solute transport module in HYDRUS was parameterized to simulate gas flow because solute and gas transport in porous media follow Fick's first and second laws (Eqs. 5.8 and 5.11). Consumption of oxygen in the pore voids lowers the oxygen concentration within the pile. The difference between oxygen concentration in the pile and in the atmosphere results in oxygen flow from the atmosphere into the piles. Oxygen concentrations at the upper boundary and oxygen concentrations for initial conditions in the pore voids were set at atmospheric conditions. Pyrite content was approximately 1% in WR and 0.3% in the GW, which were converted to K_r = 0.3 and 0.1 d^{-1} for WR and GW, respectively (Eq. 5.13).

5.4 Results

5.4.1 Prediction of Volumetric Water Content

5.4.1.1 Hydrologic Model Comparison for the GeoWaste Pile

A comparison of predicted and measured volumetric water content (VWC) in the four layers of the GW pile is shown in Fig. 5.8. The measured VWCs plotted in Fig. 5.8 are averages of the five sensors in each layer. Predictions of VWC in Fig. 5.8 are shown for the six GW models (GW1 – GW6) summarized in Table 5.2. In general, all models predicted similar temporal fluctuations in VWC that were observed in VWCs measured during the experiment. Models GW1, GW2, and GW3 all considered hydraulic parameters that were representative of conditions at the end of the 26-month experiment. These hydraulic parameters led to under predictions of VWC relative to the other three models. Model GW4 included hydraulic parameters from laboratory specimens, and yielded consistent overpredictions of VWC relative to field measurements, which were also the highest VWCs among all models. Finally, Models GW5 and GW6 considered temporally changing hydraulic parameters from laboratory-based parameters at the onset of the model to in situ parameters at the start of Year 2. Volumetric water content predictions from GW5 and GW6 transition from predicted VWCs similar to GW4 in the first 150 d to VWC predictions more comparable to models that included in situ parameters (GW1, GW2, and GW3) until the end of the 26-month experiment duration.

During the first 120 d in Layer 1 (Fig. 5.8a), all models overpredicted peak VWC relative to the average measured VWC. The differences between predicted and measured VWC were attributed to (i) physical differences between the model and experiment and (ii) averaging the VWC measurements. Runoff and infiltration were not measured on the GW pile during the period of irrigation; however, ponded water was observed on top of the GW pile. The presence of ponded water could lead to evaporation prior to infiltration, which would correspond to lower measured VWC compared to predicted VWCs. Furthermore, HYDRUS does not simulate ponded water, and considering runoff was predicted to be zero in all models, all precipitation and irrigation water input in the model was simulated to infiltrate into the pile. This is because HYDRUS applied irrigation water uniformly during the day instead of applying irrigation in 30 minutes. The additional inflow simulated in the models explains the trend for higher predicted versus measured VWCs during the period of irrigation. Secondly, although measured VWC peaked on Day 90 at approximately 18%, this is the average of five measurements, whereas the maximum VWC measured during the first 120 d was 30% (central sensor). This higher measured VWC in the first 120 d agrees with the higher predicted VWC and suggests more appropriate comparisons between predicted and measured VWCs should include the range of measured VWCs within each layer.

The difference in hydraulic parameters used in the six GW models can be observed via the VWCs predicated for Layer 1 at the end of the irrigation period to the end of the experiment. Models GW1, GW2, and GW3 yielded VWC predictions that compared favorably with the average measured VWC at the end of irrigation (Fig. 5.8a). Subsequently from the start of the first wet season until the end of the experiment, these models generally under predicted VWC. The use hydraulic parameters based only on in situ conditions in Models GW1, GW2, and GW3 appears to limit higher moisture retention and slower seepage that would be simulated with laboratory parameters to lead to higher VWCs. For example, GW4 only incorporated laboratory-based hydraulic parameters, which included lower hydraulic conductivity and higher moisture retention characteristics (Table 5.1). Thus, the VWC in Layer 1 for GW4 is overpredicted at the start of the first wet season and for the remainder of the experiment. Finally, although VWC was overpredicted in Layer 1 at the end of irrigation for GW5 and GW6, the measured VWCs are accurately predicted for these two models towards the end of the first wet season.

Measured VWCs between Days 120 and 210 in Layer 1 only were based on one sensor located southwest of the pile center because the other four sensors were not functional during this time period. This sensor consistently recorded lower VWCs relative to the other four sensors during the entire experiment (Appendix I). Thus, measured VWCs in Layer 1 from Day 120 to Day 210 may not have represent the true average VWC for the GW pile.

The increasing and subsequently decreasing trends in measured VWC in Layer 1 from Day 210 to Day 425 were captured by all models. Models GW5 and GW6 predicted the magnitude and decreasing trend in VWC more effectively compared to the other four models. The more rapid reduction in VWC predicted with GW5 relative to GW6 was attributed to the modestly higher hydraulic conductivity used for Years 2 and 3 of the simulation (Table 5.2). Although Models GW1 through GW4 captured the temporal fluctuations in VWC in Layer 1 between 210 and 425 d, GW1, GW2, and GW3 consistently underpredicted VWC, whereas GW4 consistently overpredicted VWC (Fig. 5.8a). The measured VWC in Layer 1 increased with onset of the second wet season beginning on Day 500. All models predicted an increase in VWC at approximately the same time and all models except GW4 predicted VWCs that were comparable, but typically lower than the measured VWCs.

Comparison between measured and predicted VWC in Layer 2 of the GW pile is shown in Fig. 5.8b. Measured VWC in Layer 2 increased due to irrigation and precipitation approximately on Day 160 and reached a maximum of 21% on Day 300. Subsequently measured VWC decreased and then remained approximately constant between Day 500 and the end of the experiment. The wetting front was predicted to reach Layer 2 between 41 and 43 d for models GW1, GW2, and GW3, which was more than 100 d early relative to the measured increase in VWC. In contrast, the wetting front was predicted to reach Layer 2 on Day 178 for Model GW5 and on Day 160 for Model GW6. The predictions of arrival of the wetting front for GW5 and GW6, as well the subsequent increase in VWC measured in Layer 2 until the end of the first wet season, compared favorably with VWC measurements. However, the subsequent decrease in predicted VWC for GW5 and GW6 during the first dry season underpredicted the measured VWC. Finally, the wetting front was not predicted to arrive in Layer 2 in Model GW4, which implies that the use of only laboratory-based model parameters for the entire GW test pile throughout the entire experiment duration did not yield appropriate predictions of VWC.

Comparisons between measured and predicted VWC in Layers 3 and 4 of the GW test pile are shown in Figs. 5.8c and 5.8d, respectively. The measured response in VWC, temporal behavior of the predictions, and comparison between measured and predicted are similar for Layers 3 and 4. The measured VWC increased slightly from the start of the experiment to approximately the start of the second wet season, and then transitioned to a slow decreasing trend. The small fluctuations in measured VWC suggest that a wetting front similar to that observed via the increase in VWC in Layers 1 and 2 (Figs. 5.8a and 5.8b) did not reach Layers 3 and 4 in the GW test pile. The predicted increase in VWC that occurs around 40 to 50 d in Layers 3 and 4 based on Models GW1, GW2, and GW3 corresponds to arrival of wetting front that never developed. This predicted response suggests the hydraulic parameters used in models GW1, GW2, and GW3 include a hydraulic conductivity that was too high and/or moisture retention parameters do not promote enough retention to restrict downward water migration. Thus, the use of hydraulic parameters based on in situ measurements representative of conditions after 26 months do not yield accurate predictions of moisture movement in Layers 3 and 4 during the first 200 d of the pile experiment.

The arrival of a wetting front to Layers 3 and 4 was also predicted via Models GW5 and GW6; however, arrival occurred after 300 d and did not yield as high of a peak predicted VWC. Finally, Model GW4 predicted that the VWC in Layers 3 and 4 would not fluctuate during the entire experiment. Comparing measured VWC in Layers 3 and 4 to the more reasonable predictions observed in Models GW4, GW5, and GW6, the actual hydraulic response of the deeper layers of the GW pile (i.e., Layers 3 and 4) would appear to fall somewhere within the range of hydraulic parameters measured in the laboratory and in situ.

Differences between measured and predicted VWC in Layers 3 and 4 could be due a number of factors. First, during pile decommissioning roots were observed up to 3 m deep in the pile, whereas roots were not simulated to this depth in any of the models. The presence of roots between 0.5 m (max extent assumed in model) and 3 m can remove water from within the pile, which can decrease hydraulic conductivity and prevent a wetting front from developing and ultimately reaching Layers 3 and 4. Secondly, GW in the vicinity of Layers 3 and 4 would have less influence from pedeogenesis compared to the top half of the pile based on observations during SDRI experiment. The limited development or absence of pedogenesis at depth would lead to a lower hydraulic conductivity and higher water retention in Layers 3 and 4, whereas the pile was simulated as a homogeneous material in the models.

5.4.1.2 Evaluation of Models GW5 and GW6

Predictions of VWC in the GW test pile based on Models GW5 and GW6 yielded the most appropriate comparisons to measured VWCs. Temporal predictions of VWC in Layers 1 and 2 of the GW pile based on Models GW5 and GW6 are reproduced in Fig. 5.9 to evaluate the two models more accurately. Measured VWCs in Fig. 5.9 are plotted based on the range of VWC from the five sensors in each layer of GW pile. In addition, a secondary prediction from Models GW5 and GW6 are included in Fig. 5.9 for a node located 2 m horizontally from the central node (i.e., similar to the location of the other VWC sensors). Thus, plotting the range of measured VWC and including a second prediction allows a more robust comparison considering that measured and predicted VWCs vary spatially within the pile. Finally, predicted VWCs for Models GW5 and GW6 only are compared for Layers 1 and 2 because more pronounced temporal fluctuations in measured VWC were observed in these layers relative to Layers 3 and 4.

The range of predicted VWC for Layer 1 in the GW pile via Models GW5 and GW6 compared to measured VWC overlap during the majority of the 26-month experiment with exception of two periods. First, the predicted peak VWC in Models GW5 and GW6 were larger than measured VWCs between Days 90 and 120. The lower measured VWCs were attributed to not all applied water via irrigation infiltrating due to ponding of water on top of the GW pile. Second, measured VWCs during the dry seasons (400 d < t < 480 d; 650 d < t < 777 d) were larger than predicted VWCs from Models GW5 and GW6. The lower predicted VWCs in Models GW5 and GW6 may be due to a higher water retention of the GW pile in comparison with the modeled parameters.

Comparison between predicted and measured VWCs in Layer 2 of the GW pile show excellent agreement during the first 300 d of the experiment (Fig. 5.9b). However, the hydrologic models predicted a much more rapid reduction in VWC starting at the end of the first wet season that corresponded with a consistent underprediction of VWC compared to the measured VWC. The higher measured VWC and smaller decrease measured during the first dry season may be attributed to the lower water retention of the modeled material compared with the actual GW pile.

Between these models, GW6 provided a better prediction that GW5. In both Layers 1 and 2, GW6 suggested a closer prediction of VWC to the measured values at t > 320 days. Additionally, since models considered the whole pile as a single material, the properties at the end of the GW6 model are more representative of the average pile. The properties at the end of the GW6 model, were obtained while the wetting front was in the lower half of the pile (Table 5.2).

5.4.1.3 Hydrologic Model Comparison for the Waste Rock Pile

A comparison of measured and predicted VWC in the four layers of the WR pile is shown in Fig. 5.10. Volumetric water content measurements in the WR pile only were available for two periods: (i) 0 to 120 d and (ii) 210 to 480 d. With exception of these two periods, VWC measurements were not recorded (sensors failed). In Layers 1 and 2, the two numerical models (WR1 and WR2) both over predicted VWC during the first period (0-120 d) and under predicted VWC during the second period (210-480 d). The models similarly overpredicted VWC in Layers

3 and 4 during the first period of measured data (Fig. 5.10c, 5.10d). Although the magnitude of VWCs predicted for Layers 3 and 4 at the start of the second period measured data (Day 210) were comparable, both Models WR1 and WR2 tended to overpredict VWC during the first dry season. Overall the predicted and measured VWCs in the WR pile do not compare well. A single reason for the lack of comparison between measured and predicted VWCs in the WR pile was not identified; however, some lines of evidence are presented to explain the differences.

The predicted VWC at the start of the experiment increased more rapidly compared to the measured VWC in all four layers in the WR pile. In situ hydraulic parameters used for the WR pile models were representative of the end of the experiment. Thus, the higher rate of predicted infiltration that led to higher VWCs as the start of the experiment indicate that end-state hydraulic parameters were not representative of hydraulic parameters in the WR at the start. Laboratory-measured hydraulic parameters for WR were not available; however, based on observations in the GW pile, laboratory-measured parameters for the WR likely would have generated improved predictions of VWC at the start of the experiment.

In situ hydraulic parameters of the WR at the end of the experiment appear to underestimate water retention of the WR pile. Measured VWCs suggest that water from irrigation required more time to infiltrate relative to the predictions, and also water remained within the WR at a much higher VWC relative to the predictions.

Temporal fluctuations and the general decreasing trends observed in measured VWCs for Layers 1 and 2 during the second period of data (210 to 480 d) compare well with the predicted trends from Models WR1 and WR2 (Figs. 5.10a and 5.10b). In spite of the large under prediction, there is agreement between the decreasing trends in both the measured and predicted VWCs. Similarity in the rate of reduction in predicted and measured VWC suggests that the hydraulic parameters were simulating reasonable moisture movement within and out of the top two layers of the WR pile from Day 210 to Day 480.

Predicted VWCs for Layers 3 and 4 in the WR pile disagree with measurements (Figs. 5.10c and 5.10d). The predicted VWCs increased with a wetting front developing during the irrigation period followed by a general decreasing trend representative of a material with low water retention potential and decent drainage. In contrast, measured VWCs in Layers 3 and 4 of the WR pile remained unchanged during the period of irrigation and then corresponded to a wetting front arriving to Layer 3 approximately on Day 250 and to Layer 4 between Days 250 and 400. Laboratory-measured parameters for the GW pile show closer comparison to VWC in Layers 3 and 4 compared to VWCs predicted via in situ parameters. Thus, predicting VWC in Layers 3 and 4 of the WR pile with laboratory-measured hydraulic parameters is hypothesized to lead to better predictions of VWC in these two layers.

5.4.2 Oxygen Concentration within the GW Test Pile

Oxygen concentration within mine waste depends on the consumption rate, which is a function of pyrite content and soil specific surface area (Eq. 5.14) and degree of saturation (Eq. 5.13). The O_2 concentration in the GW pile was computed considering K_r = 0.1 d^{-1} based on GW mineralogy and Eq. 5.14. Predictions of O_2 concentration from HYDRUS 1D are considered representative of 2D conditions considering similar predictions in VWC were obtained from HYDRUS 1D and HYDRUS 2D. Oxygen concentration only was predicted based on VWC prediction in Model GW6 because this model yielded the best overall prediction of hydrological behavior of the GW pile. Oxygen concentration models were not performed on the WR pile since the prediction of volumetric water content models were poor.

A comparison between predicted and measured O_2 concentrations in Layer 1 of the GW pile is shown in Fig. 5.11a. The predicted O_2 was in good agreement with measured O_2 during the entire duration of the GW pile experiment. The rate of reduction in O_2 was predicted faster than observed in the measurements. Oxygen concentration of 0% in Layer 1 was predicted on Day 90, whereas the measured O_2 reached 0% on Day 130. This difference was attributed to higher VWC predictions compared to measured VWCs immediately following the onset of irrigation (Fig. 5.8a). The measured O_2 fluctuated with VWC changes in Layer 1 between 130 and 300 d, and the model predicted the change in O_2 accurately during this period (Fig. 5.11a). Measured O_2 was approximately in the range of 16% to 18% from the first dry season until the end of the experiment. The two small decreases in measured O_2 (approximately Days 500 and 630) corresponded with predicted (and measured) increases in VWC (Fig. 5.8a). The predicted O_2 during this same time period was approximately 18%, and both localized decreases in measured O_2 were captured by the model.

A comparison between predicted and measured O_2 in Layer 2 of the GW pile is in Fig. 5.11b. The overall prediction of O_2 showed close agreement to temporal changes and magnitude of the measurements. Similar to Layer 1, predicted O_2 decreased at a faster rate relative to the measured O_2, and a concentration of 0% was predicted on Day 85, whereas an O_2 of 0% was measured on Day 125. Subsequent to this date, predicted and measured O_2 were in close agreement for the remainder of the experiment. Predicted and measured O_2 increased at the same rate between Day 250 and 440, and predictions typically were 2% higher than measured. The reduction in measured O_2 that coincided with the second wet season (Day ~ 500) and increase in VWC in Layer 1 (Fig. 5.8a), was effectively predicted by the model. After the second wet season, predicted O_2 was approximately 2% lower than measured O_2 until the end of the experiment.

Predicted and measured O_2 in Layers 3 and 4 of the GW pile are shown in Figs. 5.11c and 5.11d. Similar to Layers 1 and 2, the rate of reduction in O_2 in the model was faster than observed in the measurements for Layers 3 and 4. Prediction O_2 in both layers agreed well with measured O_2 up to Day 500. However, predicted O_2 in Layers 3 and 4 were consistently smaller than measured values from Day 500 to the end of the experiment. The higher O_2 measurements were attributed, in part, to a small air leak detected within the pipe network and cistern that were connected to the base lysimeter of the GW pile. Thus, higher measured O_2

may be attributed to atmospheric air entering the base lysimeter that potentially increased O_2 measured in Layers 3 and 4.

5.4.3 Long-Duration Hydrologic Modeling

Additional hydrologic models were conducted with the objective to evaluate long-term trends in saturation and O_2 concentrations in GW. During monitoring the piles, extreme irrigation was added to piles to simulate very wet years on records. The main goal of the long-duration hydrologic modeling is to understand how VWC and O_2 concentration profile change under long-term and natural climatic condition. Two models were created to predict VWC and O_2 in a GW pile that had the same dimensions as the pile experiment (Fig. 5.2). Precipitation data were available for the last 48 yr from a site approximately 25 km northwest of the mine site in a similar climatic region. The other meteorological data and pan evaporation required were not available for this same 48-yr period. Thus, MET data and PET from 2017 and 2018 (i.e., duration of the pile experiment) were repeated 24 times to pair with the available precipitation data needed for the long-term prediction. Vegetation parameters were simulated as measured (root density) and estimated (LAI) parameters representative of the GW pile after 26 months of operation.

The initial VWC distribution for the 48-yr model and hydrologic parameters for the model simulations were considered representative of in situ conditions measured at the end of the pule experiment (i.e., Model GW 2 or second year of Model GW6). The difference between two 48-yr models was the pyrite consumption rate: the first model used $K_r = 0.1$ d^{-1}, which was the O_2 consumption rate estimated for the GW used in this study, and the second model used $K_r = 0.3$ d^{-1}, which simulated GW with a greater pyrite content and higher ARD potential.

Results of the 48-yr simulations are shown in Fig. 5.12. The range of saturation is shown on the primary Y-axis as the shaded background, and the ranges of O_2 concentration simulated with $K_r = 0.1$ and $K_r = 0.3$ d^{-1} are shown on the secondary Y-axis. In the model with

$K_r = 0.1\ d^{-1}$, the average oxygen concentration stayed near atmospheric condition at a depth of 0.5 m into the pile (i.e., Fig. 5.12a), while the average O_2 dropped approximately to 1/2 , 1/3, and 1/4 of atmospheric concentrations at depths of 2.0 m, 3.5 m, and 4.8 m, respectively (Figs. 5.12b, 5.12c, and 5.12d). In the model with $K_r = 0.3\ d^{-1}$, the average O_2 dropped to approximately 2/3 of atmospheric conditions only 0.5 m into the pile (Fig. 5.12a), while the average O_2 was less than 1/4 of atmospheric conditions 2.0 m into the pile (Fig. 5.12b). The O_2 concentration in the pile at a specific depth anticipated to be a function of saturation degree in the top layer or the saturation degree of that depth. To evaluate this question, O_2 concentration versus saturation of the top layer for $K_r = 0.1$ and $0.3\ d^{-1}$ was plotted in Figs. 5.13 and O_2 versus saturation of the same layer for $K_r = 0.1$ and $0.3\ d^{-1}$ in Fig. 5.14. In general, a better relationship was observed between saturation degree of the top layer and O_2 concentration at varying depth (i.e., Figs. 5.13a and 5.13b) in compared with the case that saturation degree and O_2 concentration were compared at the same depths (Figs. 5.14a and 5.14b).

5.5 Conclusions

Volumetric water content (VWC) and oxygen concentration (O_2) profiles of GeoWaste (GW) and waste rock (WR) test piles were predicted in HYDRUS-1D and HYDRUS-2D and compared to 26-months of in situ monitoring data. Predictions included hydraulic parameters measured in field- and laboratory-scale experiments and incorporated site-specific climate and vegetation data. Comparisons were made between predicted and modeled VWC and O_2 at depths of 0.5 m, 2.0 m, 3.5 m, and 4.8 m. The following conclusions were drawn from this study.

- Close comparison between VWC predictions for the GW pile HYDRUS 1D and 2D indicated that HYDRUS 1D could predict water movement in the field-scale test piles with similar accuracy as HYDRUS 2D. This comparison supported the use of HYDRUS 1D to predict O_2 based on the solute flux module.

- Volumetric water content in the GW pile was overpredicted in all four layers when using laboratory-measured hydraulic parameters. In contrast, VWC predominantly was underpredicted via in situ hydraulic parameters measured at the end of monitoring (i.e., after 26 months of pile operation). Two models that incorporated a transient change from laboratory-measured to in situ measured hydraulic parameters yielded the best predictions of VWC in the GW pile.
- Predictions of volumetric water content in the WR pile consistently underpredicted measured VWCs and did not compare well. The inaccurate prediction was attributed to inaccuracy in estimating hydraulic parameters during the infiltration experiment.
- Predictions of O_2 for the GW pile were in close agreement with measured values throughout the entire 26-month experiment.
- HYDRUS can effectively be used to predict the water content and O_2 concentration profile of a GW pile. Validating HYDRUS can help to understand the volume of leachate and/or acid rock generation potential in the long-term or in extreme conditions in any field.
- A 48 year-long simulation on the GW pile suggested that oxygen concentrations can be reduced to approximately 1/3 atmospheric conditions at 4.8-m deep into the pile. In addition simulations completed with hypothetically higher pyrite content (i.e., 3X the content in the GW pile) suggest a decrease in oxygen concentration to 1/10 atmospheric conditions at 4.8-m deep.

Table 5.1. Summary of meteorological and irrigation data from February 2017 to March of 2019.

Month	Total Precipitation (mm)	Total Irrigation (WR Pile) (mm)	Total Irrigation (GW Pile) (mm)	Average Temperature (^{0}C)	Average Relative Humidity (%)	Average Solar Radiation (W/m^2)	Average Wind Speed (m/s)
Feb-17	0.5	45.1	68.9	19.4	51.9	12.5	1.93
Mar-17	7.9	638.4	474.3	18.2	60.2	13.3	1.87
Apr-17	120.4	347.9	492.72	19.9	58.2	13.0	1.82
May-17	137.0	10.9	16.05	21.0	70.2	13.2	1.46
Jun-17	221.0	0	0	19.4	81.7	14.7	1.04
Jul-17	69.3	0	0	18.1	75.9	14.5	1.51
Aug-17	74.4	0	0	19.0	76.0	11.7	1.31
Sep-17	156.7	0	0	19.1	84.2	11.4	0.94
Oct-17	88.1	0	0	18.7	80.1	12.9	1.23
Nov-17	13.7	0	0	17.0	72.4	12.4	1.46
Dec-17	11.9	0	0	16.1	70.3	13.5	1.50
Jan-18	14.0	0	0	15.1	68.2	13.2	1.70
Feb-18	0.0	0	0	16.0	69.4	16.5	2.03
Mar-18	3.8	0	0	19.4	51.7	13.4	1.89
Apr-18	38.9	0	0	18.9	64.8	12.8	1.65
May-18	113.0	0	0	20.2	69.4	16.3	1.67
Jun-18	213.4	0	0	18.8	78.4	13.7	1.28
Jul-18	8.4	0	0	18.2	67.5	18.8	1.69
Aug-18	85.1	0	0	19.0	66.2	17.0	1.83
Sep-18	77.7	0	0	19.4	74.6	15.3	1.37
Oct-18	136.1	0	0	18.5	78.4	11.4	1.18
Nov-18	27.7	0	0	18.0	71.5	13.9	1.45
Dec-18	0.3	0	0	16.7	68.8	12.8	1.50
Jan-19	0	0	0	13.1	69.5	13.2	1.50
Feb-19	0	0	0	13.9	68.8	16.5	1.50
Mar-19	0	0	0	14.5	65.8	13.5	1.51

Table 5.2. Summary of parameters used for variable models in GeoWaste and waste rock piles.

Model	Method			Parameters		
	α and *n*	*k* (m/s)	Wetting front	α (1/m)	*n*	*k* (m/s)
GW1	Inverse solution in infiltration experiment	Inverse solution in infiltration experiment	Upper 2.0 m	3.47	1.75	2.9×10^{-6}
GW2	Inverse solution in infiltration experiment	Sealed double ring infiltrometer	Upper 2.0 m	0.41	1.75	1.8×10^{-6}
GW3	Inverse solution in infiltration experiment	Inverse solution in infiltration experiment	Lower 2.7 m	0.38	1.74	7.2×10^{-7}
GW4	Laboratory measured	Laboratory measured	NA	0.68	1.25	1.4×10^{-8}
GW5	Year 1: GW4 to GW1 in 12 steps (monthly)	Year 1: GW4 to GW1 in 12 steps (monthly)	NA	0.68→3.47	1.25→1.75	$1.4\times10^{-8}\rightarrow2.9\times10^{-6}$
	Year 2 and 3: GW1	Year 2 and 3: GW1	NA	3.47	1.75	2.9×10^{-6}
GW6	Year 1: GW4 to GW2 in 12 steps (monthly)	Year 1: GW4 to GW2 in 12 steps (monthly)	NA	0.68→0.41	1.25→1.75	$1.4\times10^{-8}\rightarrow1.8\times10^{-6}$
	Year 2 and 3: GW2	Year 2 and 3: GW2	NA	0.41	1.75	1.8×10^{-6}
WR1	Inverse solution in infiltration experiment	Inverse solution in infiltration experiment	Lower half	0.51	2.22	2.6×10^{-6}
WR2	Inverse solution in infiltration experiment	Sealed double ring infiltrometer	Lower half	0.54	2.09	2.8×10^{-6}

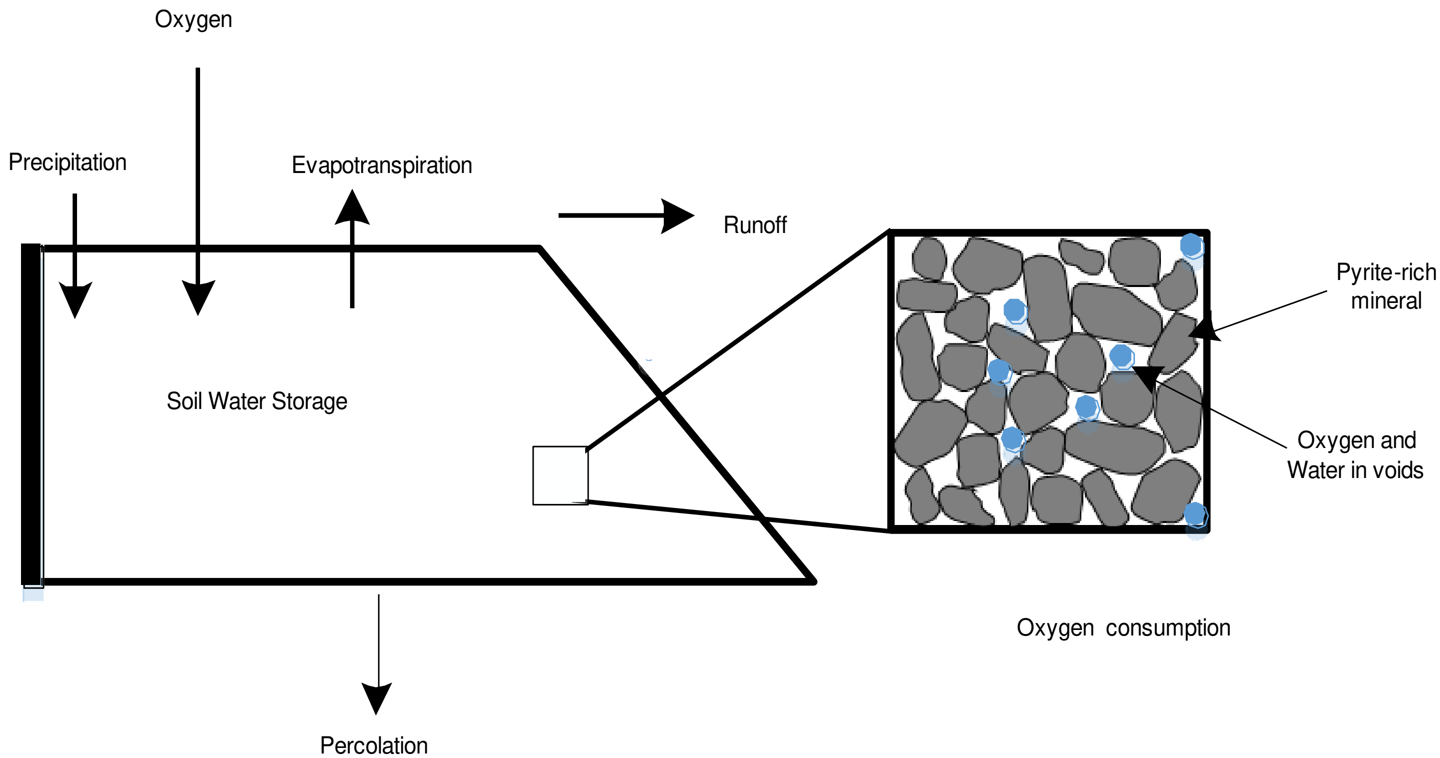

Fig. 5.1. Schematic of water and oxygen flow in a mine waste deposit.

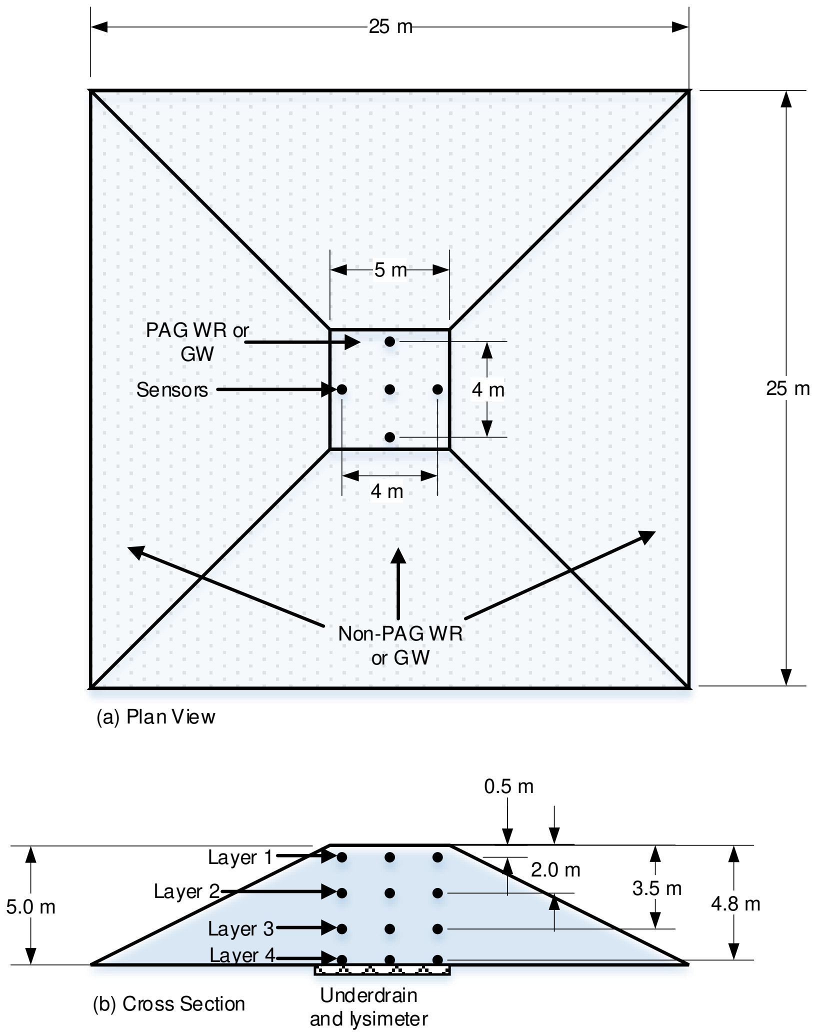

Fig. 5.2. Schematic of dimensions and sensor location for GeoWaste and waste rock piles: (a) plan view, and (b) cross sectional view.

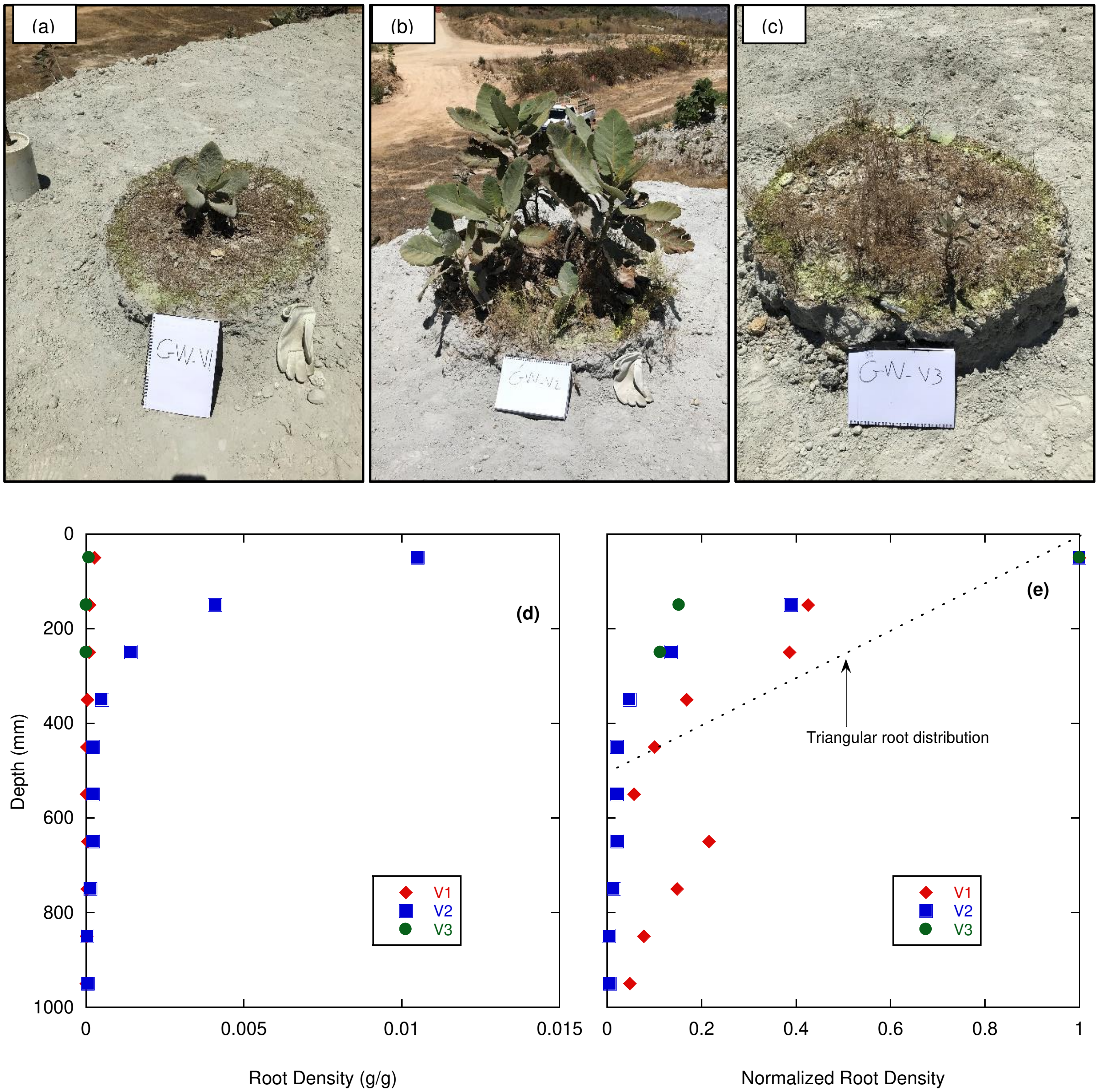

Fig. 5.3. Vegetation properties in the GeoWaste pile in three locations of V1 (average), V2 (dense), and V3 (sparse): (a), (b), and (c) pictures from sampling locations of V1, V2, and V3, respectively, (d) normalized root density (root density/maximum root density), (e) root density (mass of root over mass of soil).

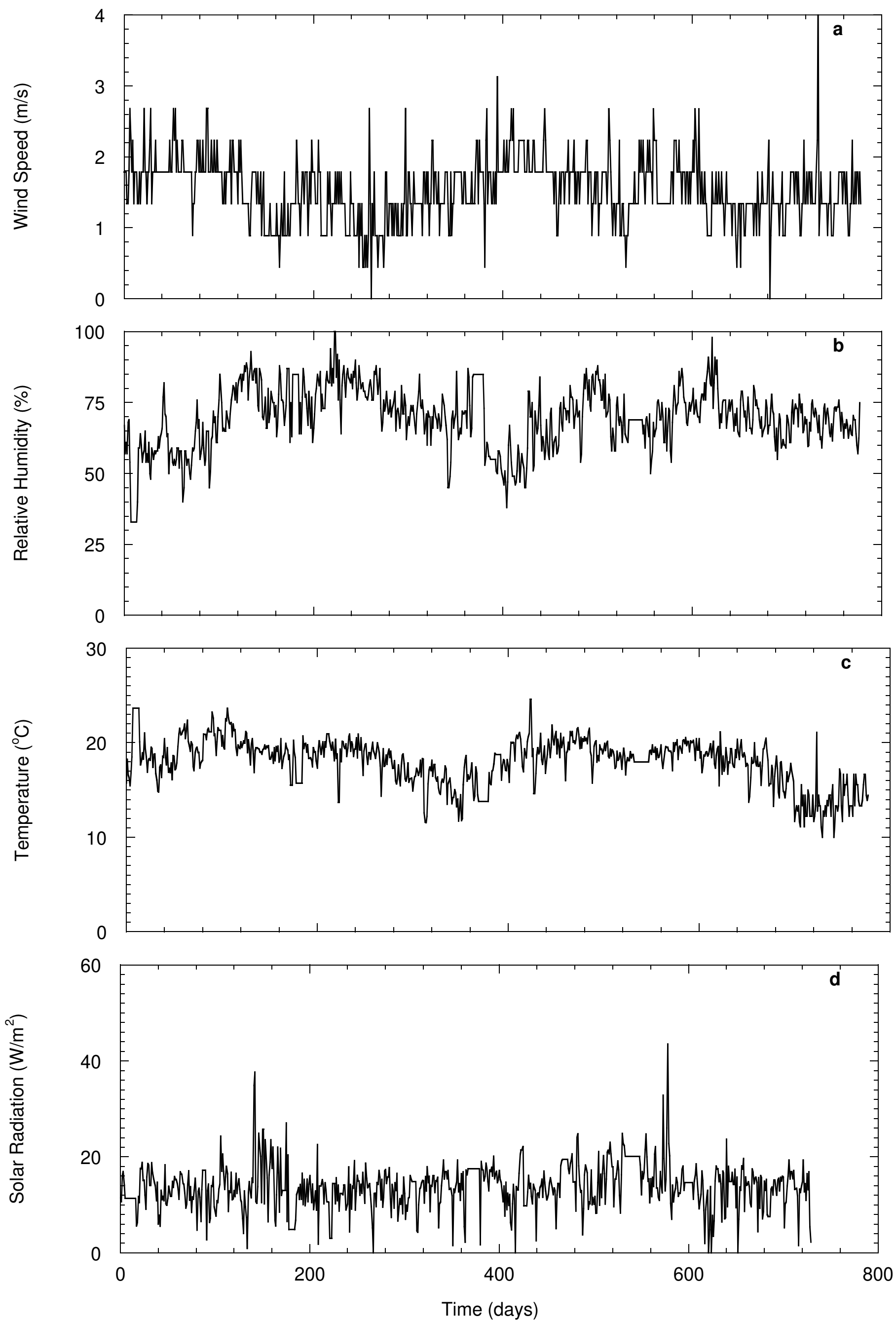

Fig. 5.4. Average daily wind speed, relative humidity, temperature, and solar radiation from February of 2017 to March of 2019.

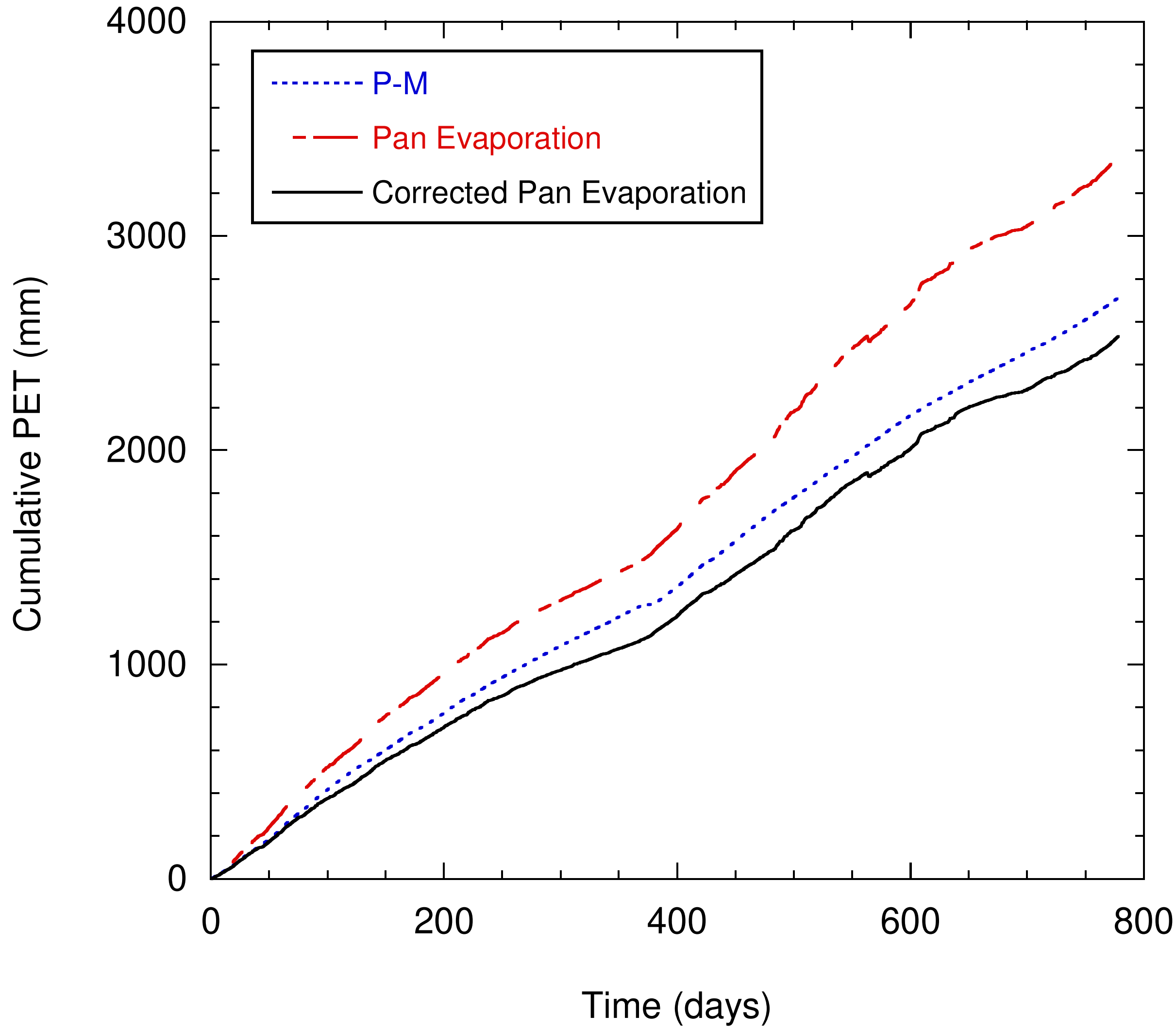

Fig. 5.5. Cumulative Potential evapotranspiration calculated based on Penman-Monteith equation (P-M), pan evaporation, and corrected pan evaporation from February of 2017 to March of 2019.

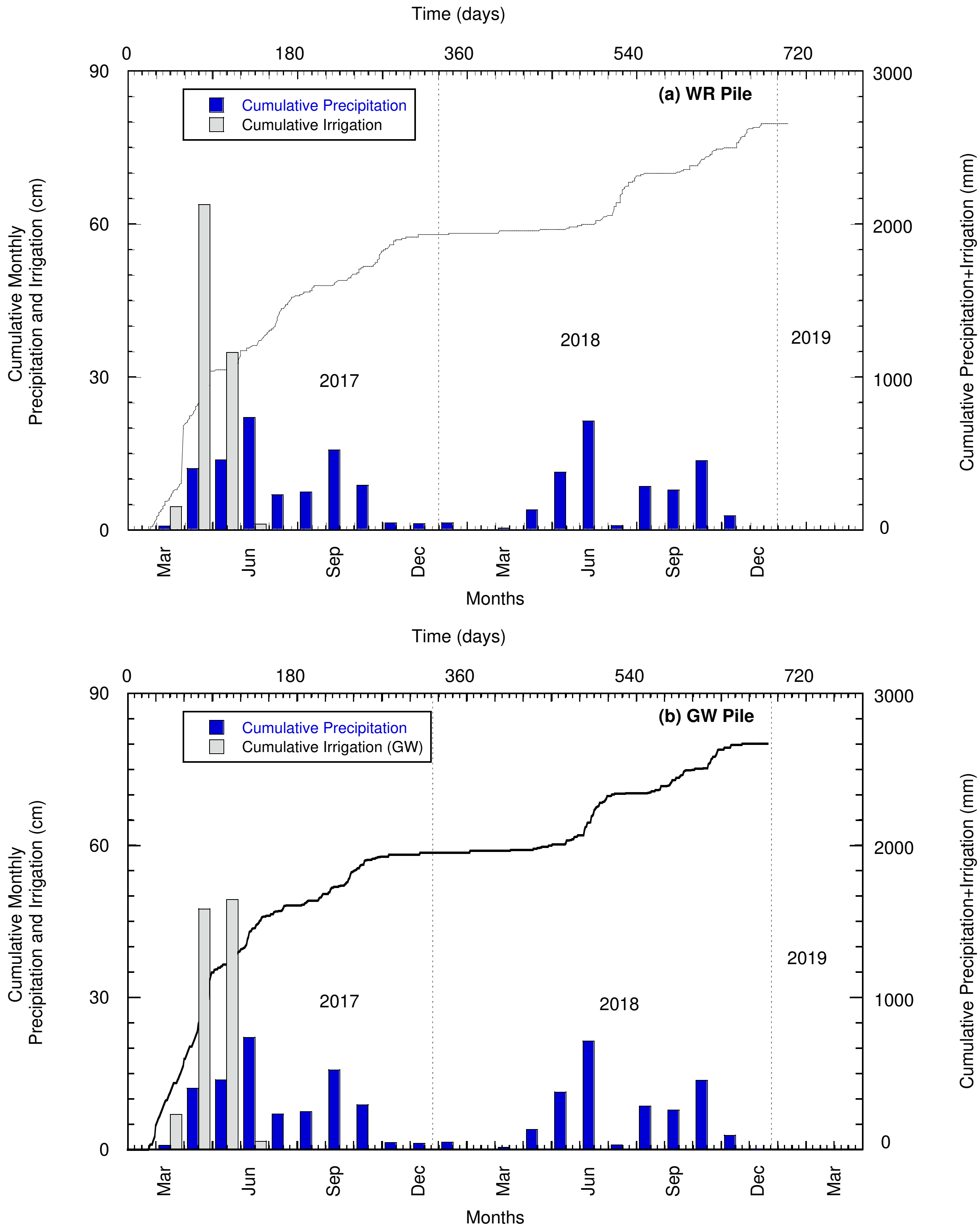

Fig. 5.6. Monthly total precipitation and irrigation and total cumulative precipitation and irrigation in the waste rock and GeoWaste pile from February of 2017 to March of 2019.

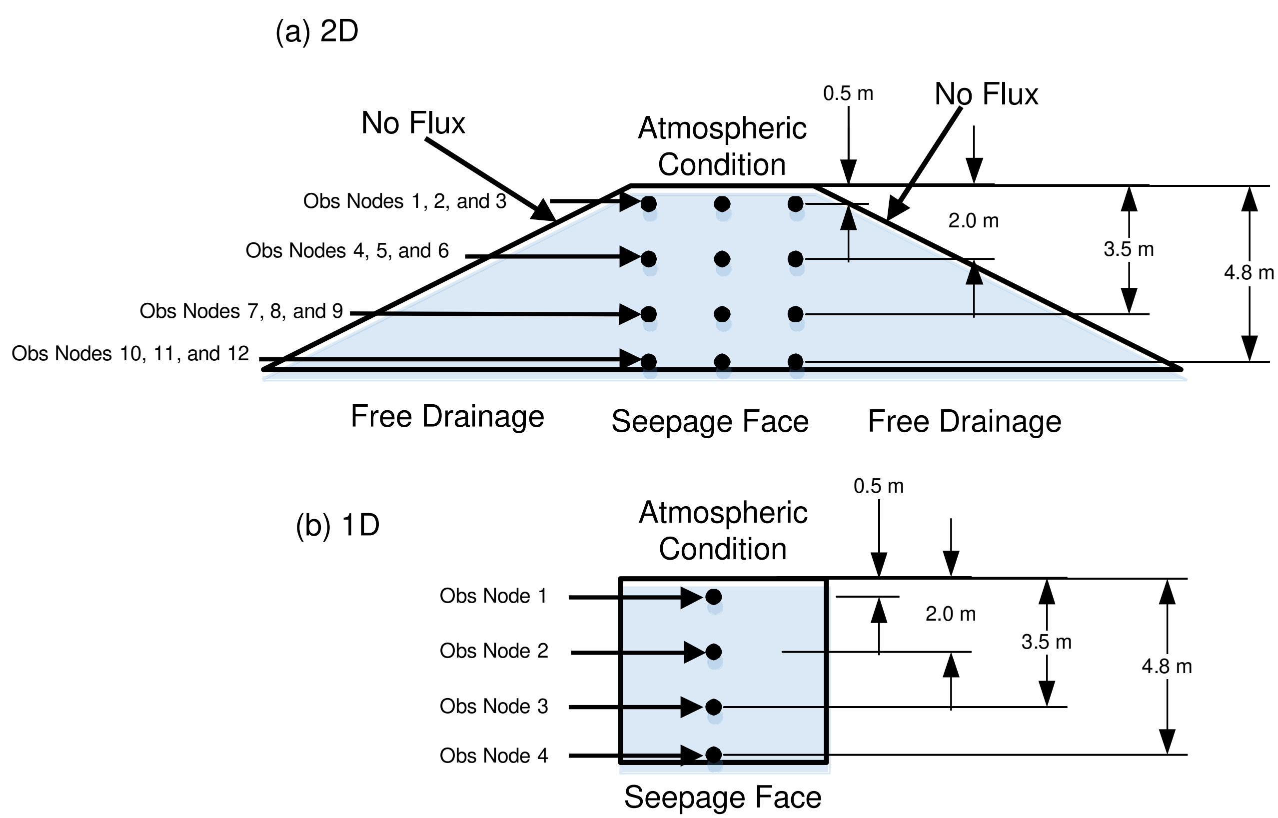

Fig. 5.7. Boundary conditions and observational nodes in HYDRUS: (i) 2D and (ii) 1D.

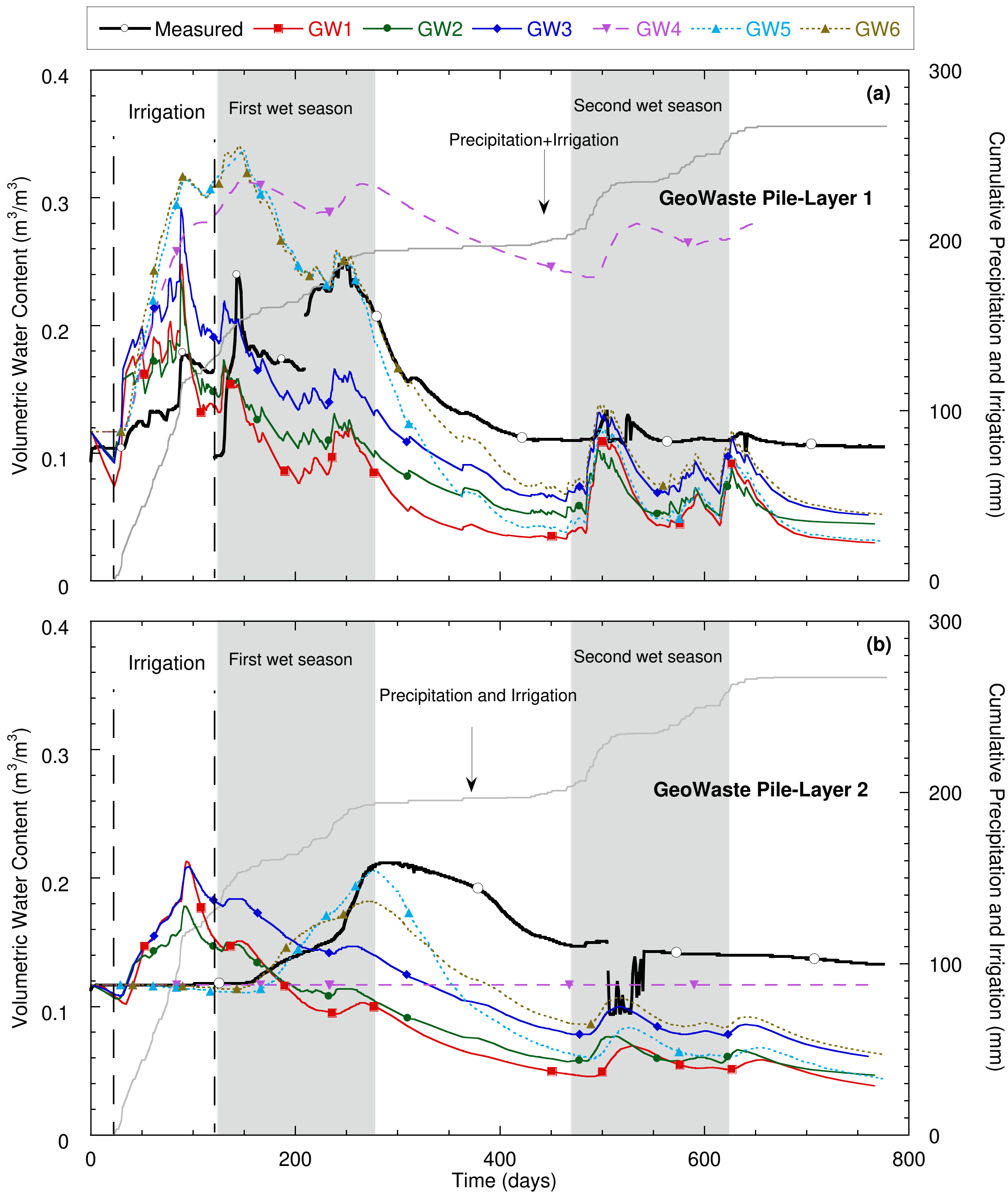

Fig. 5.8. Comparison between temporal volumetric water content of Models GW1-GW6 and measured values in GeoWaste pile in (a) Layer 1, and (b) Layer 2.

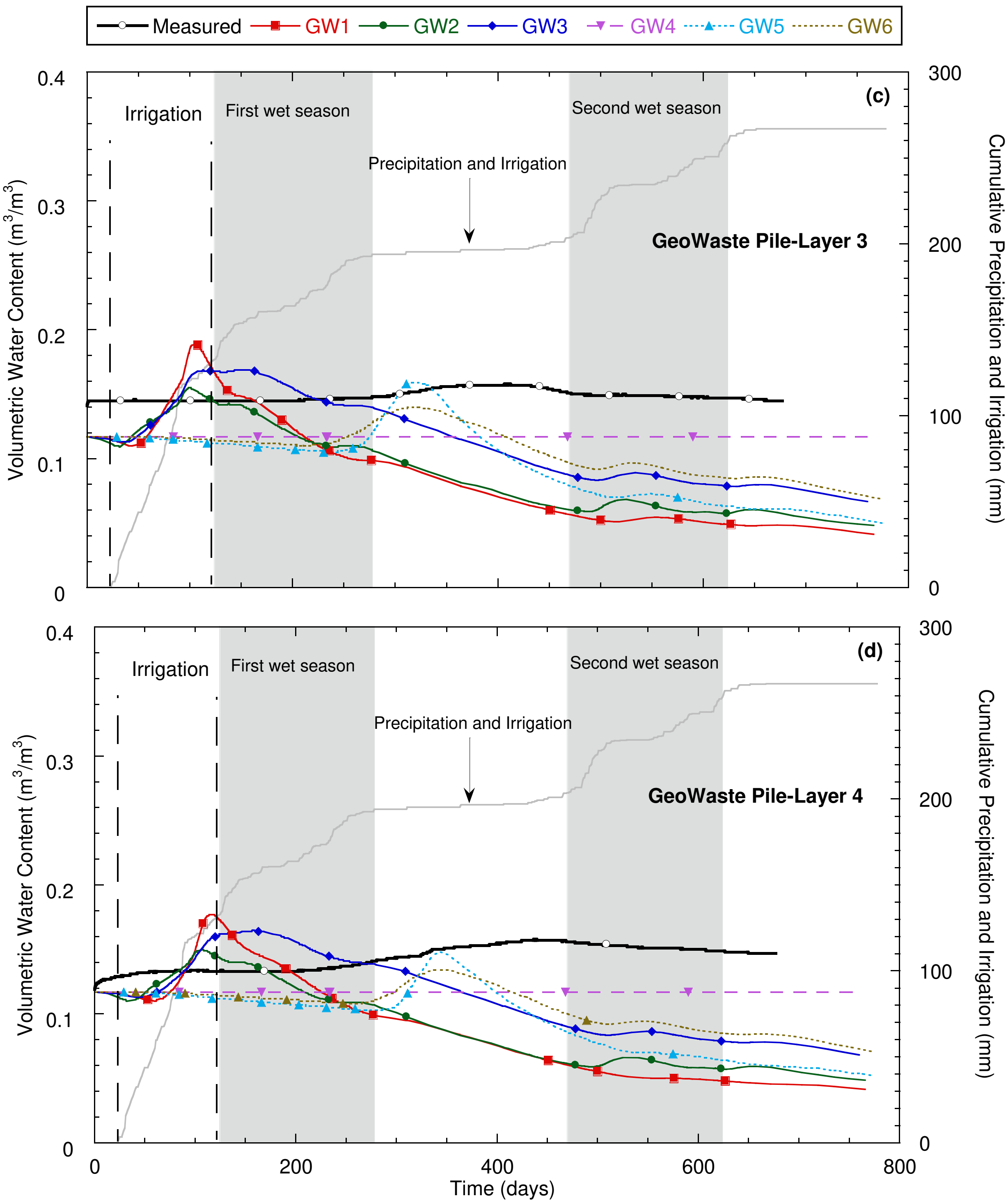

Fig. 5.8 Continued. Comparison between temporal volumetric water content of Models GW1-GW6 and measured values in GeoWaste pile in (c) Layer 3, and (b) Layer 4.

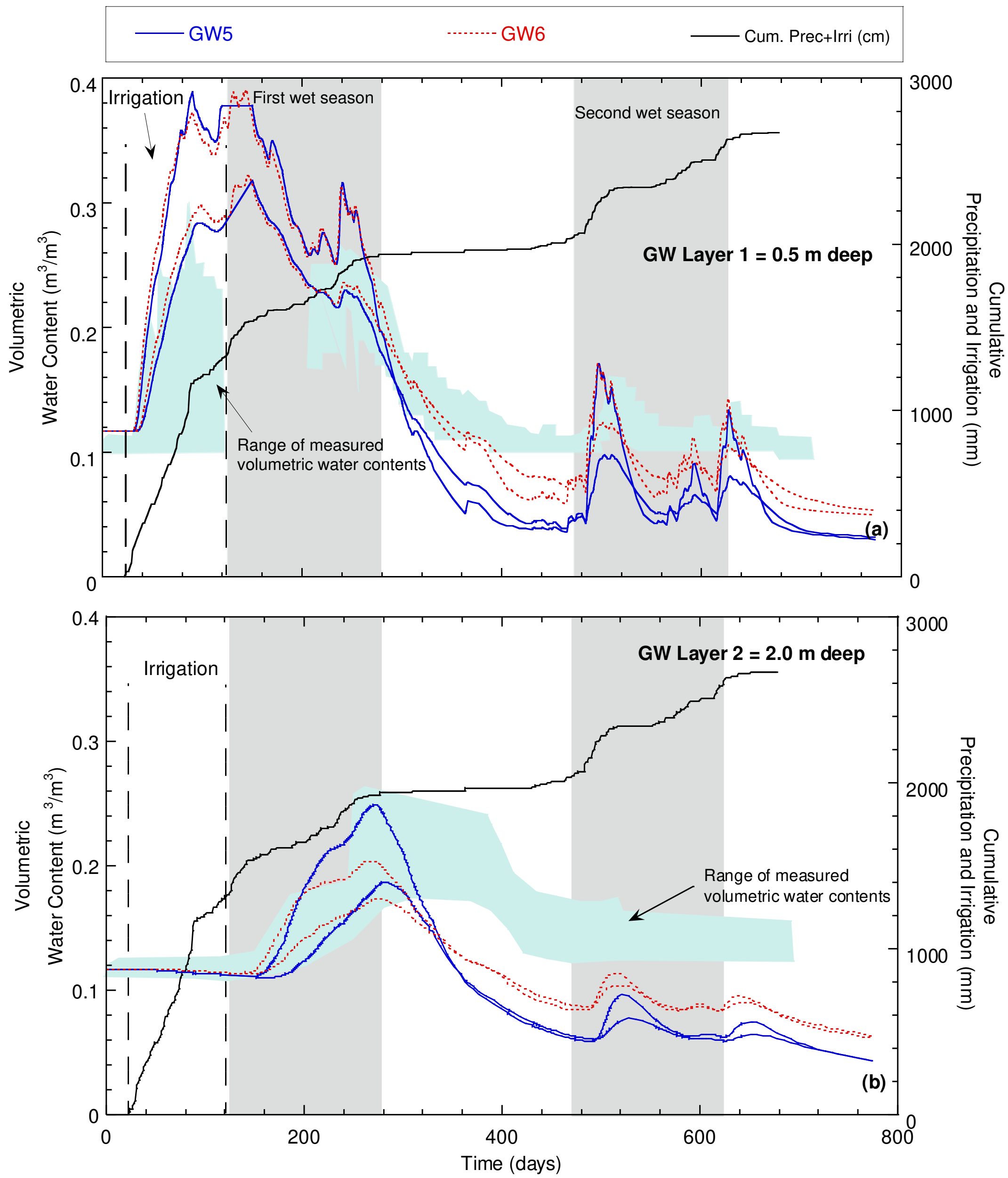

Fig. 5.9. Comparison between temporal volumetric water content in the Layer 1 measured and Models GW5 and GW6 as well as measured values in GeoWaste pile in (a) Layer 1, and (b) Layer 2.

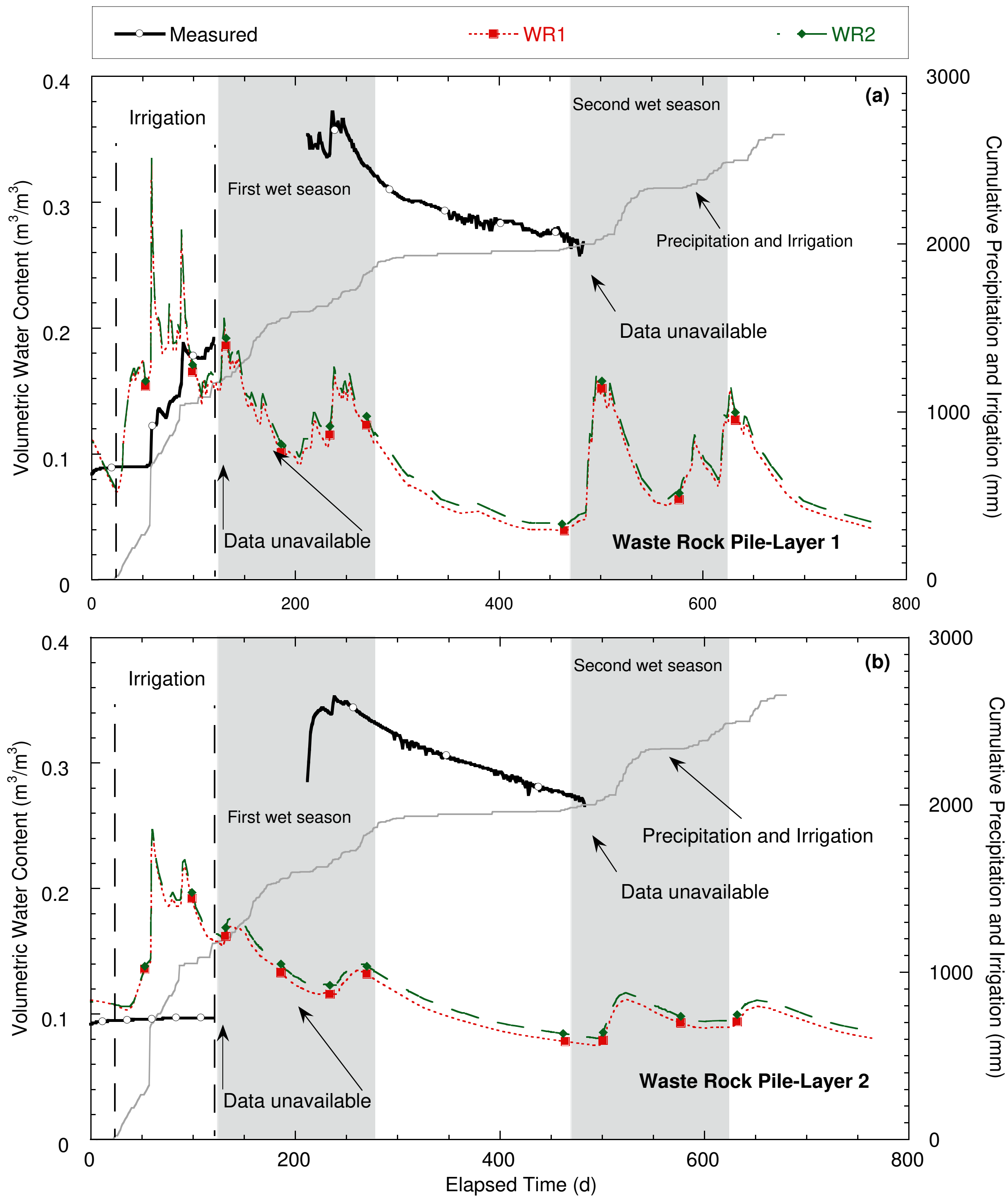

Fig. 5.10. Comparison between temporal volumetric water content of Models WR1 and WR2 and measured values in waste rock pile in (a) Layer 1, and (b) Layer 2.

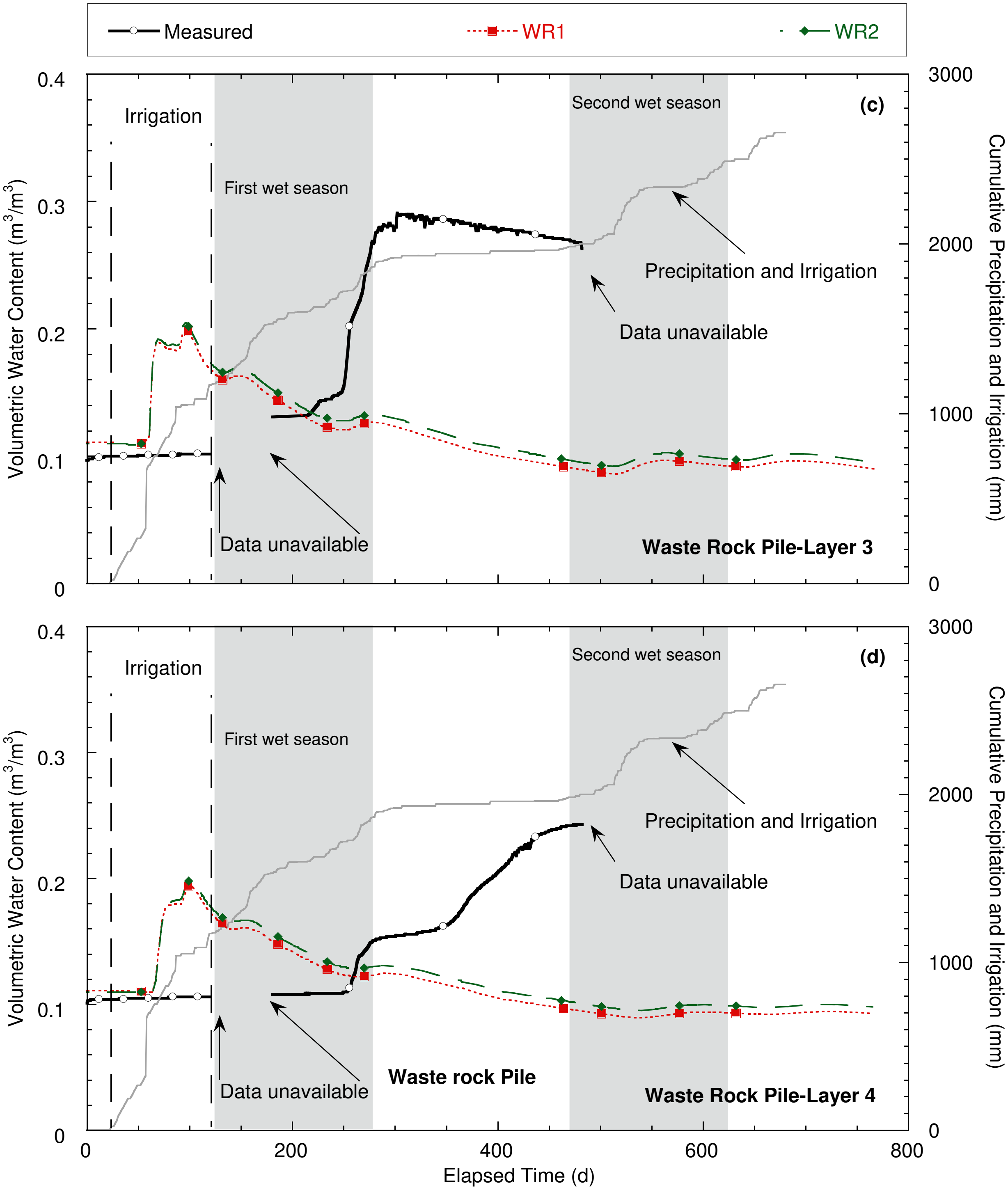

Fig. 5.10. Comparison between temporal volumetric water content of Models WR1 and WR2 and measured values in waste rock pile in (c) Layer 3, and (d) Layer 4.

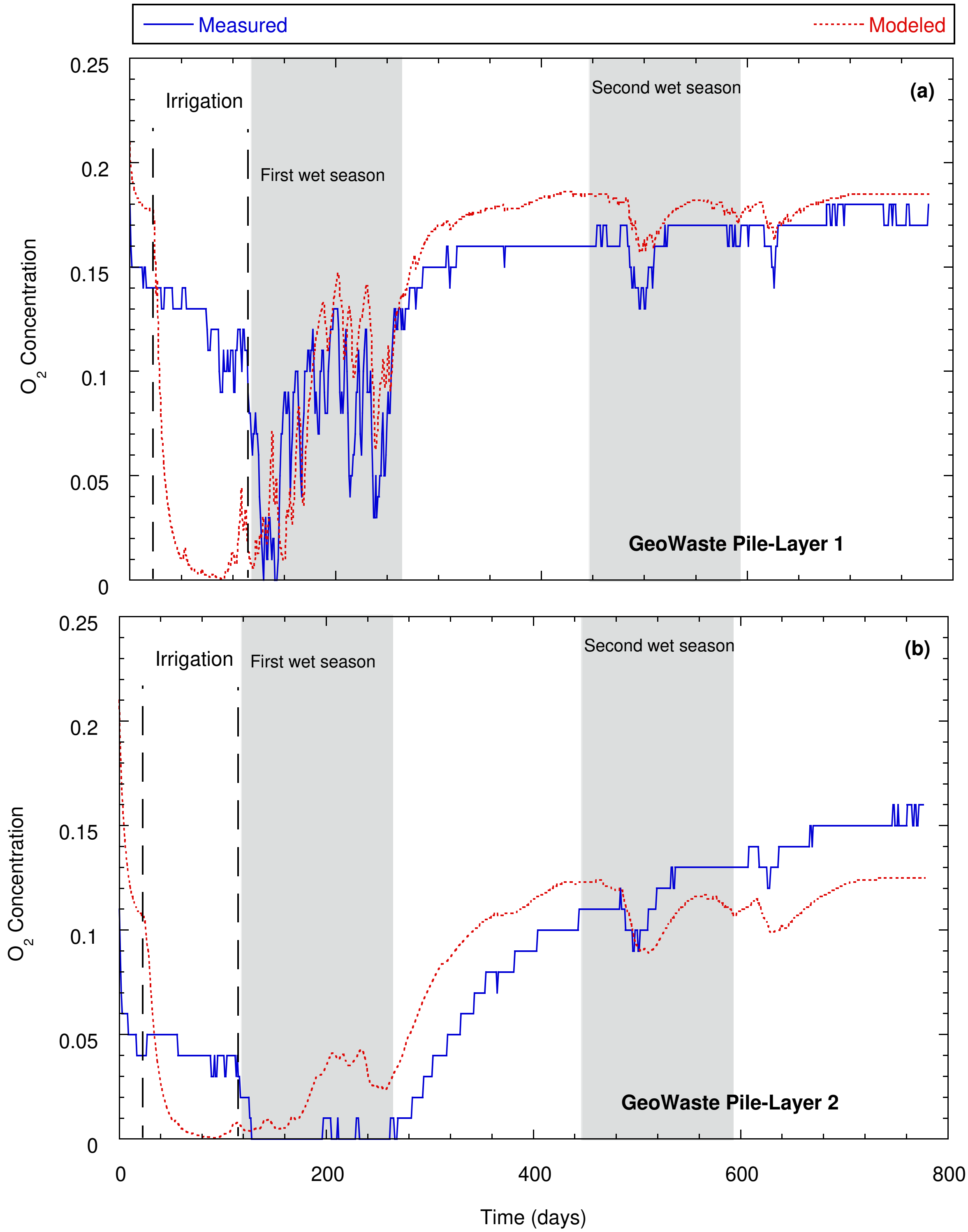

Fig. 5.11. Comparison between temporal oxygen concentration of Model GW6 and measured values in GeoWaste pile in (a) Layer 1, and (b) Layer 2.

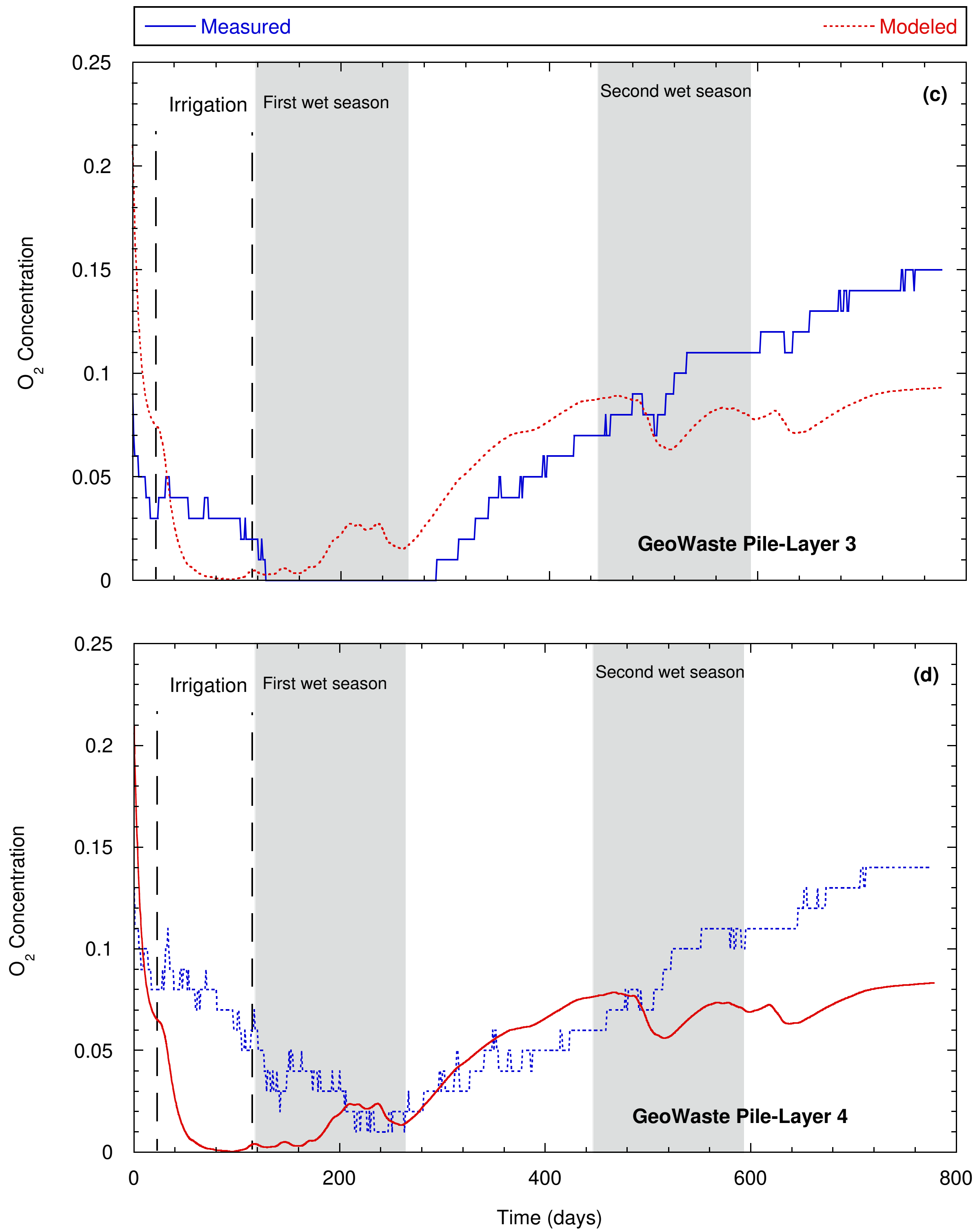

Fig. 5.11. Continue. Comparison between temporal oxygen concentration of Model GW6 and measured values in GeoWaste pile in (c) Layer 3, and (d) Layer 4.

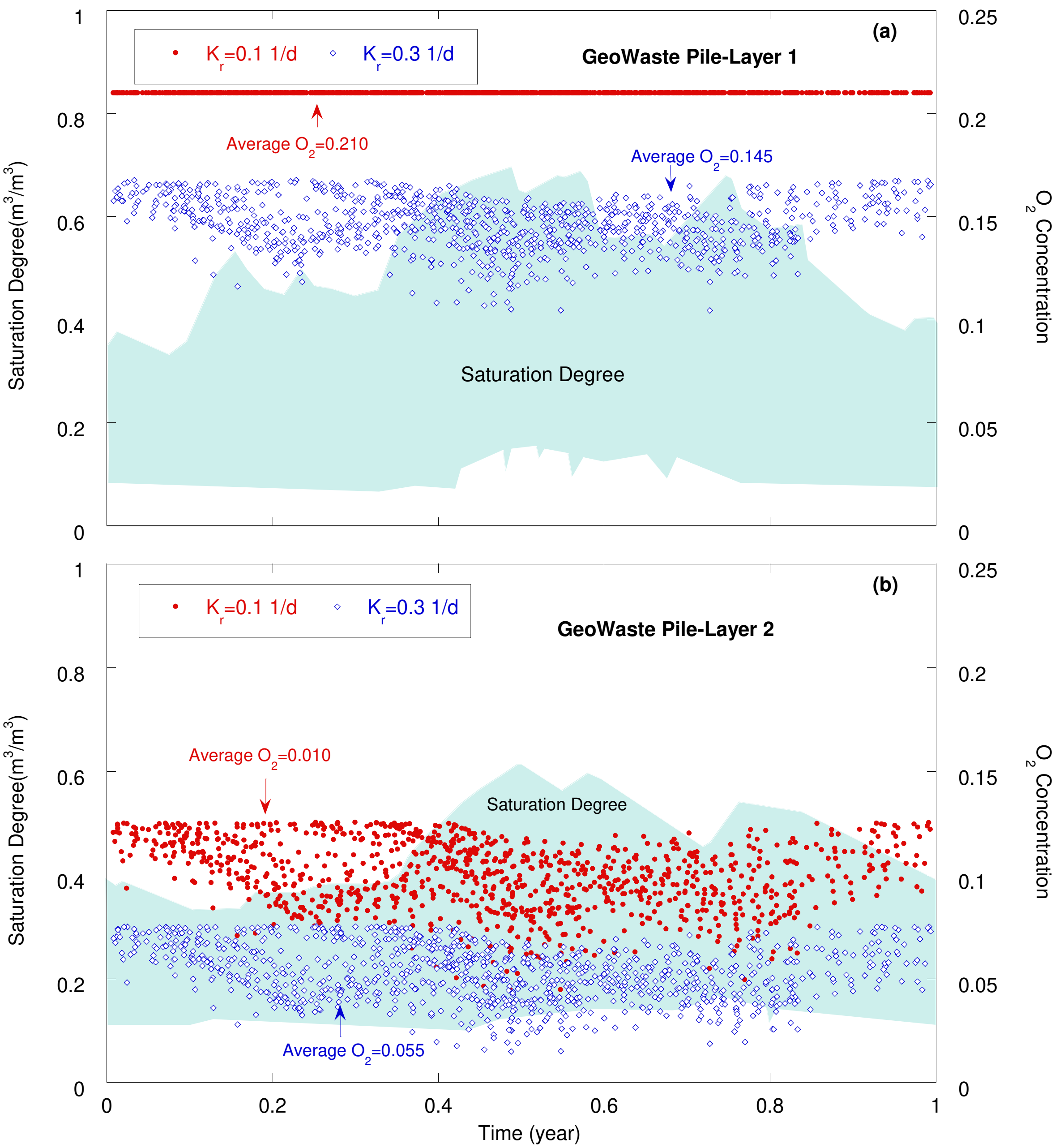

Fig. 5.12. Temporal relationship of saturation degree and oxygen concentration for a GeoWaste pile with K_r=0.1 and 0.3 d^{-1} at: (a) Layer 1 (0.5 m from the surface), (b) Layer 2 (2.0 m from the surface). The background is range of saturation degree.

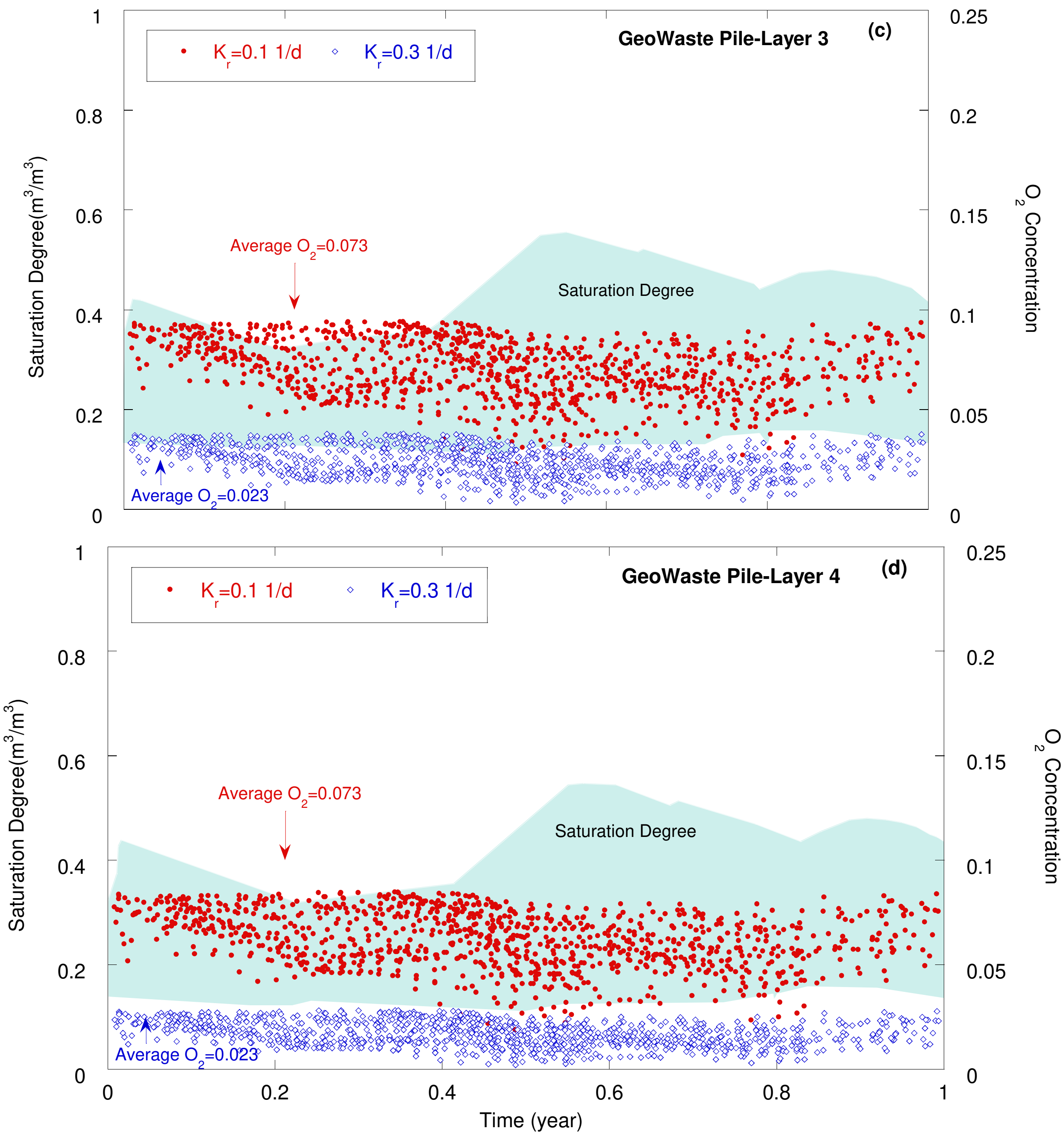

Fig. 5.12. Continue. Temporal relationship of saturation degree and oxygen concentration for a GeoWaste pile with K_r=0.1 and 0.3 d^{-1} at: (c) Layer 3 (3.5 m from the surface), (d) Layer 4 (4.8 m from the surface). The background is range of saturation degree.

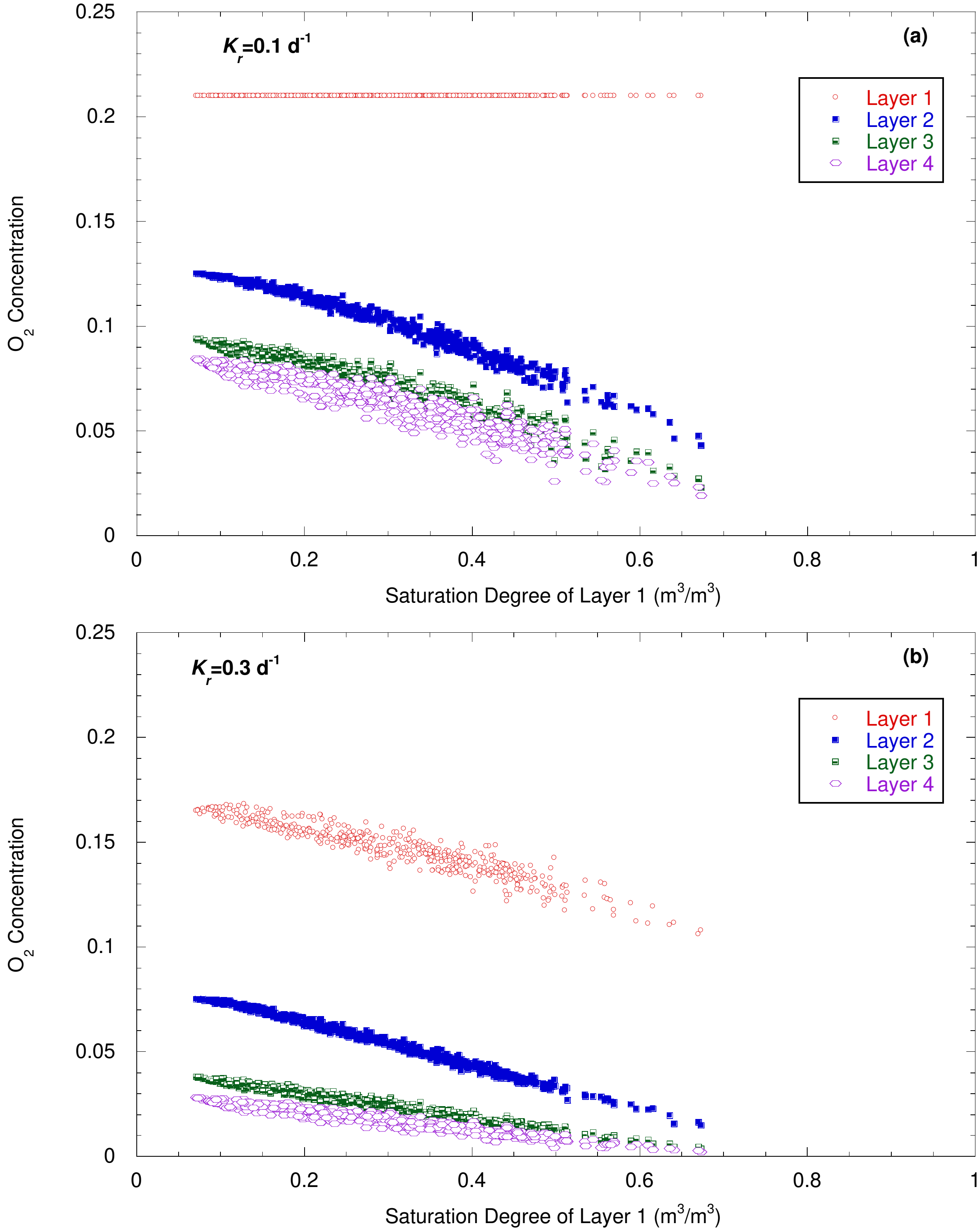

Fig. 5.13. Relationship between saturation degree of the Layer 1 (0.5 m deep) and oxygen concentration at different layers of GeoWaste pile over 48 years of simulation considering: (a) K_r=0.1 d^{-1}, and (b) K_r=0.3 d^{-1}.

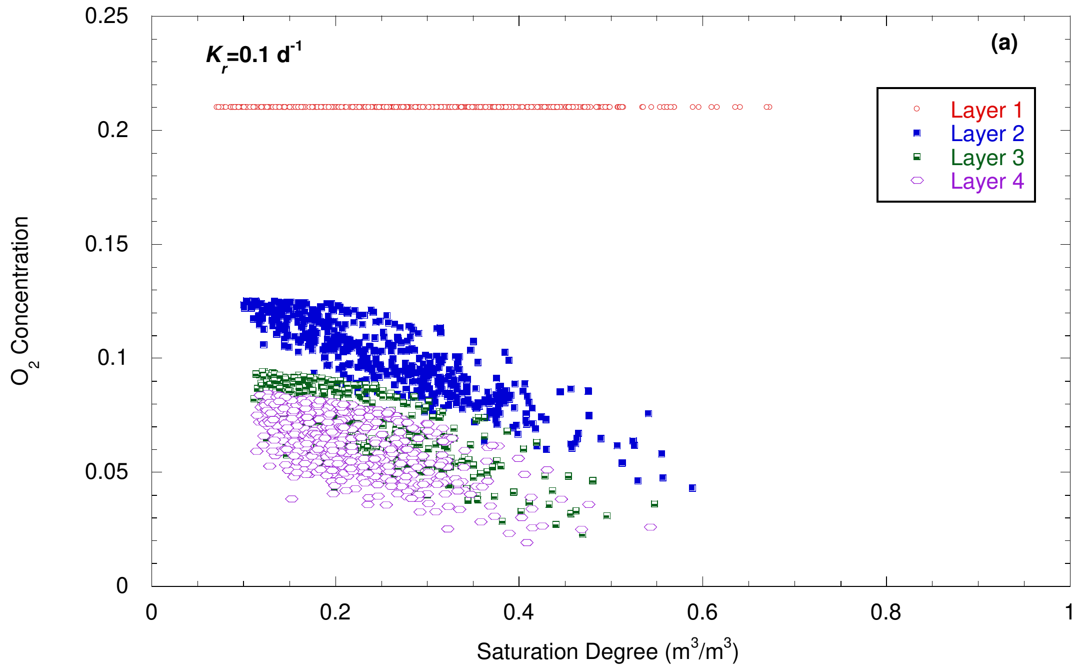

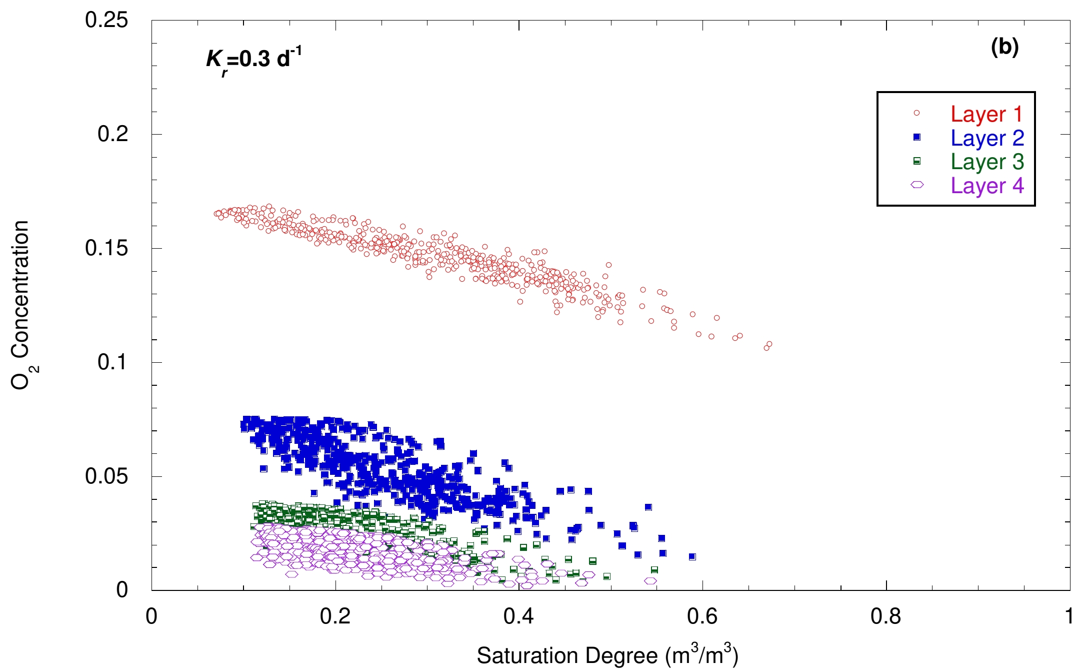

Fig. 5.14. Relationship between saturation degree and oxygen concentration of each layer of GeoWaste pile over 48 years of simulation considering: (a) K_r=0.1 d^{-1}, and (b) K_r=0.3 d^{-1}.

6 FUTURE RESEARCH

This study focused on GeoWaste (GW) and waste rock (WR) test piles constructed at a mine in Central America. The test piles were constructed to evaluate the hypothesis that ***GeoWaste can suppress sulfide oxidation and production of metal-rich acid mine generation relative to potentially-acid generating waste rock***. This study included four objectives: (i) evaluate and compare hydrologic and environmental behavior of the GW and WR piles under natural climatic conditions; (ii) determine in situ hydraulic conductivity and dry densities of the GW and WR piles; (iii) determine saturated hydraulic conductivity and soil water retention parameters of the GW and WR piles via numerical inverse solutions of an infiltration test; and (iv) predict volumetric water content and oxygen concentration within the test piles to compare with 26-months of in situ monitoring data. Conclusions related to each objective are at the end of Chapters 2, 3, 4, and 5.

This research enhances the current understanding of the hydraulic and environmental behavior of GeoWaste; however, a thorough understanding of mine waste management that includes GeoWaste relative to traditional tailings and waste rock management approaches requires additional research on abroad range of topics (e.g., mechanical and environmental), materials (e.g., tailings and waste rock particle-size distribution and acid generation potential), and site location (from arid to humid). The followings are two research projects that are proposed as examples to continue GeoWaste-related research.

6.1 Application of GeoWaste as Water Balance Covers

The goal of this task is to evaluate the use of GeoWaste as a water balance cover material under natural climate conditions for final closure of mine waste. An effective water balance cover system shall provide long-term resistance to percolation of precipitation and ingress of oxygen into underlying waste. A capillary barrier cover is a type of water balance cover that works based on soil-atmosphere interaction in the top of the cover (ground surface) and capillary boundary condition at the bottom of cover. A capillary barrier cover has the potential to reduce percolation and oxygen ingress relative to a monolithic water balance cover (all else being equal) based on the capacity to enhance water retention. Thus, evaluating the potential of GeoWaste as a capillary cover material is proposed.

Twelve columns were constructed for this study as shown in Table 6.1 and Fig. 6.1 and monitoring was initiated in September of 2018. A schematic of the columns is shown in Fig. 6.2. Each column was instrumented with three moisture content sensors, one thermocouple, one water potentiometer sensor, and in addition, four columns include oxygen sensors (Fig. 6.2). The volume and pH of percolated water from the bottom of each column will be measured weekly. Columns will be monitored for at least two more years and enhanced precipitation will be added to columns via irrigation. Columns are designed to address the following variables:

- The effect of mixture ratio on percolation rate of capillary barrier covers will be investigated by comparing Columns 1, 2, 5 and 8 (R = 0, 0.4, 1.0, and ∞) for mine waste from Mine P and Columns 3, 4, 7, and 9 (R = 0, 0.4, 1.0, and ∞) for mine waste from Mine M;
- The effect of GeoWaste density on percolation rate of capillary barrier covers will be investigated by comparing Columns 6, 10, and 11 (85 %, 90 %, and 95 % of $\gamma_{d\text{-}max}$);
- The effect of material type on percolation rate of capillary barrier covers will be investigated by comparing (i) tailings only Columns 8 and 9, (ii) GeoWaste Columns 1, 2, 3, and 4, (iii) waste rock only Columns 5 and 7, and (iv) natural soil Column 12; and
- The effectiveness of a GeoWaste capillary barrier cover at limiting oxygen ingress and generation of low pH effluent will be investigated by comparing Columns 2, 5, 6, and 7.

6.2 Effect of Mine Waste Materials and Climate

The goal of this proposed research is to compare the behavior of GeoWaste and waste rock piles using mine waste from another source and under different climatic conditions. One waste rock and one GeoWaste pile were constructed at a mine site in North America and monitoring initiated in summer of 2017. The main differences between mine waste in this study and the proposed study include the following: (i) waste rock in the North America mine site have no fines, which can provide more distinct hydraulic behavior difference between GeoWaste and waste rock piles; and (ii), although some sulphide minerals were identified in mine waste at the North America mine site, both tailings and waste rock are categorized as non-acid generating materials.

A similar analysis as carried out in this project can be applied to analyze the North America mine site.

- In situ testing to determine hydraulic properties (i.e., hydraulic conductivity and soil water characteristic curve) via sealed-double ring infiltrometers (SDRI) and monitoring of the wetting front via the in-place water content sensors.
- Destructive sampling to determine in situ characteristics of the test piles (e.g., density, water content, void ratio, and waste rock to tailings mixture ratio) and spatial variability in these characteristics.
- Verification that hydraulic parameters and material characteristics can be used to predict observed behavior in the 2-year test pile experiment.
- Overall comparison between GeoWaste piles constructed in two mine sites.

Table 6.1. Summary of the column tests.

Column Number	Cover Type	Storage Layer Material	*R* of Storage Layer	Density of storage layer (% of $\gamma_{d\text{-}max}$)	Capillary Layer Material	Oxygen Sensor
1	Capillary	P-GeoWaste	0.4	85	NON-PAG Waste Rock	No
2	Capillary	P-GeoWaste	1.0	85	NON-PAG Waste Rock	Yes
3	Capillary	M-GeoWaste	0.4	85	NON-PAG Waste Rock	No
4	Capillary	M-GeoWaste	1.0	85	NON-PAG Waste Rock	No
5	Monolithic	Non-PAG Waste Rock	∞	85	NA	Yes
6	Capillary	P-GeoWaste	1.0	85	PAG Waste Rock	Yes
7	Monolithic	PAG Waste Rock	∞	85	NA	Yes
8	Capillary	P-Tailings	0.0	85	NON-PAG Waste Rock	No
9	Capillary	M-Tailings	0.0	85	NON-PAG Waste Rock	No
10	Capillary	P-GeoWaste	1.0	90	NON-PAG Waste Rock	No
11	Capillary	P-GeoWaste	1.0	95	NON-PAG Waste Rock	No
12	Capillary	Natural Fort Collins Soil	NA	85	NON-PAG Waste Rock	No

R = mixture ratio, PAG = potentially acid generating, NA = not applicable, $\gamma_{d\text{-}max}$ = maximum dry density.

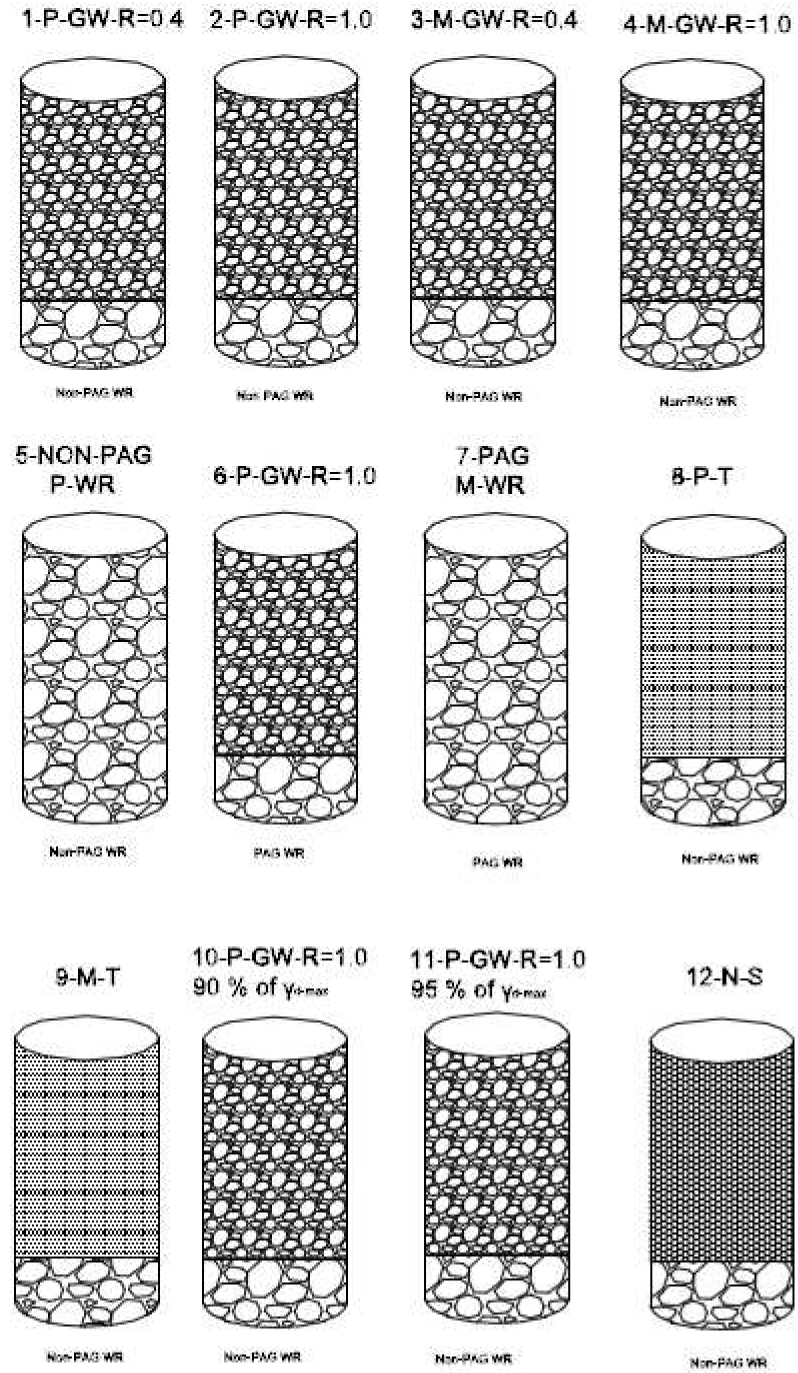

Fig. 6.1. List of constructed columns. GW = GeoWaste, *R* = mixture ratio, WR = waste rock, T = tailings.

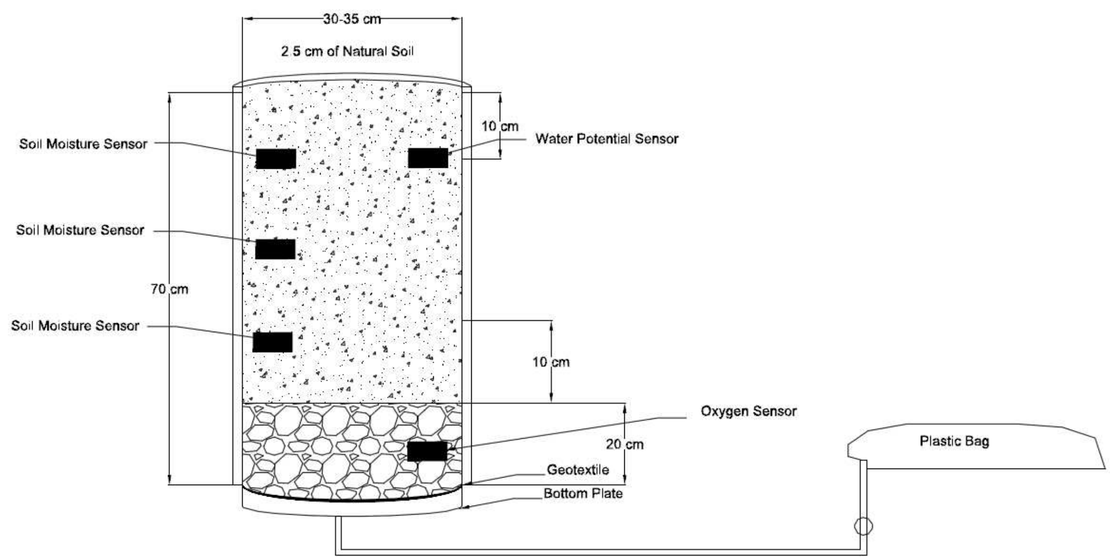

Fig. 6.2. Schematic of the column design.

REFERENCES

Akcil, A., and Koldas, S. (2006). Acid mine drainage (AMD): causes, treatment and case studies. *Journal of cleaner production*, *14*(12-13), 1139-1145.

Albright, W. H., Benson, C. H., and Waugh, W. J. (2010). Water balance covers for waste containment: principles and practice. American Society of Civil Engineers, Reston, VA.

ASTM. (2007). Standard test method for particle-size analysis of soils. *D 422-63*, West Conshohocken, PA.

ASTM. (2014a). Standard test methods for liquid limit, plastic limit, and plasticity index of soils. *D4318-10*, West Conshohocken, PA.

ASTM. (2014b). Standard test methods for laboratory compaction characteristics of soil using standard effort (12400ft-lbf/ft3 (600 kN-m/m3)). *D698-12*, West Conshohocken, PA.

Aubertin, M., Bussiere, B., and Chapuis, R. P. (1996). Hydraulic conductivity of homogenized tailings from hard rock mines. *Canadian Geotechnical Journal*, *33*(3), 470-482.

Bareither, C. A., Gorakhki, M. H., Scalia, J., and Jacobs, M. (2018). Compression and hydraulic behavior of filtered tailings and waste rock mixtures, In *Proceeding of Tailings and Mine Waste 2018, Keystone, Colorado*.

Benson, C. H., and Bareither, C. A. (2012). Designing water balance covers for sustainable waste containment: Transitioning state of the art to state of the practice. In *Geotechnical Engineering State of the Art and Practice: Keynote Lectures from GeoCongress 2012*.

Blight, G. (2009). Geotechnical engineering for mine waste storage facilities, Taylor & Francis, London, UK.

Blowes, D. W., Ptacek, C. J., Jambor, J. L., and Weisener, C. G. (2003). The geochemistry of acid mine drainage. *Treatise on geochemistry*, *9*, 612.

Borja Castillo, R. N. (2019). Undrained shear behavior and critical state analysis of mixed mine waste rock and tailings (M.S. thesis, Colorado State University).

Burden, R.N., Williams, D., Ward W. (2017). Summary of results for the University of Alberta/University of Queensland, Eco-tails Testing Program, Draft. Department of Civil & Environmental Engineering, University of Alberta.

Bussière, B. (2007). Colloquium 2004: Hydrogeotechnical properties of hard rock tailings from metal mines and emerging geoenvironmental disposal approaches. *Canadian Geotechnical Journal*, *44*(9), 1019-1052.

Bussière, B, and Aubertin, M. (1999). Clean tailings as cover material for preventing acid mine drainage: an in situ experiment. In *Proceedings of Sudbury* (Vol. 99, pp. 19-28).

Collin, M. 1987. Mathematical modeling of water and oxygen transport in layered soil covers for deposits of pyritic mine tailings. Licenciate Treatise. *Royal Institute of Technology. Department of Chemical Engineering. S-10044 Stockholm, Sweden*.

Daliri, F., Kim, H., Simms, P., and Sivathayalan, S. (2014). Impact of desiccation on monotonic and cyclic shear strength of thickened gold tailings. *Journal of Geotechnical and Geoenvironmental Engineering*, *140*(9), 04014048.

Davies, M. (2011). Filtered dry stacked tailings–the fundamentals. In *Proceedings tailings and mine waste Conference*, BC, Canada.

Elberling, B., Nicholson, R. V., Reardon, E. J., and Tibble, R. (1994). Evaluation of sulphide oxidation rates: a laboratory study comparing oxygen fluxes and rates of oxidation product release. *Canadian Geotechnical Journal*, *31*(3), 375-383.

Gorakhki, M. H., Bareither, C. A., Scalia, J., Aparacio, M., and Jacobs, M. (2019). In situ hydraulic conductivity testing of a GeoWaste test pile. In *Proceedings of Tailings and Mine Waste 2019*, Keystone, Colorado.

Hamade, M. M., and Bareither, C. A. (2018). Consolidated undrained shear behavior of synthetic waste rock and synthetic tailings mixtures. *Geotechnical Testing Journal*, *42*(5), 1207-1232.

Harries, J. R., and Ritchie, A. I. M. (1985). Pore gas composition in waste rock dumps undergoing pyritic oxidation. *Soil Science*, *140*(2), 143-152.

Hilhorst, M. A. (2000). A pore water conductivity sensor. *Soil Science Society of America Journal*, *64*(6), 1922-1925.

Jehring, M.M. and Bareither, C.A. (2016). Tailings composition effects on shear strength behavior of co-mixed mine waste rock and tailings, *Acta Geotechnica*, 11(5), 1147-1166.

Johnson, D. B., and Hallberg, K. B. (2005). Acid mine drainage remediation options: a review. *Science of the total environment*, *338* (1-2), 3-14.

Khalili, A., Wijewickreme, D., and Wilson, W. (2010). Mechanical response of highly gap-graded mixtures of waste rock and tailings. Part I: Monotonic shear response, *Canadian Geotechnical Journal*, 47(5), 552-565.

Leduc, M., Backens, M., and Smith, M. E. (2004). Tailings co-disposal at the Esquel gold mine Patagonia, Argentina. In *Proceedings of the SME Annual Meeting, Denver, Colorado,* 23-25.

Matyas, E. L., Welch, D. E., and Reades, D. W. (1984). Geotechnical parameters and behaviour of uranium tailings. *Canadian Geotechnical Journal*, *21*(3), 489-504.

Millington, R. J., and Quirk, J. P. (1961). Permeability of porous solids. *Transactions of the Faraday Society*, *57*, 1200-1207.

Morgenstern, N.R., Vick, S.G., and Van Zyl, D. (2015). Report on Mount Polley tailings storage facility breach. Report of independent expert engineering investigation and review panel. Prepared on behalf of the British Columbia government and the Williams Lake and Soda Creek Indian Bands.

Morgenstern, N.R., Vick, S.G., Viotti, C.B., and Watts, B.D. (2016). Fundão Tailings Dam Review Panel Report on the Immediate Causes of the Failure of the Fundão Dam. *SAMARCO, SA, Vale, SA, Eds*, 76.

Penman, H. L. (1940). Gas and vapour movements in the soil: I. The diffusion of vapours through porous solids. *The Journal of Agricultural Science*, *30*(3), 437-462.

Qiu, Y., and Sego, D. C. (2001). Laboratory properties of mine tailings. *Canadian Geotechnical Journal*, 38(1), 183-190.

Robertson, P. K., Melo, L. D., Williams, D. J., and Wilson, W. (2019). Report of the expert panel on the technical causes of the failure of Feijao Dam I.

Simms, P., Williams, M. P. A., Fitton, T. G., and McPhail, G. (2011). Beaching angles and evolution of stack geometry for thickened tailings-a review. *In Proceedings of the 14th International Conference on Paste and Thickened Tailings, Edited by R. Jewell and A. Foruie, Perth, Australia*, 171-190.

Tutu, H., McCarthy, T. S., and Cukrowska, E. (2008). The chemical characteristics of acid mine drainage with particular reference to sources, distribution and remediation: The Witwatersrand Basin, South Africa as a case study. *Applied Geochemistry*, *23*(12), 3666-3684.

Wickland, B.E., and Wilson, G.W. (2005). Self-weight consolidation of mixtures of mine waste rock and tailings, *Canadian Geotechnical Journal*, 42(2), 327-339.

Wickland, B.E., Wilson, G.W., Wijewickreme, D., and Klein, B. (2006). Design and evaluation of mixtures of mine waste rock and tailings, *Canadian Geotechnical Journal*, 43(9), 928-945.

Wickland, B. E., Wilson, G. W., and Wijewickreme, D. (2010). Hydraulic conductivity and consolidation response of mixtures of mine waste rock and tailings. *Canadian Geotechnical Journal*, *47*(4), 472-485.

Williams, D.J., Wilson, G.W., and Panidis, C. (2003). Waste rock and tailings mixtures as a possible seal for potentially acid forming waste rock. In *Proceeding of 6th International Conference on Acid Rock Drainage,* Cairns, QLD, 427-435.

Yilmaz, E. (2011). Advances in reducing large volumes of environmentally harmful mine waste rocks and tailings. *Gospodarka Surowcami Mineralnymi*, *27*, 89-112.

.

APPENDIX I: SUMMARY OF SENSORS IN THE GEOWASTE AND WASTE ROCK PILES

Table I-1. Sensors in the GeoWaste and Waste Rock piles and period sensors were functional.

Waste rock pile				GeoWaste pile			
Sensor	Layer	Location	Active periods (d)	Sensor	Layer	Location	Active periods (d)
TDR(A1)	4	Southwest	(0-121) & (213-484)	TDR(B1)	4	Southwest	(0-776)
TDR(A2)	4	Northwest	(0-121) & (213-484)	TDR(B2)	4	Northwest	(0-776)
TDR(A3)	4	Northeast	(0-121) & (213-484)	TDR(B3)	4	Northeast	(0-776)
TDR(A4)	4	Southeast	(0-121) & (213-484)	TDR(B4)	4	Southeast	(0-776)
TDR(A5)	4	Center	(0-121) & (213-484)	TDR(B5)	4	Center	(0-776)
TDR(A6)	3	Southwest	(0-121) & (213-303)	TDR(B6)	3	Southwest	(0-506)
TDR(A7)	3	Northwest	(0-121) & (213-484)	TDR(B17)	3	Northwest	(0-506)
TDR(A8)	3	Northeast	(0-121) & (213-484)	TDR(B8)	3	Northeast	(0-776)
TDR(A9)	3	Southeast	(0-121) & (213-776)	TDR(B9)	3	Southeast	(0-776)
TDR(A10)	3	Center	(0-121) & (213-484)	TDR(B10)	3	Center	(0-776)
TDR(A11)	2	Southwest	(0-121) & (213-484)	TDR(B11)	2	Southwest	(0-506)
TDR(A12)	2	Northwest	(0-121) & (213-484)	TDR(B12)	2	Northwest	(0-506)
TDR(A13)	2	Northeast	(0-121) & (213-484)	TDR(B13)	2	Northeast	(0-776)
TDR(A14)	2	Southeast	(0-121) & (213-484)	TDR(B14)	2	Southeast	(0-776)
TDR(A15)	2	Center	(0-121) & (213-484)	TDR(B15)	2	Center	(0-776)
TDR(A16)	1	Southwest	(0-121) & (213-484)	TDR(B16)	1	Southwest	(0-776)
TDR(A17)	1	Northwest	(0-121) & (213-484)	TDR(B17)	1	Northwest	(0-121) & (210-698)
TDR(A18)	1	Northeast	(0-121) & (213-484)	TDR(B18)	1	Northeast	(0-121) & (210-776)
TDR(A19)	1	Southeast	(0-121) & (213-484)	TDR(B19)	1	Southeast	(0-121) & (210-776)
TDR(A20)	1	Center	(0-121) & (213-484)	TDR(B20)	1	Center	(0-121) & (210-776)
O_2(A1)	4	Southwest	(0-121) & (213-776)	O_2(B1)	4	Southwest	(0-776)
O_2(A2)	4	Northwest	(0-121) & (213-776)	O_2(B2)	4	Northwest	(0-776)
O_2(A3)	4	Northeast	(0-121) & (213-776)	O_2(B3)	4	Northeast	(0-776)
O_2(A4)	4	Southeast	(0-121) & (213-776)	O_2(B4)	4	Southeast	(0-776)
O_2(A5)	4	Center	(0-121) & (213-776)	O_2(B5)	4	Center	(0-776)
O_2(A6)	3	Southwest	(0-121) & (213-776)	O_2(B6)	3	Southwest	(0-776)
O_2(A7)	3	Northwest	(0-121) & (213-776)	O_2(B7)	3	Northwest	(0-776)
O_2(A8)	3	Northeast	(0-121) & (213-776)	O_2(B8)	3	Northeast	(0-776)
O_2(A9)	3	Southeast	(0-121) & (213-776)	O_2(B9)	3	Southeast	(0-776)
O_2(A10)	3	Center	(0-121) & (213-776)	O_2(B10)	3	Center	(0-776)
O_2(A11)	2	Southwest	(0-121) & (213-776)	O_2(B11)	2	Southwest	(0-776)
O_2(A12)	2	Northwest	(0-121) & (213-776)	O_2(B12)	2	Northwest	(0-776)
O_2(A13)	2	Northeast	(0-121) & (213-776)	O_2(B13)	2	Northeast	(0-776)
O_2(A14)	2	Southeast	(0-121) & (213-776)	O_2(B14)	2	Southeast	(0-776)
O_2(A15)	2	Center	(0-121)	O_2(B15)	2	Center	(0-415)
O_2(A16)	1	Southwest	(0-121) & (213-776)	O_2(B16)	1	Southwest	(0-776)
O_2(A17)	1	Northwest	(0-121) & (213-776)	O_2(B17)	1	Northwest	(0-776)
O_2(A18)	1	Northeast	(0-121) & (213-776)	O_2(B18)	1	Northeast	(0-776)
O_2(A19)	1	Southeast	(0-121) & (213-776)	O_2(B19)	1	Southeast	(0-776)
O_2(A20)	1	Center	(0-121) & (213-776)	O_2(B20)	1	Center	(0-776)

APPENDIX II: TEMPORAL TRENDS OF VOLUMETRIC WATER CONTENT, TEMPERATURE, OXYGEN CONCENTRATION, AND ELECTRICAL CONDUCTIVITY MEASUREMENTS OF INDIVIDUAL MEASUREMENTS.

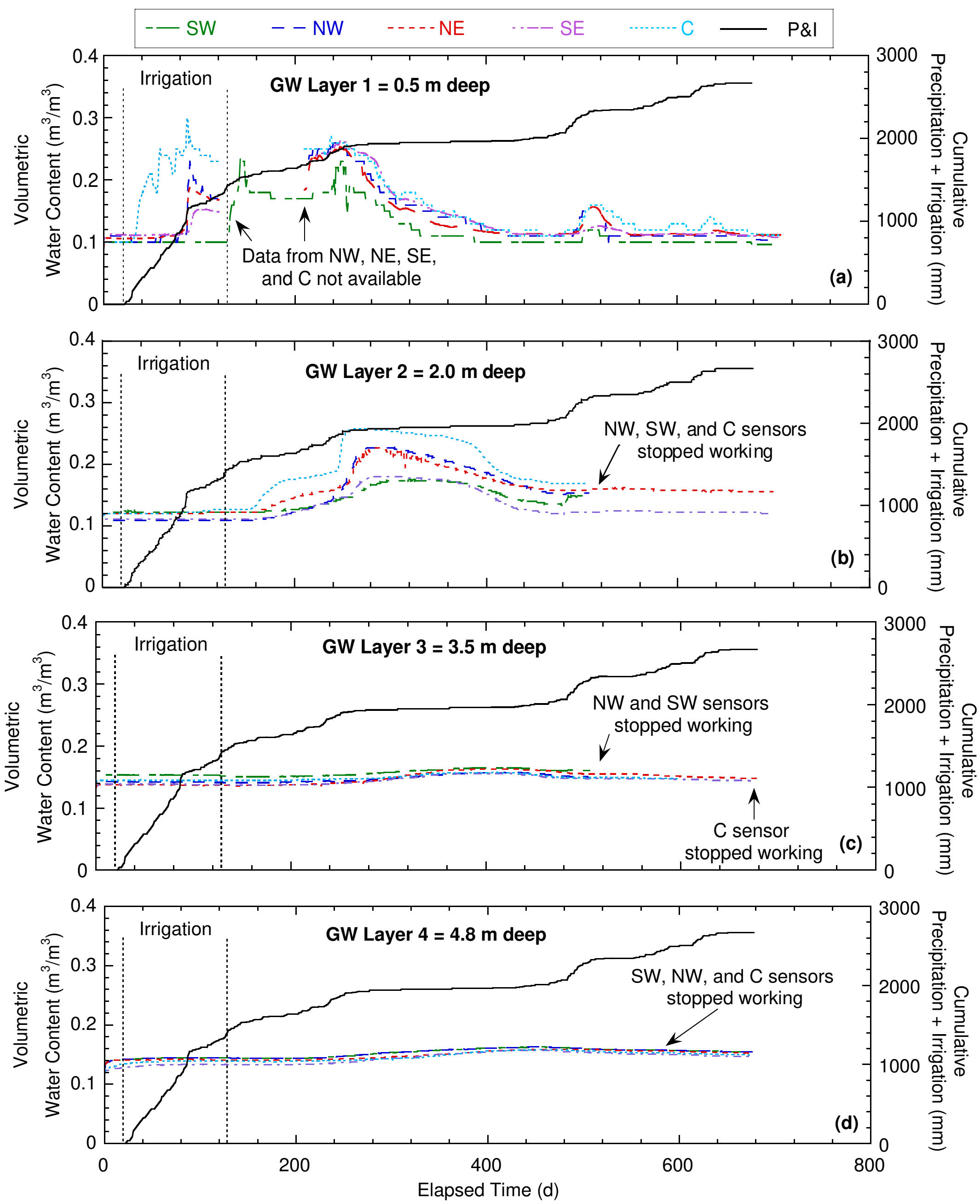

Fig. II.1. Temporal trends of volumetric water content measurements from five sensors in four different layers in the GeoWaste pile (a) Layer 1 = 0.5 m deep, (b) Layer 2 = 2 m deep, (c) Layer 3 = 3.5 m deep, and (d) Layer 4 = 4.8 m deep. All depths relative to original surface elevation. Sensors for each layer are labeled based on their spatial location in plan view: Center (C), Northwest (NW), Northeast (NE), Southwest (SW), and Southeast (SE). Cumulative precipitation and irrigation (P&I) on the surface of the pile is included for comparison in each plot.

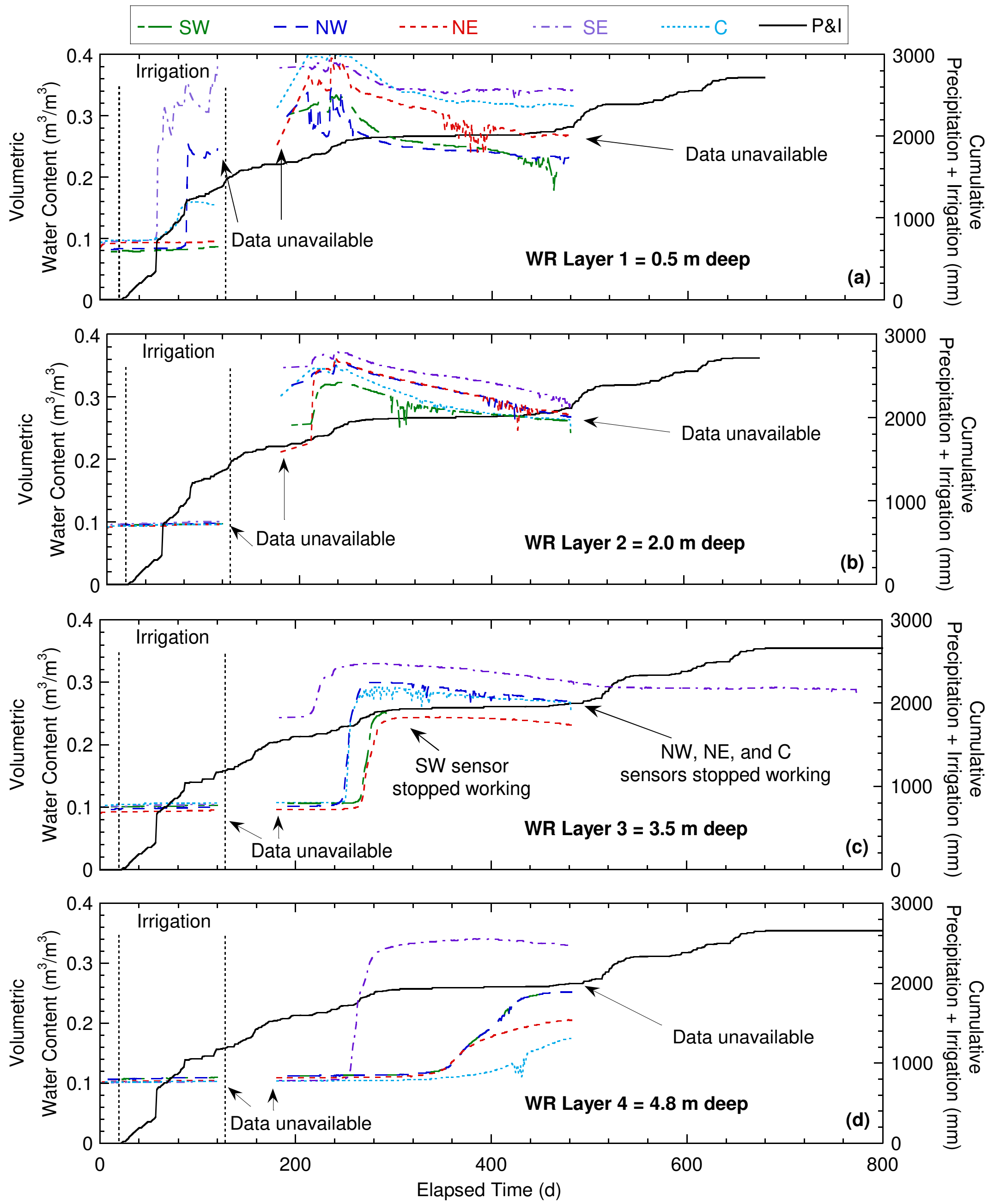

Fig. II.2. Temporal trends of volumetric water content measurements from five sensors in four different layers in the waste rock pile (a) Layer 1 = 0.5 m deep, (b) Layer 2 = 2 m deep, (c) Layer 3 = 3.5 m deep, and (d) Layer 4 = 4.8 m deep. All depths relative to original surface elevation.

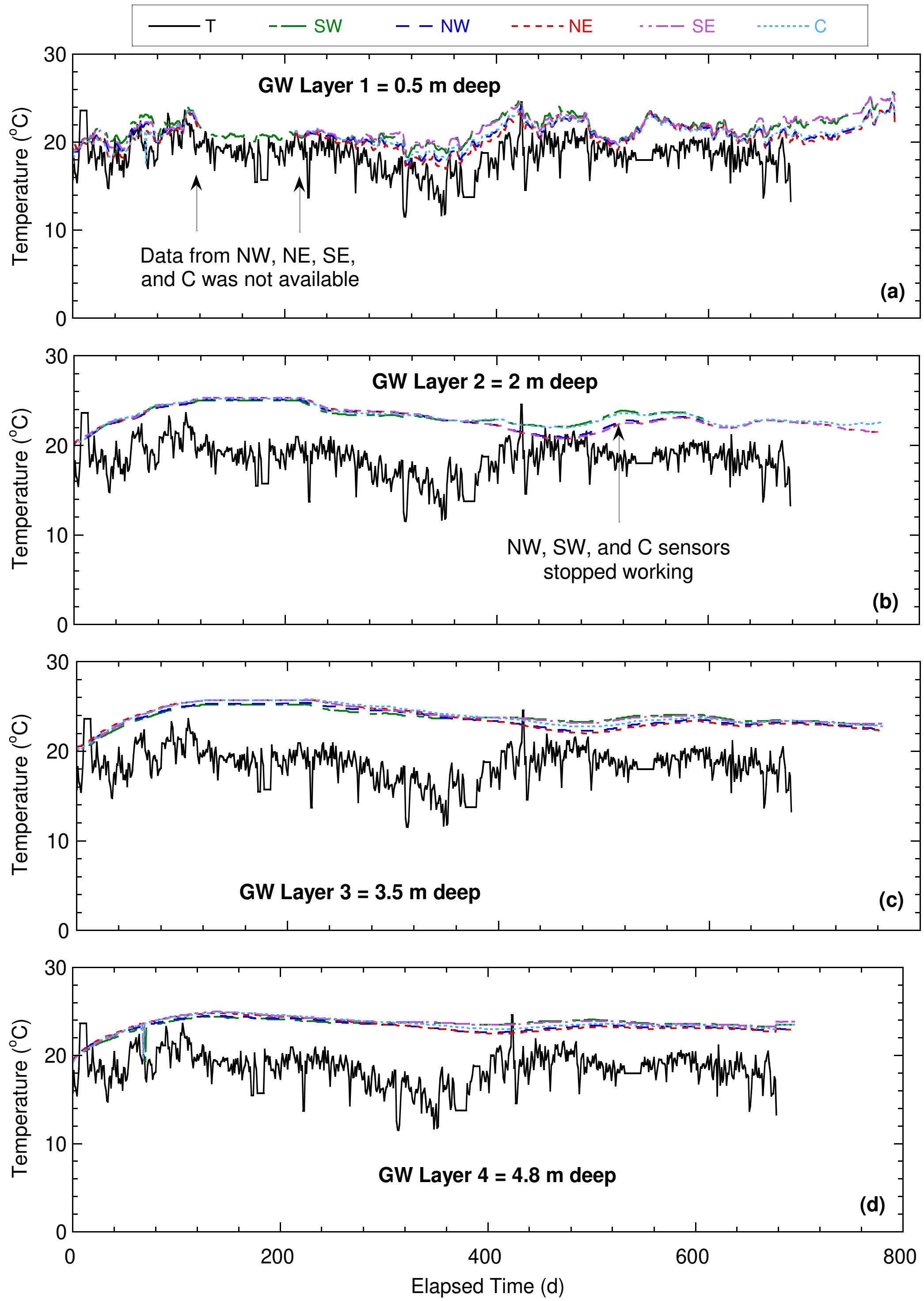

Fig. II.3. Temporal trends of temperature measurements from five sensors in four different layers in the GeoWaste pile (a) Layer 1 = 0.5 m deep, (b) Layer 2 = 2 m deep, (c) Layer 3 = 3.5 m deep, and (d) Layer 4 = 4.8 m deep. All depths relative to original surface elevation. T = atmospheric temperature.

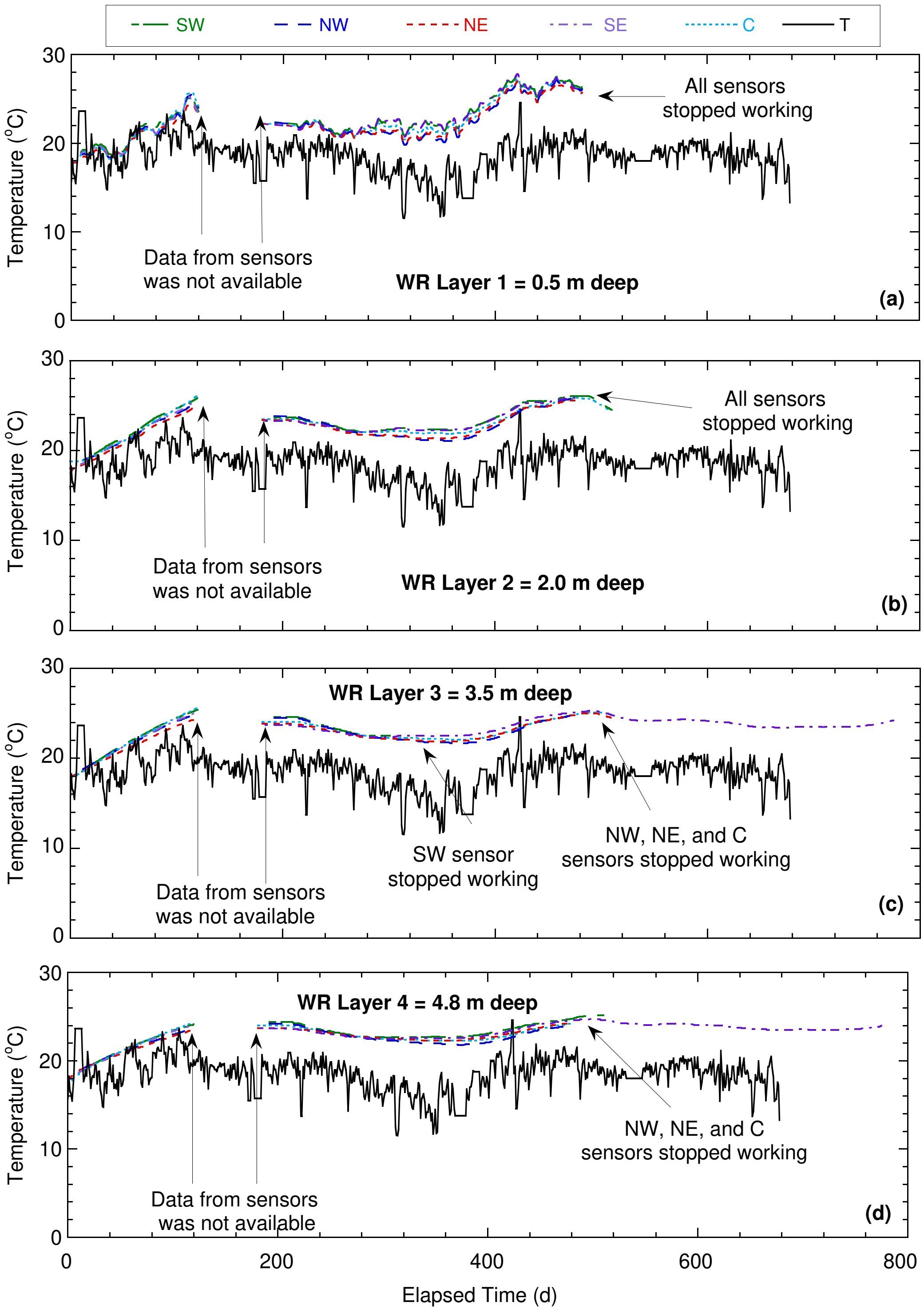

Fig. II.4. Temporal trends of temperature measurements from five sensors in four different layers in the waste rock pile (a) Layer 1 = 0.5 m deep, (b) Layer 2 = 2 m deep, (c) Layer 3 = 3.5 m deep, and (d) Layer 4 = 4.8 m deep. All depths relative to original surface elevation. T = atmospheric temperature.

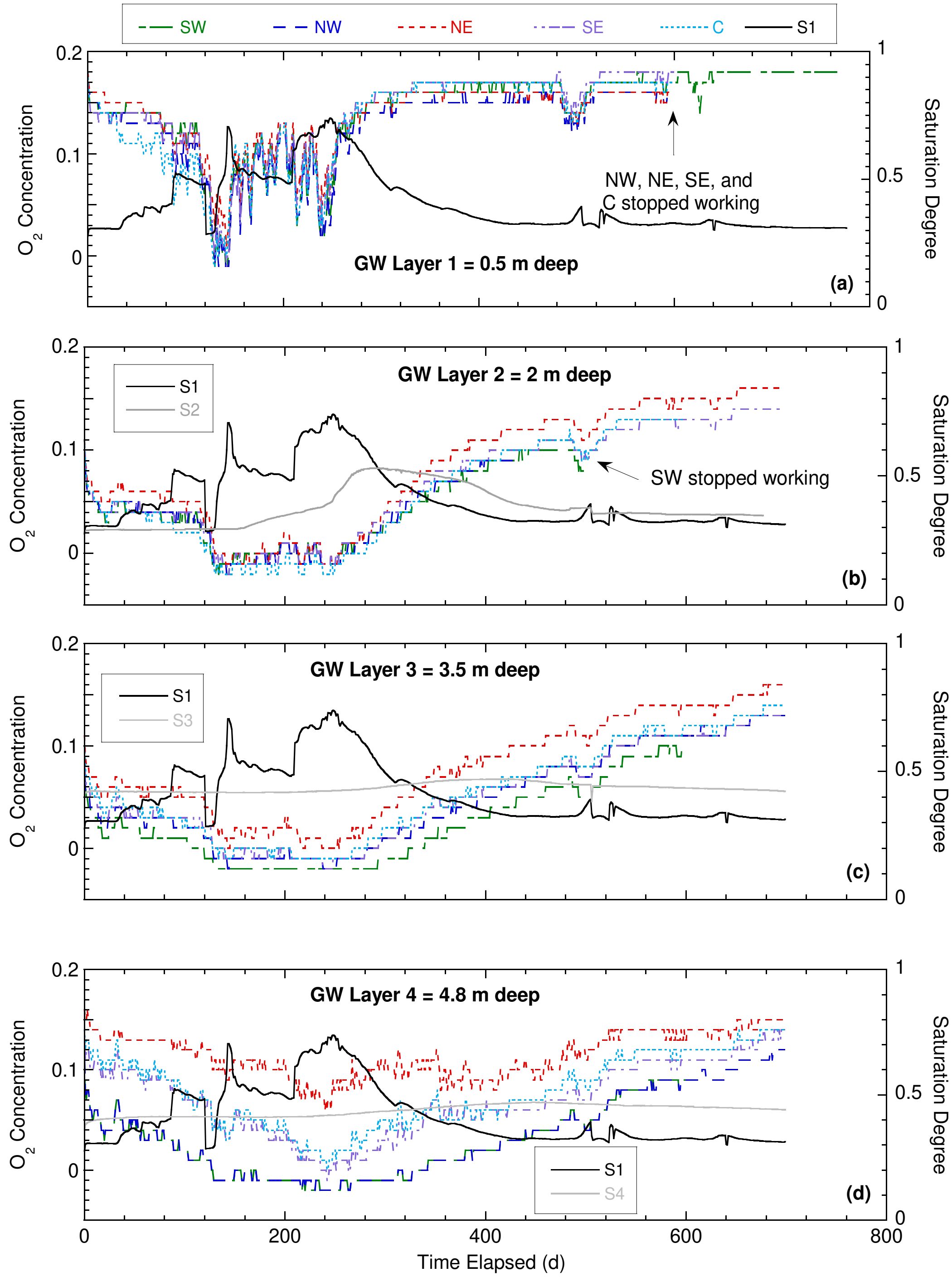

Fig. II.5. Temporal trends of oxygen concentration measurements from five sensors in four different layers in the waste rock pile (a) Layer 1 = 0.5 m deep, (b) Layer 2 = 2 m deep, (c) Layer 3 = 3.5 m deep, and (d) Layer 4 = 4.8 m deep. All depths relative to original surface elevation. Saturation degree of different layers is included for comparison in each plot. S1, S2, S3, and S4 = saturation degree in the first, second, third, and fourth layers respectively.

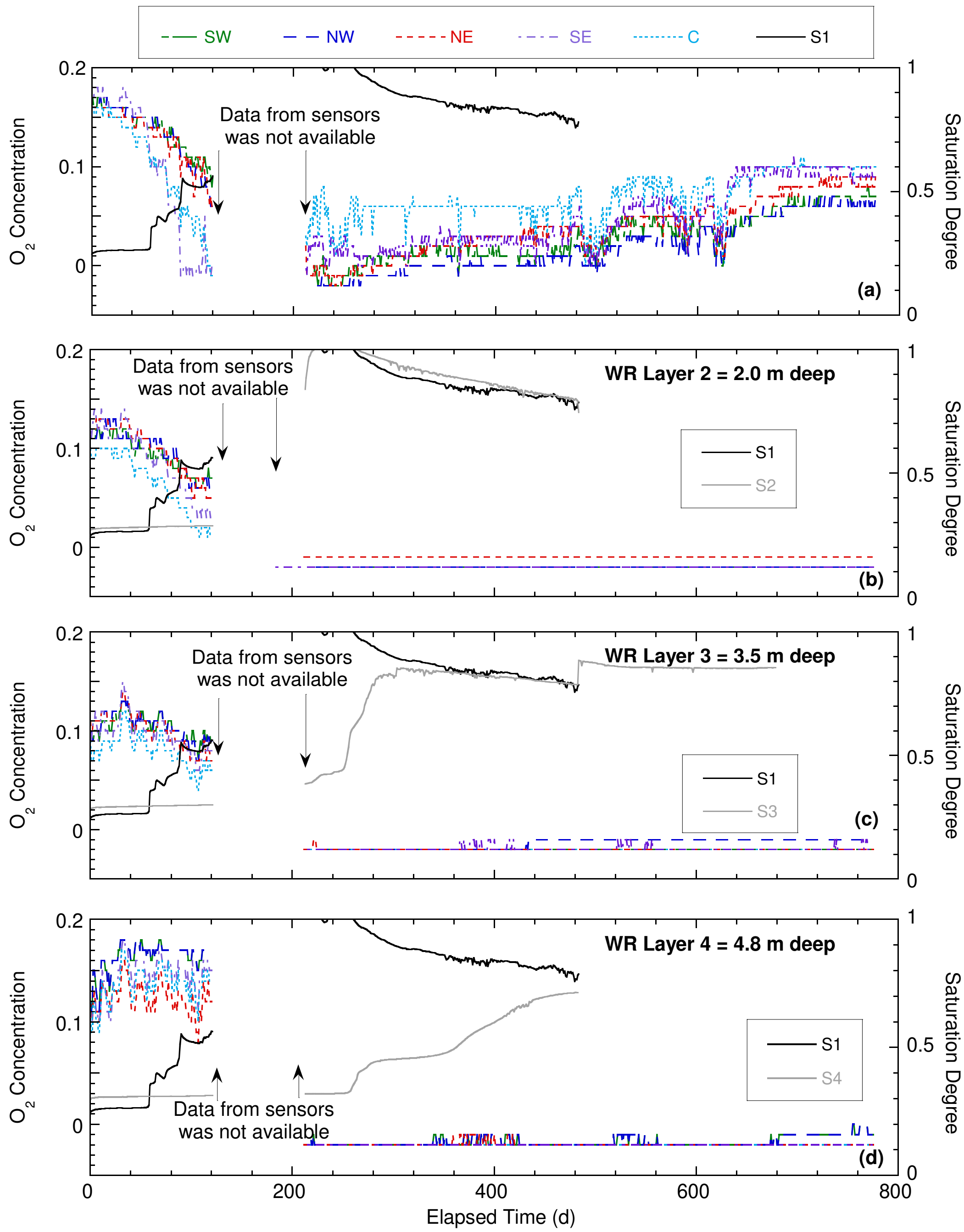

Fig. II.6. Temporal trends of oxygen concentration measurements from five sensors in four different layers in the waste rock pile (a) Layer 1 = 0.5 m deep, (b) Layer 2 = 2 m deep, (c) Layer 3 = 3.5 m deep, and (d) Layer 4 = 4.8 m deep. All depths relative to original surface elevation. Saturation degree of different layers is included for comparison in each plot. S1, S2, S3, and S4 = saturation degree in the first, second, third, and fourth layers respectively.

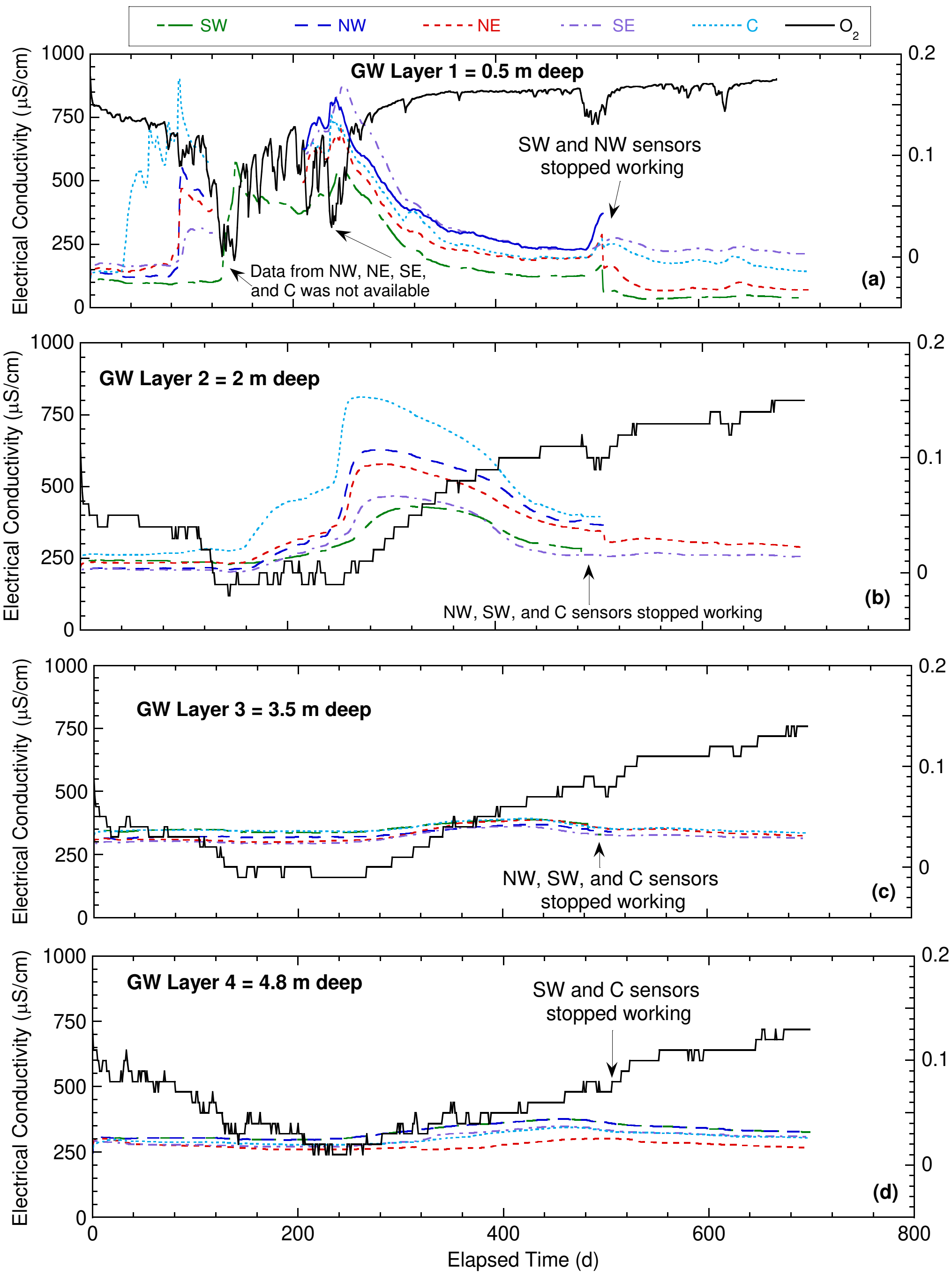

Fig. II.7. Temporal trends of electrical conductivity (EC) measurements from five sensors in four different layers in the GeoWaste pile. Oxygen (O_2) concentrations of different layers is included for comparison in each plot.

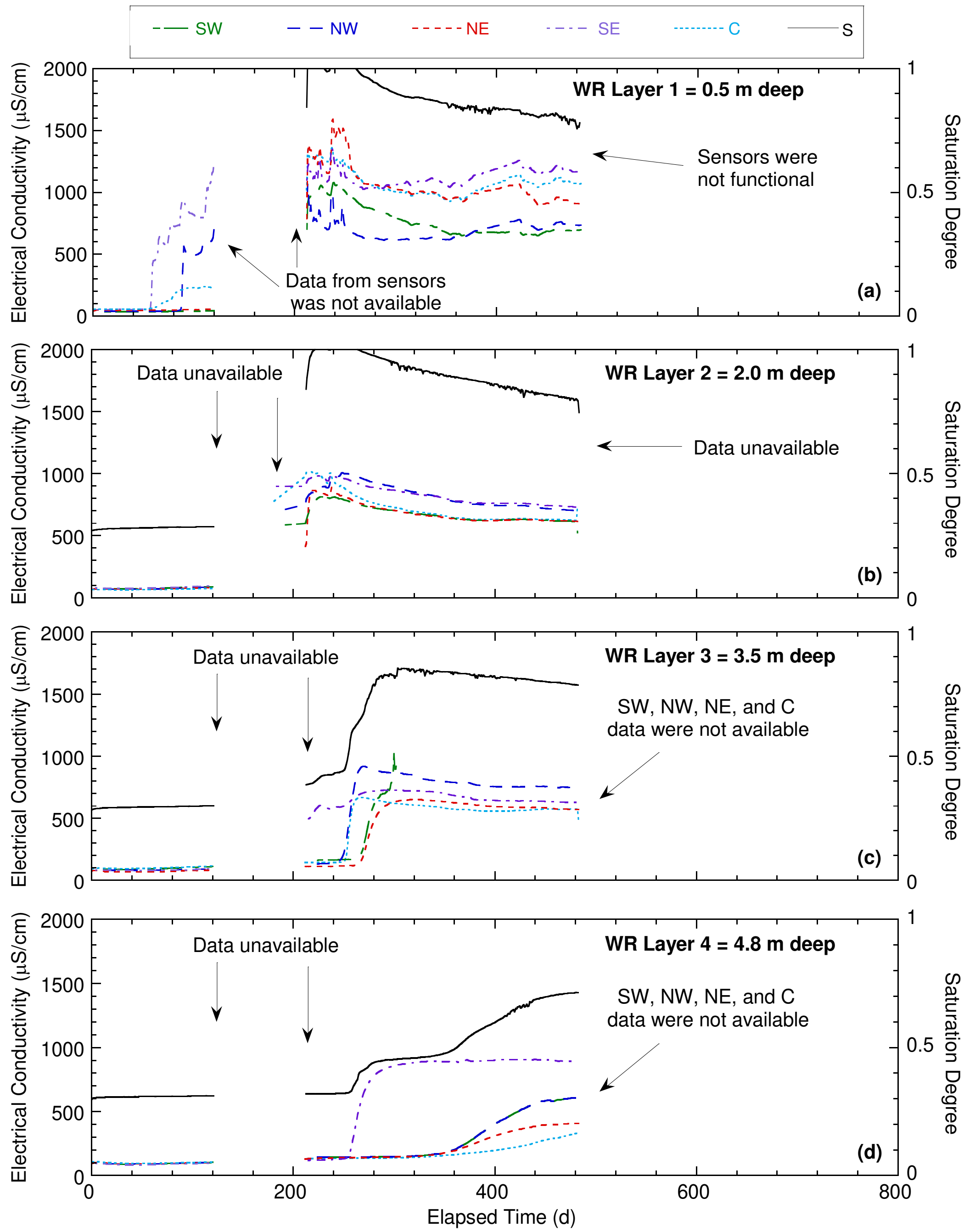

Fig. II.8. Temporal trends of electrical conductivity (EC) measurements from five sensors in four different layers in the waste rock pile. Saturation degree of different layers is included for comparison in each plot. S = saturation degree.